

MIMO Antenna Design and Channel Modeling

Guest Editors: Wenhua Chen, Manos M. Tentzeris, Yuan Yao, Yan Zhang, and Li Yang





MIMO Antenna Design and Channel Modeling

International Journal of Antennas and Propagation

MIMO Antenna Design and Channel Modeling

Guest Editors: Wenhua Chen, Manos M. Tentzeris, Yuan Yao,
Yan Zhang, and Li Yang



Copyright © 2012 Hindawi Publishing Corporation. All rights reserved.

This is a special issue published in “International Journal of Antennas and Propagation.” All articles are open access articles distributed under the Creative Commons Attribution License, which permits unrestricted use, distribution, and reproduction in any medium, provided the original work is properly cited.

Editorial Board

- M. Ali, USA
Charles Bunting, USA
Felipe Catedra, Spain
Dau-Chyrh Chang, Taiwan
Deb Chatterjee, USA
Z. N. Chen, Singapore
Michael Yan Wah Chia, Singapore
Christos Christodoulou, USA
Shyh-Jong Chung, Taiwan
Lorenzo Crocco, Italy
Tayeb A. Denidni, Canada
Antonije R. Djordjevic, Serbia
Karu P. Esselle, Australia
Francisco Falcone, Spain
Miguel Ferrando, Spain
Vincenzo Galdi, Italy
Wei Hong, China
Hon Tat Hui, Singapore
Tamer S. Ibrahim, USA
Nemai Karmakar, Australia
- Se-Yun Kim, Republic of Korea
Ahmed A. Kishk, Canada
Tribikram Kundu, USA
Byungje Lee, Republic of Korea
Ju-Hong Lee, Taiwan
L. Li, Singapore
Yilong Lu, Singapore
Atsushi Mase, Japan
Andrea Massa, Italy
Giuseppe Mazzarella, Italy
Derek McNamara, Canada
C. F. Mecklenbräuker, Austria
Michele Midrio, Italy
Mark Mirotznik, USA
Ananda S. Mohan, Australia
P. Mohanan, India
Pavel Nikitin, USA
A. D. Panagopoulos, Greece
Matteo Pastorino, Italy
Massimiliano Pieraccini, Italy
- Sadasiva M. Rao, USA
Sembiam R. Rengarajan, USA
Ahmad Safaai-Jazi, USA
Safieddin Safavi-Naeini, Canada
Magdalena Salazar-Palma, Spain
Stefano Selleri, Italy
Krishnasamy T. Selvan, India
Zhongxiang Q. Shen, Singapore
John J. Shynk, USA
Mandeep Singh Jit Singh, Malaysia
Seong-Youp Suh, USA
Parveen Wahid, USA
Yuanxun Ethan Wang, USA
Daniel S. Weile, USA
Quan Xue, HongKong
Tat Soon Yeo, Singapore
Young Joong Yoon, Republic of Korea
Wenhua Yu, USA
Jong Won Yu, Republic of Korea
Anping Zhao, China

Contents

MIMO Antenna Design and Channel Modeling, Wenhua Chen, Manos M. Tentzeris, Yuan Yao, Yan Zhang, and Li Yang

Volume 2012, Article ID 570718, 2 pages

Reduced-Complexity Radio Architectures for Enhanced Receive Selection Combining in Multiuser Diversity Systems, Elpiniki P. Tsakalaki, Osama N. Alrabadi, Constantinos B. Papadias, and Ramjee Prasad

Volume 2012, Article ID 454210, 10 pages

Modified MIMO Cube for Enhanced Channel Capacity, Lajos Nagy

Volume 2012, Article ID 734896, 10 pages

Controlling Initial and Final Radii to Achieve a Low-Complexity Sphere Decoding Technique in MIMO Channels, atemeh Eshagh Hosseini and Shahriar Shirvani Moghaddam

Volume 2012, Article ID 192964, 9 pages

Compact Multiantenna, L. Rudant, C. Delaveaud, and P. Ciais

Volume 2012, Article ID 748070, 6 pages

Indoor Off-Body Wireless Communication: Static Beamforming versus Space-Time Coding, Patrick Van Torre, Maria Lucia Scarpello, Luigi Vallozzi, Hendrik Rogier, Marc Moeneclaey, Dries Vande Ginste, and Jo Verhaevert

Volume 2012, Article ID 413683, 13 pages

Tetraband Small-Size Printed Strip MIMO Antenna for Mobile Handset Application, Qinghao Zeng, Yuan Yao, Shaohua Liu, Junsheng Yu, Peng Xie, and Xiaodong Chen

Volume 2012, Article ID 320582, 8 pages

Virtual Antenna Array Analysis for MIMO Synthetic Aperture Radars, Wen-Qin Wang

Volume 2012, Article ID 587276, 10 pages

Novel Compact Multiband MIMO Antenna for Mobile Terminal, Cheng Yang, Yuan Yao, Junsheng Yu, and Xiaodong Chen

Volume 2012, Article ID 691681, 9 pages

Measurement-Based Analysis of Transmit Antenna Selection for In-Cabin Distributed MIMO System, Yan Zhang, Zhenghui Li, Fengyu Luan, Limin Xiao, Shidong Zhou, and Jing Wang

Volume 2012, Article ID 598049, 6 pages

Channel Parameter Estimation for Scatter Cluster Model Using Modified MUSIC Algorithm,

Jinsheng Yang, Xuzhao Wu, and Qing Wang

Volume 2012, Article ID 619817, 6 pages

A Novel Dual-Band MIMO Antenna with Lower Correlation Coefficient, Jian Zhang, Jun OuYang, Kai Zhi Zhang, and Feng Yang

Volume 2012, Article ID 512975, 7 pages

Spatial Correlation and Ergodic Capacity of MIMO Channel in Reverberation Chamber, Xiaoming Chen

Volume 2012, Article ID 939104, 7 pages

Effect of Polarization on the Correlation and Capacity of Indoor MIMO Channels, Hsun-Chang Lo, Ding-Bing Lin, Teng-Chieh Yang, and Hsueh-Jyh Li

Volume 2012, Article ID 246348, 11 pages

A New Generation Method for Spatial-Temporal Correlated MIMO Nakagami Fading Channel,

Qiu-Ming Zhu, Xiang-Bin Yu, Jun-Bo Wang, Da-Zhuan Xu, and Xiao-Min Chen

Volume 2012, Article ID 713594, 8 pages

Multiband Planar Monopole Antenna for LTE MIMO Systems, Yuan Yao, Xing Wang, and Junsheng Yu

Volume 2012, Article ID 890705, 6 pages

Design of Ultra-Wideband MIMO Antenna for Breast Tumor Detection, Liting Wang and Bin Huang

Volume 2012, Article ID 180158, 7 pages

Design of Compact Dual-Polarized Antennas for MIMO Handsets, Wenhua Chen, Xin Wang, and Zhenghe Feng

Volume 2012, Article ID 954742, 8 pages

Impact of Mutual Coupling and Polarization of Antennas on BER Performances of Spatial Multiplexing MIMO Systems, Jianfeng Zheng, Yue Li, and Zhenghe Feng

Volume 2012, Article ID 795205, 12 pages

Editorial

MIMO Antenna Design and Channel Modeling

Wenhua Chen,¹ Manos M. Tentzeris,² Yuan Yao,³ Yan Zhang,¹ and Li Yang⁴

¹ Department of Electronic Engineering, Tsinghua University, Beijing 100084, China

² The School of Electrical and Computer Engineering, Georgia Institute of Technology, Atlanta, GA 30332-0250, USA

³ School of Electronic Engineering, Beijing University of Posts and Telecommunications, Beijing 100876, China

⁴ High-Performance Analog Division, Texas Instruments, Dallas, TX 75266-0199, USA

Correspondence should be addressed to Wenhua Chen, chenwh@tsinghua.edu.cn

Received 31 October 2012; Accepted 31 October 2012

Copyright © 2012 Wenhua Chen et al. This is an open access article distributed under the Creative Commons Attribution License, which permits unrestricted use, distribution, and reproduction in any medium, provided the original work is properly cited.

The multiple-input multiple-output (MIMO) wireless technique represents a breakthrough in the use of antenna arrays in wireless systems. MIMO technology has attracted attention in wireless communications, because it offers significant increases in data throughput and link range without additional bandwidth or increased transmit power. It achieves this goal by spreading the same total transmit power over the antennas to achieve an array gain that improves the spectral efficiency (more bits per second per hertz of bandwidth) or to achieve a diversity gain that improves the link reliability (reduced fading). As demonstrated in Figures 1(a) and 1(b), the research topic on MIMO antenna design has become a quite popular field in wireless communication area.

Unlike traditional phased arrays or diversity techniques that improve the sensitivity to one signal of interest, MIMO systems employ antenna arrays jointly at transmit and receive sides to spatially multiplex signals over multipath or near-field channels. The design of MIMO antennas and propagation channels will affect the channel correlation significantly, and this will in turn determine the system capacity. In a multipath-rich environment, it can utilize uncorrelated channels exploited by multiple antennas at both the transmitter and receiver to convey different signals simultaneously without expanding bandwidth. Antenna design plays an important role in MIMO systems since antenna characteristics, including radiation pattern, polarisation, array arrangement, and mutual coupling, have great impact on the correlation between different signal branches. For small terminal devices such as personal digital assistant (PDAs), MIMO antenna design is more challenging, because

the antenna structure is required to be more compact and easily assembled with the device as well as suitable for preserving channel capacity.

As the transmission medium for wireless and mobile communications, radio channel modeling is the fundamental work to the communications systems. The accurate understanding of actual propagation channel is deterministic for algorithm design and optimization, equipment development, system deployment and operation. Channel modeling work also plays an important role in the communication standardization process.

With the continuous and rapid improvement of the communication techniques, the realization of radio channel modeling developed from large scale to small scale, from static to dynamic, and from narrowband to broadband. In recent years, the channel characteristics research went into the more sophisticated spatial area. Multiple-input multiple-output (MIMO) technology makes the space, together with time and frequency, become a resource improving the performance of wireless communication. With the proposals and application for distributed antennas, large MIMO, and 3D MIMO technologies, the demand for the spatial characteristics of the channel modeling is growing continuously. The coupling relationship between the space, time, and frequency has an important role for the performance of wireless communication systems.

Multilink collaboration will act as the main feature for the future systems. Then multipoint network channel model is increasingly required to provide guides in the basic research field. In the networking collaboration environment, the correlation between the parameters and links, which is

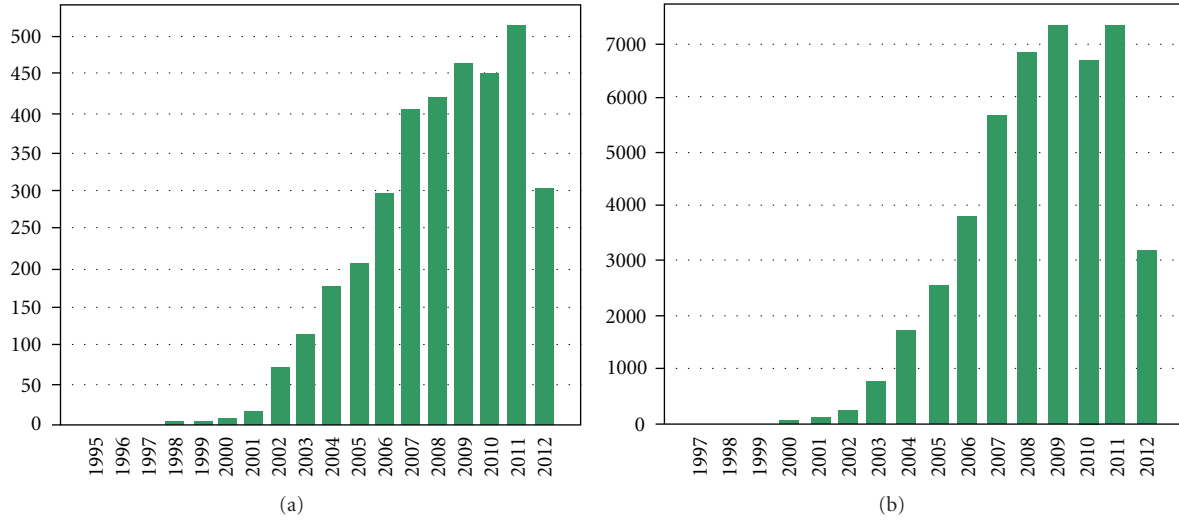


FIGURE 1: (a) Paper number published per year. (b) Paper citation per year.

ignored in previous studies, will determine the network's coverage, the reliability, and capacity. These correlations may be the key to solving the future channel modeling problem.

Wenhua Chen
Manos M. Tentzeris
Yuan Yao
Yan Zhang
Li Yang

Research Article

Reduced-Complexity Radio Architectures for Enhanced Receive Selection Combining in Multiuser Diversity Systems

Elpiniki P. Tsakalaki,^{1,2} Osama N. Alrabadi,² Constantinos B. Papadias,¹ and Ramjee Prasad²

¹Broadband Wireless and Sensor Networks Group, Athens Information Technology, 19002 Athens, Greece

²Department of Electronic Systems, Aalborg University, 9220 Aalborg East, Denmark

Correspondence should be addressed to Elpiniki P. Tsakalaki, et@es.aau.dk

Received 1 August 2011; Revised 16 November 2011; Accepted 4 December 2011

Academic Editor: Li Yang

Copyright © 2012 Elpiniki P. Tsakalaki et al. This is an open access article distributed under the Creative Commons Attribution License, which permits unrestricted use, distribution, and reproduction in any medium, provided the original work is properly cited.

Although antenna selection is a simple and efficient technique for enhancing the downlink performance of multiuser diversity systems, the large antenna interelement spacing required for achieving spatial diversity is prohibitive for user terminals due to size restrictions. In order to allay this problem, we propose miniaturized switched beam receiver designs assisted by low-cost passive reflectors. Unlike conventional spatial receive diversity systems, the proposed angular diversity architectures occupy a small volume whereas the antenna system properties are optimized by controlling the strong reactive fields present at small dimensions. The systems are designed for maximum antenna efficiency and low interbeam correlation, thus yielding N practically uncorrelated receive diversity branches. The simulation results show that the proposed enhanced diversity combining systems improve the average throughput of a multiuser network outperforming classical antenna selection especially for small user populations and compact user terminal size.

1. Introduction

Recent studies have shown that the capacity-achieving strategy for the cellular downlink is dirty paper coding (DPC) at the multiple antenna base station (BS) [1]. A less computationally complex zero-forcing (ZF) technique is proposed in [2] exhibiting an identical growth rate of the sum rate with respect to the number of user terminals (UTs). However, both DPC and ZF require perfect channel state information at the transmitter (CSIT). Since perfect CSIT is practically infeasible, the focus is on low-rate feedback techniques exploiting *multiuser diversity* by scheduling opportunistically transmissions to the users when their channel is good. These techniques, termed as opportunistic beamforming (OB), were introduced in [3]. Therein, taking into account fairness, the BS schedules in each time slot data transmission to the UT with the best normalized instantaneous channel condition relative to a random beamforming precoding. This approach achieves the asymptotic average throughput

of coherent beamforming with modest signal-to-noise ratio (SNR) feedback. Several extensions to this technique are mentioned in the literature. Indicatively, [4] proposes an OB and scheduling algorithm that enhances the throughput and delay characteristics of the system whereas, in [5], multiple orthonormal random beams at the BS serve multiple UTs simultaneously in each time slot.

OB techniques rely on the assumption that, with a large number of UTs, there is a high probability that an arbitrary choice of a BS beamforming vector will be aligned to a user's channel vector [6]. Thus, the benefits of OB are more evident when the number of users is large. To further improve the data rates of multiuser diversity systems, especially for reasonable user populations, the authors in [6–9] consider multiple antenna UTs with different combining techniques ranging from the simple antenna selection combining (SC) to the more sophisticated equal gain combining (EGC), maximum ratio combining (MRC), and optimum combining (OC). However, complex architectures including

multiple receive antennas are often prohibitive in UTs due to implementation complexity and size restrictions. Note that SC is the simplest combining method in terms of hardware complexity keeping the same diversity gain as that for MRC or EGC [9]. Moreover, the small spacing of the antenna elements at the UTs often results in significant correlation and coupling degrading the efficiency of the receive antenna system. Therefore, it is desirable to investigate simple to implement solutions ensuring low-power consumption and efficient performance at a constrained size.

In this paper, we propose two compact UT antenna architectures accompanied with SC aiming at enhancing the performance of a multiuser system in the downlink. The first antenna architecture consists of a simple switched uniform circular array (S-UCA) of N antenna elements and a central common passive reflector (PR) terminated with a passive load (reactance) (Figure 1(a)). The second antenna architecture comprises a simple switched parasitic array (S-PA) [10, 11] of a single RF chain circularly surrounded by N PRs terminated with passive loads (Figure 1(b)). The two proposed architectures (S-UCA and S-PA) satisfy the aforementioned cost, size, and power restrictions as they both require a single RF chain and low-cost passive antenna hardware [12]. Moreover, the antenna size is kept small by reducing significantly the radius of the S-UCA and of the S-PA. In this way, the antenna systems retain strong beamforming capabilities due to the intense reactive fields egressed at such small spacing [13]. By optimizing the S-UCA and the S-PA loading conditions a high antenna efficiency is maintained whereas the N beampatterns obtained by the receive architectures remain uncorrelated despite the small interelement spacing. Consequently, besides multiuser diversity, angular diversity is also made available resulting in significant multiuser performance gains compared not only to conventional single antenna UTs, but also to classical antenna SC with realistic receive antenna systems.

The two proposed antenna architectures preserve the compactness and cost constraints of UT antennas, whereas one can be thought of as the “dual” architecture of the other: the central element of the S-UCA is a PR surrounded by potentially active antenna elements (Figure 1(a)), whereas in the case of S-PA the central element is an active antenna surrounded by a ring of PRs (Figure 1(b)). It should be noted that the S-PA necessitates a more complicated control circuit as compared to the S-UCA which requires a simple conventional antenna switching mechanism, resembling a classical switched UCA topology with the mere modification of inserting a common central PR. On the other hand, the RF switch needed for changing the RF path among the S-UCA antenna elements constitutes a liability in terms of additional insertion losses.

Notice that [14] proposes a compact single RF antenna system assisted by passive elements extracting a maximum diversity order of 3 (equal to the number of the considered basis beampatterns) in multiuser environments. However, the optimal antenna loading conditions are found according to the *instantaneous* SNR, thus adding extra computational complexity and delay. On the contrary, in our work the optimal loads are found *off-line* within a *single-step design*

and remain fixed during communication. More important, tuning the antenna loads at such small spacing degrades the antenna efficiency, unless a dynamic matching circuit is assumed, thus complicating the whole system design. The efficiency degradation is an important issue addressed in this paper.

Another relevant previous work on miniaturized antenna systems with desired antenna properties is [15] describing a method to design a decoupling and matching network (DMN) for a set of preselected desired beampatterns and for compact antenna arrays. The present work is different from [15] in the sense that

- (i) a single active antenna and, thus, a single radio are used in the proposed architectures compared to the all-active antenna system of [15];
- (ii) the DMN with shunt connections between the ports in [15] results in significant bandwidth reduction, enhanced Ohmic losses, and, thus, smaller power gain compared to the type of uncoupled port matching of the proposed antenna systems [16, 17];
- (iii) in the proposed work, we are able to express analytically the desired antenna properties in terms of antenna efficiency and diversity as function of the antenna loading conditions. This permits the proposed reduced-complexity radio architectures to be optimized for both antenna efficiency and angular diversity using a single optimization procedure (as described in Section 3). However, [15] follows a different approach according to which two iterative processes are required. The first iterative process aims at designing a DMN fulfilling the power conservation under a hypothetical lossless network assumption and certain desired port pattern properties whereas the second iterative process describes the creation of a realizable lossy DMN.

The following notations are used throughout the paper. \mathbf{X} refers to a matrix and \mathbf{x} refers to a vector of the specified size. $\|\mathbf{x}\|$ denotes the Euclidean norm of the vector \mathbf{x} , and $|Z|$ gives the amplitude of the complex number Z . \mathbb{E} is the expectation operator and \mathbb{C} denotes the set of complex numbers of the specified dimensions. The superscripts T and H denote transpose and transpose conjugate, respectively.

The rest of the paper is organized as follows. In Section 2, the system model is presented whereas Section 3 describes the proposed UT antenna design approaches. Section 4 encompasses various practical enhanced receive SC antenna design examples and their performance evaluation. Finally, Section 5 concludes the paper.

2. System Model

The downlink scenario of a single-cell multiuser wireless communication system is considered with one BS serving K UTs. We assume the BS equipped with M uncorrelated antennas whereas each of the UTs has N beampatterns serving as N virtual antenna elements. A narrowband, quasistatic fading channel model is considered so that the

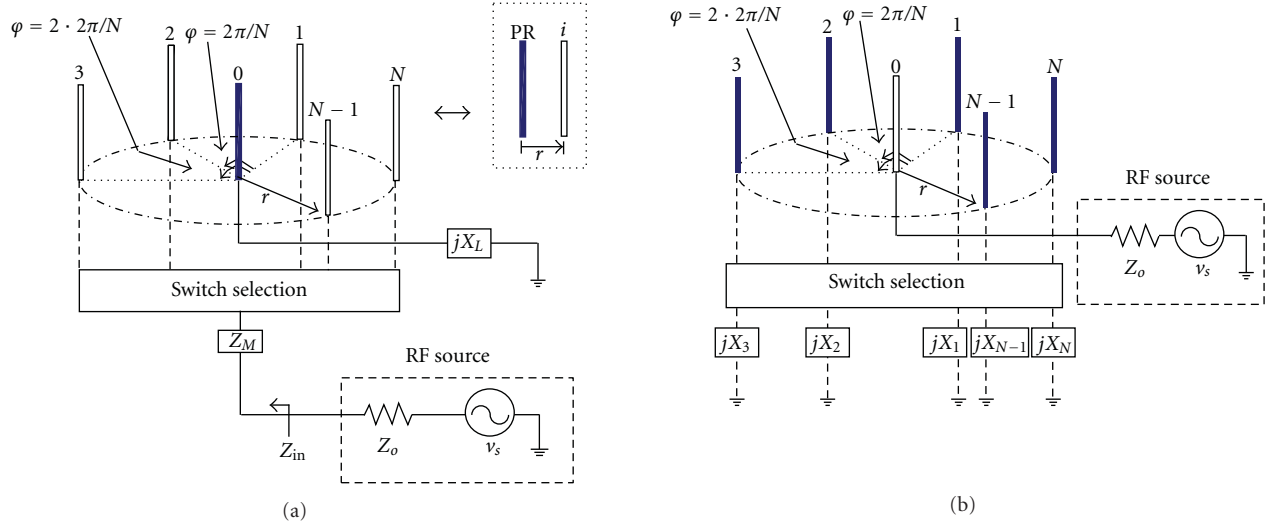


FIGURE 1: The proposed UT antenna configurations. (a) S-UCA of N antenna elements surrounding a single passive reflector (element 0). (b) S-PA of N passive reflectors surrounding a single active element (element 0).

channel response remains constant during one time slot, and then it abruptly changes to a new independent realization. At the beginning of each time slot, the base station is initialized subject to a random beamforming vector and retains its beamforming configuration constant over the slot. Collecting signals received from N beams at the k th UT into one vector $\mathbf{y}_k \in \mathbb{C}^{N \times 1}$, we get

$$\mathbf{y}_k = \underbrace{(\eta \mathbf{R})^{1/2} \mathbf{H}_{w,k}}_{\mathbf{H}_k} \mathbf{w} s + \mathbf{n}_k = [y_{k,1} \ y_{k,2} \ \cdots \ y_{k,N}]^T, \quad (1)$$

where $s \in \mathbb{C}^{1 \times 1}$ is the transmitted symbol whereas the transmit power level is fixed at P (i.e., $\mathbb{E}\{|s|^2\} = P$). $\mathbf{w} \in \mathbb{C}^{M \times 1}$ is the transmit beamforming vector applied at the BS in a random fashion with unitary allocated power (i.e., $\|\mathbf{w}\|^2 = 1$). $\mathbf{n}_k \in \mathbb{C}^{N \times 1}$ is the noise vector at the k th UT having independent and identically distributed (i.i.d.) circularly symmetric Gaussian entries with zero mean and variance σ_n^2 , that is, $\mathbf{n}_k \sim \mathcal{CN}(0, \sigma_n^2 \mathbf{I}_N)$. Assuming closely spaced antennas on the receiver side and UTs equipped with identical antenna systems, the spatial correlation and the antenna efficiency are modeled by the receive correlation matrix $\mathbf{R} \in \mathbb{C}^{N \times N}$ and the efficiency of the UT antenna system $\eta \in [0, 1]$, respectively. $\mathbf{H}_k \in \mathbb{C}^{N \times M}$ is the total channel matrix, $\{\mathbf{H}_k\}_{i,j}$ being the complex channel gain from the j th antenna at the BS to the i th antenna at the k th UT, given by $\mathbf{H}_k = (\eta \mathbf{R})^{1/2} \mathbf{H}_{w,k}$. This equation results by applying the well-established Kronecker model [18] with single-sided (i.e., only receive) correlation, incorporating the receive antenna efficiency. $\mathbf{H}_{w,k} \in \mathbb{C}^{N \times M}$ has i.i.d. entries distributed as $\{\mathbf{H}_{w,k}\}_{i,j} \sim \mathcal{CN}(0, 1)$.

The equivalent single-input-multiple-output (SIMO) channel $\mathbf{h}_k \in \mathbb{C}^{N \times 1}$ at the k th UT can be written as $\mathbf{h}_k = \mathbf{H}_k \cdot \mathbf{w} = [h_{k,1} \ h_{k,2} \ \cdots \ h_{k,N}]^T$, where $h_{k,i}$ is the equivalent

channel seen at the i th antenna. Thus, the SNR perceived by the i th antenna at the k th UT is given by $\gamma_{k,i} = P|h_{k,i}|^2/\sigma_n^2$.

3. Enhanced Selection Combining Antenna Architectures

In this section we describe the two proposed antenna architectures for enhanced SC at the UT, that is, the S-UCA (Figure 1(a)) and the S-PA (Figure 1(b)). The S-UCA and the S-PA are smart antenna systems that present a significant advantage over their classical all-active antenna array counterparts; they are able to control their beam patterns as any smart antenna system, while being implemented using a *single RF chain*. The suggested architectures are depicted with wire antenna elements in Figure 1. However, it should be noted that the following analysis is general regardless of the specific antenna element deployed and that the proposed designs accept any kind of antenna elements that can be practically integrated into compact UTs, such as printed monopoles, slot antennas, planar inverted-F antennas (PIFAs), and fractal antennas.

3.1. Switched Uniform Circular Array. The first proposed UT antenna architecture is a S-UCA comprising a ring of N antenna elements (elements 1, 2, ..., N in Figure 1(a)) surrounding a central common PR (element 0 in Figure 1(a)) at relative local angles of $0, 2\pi/N, \dots, (N-1)2\pi/N$, respectively. According to the antenna SC, only one antenna out of the N available ones is active at each slot, that is, connected to the single RF chain via a switch and used for communication. The PR is short-circuited and loaded with a reactance jX_L rather than being connected to the RF port. The PR is fed inductively by radiated energy coming from the active (driven) element.

The i th (active) antenna, $i \in \{1, 2, \dots, N\}$, has a corresponding beampattern $B_i(\varphi)$ given by

$$B_i(\varphi) = \mathbf{i}^T \boldsymbol{\alpha}_i(\varphi), \quad (2)$$

where φ denotes the azimuthal angle representing the angle of arrival (AoA). $\boldsymbol{\alpha}_i(\varphi)$ is the 2×1 response vector given by

$$\boldsymbol{\alpha}_i(\varphi) = \left[1 \quad e^{-j\kappa r \cos[\varphi - (2\pi/N)(i-1)]} \right]^T, \quad (3)$$

where λ is the carrier wavelength and $\kappa = 2\pi/\lambda$ is the wavenumber. r is the radius of the S-UCA corresponding to the spacing between each i th antenna and the PR. Let I_A and I_P denote the current on each i th antenna and the current induced on the PR, respectively. $\mathbf{i} \in \mathbb{C}^{2 \times 1}$ is the corresponding current vector, given by

$$\mathbf{i} = \mathbf{v}_s [\mathbf{Z} + \mathbf{Z}_L]^{-1} \mathbf{u} = [I_A \quad I_P]^T. \quad (4)$$

From (2)–(4) notice that the beampatterns $B_i(\varphi)$, $i \in \{1, 2, \dots, N\}$ are circularly symmetric to each other. In (4), \mathbf{v}_s represents the transmitted voltage signal source with the amplitude and the phase from the driven RF port whereas $\mathbf{u} = [10]^T$. $\mathbf{Z} \in \mathbb{C}^{2 \times 2}$ is the mutual impedance matrix given by

$$\mathbf{Z} = \begin{bmatrix} Z_{AA} & Z_{AP} \\ Z_{PA} & Z_{PP} \end{bmatrix}, \quad (5)$$

where Z_{AA} and Z_{PP} is the self-impedance of each i th antenna and of the PR, respectively. $Z_{AP} = Z_{PA}$ is the mutual impedance between each i th antenna and the PR. The loading matrix $\mathbf{Z}_L \in \mathbb{C}^{2 \times 2}$ can be defined as

$$\mathbf{Z}_L := \text{diag}([Z_o + Z_M \quad jX_L]), \quad (6)$$

where Z_o denotes the terminal impedance at the active port (equal to the characteristic impedance of 50Ω). $Z_M = R_M + jX_M$ represents the matching impedance attached to the active element as an additional degree of freedom (besides jX_L) when optimizing the antenna system for efficiency and diversity.

Defining the row vector

$$\mathbf{B}(\varphi) := [B_1(\varphi) B_2(\varphi) \cdots B_N(\varphi)] \quad (7)$$

and assuming a uniform power angular spectrum (PAS), the correlation matrix \mathbf{R} , whose entry $\mathbf{R}_{i,j}$ denotes the correlation between the i th and j th beam, can be written as

$$\mathbf{R} = \frac{1}{2\pi} \int_{-\pi}^{+\pi} \mathbf{B}^H(\varphi) \mathbf{B}(\varphi) \cdot d\varphi, \quad (8)$$

where $\mathbf{R}_{i,i} = 1$ and $\mathbf{R}_{i,j} = \mathbf{R}_{j,i}$, $i, j \in \{1, 2, \dots, N\}$ by reciprocity. Notice that \mathbf{R} is real valued for circularly symmetric beampatterns over a full angular spread [19]. Moreover, the structure of \mathbf{R} is characterized by the expression

$$\forall n \in \left\{ 1, 2, \dots, \left\lfloor \frac{N}{2} \right\rfloor \right\}, \quad i \in \{0, 1, \dots, N-2\} : \quad (9)$$

$$\mathbf{R}_{1+(i \bmod N), [1+(i+n \bmod N)] \bmod N} = \mathbf{R}_{2+(i \bmod N), [2+(i+n \bmod N)] \bmod N}$$

which comes from the topology symmetry of any UCA and from the fact that pairs of equidistant antenna elements have the same correlation. The efficiency of the S-UCA is given by

$$\eta = 1 - \left| (Z_{\text{in}} + Z_o)^{-1} (Z_{\text{in}} - Z_o) \right|^2, \quad (10)$$

where Z_{in} is the driving point impedance seen by any active antenna such that

$$Z_{\text{in}} = Z_{AA} + Z_M + \frac{I_P}{I_A} Z_{AP} = Z_{AA} + Z_M - \frac{Z_{AP}^2}{Z_{AP} + jX_L}. \quad (11)$$

Notice that Z_{in} remains constant for all $i \in \{1, 2, \dots, N\}$, and thus η is maintained for any active antenna due to topology symmetry.

In order to find the optimal loading conditions that jointly maximize the S-UCA efficiency and minimize the maximum correlation among the available set of antennas, we solve the following optimization problem over the variable loads Z_M and X_L :

$$\begin{aligned} & \underset{(\text{over } R_M, X_M, X_L)}{\text{maximize}} && \eta \\ & \text{subject to} && \max(\mathbf{R}_{i,j}) \leq 0.7, \quad i, j \in \{1, 2, \dots, N\}, \\ & && 0 \leq R_M \leq R_{\text{UB}}, \\ & && X_{\text{LB}} \leq X_M, X_L \leq X_{\text{UB}}. \end{aligned} \quad (12)$$

We have constrained the magnitude of maximum correlation to be less than 0.7, which is an empirical value at which diversity action takes place (see the detailed work in [19]). The constraints on R_M , X_M , and X_L depend on the realizable range of the loads, where R_{UB} is the upper bound on R_M whereas X_{LB} and X_{UB} are the lower and the upper bound on X_M or X_L , respectively.

3.2. Switched Parasitic Array. The second proposed UT antenna architecture is a S-PA (see [10] and references therein). The single active element is surrounded by a ring of PRs where every PR is short-circuited and loaded with passive loads via on/off switches, rather than being connected to the RF port. A S-PA has as many possible main beampatterns as the number of PRs (given by N). The characteristics of the beampatterns (e.g., width, gain, and nulls) depend on the PRs loading and the array dimensions. The S-PA can switch among the N beam positions by properly controlling the state of the switches. This operation can be performed very fast; for example, a PIN diode has a transient switching time in the order of nanoseconds [20].

The proposed S-PA comprises N PRs (elements $1, 2, \dots, N$ in Figure 1(b)) surrounding the single active element (element 0 in the same figure) at relative local angles of $0, 2\pi/N, \dots, (N-1)2\pi/N$. Similarly to the S-UCA, each of the N beampatterns (in the far-field) is denoted by $B_i(\varphi)$, $i \in \{1, 2, \dots, N\}$ and is given by

$$B_i(\varphi) = \mathbf{i}_i^T \boldsymbol{\alpha}(\varphi). \quad (13)$$

The n th element of the S-PA $N \times 1$ response vector $\boldsymbol{\alpha}(\varphi)$ is given by $e^{-j\kappa r \cos[\varphi - (2\pi/N)(n-1)]}$. r is the spacing between the

active element and the PRs and is equal to the radius of the S-PA. \mathbf{i}_i is the vector of induced currents on the antenna elements, required for creating the i th beampattern, given by

$$\mathbf{i}_i = v_s [\mathbf{Z} + \mathbf{X}_i]^{-1} \mathbf{u} = [I_{i,0} \ I_{i,1} \ \cdots \ I_{i,N}]^T, \quad (14)$$

where v_s represents the transmitted voltage signal source. $\mathbf{Z} \in \mathbb{C}^{(N+1) \times (N+1)}$ is the mutual impedance matrix whose entry $Z_{m,m}$, $m \in \{0, 1, \dots, N\}$ is the self-impedance of the m th antenna element, and $Z_{m,n}$, $m \neq n$ is the mutual impedance between the m th and the n th antenna element (where $Z_{m,n} = Z_{n,m}$, $m, n \in \{0, 1, \dots, N\}$ by reciprocity). The vector \mathbf{u} is given by $\mathbf{u} = [1 \ \underbrace{0 \ \cdots \ 0}_N]^T$.

Let the loading vector $\mathbf{x} = [X_1 \ X_2 \ \cdots \ X_N] \Omega$ denote the set of N loads to be mapped to the N PRs, such that the circular rotation of the loading vector rotates the beampattern to one of the N angular positions (based on the image theory). Then, the matrix $\mathbf{X}_i \in \mathbb{C}^{(N+1) \times (N+1)}$ can be defined as

$$\mathbf{X}_i := \text{diag}([Z_0 \ j\hat{\mathbf{x}}_i]), \quad (15)$$

where $\hat{\mathbf{x}}_i$, $i \in \{1, 2, \dots, N\}$, is a circular permutation of \mathbf{x} at which the i th beampattern is created and Z_0 is the terminal impedance at the central active port. The m th element of $\hat{\mathbf{x}}_i$ is simply given by $X_{1+[(i+m-2) \bmod N]}$.

Similarly to the S-UCA, defining the row vector $\mathbf{B}(\varphi)$ as in (7) and assuming a uniform PAS, the $N \times N$ correlation matrix \mathbf{R} , whose entry $R_{i,j}$ denotes the correlation between the i th and j th beampattern, is given by (8) whereas the S-PA efficiency η is given by (10). However, in the case of the S-PA, the driving point impedance seen by the central active element Z_{in} is

$$\begin{aligned} Z_{\text{in}} &= Z_{0,0} + \sum_{m=1}^N \left(\frac{I_{i,m}}{I_{i,0}} \right) Z_{0,i} \\ &= \frac{\mathbf{u}^T \mathbf{Z} (\mathbf{Z} + \mathbf{X}_i)^{-1} \mathbf{u}}{\mathbf{u}^T (\mathbf{Z} + \mathbf{X}_i)^{-1} \mathbf{u}}. \end{aligned} \quad (16)$$

Z_{in} remains constant for all $i \in \{1, 2, \dots, N\}$ and thus η is maintained for all $B_i(\varphi)$, due to topology symmetry.

In the S-PA case, the optimization problem yielding the set of the optimal reactive loads that jointly maximize the S-PA efficiency and minimize the maximum correlation among the available set of beams over the reactance space \mathbf{x} can be written as

$$\begin{aligned} &\underset{(\text{over } \mathbf{x})}{\text{maximize}} \quad \eta \\ &\text{subject to} \quad \max(\mathbf{R}_{i,j}) \leq 0.7, \quad i, j \in \{1, 2, \dots, N\}, \\ &\quad \quad \quad X_{\text{LB}} \leq X_m \leq X_{\text{UB}}, \quad m \in \{1, 2, \dots, N\}, \end{aligned} \quad (17)$$

where X_{LB} is the lower bound and X_{UB} is the upper bound on the realizable range of the reactances X_m .

Comparing the optimization problems (12) and (17), we observe that the number of (real-valued) control variables is limited to 3 in the case of the S-UCA, whereas the S-PA has $2 \cdot N$ control variables. Thus, depending on the value of

N (design parameter), the S-PA may have more degrees of freedom with respect to optimization flexibility compared to the S-UCA.

From hardware point of view, while the RF path is switched in case of the S-UCA, the RF path remains unchanged in the S-PA as the loads surrounding the central active element are rotated. Mathematically this has been represented by a constant current vector and a permuting steering vector in the S-UCA case, whereas a fixed steering vector and a permuting current vector express the S-PA switching mechanism.

3.3. Average Throughput. Since this work is focused on specific UT architectures and their impact on multiuser performance, a specific scheduling algorithm, such as proportional fair scheduling, is not considered. Within SC and assuming all UTs equipped with the described optimally loaded S-UCA or S-PA, the antenna element with the highest SNR $\gamma_{k,i}$ is selected to receive the signal for the k th UT. Once the k th UT selects the best beampattern and feeds back the corresponding SNR $\gamma_k^* = \max(\gamma_{k,1}, \dots, \gamma_{k,N})$, the BS can schedule the user with the strongest γ_k^* . The resulting average throughput can be computed as [8]

$$C = \mathbb{E} \left\{ \log_2 \left[1 + \max_{k=1, \dots, K} (\gamma_k^*) \right] \right\}. \quad (18)$$

4. Enhanced Selection Combining Antenna Design Examples and Performance Evaluation

4.1. Design Examples Using Thin Electrical Dipoles

4.1.1. Throughput Performance. In this part we consider S-UCA set-ups of thin electrical dipoles vertical to the azimuth plane with $r = \lambda/20$ and different number of antenna elements, that is, $N \in \{2, 3, 4, 5, 6\}$. The \mathbf{Z} matrix is calculated using Gauss-Legendre numerical integration [21] obtaining $Z_{AA} = Z_{PP} = 73.079 + j42.499$ and $Z_{AP} = 71.607 + j24.251$. In order to solve the nonlinear optimization problem in (12), we utilize a constrained nonlinear optimization multivariate MATLAB routine [22]. We set $X_{\text{LB}} = -100 \ \Omega$ and $X_{\text{UB}} = 100 \ \Omega$ as a feasible realizable range for X_M or X_L whereas R_M is upper bounded by $R_{\text{UB}} = 100 \ \Omega$. The efficiency is found maximum ($\eta = 1$) for all S-UCA setups whereas the calculated optimal loads and correlation values are shown in Table 1. The normalized magnitude of the obtained beampattern $B_1(\varphi)$ at the first antenna is illustrated in Figure 2 for the different S-UCA set-ups. The front-to-back ratio (FBR) of the beampatterns, defined as $20 \log_{10} |B_1(0)/B_1(\pi)|$, is also included in Table 1 which summarizes the favorable properties of the proposed S-UCA: maximum efficiency, low correlation values, and high FBR are available within a compact single radio UT antenna system.

In order to evaluate the SC via the proposed UT architecture, we consider the optimally loaded S-UCA with $N = 6$ antennas. We compare to classical antenna SC

TABLE 1: Optimized S-UCA characteristics ($\eta = 1$).

N	Optimal loads (Ω) $\{R_M, X_M, X_L\}$	Correlation	FBR (dB)
2	{45, -32, -3}	$\mathbf{R}_{1,2} = 0.0058$	9.2
3	{45, -8, -30}	$\mathbf{R}_{1,2} = 0.4752$	8.8
4	{45, -6, -32}	$\mathbf{R}_{1,2} = 0.6000$ $\mathbf{R}_{1,3} = 0.2379$ $\mathbf{R}_{1,4} = 0.6000$	10.6
5	{46, -27, -10}	$\mathbf{R}_{1,3} = 0.0078$ $\mathbf{R}_{1,2} = 0.5942$	5.3
6	{50, -8, -27}	$\mathbf{R}_{1,3} = 0.2030$ $\mathbf{R}_{1,4} = 0.5935$	6.3

with the same number of diversity branches [23]. For this reason, we consider a conventional UCA of the same radius r consisting of $N = 6$ dipoles with the same self-impedance $Z_{AA} = 79.33 - j19.65$. The UCA structure is similar to the proposed S-UCA structure of Figure 1(a), assuming the elements 1, 2, ..., 6 as the available set of antennas and omitting the central dipole (element 0). We assume each dipole matched for maximum efficiency ($\eta = 1$). The correlation is given by a real-valued 6×6 receive correlation matrix \mathbf{R} . From [19] the correlation between any two antenna elements of the UCA assuming uniform PAS is given by $\mathbf{R}_{m,n} = (1/2\pi) \int_{-\pi}^{+\pi} e^{j\kappa d^{(m,n)} \cos \varphi} \cdot d\varphi = J_0(\kappa d^{(m,n)})$, where $d^{(m,n)}$ is the distance between the m th and the n th antenna element, $m, n \in \{1, 2, \dots, 6\}$. In our case, $d^{(1,2)} = 2r \sin((2\pi/6)/2)$, $d^{(1,3)} = 2r \sin((2\pi/3)/2)$ and $d^{(1,4)} = 2r \sin((2\pi/2)/2)$. Therefore, we get $\mathbf{R}_{1,2} = 0.9755$, $\mathbf{R}_{1,3} = 0.9273$ and $\mathbf{R}_{1,4} = 0.9037$. As an upper bound on the achieved average throughput, we also consider the ideal case of SC with $\eta = 1$ and $N = 6$ fully uncorrelated diversity branches, that is, $\mathbf{R}_{i,j} = 0, i \neq j, i, j \in \{1, 2, \dots, 6\}$.

From Figure 3 it is evident that SC with the proposed optimally loaded S-UCA provides significant increase to the average throughput as compared to the conventional single-antenna UTs as well as to classical antenna SC for $M = 2$ and $P/\sigma_n^2 = 0$ dB. The observed gain for 3 users is 54% whereas classical antenna SC achieves only 17% with respect to single antenna UTs, revealing the significance of the proposed technique for small user populations. For 60 users, where the multiuser diversity gain dominates, the gain of SC with the proposed S-UCA decreases to 17%, whereas the gain of antenna SC with conventional UCAs drops to 6.5%. Notice that the performance of SC with the proposed practical antenna architecture almost achieves the throughput of the ideal case of 6 fully uncorrelated diversity branches.

Figure 4 shows the number of users required to achieve a target average throughput under different receive techniques ($M = 2$ and $P/\sigma_n^2 = 0$ dB). The figure shows that the SC with the proposed S-UCA requires almost one-sixth of the user population in order to obtain a certain performance

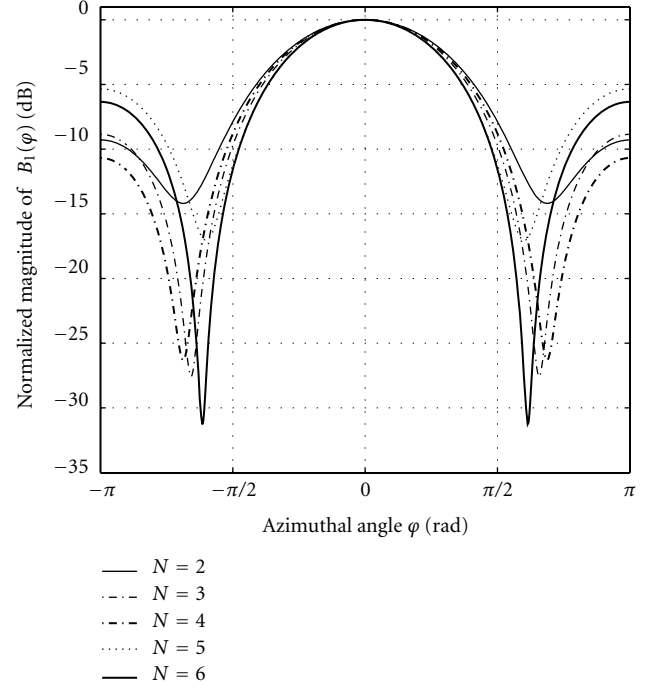
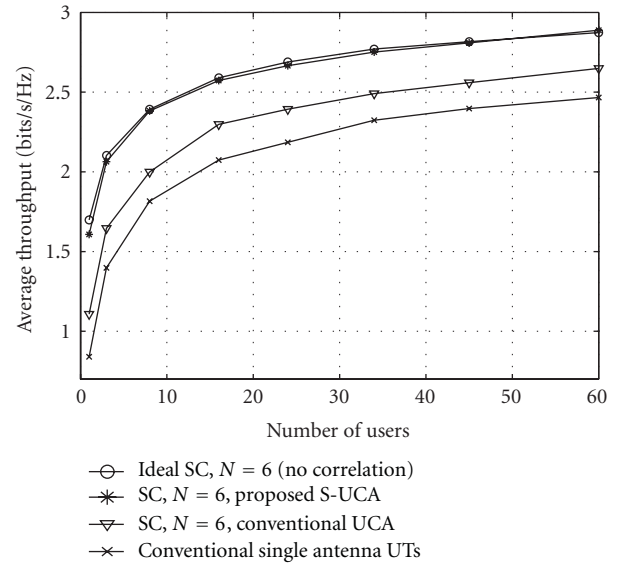
FIGURE 2: The normalized magnitude of the beampattern $B_1(\varphi)$ for the different N -element S-UCAs.

FIGURE 3: Average throughput as a function of the number of users.

compared to single antenna UTs. This confirms that SC represents an inherent form of multiuser diversity so that the degrees of freedom in the maximum selection increase from K to $K \cdot N$ [7]. It should be noted that comparable performance gains of SC using the proposed S-PA compared to the classical antenna SC have been obtained as illustrated in the simulation results of [11].

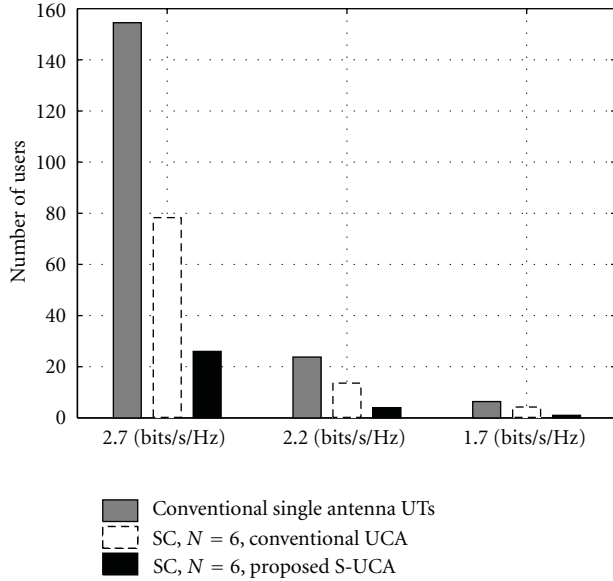


FIGURE 4: Number of users achieving a target average throughput.

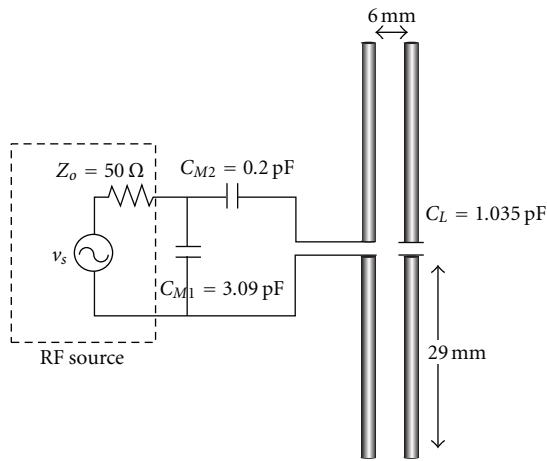


FIGURE 5: A four-element S-UCA design example comprising 60 mm long dipoles of 1 mm radius. At each time instant one dipole (out of the four) is active and closely coupled to the central passive one that is closed on a loading capacitor C_L .

4.1.2. Bandwidth Performance. The previous calculations are solely valid at the resonant frequency. In this part we aim at investigating the frequency response of the proposed antenna system. In general, the array bandwidth decreases as the mutual coupling level increases which is a natural phenomenon when considering closely spaced antenna elements where the strength of the reactive fields increases the quality factor of the antenna system. The problem worsens when decoupling the antennas using a DMN [16, 17]. In this work, however, we perform a type of uncoupled matching (i.e., without any shunt connections between the ports) for maximum efficiency and low correlation. In order to examine the frequency response of the proposed enhanced receive diversity system we establish a well-defined

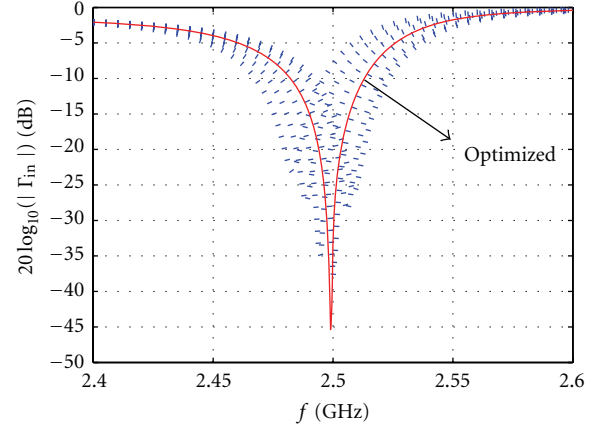


FIGURE 6: Frequency response of the four-dipole S-UCA design of Figure 5.

design of a four-element S-UCA comprising 60 mm long dipoles, each having a radius of 1 mm. A stand-alone dipole with these characteristics resonates at $f = 2.5$ GHz. A parasitic dipole (PR) with the same dimensions closed on a capacitor C_L is placed at the center of the S-UCA (i.e., $X_L = (2\pi f C_L)^{-1}$). Figure 5 shows the proposed S-UCA structure depicting only one out of the four potentially active dipoles in close proximity to the central PR. The RF source has a characteristic impedance $Z_o = 50 \Omega$ and is assumed to be frequency independent and attached to the S-UCA through a L-section matching network of two capacitors C_{M1} and C_{M2} , after which a switch selects one of the four dipoles. An ideal RF switch modeled as short and open circuit at the on and off state, respectively, is assumed. The impedance parameters of the antenna system were obtained by full-wave electromagnetic (EM) modeling, using the commercially available EM simulator IE3D. The 2×2 impedance matrix at the operating frequency of 2.5 GHz is $\mathbf{Z} = \begin{bmatrix} 113.84 + j36.01 & 112.27 - j29.30 \\ 112.27 - j29.30 & 113.84 + j36.01 \end{bmatrix}$. The values of the matching capacitors and the loading capacitor C_{M1} , C_{M2} , and C_L , respectively, are obtained by solving the optimization formulation in (12) (the optimal values are shown in Figure 5) leading to a maximum correlation of 0.5983 and efficiency of $\eta = 1$. The frequency response of this S-UCA at the optimal component values is shown in red color in Figure 6 which depicts the value of the input reflection coefficient Γ_{in} in dB. The fractional bandwidth is 1.28% which maps to 32 MHz. It should be noted that an attempt to optimize the bandwidth has not been attained. Moreover, modern wideband systems requiring more bandwidth do not usually claim the whole band at one time; thus, the loading values can be tuned on demand in order to cover other bands as well.

Furthermore, in order to investigate the tolerance of the input return loss on the antenna loading, we varied C_L over a 16Ω range in steps of 2Ω and obtained the frequency responses corresponding to the blue-dotted curves

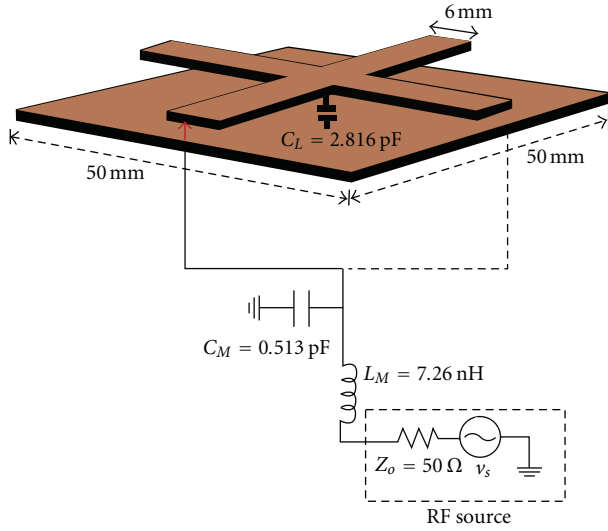


FIGURE 7: Practical S-UCA antenna design of four merged PIFA elements at 2.5 GHz.

in Figure 6. It is obvious from Figure 6 that the change in the load does not alter the operational bandwidth but it alters the central frequency. This, however, can be recovered by local handset calibration which is already required in practice to compensate for the user proximity effects [24].

4.2. Design Examples Using Practically Integrable Antenna Elements. A design example of a S-UCA with antenna elements that can be practically integrated into compact UTs is the four-modified PIFA antenna system shown in Figure 7, which has been designed on a 50 mm \times 50 mm printed circuit board (PCB) (almost half of the PCB area required for a bar-type phone chassis) operating at $f = 2.5$ GHz. The PIFA elements of this antenna system are modified in the sense that the excitation is done at the edge and the shorting is done in the middle of the element, whereas the inverse holds in a conventional PIFA element. The four antennas are merged over their common areas while a common shorting pin is terminated with a loading capacitor C_L mounted on the antenna structure itself (i.e., $X_L = (2\pi f C_L)^{-1}$). The dimensions of the antenna are given on the same figure.

Figure 8 shows how the proposed structure has evolved from two opposite modified PIFAs which are merged together. The operation is repeated on the second and fourth edges of the PCB. The RF source in Figure 7 has a characteristic impedance $Z_o = 50 \Omega$ and is assumed to be frequency independent and attached to the S-UCA through a L-section matching network of a capacitor C_M and an inductor L_M , after which a switch selects one of the four ports of the merged PIFA structure (an ideal RF switch model is also assumed here). The red arrow in Figure 7 indicates such a potentially active PIFA port. The correlation between the PIFA pairs was obtained by full-wave EM modeling, using the EM simulator IE3D. The reference port patterns (i.e., the radiation pattern of each port when excited by a unit voltage signal and the other ports are terminated with 50Ω) at the

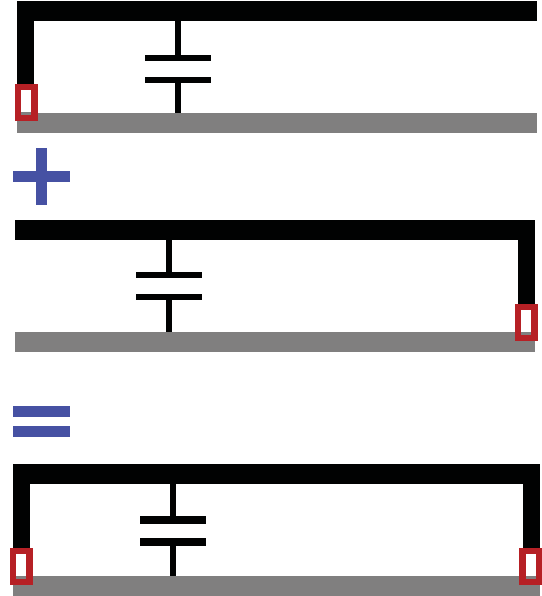


FIGURE 8: Two opposite merged modified PIFA antennas comprising the building block of the proposed S-UCA structure of Figure 7.

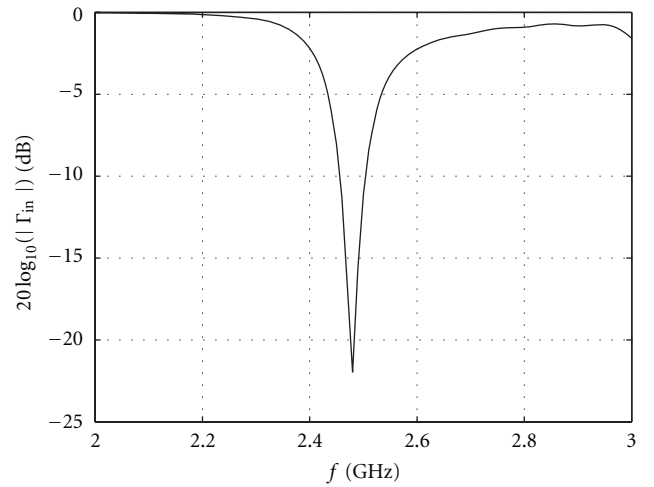


FIGURE 9: Frequency response of the practical receive diversity antenna design of Figure 7.

operating frequency of 2.5 GHz were extracted and exported to a MATLAB routine out of which the correlation between the communication beams is found, in a procedure similar to the one in [25]. The 2×2 impedance matrix at 2.5 GHz is obtained as $\mathbf{Z} = \begin{bmatrix} 17.88 + j382.60 & 1.06 - j29.71 \\ 1.06 - j29.71 & 1.13 + j25.12 \end{bmatrix}$. The L-section matching of C_M and L_M as well as the value of the loading capacitor C_L is optimized for low correlation and maximum efficiency according to the optimization formulation in (12). The optimal values of the load C_L and matching elements C_M , L_M are given on Figure 7. The maximum correlation at the designated values in Figure 7 is found equal to 0.63 whereas the efficiency is $\eta = 0.99$. The frequency response of the antenna is given in Figure 9.

Another excellent example of extremely compact antennas for mobile terminals is element couplers [26] where the antenna is simply a matching component that excites the characteristic modes of the ground plane of the mobile device (i.e., the mobile device chassis modes) [27]. This type of antenna, namely, the switched-chassis mode system, is capable of exciting different weakly correlated modes acting as virtual uncorrelated antennas. It should be noted that an analysis similar to the one proposed for the S-UCA or the S-PA system can be also applied to the switched-chassis mode system.

5. Conclusion

The paper proposes SC via optimized realistic receive antenna architectures for compact low-cost UTs in multiuser environments. It has been shown that the proposed compact S-UCA or S-PA antenna systems are able to achieve performance gains in terms of average throughput comparable to widely spaced antennas, by properly optimizing the antenna loading conditions for both antenna efficiency and diversity.

Acknowledgments

This research work has been performed in the context of collaboration between Aalborg University/Center for TeleInfraStruktur and Athens Information Technology for the joint offering of a Doctoral Program. The work was supported by the Future and Emerging Technologies (FET) Programme within the Seventh Framework Programme for Research of the European Commission, under FET-Open Grant CROWN-233843. This work is an extension to and generalization of the material presented in [11].

References

- [1] G. Caire and S. Shamai, "On the achievable throughput of a multiantenna Gaussian broadcast channel," *IEEE Transactions on Information Theory*, vol. 49, no. 7, pp. 1691–1706, 2003.
- [2] T. Yoo and A. Goldsmith, "On the optimality of multiantenna broadcast scheduling using zero-forcing beamforming," *IEEE Journal on Selected Areas in Communications*, vol. 24, no. 3, pp. 528–541, 2006.
- [3] P. Viswanath, D. N. C. Tse, and R. Laroia, "Opportunistic beamforming using dumb antennas," *IEEE Transactions on Information Theory*, vol. 48, no. 6, pp. 1277–1294, 2002.
- [4] D. Avidor, J. Ling, and C. Papadias, "Jointly opportunistic beamforming and scheduling for downlink packet access," in *Proceedings of the IEEE Int'l Conference on Communication (ICC '04)*, Paris, France, June 2004.
- [5] M. Sharif and B. Hassibi, "On the capacity of MIMO broadcast channels with partial side information," *IEEE Transactions on Information Theory*, vol. 51, no. 2, pp. 506–522, 2005.
- [6] L. Zan and S. A. Jafar, "Combined opportunistic beamforming and receive antenna selection [cellular downlink applications]," in *Proceedings of the IEEE Wireless Communications and Networking Conference (WCNC '05)*, vol. 2, pp. 1007–1011, March 2005.
- [7] R. Bosisio and U. Spagnolini, "On the sum-rate of opportunistic beamforming schemes with multiple antennas at the receiver," in *Proceedings of the IEEE International Conference on Communications (ICC '07)*, pp. 1048–1053, Glasgow, UK, June 2007.
- [8] M. O. Pun, V. Koivunen, and H. V. Poor, "Opportunistic scheduling and beamforming for MIMO-SDMA downlink systems with linear combining," in *Proceedings of the 18th Annual IEEE International Symposium on Personal, Indoor and Mobile Radio Communications (PIMRC '07)*, pp. 1–6, Athens, Greece, September 2007.
- [9] C. H. Chang and Y. Lee, "Opportunistic beamforming systems with diversity combining," in *Proceedings of the 7th International Conference on Information, Communications and Signal Processing (ICICS '09)*, pp. 1–5, Macau, China, December 2009.
- [10] D. V. Thiel, "Switched parasitic antennas and controlled reactance parasitic antennas: a systems comparison," in *IEEE Antennas and Propagation Society Symposium*, vol. 3, pp. 3211–3214, June 2004.
- [11] E. P. Tsakalaki, O. N. Alrabadi, C. B. Papadias, and R. Prasad, "Enhanced selection combining for compact single RF user terminals in multiuser diversity systems," in *Proceedings of the IEEE Int'l Symposium on Personal, Indoor, and Mobile Radio Communications (PIMRC '10)*, pp. 951–954, Istanbul, Turkey, September 2010.
- [12] R. Vaughan, "Switched parasitic elements for antenna diversity," *IEEE Transactions on Antennas and Propagation*, vol. 47, no. 2, pp. 399–405, 1999.
- [13] E. P. Tsakalaki, O. N. Alrabadi, C. B. Papadias, and R. Prasad, "Spatial spectrum sensing for wireless handheld terminals: design challenges and novel solutions based on tunable parasitic antennas [Dynamic Spectrum Management]," *IEEE Wireless Communications Magazine*, vol. 17, no. 4, pp. 33–40, 2010.
- [14] V. Barousis, A. G. Kanatas, N. D. Skentos, and A. Kalis, "Pattern diversity for single RF user terminals in multiuser environments," *IEEE Communications Letters*, vol. 14, no. 2, Article ID 5403617, pp. 151–153, 2010.
- [15] J. Weber, C. Volmer, K. Blau, R. Stephan, and M. A. Hein, "Miniaturized antenna arrays using decoupling networks with realistic elements," *IEEE Transactions on Microwave Theory and Techniques*, vol. 54, no. 6, pp. 2733–2740, 2006.
- [16] B. K. Lau, J. B. Andersen, G. Kristensson, and A. F. Molisch, "Impact of matching network on bandwidth of compact antenna arrays," *IEEE Transactions on Antennas and Propagation*, vol. 54, no. 11, pp. 3225–3238, 2006.
- [17] O. N. Alrabadi, *MIMO communication using single feed antenna arrays*, PhD Dissertation, Aalborg Universitet, 2011.
- [18] D. S. Shiu, G. J. Foschini, M. J. Gans, and J. M. Kahn, "Fading correlation and its effect on the capacity of multielement antenna systems," *IEEE Transactions on Communications*, vol. 48, no. 3, pp. 502–513, 2000.
- [19] R. G. Vaughan and J. B. Andersen, "Antenna diversity in mobile communications," *IEEE Transactions on Vehicular Technology*, vol. 36, no. 4, pp. 149–172, 1987.
- [20] D. M. Pozar, *Microwave Engineering*, John Wiley & Sons, Hoboken, NJ, USA, 2005.
- [21] S. J. Orphanides, *Electromagnetic Waves and Antennas*, Rutgers University, 2008.
- [22] The Mathworks, Natick, Mass, USA, <http://www.mathworks.com/>.
- [23] M. K. Simon and M.-S. Alouini, *Digital Communication Over Fading Channels*, John Wiley & Sons, 2005.
- [24] R. Mohammadkhani and J. S. Thompson, "MIMO capacity improvement in the presence of antenna mutual coupling,"

- in *Proceedings of the 18th Iranian Conference on Electrical Engineering (ICEE '10)*, pp. 167–171, Isfahan, Iran, May 2010.
- [25] O. N. Alrabadi, J. Perruisseau-Carrier, and A. Kalis, “MIMO transmission using a single RF source: theory and antenna design,” *IEEE Transactions on Antennas and Propagation*, vol. 60, no. 2, pp. 654–664, 2012.
- [26] W. L. Schroeder, P. Schmitz, and C. Thome, “Miniaturization of mobile phone antennas by utilization of chassis mode resonances,” in *Proceedings of the German Microwave Conference (GeMiC '06)*, no. 7b-3, Karlsruhe, Germany, 2006.
- [27] R. F. Harrington and J. R. Mautz, “Theory of characteristic modes for conducting bodies,” *IEEE Transactions on Antennas and Propagation*, vol. 19, no. 5, pp. 622–628, 1971.

Research Article

Modified MIMO Cube for Enhanced Channel Capacity

Lajos Nagy

Department of Broadband Infocommunications and Electromagnetic Theory, Budapest University of Technology and Economics, Goldmann György ter 3, 1111 Budapest, Hungary

Correspondence should be addressed to Lajos Nagy, nagy@mht.bme.hu

Received 1 August 2011; Revised 9 October 2011; Accepted 18 October 2011

Academic Editor: Wenhua Chen

Copyright © 2012 Lajos Nagy. This is an open access article distributed under the Creative Commons Attribution License, which permits unrestricted use, distribution, and reproduction in any medium, provided the original work is properly cited.

This paper deals with the optimization of MIMO antenna elements' position in modified MIMO cube for getting maximal channel capacity in indoor environment. The dependence of the channel capacity on the antenna orientation was analyzed by simulations. We have also examined the effect of the frequency dependence of the antenna system (in case of conjugate matching and nonconjugate matching) for the channel capacity. Based on the simulation results in the created and measured antenna system, the antennas were at a right angle to each other. At the two chosen different structures, we measured the antenna parameters and the channel capacity. In this paper, we present the results of the measurements which clearly confirm our simulations. We will point out the differences between the two antenna structures.

1. Introduction

Wideband indoor wireless systems are gaining increasing importance nowadays. This is why the analysis of MIMO systems which eliminate the problems of indoor propagation is of primary significance. In case of indoor propagation, a frequent problem is that there are disturbing objects between the transmitter and the receiver antennas consequently there is no direct line of sight in the wireless channel. The objects in the channel adversely affect the transmission because they scatter and reflect the signals, resulting in attenuation and phase errors. MIMO systems can be a solution to these problems.

MIMO system can eliminate the phase, distance, and polarization diversity. Thus, in an indoor environment, the theoretically highest channel capacity can be nearly achieved. It is known that the channel capacity scales linearly with the number of antennas at both the receiver and transmitter for complex Gaussian fading channels.

When designing a complete multiple-antenna system, we have to try to approach a maximal mean capacity with a minimal number of antennas in the system. For multiple-antenna systems, an important problem is the reduction of the number of antennas for practicability and usability reasons. We will assume that the multiple-antenna system with

three elements on both the receiver and transmitter issues is the simplest structure for the highest mean capacity.

When finding the best totally free structure for optimal channel capacity, the simulations come too little if the analyzed structures are chosen randomly and because most of the structure would be analyzed. Therefore, we have searched a right method for the optimal selection of the structure.

The MIMO cube as a compact antenna is one of a possible realization for MIMO antenna system [1, 2], but especially for higher frequencies the loss and coupling between the dipoles decreases the capacity of the system. The slot dipole is promising a cheap and lossless solution for MIMO cube, and this was investigated also in form of simulations and measurements. In [3] the MIMO antenna formed by slot antennas is already presented by our group, and later in many researches slot antennas are used as MIMO elementary antennas [4–7]. In this paper, a MIMO cube prototype consisting of three slot-type dipole antennas is fabricated and tested accordingly.

The authors of [8] reported study on the effect of mutual coupling. In [9] the effect of mutual coupling has been shown to reduce capacity substantially especially when packing higher number of receiving antennas for a fixed aperture. Based on this published effect, our present investigation

takes into account the mutual coupling at the capacity optimization procedure at the MIMO antenna design.

The MIMO capacity optimization procedure uses the (Genetic Algorithm) GA which has its main advantages, cannot stick in a local extreme, can be simply implemented, and can find the global minimum or maximum of the composite multivariable function. Like the terrestrial evolution, the GA handles the functional parameters as biological gene. The different input parameters are crossed among the population where the population is defined as a set of all-time actual available input parameters. Just like in biology, the survival rate of the strongest candidates has a higher probability; furthermore, the reproduction of the next-generation parameter set is influenced by mutation of earlier analyzed-selected input parameters. The variety of the first-generation initial input parameter set is guaranteed by initialization of the GA with random values [10–12]. The antenna orientations are the optimized variables in our GA procedures, and the cost function is the channel capacity.

The scattering environment model which we applied in the simulation was a three-dimensional (3D) double-bouncing (DB) stochastic scattering channel model with wide angular spread as a basis at both ends. By using this model, we wrote down perfectly an unmitigated office indoor environment.

In this model, the scatterers are on a spherical surface around transmitter and receiver antennas. In an indoor scenario, the standard propagation is NLOS (nonline of sight); thus, there are several jamming objects between the transmitter and the receiver devices. The disturbing objects around the antennas change phase and level of transmitted signal. The model statistically describes the material, surface, and place of these objects which results in phase and amplitude error in the course of propagation. Waves of arbitrary polarizations are incident on the antenna structure from all possible directions as can be seen in Figure 12. The transmission matrix (\mathbf{H}) which connects the receiver and transmitter antennas is filled by assuming DB scattering. The effect of mutual coupling is taken into account in the channel matrixes by using mutual impedances. By this method, we could describe the continuously varying indoor environment.

In this paper, finally, we present simulation and measurement results for the channel capacity of a 3×3 MIMO antenna system. The aim of this research is the enhancing of the MIMO channel capacity for indoor environment.

In addition we have examined the effect of the frequency dependence of the antenna system (in case of conjugate matching and nonconjugate matching) for the channel capacity. Based on the result of the simulation, we have created the antenna system and measured the antenna parameters and the channel capacity. In this paper, we would like to show the results of the measurements which clearly confirm our simulations. We will point out the differences which are between the two antenna structures and certificate our allegations.

At the research work, the target frequency for the MIMO antennas were different for Sections 2 and 5. On the one hand, the working frequency for first experimental version

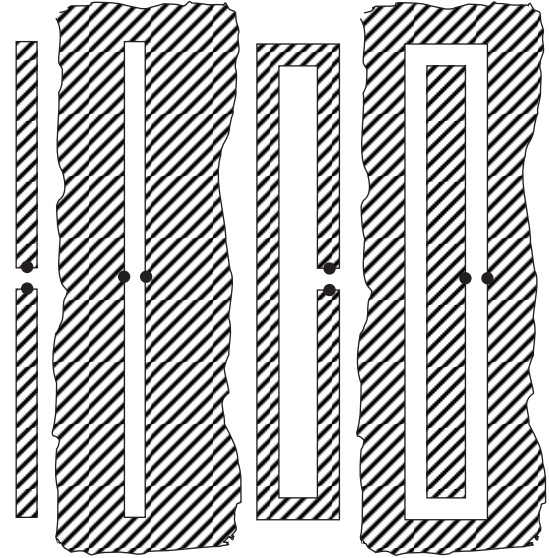


FIGURE 1: Dipole and folded dipole as complementary structures.

was at 4.6 GHz for a special requirement, on the other hand the channel capacity enhancement and MIMO antenna design was performed at 2.2 GHz range as the possible UMTS application.

2. The MIMO Antenna

Slot dipole antennas are used as basic elements of the MIMO antennas investigated. Experimental results show that especially at higher frequencies of various wireless applications the additional loss of the printed antennas increase, and therefore implementation of such antennas is not always possible above 1-2 GHz.

In our first test the single-slot antennas were designed, manufactured, and measured without taking into account the mutual coupling between them in case of forming MIMO antennas from them.

Wire dipole and a slot are complementary antennas. The solution for the slot can be found from the solution to an equivalent dipole by an interchange of the electric and magnetic fields. Not only the pattern but also the input impedance can be found.

Figure 1 shows two such complementary structures. Babinet's principle of optical screens extended by Booker is used to vector electromagnetic fields. If we take two such complementary screens and perform line integrals over identical paths to compute the impedance of each, we obtain the result for the input impedances

$$Z_1 \cdot Z_c = \frac{\eta^2}{2}, \quad (1)$$

where Z_1 is the input impedance of the structure, Z_c the input impedance of the complementary structure, and η the impedance of free space (120π).

Both the structure and its complementary one radiate the same pattern but differ in polarization.

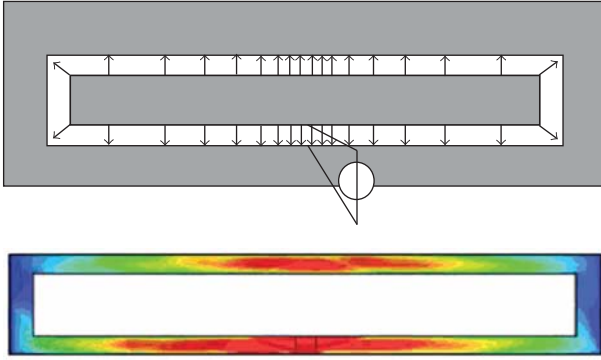


FIGURE 2: Electrical field strength on the slot, theoretical and simulated.

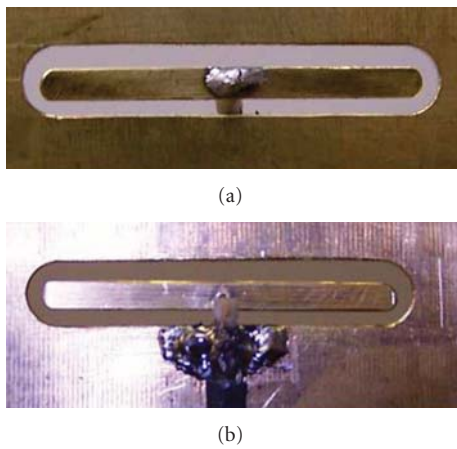


FIGURE 3: Folded slot forward and backward side.

TABLE 1: Slot antenna resonance frequency by changing the size of ground plane (measurement).

Size of ground plane	Resonance frequency (GHz)
$10 \lambda \times 10 \lambda$	4.585
$5 \lambda \times 5 \lambda$	4.650
$\lambda \times \lambda$	4.835
$0.5 \lambda \times 0.5 \lambda$	4.325

Using (1) the folded slot dipole (Figure 3) was chosen to be the basic dipole element of the MIMO antenna because of its well-matched impedance to 50 ohm coaxial transmission line without necessity of using any matching circuit.

As start the simulation and optimization of the simple folded slot dipole over plane ground conductor was made. The theoretical electrical vector field distribution and the simulated one can be seen in Figure 2.

After the first simulations and modeling, the slot antennas were designed using Ansoft HFSS electromagnetic simulator. Optimization was used to get matched input impedance at the desired working frequency. Finally the antennas are realized on copper plate with a thickness of 0.5 mm, and the excitation is through 50 ohm coaxial cables.

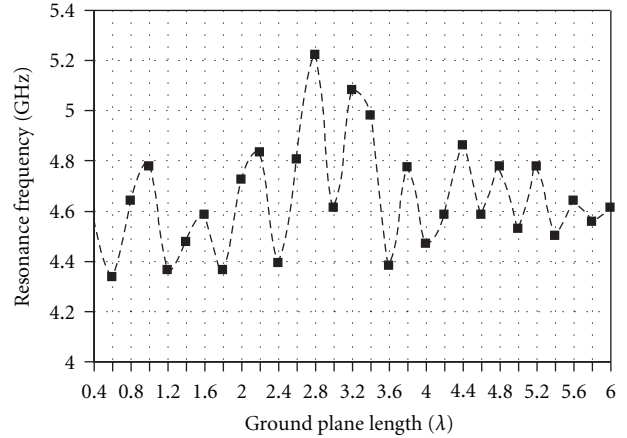


FIGURE 4: Resonance frequency of slot antenna versus ground plane size.

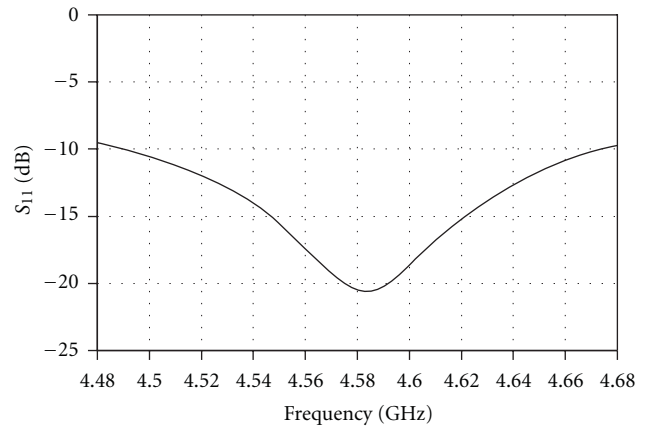


FIGURE 5: Measured input reflection of slot dipole over a 10λ by 10λ ground plane conductor.

The slot antenna over a notable size copper plate was realized and measured. The first results showed good agreement on HFSS-based simulations. In the simulation and at the realization size of 10λ by 10λ ground plane was used, but later at forming the MIMO cube the size of plane was reduced and the antenna resonance frequency remarkably changed (Figure 5).

The effect of rectangular ground plane size was also investigated on the resonance frequency by HFSS simulations as can be seen on Figure 4.

Figure 4 shows a notable change of resonance frequency especially in the 2.4λ length range and for feasible sizes notably decreases but at the design of MIMO antenna has to be taken into account (Table 1).

The investigated antenna elements provide almost lossless realization on cheap metallic plate. Two types of slots are simulated, optimized, and measured for 4.5-4.6 GHz. Coupling between dipoles is also measured and presented. The cube antennas exhibit an impedance bandwidth (VSWR < 2) of 18% and 7%.

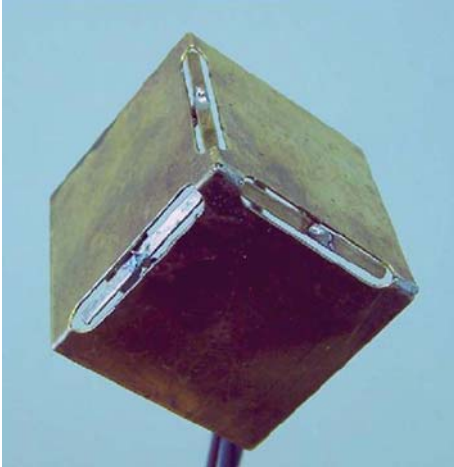


FIGURE 6: MIMO cube with slot dipoles on edges.

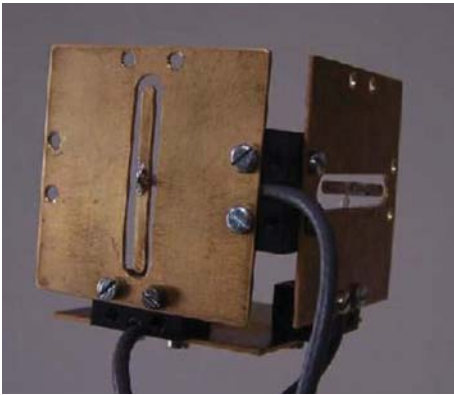


FIGURE 7: MIMO cube with slot dipoles on separated planes.

Results of simulations show that the theoretical capacity due to mutual coupling between MIMO antennas is lower than for implemented antennas with mutual coupling for cube side lengths less than about 0.3λ . For the prototype antenna, the S parameter isolation between ports is below -35 dB over a bandwidth of 300 MHz, and therefore excellent MIMO antenna can be formed without capacity degradation.

After the first tests two MIMO cube antennas have been analyzed and realized for the measurements and comparison of especially the mutual coupling between the antenna elements.

The first structure realized prototype is a part of a MIMO cube with slot dipole on the edges (Figure 6). The detailed analysis indicates that surface currents flow on the board, giving an isolation decrease. Our second structure applies therefore separated boards for decreasing the coupling (Figure 7).

For each antenna, the input reflection is acceptable for many mobile communications application over a bandwidth of at least 300 MHz. The coupling between slot dipoles contrarily is unacceptable for the first MIMO cube in Figure 8 without any compensation in comparison with Figure 9. The effect of coupling can cause MIMO capacity

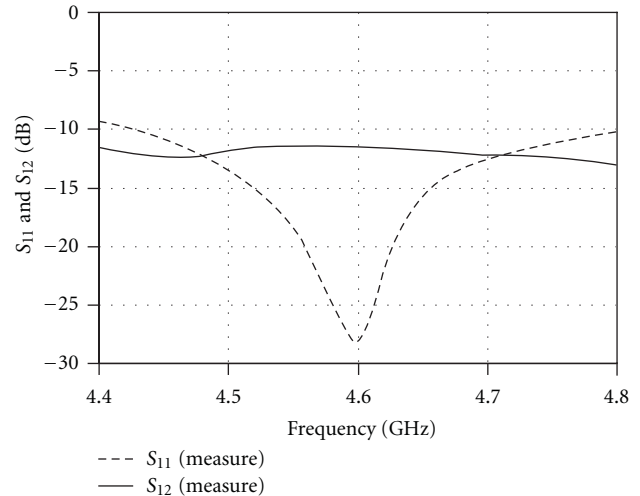


FIGURE 8: Measured MIMO antenna input reflection and coupling (S_{11} and S_{21}) for dipoles on edges.

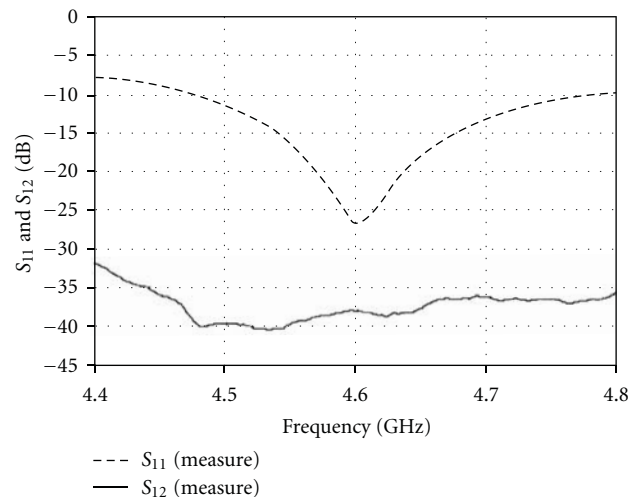


FIGURE 9: Measured MIMO antenna input reflection and coupling (S_{11} and S_{21}) for dipoles on separated planes.

degradation in real applications. The other effect on forming the MIMO cube from our antennas is the slight change in the resonance frequency which can be easily corrected by increasing the slot antenna length.

These first results enforced our farther investigation toward implementing optimization procedure which can take into account the mutual coupling effect for MIMO cubes and can be applied to capacity optimization. In the next part of the paper, the geometry optimization of MIMO antenna is shown for enhanced capacity.

3. MIMO Antenna Simulation Model

In our next simulation investigation, the MIMO system contains three wire dipole antennas both on the transmitter and the receiver sides.

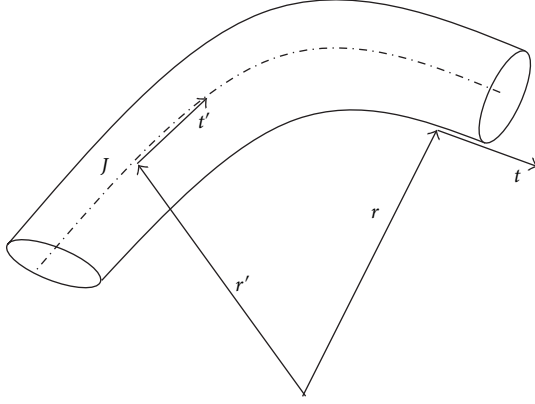


FIGURE 10: Thin wire geometry.

3.1. Wire Antenna Analysis. Let us consider an antenna consisting of many arbitrary-oriented wire elements. Starting with Maxwell equations and by enforcing the boundary condition for the total tangential electrical field on the antenna wire, it is possible to obtain the simplified general integral equation for arbitrary-oriented wires. Enforcing the boundary condition, the electrical field can be derived from the A magnetic vector potential.

Pocklington's procedure applied to our slot dual wire antennas supposes the current to be located over a thin filament over the conductor (Figure 10).

Pocklington's integral equation can be gotten finally:

$$E_{\text{tan}}^i = -\frac{1}{4\pi j\omega\epsilon} \int_L \left(t \cdot t' k^2 I \frac{e^{-jkR}}{R} + \frac{\partial}{\partial l'} I \frac{\partial}{\partial l} \frac{e^{-jkR}}{R} \right) dl'. \quad (2)$$

The solution of (2) should be determined using standard MM and Galerkin method. To solve (2) we used piecewise sinusoidal expansion and weighting functions.

The resulting mutual impedance between MIMO antenna elements can be obtained using the N port analysis to the whole system of antennas.

At the optimization process described in Section 3.3 the angle between antennas is the optimization variable as we are searching for the maximum channel capacity. In our simple case only these angles of the orientation of antennas are changed, but the method introduced is applicable also for general antenna position optimization.

For a MIMO radio channel with channel matrix H , the SVD is given as $\mathbf{H} = \mathbf{S}\mathbf{V}\mathbf{D}^H$, where \mathbf{S} and \mathbf{D}^H (complex conjugate transpose of \mathbf{D}) are complex unitary matrices, $\mathbf{V} = \text{diag}(\sqrt{\lambda_1}, \dots, \sqrt{\lambda_r})$ diagonal square matrix with $\lambda_1, \lambda_2, \dots, \lambda_r$ being the positive eigenvalues of $\mathbf{H}\mathbf{H}^H$, and $r \leq \min\{Mt, Nr\}$ denotes the rank of $\mathbf{H}\mathbf{H}^H$. With the assumption of known channel at the transmitter, the theoretical capacity from water filling is given as

$$C = \sum_{i=1}^{r'} \log_2(1 + \lambda_i \text{SNR}_i), \quad (3)$$

where $\text{SNR}_i = P_t/\sigma^2$ is the individual SNR of the eigenmodes after water filling and r' denotes the number of useful eigenmodes with positive power allocation.

In the course of calculation, the channel matrix is normalized with the average path gain Ψ :

$$\Psi^2 = \left\{ \frac{1}{m_{\text{tr}}m_{\text{re}}} \sum_{i=1}^{m_{\text{tr}}} \sum_{j=1}^{m_{\text{re}}} |H(i, j)|^2 \right\}, \quad (4)$$

where m_{tr} and m_{re} are the numbers of antennas on both sides. For computing the average path gain it shall make the expectation value for all random channels.

3.2. 3D-Environment Simulation Model. The antenna system is situated in a 3D scattering environment indoor channel. Waves of arbitrary polarizations are incident on the antenna structure from all possible directions. The waves launch from the transmitter antennas, and first they reach the elements of the primary reflection surface, and from here they rescatter to the second group of scatterers, and finally they are reflected to the receiving antennas. The transmission matrix (\mathbf{H}) which connects the receiver and transmitter antennas is filled by assuming DB scattering [13, 14].

The scatterers have a random scattering polarization matrix, and they are positioned randomly and uniformly on a ball-shaped surface around the transmitter and the receiver antennas.

\mathbf{H} matrix of the DB model consists of three different-sized submatrices:

$\mathbf{H}_{\text{tr-sc1}}$ means the transfer between the transmitter unit and the first surface of scatterers;

$\mathbf{H}_{\text{sc1-sc2}}$ is the connection between the first group and the second group of scatterers;

$\mathbf{H}_{\text{sc2-re}}$ is like the first matrix that can describe the path from the second group of scatterers to the receiver.

We chose the number of scatterer points on the reflection surface to be hundred. The transmission matrices $\mathbf{H}_{\text{tr-sc1}}$, $\mathbf{H}_{\text{sc1-sc2}}$, and $\mathbf{H}_{\text{sc2-re}}$ are of sizes $S_m \times M_t$, $S_n \times S_m$, and $N_r \times S_n$. Therefore, the complete MIMO transmission matrix, \mathbf{H} , may be given as

$$\mathbf{H} = \mathbf{H}_{\text{sc2-re}} \cdot \mathbf{H}_{\text{sc1-sc2}} \cdot \mathbf{H}_{\text{sc1-tr}}, \quad (5)$$

where \mathbf{H} is of size $N_r \times M_t$ (in this case the element number of \mathbf{H} is 9) with entries $\mathbf{H}[n, m]$ which describe the path from n_{th} receiver to m_{th} transmitter.

Each entry of the transmission matrices is computed using (5) for every radiation direction pointing either to or from the scatterers. The received incident electric field at the elements of the first reflection surface (at the first scatter points) around the transmitter unit has θ and φ direction components:

$$\begin{aligned} \mathbf{H}_{\text{sc1-re},\theta} &= E_{\text{rad},\theta}, \\ \mathbf{H}_{\text{sc1-re},\varphi} &= E_{\text{rad},\varphi}. \end{aligned} \quad (6)$$

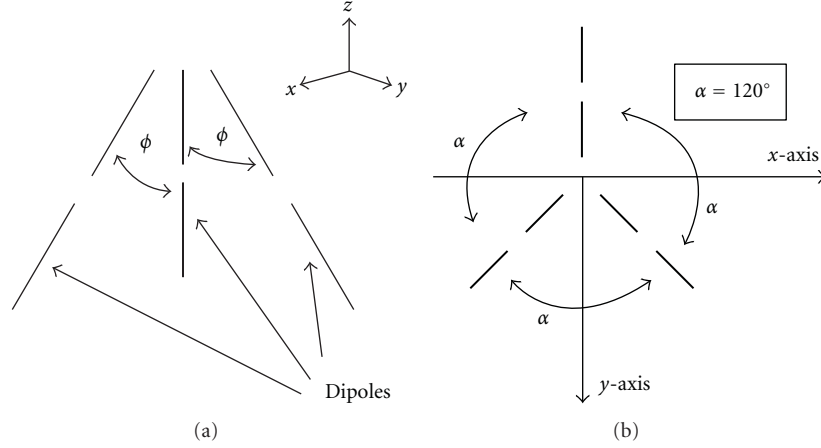


FIGURE 11: The 3×3 MIMO antenna structure for maximizing the mean capacity by rotation of the antennas, parallel at the transmitter and the receiver units, from the z -axis toward $x - y$ plane (it is opened like an umbrella).

The connection between the first and the second scatterers is described in the $\mathbf{H}_{\text{sc1-sc2}}$, which is a 162×162 square matrix where its entries are random complex numbers with Gaussian distribution. In this case the incident signal at the element of the second scattering surface is given by

$$\begin{aligned} E_{r,\vartheta} &= \mathbf{H}_{\text{sc1-sc2}} \cdot \mathbf{H}_{\text{sc1-re},\vartheta}, \\ E_{r,\varphi} &= \mathbf{H}_{\text{sc1-sc2}} \cdot \mathbf{H}_{\text{sc1-re},\varphi}. \end{aligned} \quad (7)$$

The transmission matrix, \mathbf{H} , is computed from the induced voltage on the receiving antenna elements. If there are W multipath incidents on the receiving antenna, the induced voltages from the direction ϑ and φ are given as

$$\begin{aligned} V_{i,\vartheta} &= \sum_{w=1}^W E_{r,\vartheta,w} \cdot h_{\text{eff},\vartheta,w}, \\ V_{i,\varphi} &= \sum_{w=1}^W E_{r,\varphi,w} \cdot h_{\text{eff},\varphi,w}, \end{aligned} \quad (8)$$

where h_{eff} is the vector effective length of the dipole which is given as $h_{\text{eff}} = (E_{\text{rad}}/j\beta I_{\text{in}}\eta) \cdot 4\pi r e^{j\beta r}$. Here I_{in} is the excitation.

Our multiple-antenna system is composed of $M_t = 3$ and $N_r = 3$ electric dipoles at both the transmitter and the receiver units. In this way, the transmission channel matrix \mathbf{H} consists of nine transmission links (3×3). At the start of the simulation the antennas were orientated in the z -axis and later they were rotated toward the $x - y$ axes (the structure was opened like an umbrella). The radiated electric field of each dipole is applied for the calculation of the transmitter matrix. The current distribution for each electric dipole is sinusoidal, which is often supposed for finite-length dipoles. Figure 11 shows the method of rotating of antennas in the simulation structure.

This simulation model statistically describes the material, surface, and motion of these objects which results in phase and amplitude error in the course of propagation. By this method we could describe the continuously varying indoor environment.

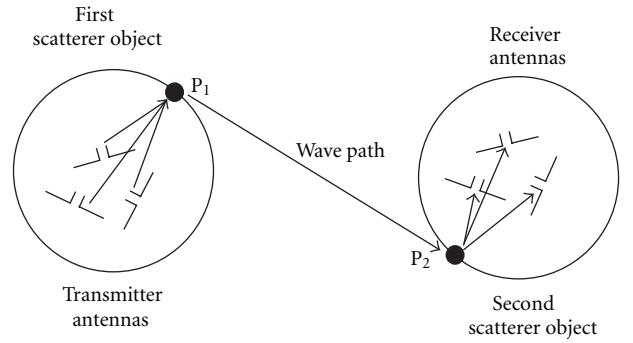


FIGURE 12: Signal wave path in a scattering environment. Transmitter and receiver dipole antennas in a DB scattering environment.

3.3. Genetic Algorithm-Based MIMO Antenna Orientation Optimization. The MIMO capacity enhancement calculation can be performed already by using the previously summarized mathematics, but because of the remarkable computational demand we do have test by using Genetic Algorithm- (GA-) based calculations for capacity maximization. In that case the antenna orientations on transmit and receive sides are coded for the GA in the region of angle $0 \dots 120$ degree (Figure 13).

Genetic Algorithms are increasingly being applied to difficult global optimization problems. GA optimizers are robust, stochastic search methods modeled on the principles and concepts of natural selection [10, 11].

If the transmit and receive antenna orientation is fully described by N_{par} parameters arranged in a vector $x = \{x_i \mid i = 1, \dots, N_{\text{par}}\}$ that is considered, then the knowledge of x permits the evaluation of the objective function $f(x)$, which indicates the worth of a design (the area coverage percentage). It is assumed that x_i takes on either real or discrete values and that $f(x)$ needs to be maximized.

In our approach in x we coded the ϕ angles and the objective function $f(x)$ is the channel mean capacity.

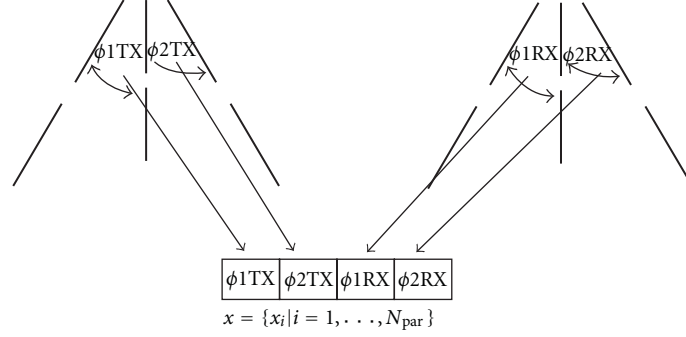


FIGURE 13: Coding scheme for GA.

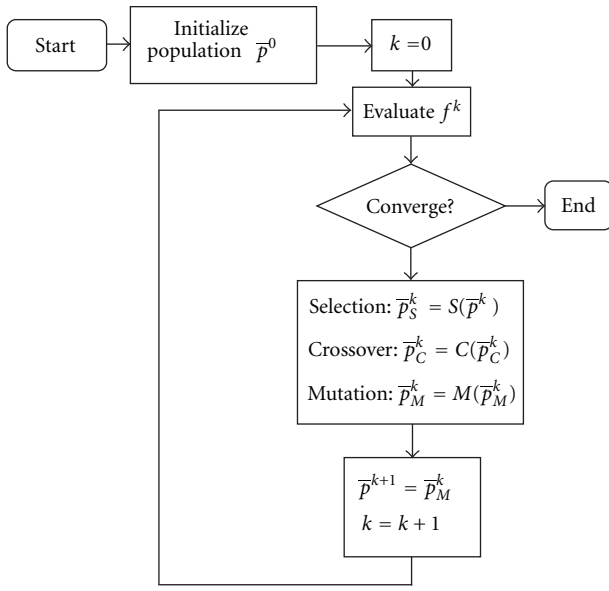


FIGURE 14: Simple GA flowchart.

The GA (Figure 14) does not operate on x but on a discrete representation or chromosome $p = \{g_i \mid i = 1, \dots, N\}$ of x , each parameter x_i being described by a gene g_i . Each gene g_i in turn consists of a set of N_{all}^i all that are selected from a finite alphabet and that together decode a unique x_i .

The GAs do not limit themselves to the iterative refinement of a single coded design candidate; instead the simple GA (SGA) simultaneously acts upon a set of candidates or population

$$\bar{p} = \{p(i) \mid i = 1, \dots, N_{\text{pop}}\}, \quad (9)$$

where N_{pop} is the population size.

Starting from an initial population \bar{p}^0 , the SGA iteratively constructs populations $\bar{p}^k, k = 1, \dots, N_{\text{gen}}$, with N_{gen} denoting the total number of SGA generations. Subsequent generations are constructed by iteratively acting upon \bar{p}^0 with a set of genetic operators. The operators that induce the

transition $\bar{p}^k \rightarrow \bar{p}^{k+1}$ are guided solely by knowledge of the vector of objective function values

$$f^k = \{f(x(p^k(i))) \mid i = 1, \dots, N_{\text{pop}}\} \quad (10)$$

and induce changes in the genetic makeup of the population leading to a \bar{p}^{k+1} comprising individuals that are, on average, better adapted to their environment than those in \bar{p}^k , that is, they are characterized by higher objective function values.

This change is affected by three operators mentioned in the introduction: selection (S), crossover (C), and mutation (M).

The selection operator implements the principle of survival of the fittest. Acting on \bar{p}^k , S produces a new population $\bar{p}_S^k = S(\bar{p}^k)$ again of size N_{pop} that is, on average, populated by the better-fit individuals present in \bar{p}^k . Among the many existing schemes, tournament selection has been chosen. The crossover operator mimics natural procreation. Specifically, C acts upon the population \bar{p}_S^k by mating its members, thereby creating a new population

$$\bar{p}_C^k = \bigcup_{i=1}^{N_{\text{pop}}/2} C(ch(\bar{p}_S^k), ch(\bar{p}_S^k)), \quad (11)$$

where the chromosome crossover operator C selects a random crossover allele $a_{N_{\text{cross}}}$ between the two chromosomes to be crossed upon which it acts with probability P_{cross} .

The mutation operator generates a new population of size

$$\bar{p}_M^k = \bigcup_{i=1}^{N_{\text{pop}}} M(\bar{p}_C^k(i)). \quad (12)$$

by introducing small random changes into \bar{p}_C^k . The action of M can be represented in operator form as

$$\bar{p}_M^k = \bigcup_{i=1}^{N_{\text{pop}}} M(\bar{p}_C^k(i)). \quad (13)$$

The cost function of the optimization procedure has been the channel mean capacity, ϕ is the angle between antennas:

$$\cos t = C(\phi). \quad (14)$$

TABLE 2: Simulation time for GA at different probability parameters (mutual coupling and conjugate antenna matching).

Mutation probability	Crossover probability	Optimization time
0.5%	1%	57 min
1%	1%	54 min
1%	2%	26 min
1%	5%	120 min

The effect of proper choose of the Crossover and Mutation probabilities on duration of optimization are illustrated in Table 2.

4. Simulation Results

4.1. Effect of Mutual Coupling for the Channel Capacity. The GA optimization procedure has been used for three cases without taking into account the antenna mutual couplings, with antenna mutual couplings using conjugate matching and with 50 ohms terminations on receiver antennas. The optimization times depend significantly on the GA parameters like mutation and crossover probabilities. In the simulation, 200 random scatterers have been used on each bounce, the angle resolution for antenna orientation 2° .

The GA gives the optimum for antenna orientation, but for comparing the three cases a full search has been made with an orientation angle resolution of 10° and the same orientation angles are used symmetrically for the transmit and receive antennas. We simulated the motion of the antennas by the above-described rotation method. First of all in this simulation the antennas are parallel to the z -axis. In the midst of the simulation the antennas opened in the space like an umbrella. In the end of the simulation the antennas reached the $x - y$ plane. In this case the antennas are on the farthest position, which by the phase between antenna and z -axis was changed from 0° to 90° . The result of the simulation shows perfect symmetry for the $x - y$ plane. We look for the perfect position for the maximal mean channel capacity in consideration of the effect of mutual coupling in case of conjugate matching and nonconjugate matching. Figure 15 shows the mean capacity versus the angle of rotation. The simulation parameters are $S/N = 20$ dB, and length of antennas are 0.45λ .

In the case of neglected antenna coupling, the maximal channel capacity is at about $\phi = 45^\circ$ antenna angle. In case of conjugate matching, the maximal channel capacity is at 70° and without conjugate matching the capacity is maximal and approximately constant from 50° .

Finally we chose the 90° structure, as a matter of fact the MIMO cube, because the realization easiness and the capacity increase in the angle region of 40 – 90° is not really considerable. The implemented GA algorithm later will be used for the general position optimization of the MIMO antennas, and with this increase of freedom we expect a much higher capacity gain and a more compact structure than the MIMO cube.

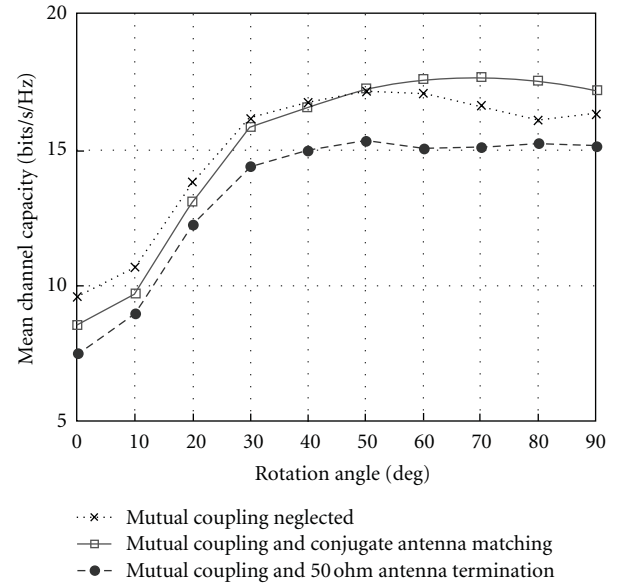


FIGURE 15: Channel capacity of a 3×3 MIMO antenna system, in case of neglected antenna coupling, mutual coupling with and without conjugate matching.



FIGURE 16: 3 antennas on the mid of the faces.

5. Final Measurement

Figures 16 and 18 show the realized antenna structures. The measurement results are the S_{ij} (mutual coupling) and S_{ii} (reflection) parameters of the antennas. Figures 17 (antennas on faces) and Figure 19 (antennas on edges) show these results.

The measurements setup is part of an existing receiver beamforming array, which has the main characteristics of operation in 2 GHz band, 4 parallel $I - Q$ receiver channel, -102 dBm receiver sensitivity for 3 dB SNR, 12 bits ADC, real-time sampling on every channel simultaneously, fast in-built DSP for embedded signal processing (380 MIPS). The system control is on USB interface using LabVIEW control and processing software. Our measurement system contains

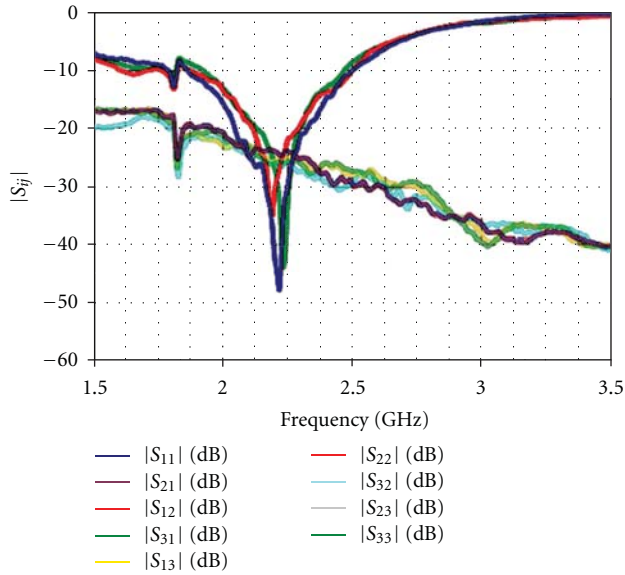


FIGURE 17: 3 antennas on the mid of the faces—measured S parameters.



FIGURE 18: 3 antennas on the edges.

three major parts: the receiver blocks, the DSP unit, and the measuring software running on a laptop computer. The four receiver units with overall 4 input channels operate at 2.2 GHz center frequency, after double conversion baseband $I - Q$ signals are sampled and converted to 12 bit data. The DSP can provide sampling numbers having the powers of 2 (1, 2, 4, ..., 256). The receiver antennas are the newly developed MIMO antennas. For our measuring setup only three-channel receiver was used from the existing 4 because of the MIMO antenna which has 3 outputs. On the transmit side, the same MIMO antenna has been used but only SIMO measurement has been performed with our single transmitter.

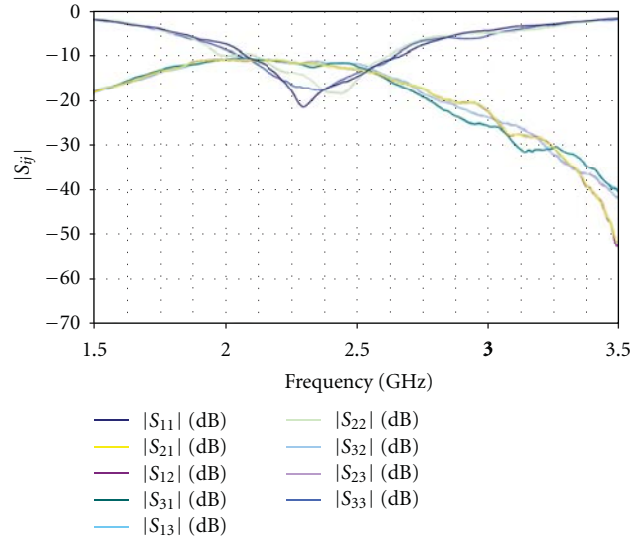


FIGURE 19: 3 antennas on the edges—measured S parameters.

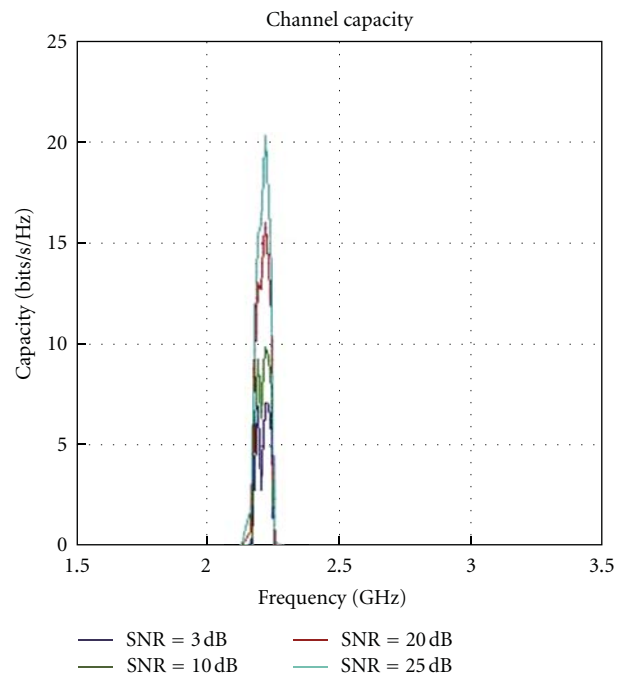


FIGURE 20: 3 antennas on the mid of the faces—calculated channel capacity (from channel transfer matrix).

Based on the three independent SIMO measurements, we got the channel transfer matrices and calculated the channel capacity using (3).

The results (Figures 20 and 21) show that the first structure (antennas on the faces) realizes higher channel capacity than the second one with antennas on edges, but this maximal capacity can be gotten only in a very narrow bandwidth; therefore, for the present wideband wireless data applications, the edge placed slots give an enhanced capacity.

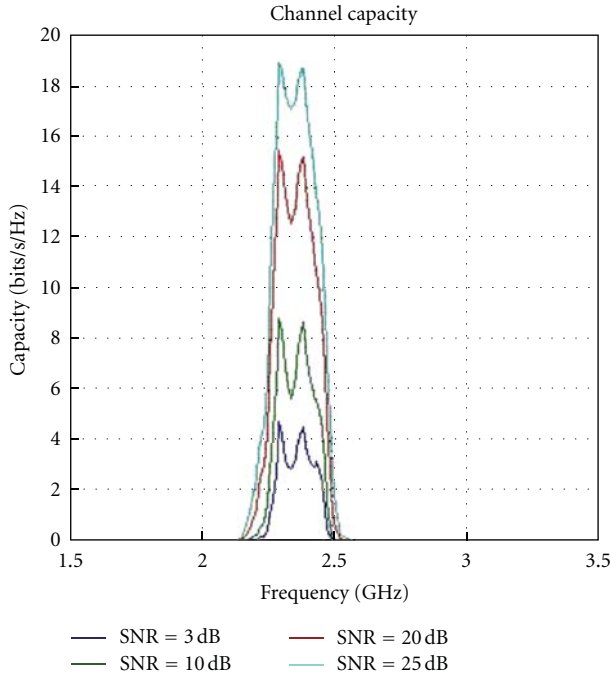


FIGURE 21: 3 antennas on the edges—calculated channel capacity (from channel transfer matrix).

6. Conclusion

In this paper, we investigated a 3×3 MIMO antennas system. We made simulations for analysis of the effects of antenna positions for the mean channel capacity. We found that the maximal channel mean capacity is affected by structure in which the antennas are perpendicular to each other. With this we examined the structure with conjugate and non-conjugate matching. Based on the result of the simulation in the realized and measured structure, the antennas were perpendicular to each other. The measurements confirm our results of simulations.

The next step in our research is developing the full MIMO transmitter-receiver measurement system, with which direct capacity measurements can be fulfilled.

Acknowledgments

The research work leading to this paper has been supported by the European Commission under SAMURAI. This work is connected to the scientific program of the “Development of quality-oriented and harmonized R+D+I strategy and functional model at BME” project. This project is supported by the New Széchenyi Plan (Project ID: TÁMOP-4.2.1/B-09/1/KMR-2010-0002).

References

[1] C. Y. Chiu and R. D. Murch, “Design of a 24-port MIMO cube,” in *IEEE Antennas and Propagation Society, AP-S International Symposium*, pp. 2397–2400, Honolulu, Hawaii, USA, June 2007.

[2] C. Y. Chiu, J. B. Yan, and R. D. Murch, “24-port and 36-port antenna cubes suitable for MIMO wireless communications,” *IEEE Transactions on Antennas and Propagation*, vol. 56, no. 4, pp. 1170–1176, 2008.

[3] Á. Németh, L. Szücs, and L. Nagy, “MIMO cube formed of slot dipoles,” in *Proceedings of the 16th IST Mobile and Wireless Communications Summit*, Budapest, Hungary, July 2007.

[4] N. Behdad, “A uniplanar dual-polarized miniaturized antenna,” in *Proceedings of the General Assembly and Scientific Symposium of the International Union of Radio Science (URSI '08)*, Chicago, Ill, USA, August 2008.

[5] A. Suyama, D. Uchida, H. Arai, Y. Inoue, and K. Cho, “A dual polarization 8-port MIMO antenna with dipole and slot antennas,” IEICE Technical Report, Macao University, Macao, China, 2009.

[6] D. Uchida, H. Arai, Y. Inoue, and K. Cho, “A low-profile dual-polarized directional antenna for enhancing channel capacity in indoor MIMO systems,” *IEICE Transactions on Communications*, vol. 93, no. 10, pp. 2570–2577, 2010.

[7] J. X. Yun and R. G. Vaughan, “Slot MIMO cube,” in *Proceedings of the IEEE International Symposium on Antennas and Propagation and CNC-USNC/URSI Radio Science Meeting (APSURSI '10)*, Toronto, Canada, July 2010.

[8] T. Svantesson and A. Ranheim, “Mutual coupling effects on the capacity of multielement antenna systems,” in *Proceedings of the IEEE International Conference on Acoustics, Speech, and Signal Processing*, vol. 4, pp. 2485–2488, Salt Lake City, Utah, USA, May 2001.

[9] R. Janaswamy, “Effect of element mutual coupling on the capacity of fixed length linear arrays,” *IEEE Antennas and Wireless Propagation Letters*, vol. 1, pp. 157–160, 2002.

[10] Z. Michalewicz, *Genetic Algorithms + Data Structures = Evolution Programs*, Springer, Berlin, Germany, 1996.

[11] E. Michielssen, Y. Rahmat-Samii, and D. S. Weile, *Electromagnetic System Design Using Genetic Algorithms*, Modern Radio Science, 1999.

[12] L. Nagy, “Indoor radio coverage optimization for WLAN,” in *Proceedings of the 2nd European Conference on Antennas and Propagation (EuCAP '07)*, no. 11961, Edinburgh, UK, November 2007.

[13] B. N. Getu and J. B. Andersen, “The MIMO cube—a compact MIMO antenna,” *IEEE Transactions on Wireless Communications*, vol. 4, no. 3, pp. 1136–1141, 2005.

[14] B. N. Getu and R. Janaswamy, “The effect of mutual coupling on the capacity of the MIMO cube,” *IEEE Antennas and Wireless Propagation Letters*, vol. 4, no. 1, pp. 240–244, 2005.

Research Article

Controlling Initial and Final Radii to Achieve a Low-Complexity Sphere Decoding Technique in MIMO Channels

Fatemeh Eshagh Hosseini¹ and Shahriar Shirvani Moghaddam²

¹Developing Research and Strategic Planning Department, Mobile Communication Company of Iran (MCI), Tehran 199195-4651, Iran

²Digital Communications Signal Processing (DCSP) Research Lab., Faculty of Electrical and Computer Engineering, Shahid Rajaee Teacher Training University (SRTTU), Tehran 16788-15811, Iran

Correspondence should be addressed to Fatemeh Eshagh Hosseini, f.hosseini@mci.ir

Received 2 August 2011; Revised 18 October 2011; Accepted 6 November 2011

Academic Editor: Wenhua Chen

Copyright © 2012 F. Eshagh Hosseini and S. Shirvani Moghaddam. This is an open access article distributed under the Creative Commons Attribution License, which permits unrestricted use, distribution, and reproduction in any medium, provided the original work is properly cited.

In order to apply sphere decoding algorithm in multiple-input multiple-output communication systems and to make it feasible for real-time applications, its computational complexity should be decreased. To achieve this goal, this paper provides some useful insights into the effect of initial and the final sphere radii and estimating them effortlessly. It also discusses practical ways of initiating the algorithm properly and terminating it before the normal end of the process as well as the cost of these methods. Besides, a novel algorithm is introduced which utilizes the presented techniques according to a threshold factor which is defined in terms of the number of transmit antennas and the noise variance. Simulation results show that the proposed algorithm offers a desirable performance and reasonable complexity satisfying practical constraints.

1. Introduction

The Nondeterministic Polynomial-time hard (NP-hard) complexity of Maximum Likelihood (ML) decoding, the optimal decoder, generally prohibits its use in practical Multiple-Input Multiple-Output (MIMO) systems [1], especially when a large signal constellation and/or many transmit antennas are involved. Some suboptimum detection algorithms, such as Kannan's algorithm which searches only over restricted parallelograms [2], the KZ algorithm [3] based on the Korkin-Zolotarev-reduced basis, and the Sphere Decoding (SD) algorithm of Fincke and Pohst [4, 5], can perform detection with much lower complexity, but at a performance degradation.

SD was first introduced in [6] to perform ML detection, and it achieves reduced complexity by searching for the closest lattice point over the points that lie in a certain sphere around a given vector. Although it significantly reduces the computational complexity of ML, it requires huge amount of computations in MIMO systems. There are several approaches to reduce the complexity of SD algorithm such

as the Schnorr-Euchner (SE) enumeration [7], descending probabilistic ordering [8], increasing radius sphere decoder [9], parallel competing branch algorithm [10], and reduced dimension maximum likelihood search [11]. Other approaches trading performance for complexity include the radius scheduling method [12], probabilistic tree pruning algorithm [13], sequential Fano decoders [14], and semi-definite relaxation [15]. The work of [16] proposes the utilization of the SE refinement of the Pohst enumeration in the *closest lattice point* search. Based on the numerical results, [16] concludes that the SE enumeration is more efficient than the Viterbo-Boutros implementation in [6]. According to the proposed method in [16], an algorithm is presented in [17] and it has been shown that it is robust to the initial choice of the sphere radius. This concept has been further discussed in different pieces of research that try to improve its performance and computational complexity which make it possible for practical real time systems.

Various papers have analyzed the complexity of SD such as [18] which shows that the expected complexity of SD the expected number of operations required by the algorithm,

$C(P, \rho)$, depends on the both number of transmit antennas, P , and the Signal-to-Noise Ratio (SNR), ρ . It is also shown in [18] that when the SNR is high, the expected number of operations required by the SD, can be approximated by a polynomial function for small P . An exact but complicated expression for the expected number of operations required by the sphere decoder has been obtained in [18]. In [19] by obtaining a lower bound, it is shown that the expected complexity of SD applied to a large class of problems is exponential in P . In this work the complexity of SE-SD algorithm is discussed from a new point of view.

Stopping criteria can be used to reduce the complexity of SD, since it results in terminating the decoding process earlier and thus prevents a huge amount of extra calculations. Some researchers have worked on these criteria for some special scenarios. This paper also discusses the convergence radius and proposes a new stopping criterion.

SD searches a lattice through a given set of points that is bounded by the search sphere with the received point as center. Therefore, the method requires determining an initial search radius, C_0 . The concept of choosing a suitable C_0 plays a crucial role in finding the nearest lattice point in a sphere. The initial radius should not only be small enough to contain at least one lattice point but also big enough to have a practical enumeration complexity of finding closest point among containing lattice points. Even though it is claimed that SE-SD is less sensitive to initial radius than the original SD, [17] shows that the complexity of SE-SD is still controlled by C_0 . To the best of our knowledge, there are no general guidelines for choosing appropriate C_0 . This paper focuses on the suitable C_0 and discusses the way of finding it easily, which is applicable to the complexity-limited wireless communication systems. This paper also demonstrates that the initial radius can affect not only the computational complexity but also BER of SE-SD algorithm significantly.

In this paper, \mathbb{Z} , \mathbb{R} , and \mathbb{C} are the sets of integer, real, and complex numbers, respectively. $\mathcal{CN}(\cdot)$ denotes circularly symmetric complex Normal distribution.

In the assumed MIMO system, $\tilde{\mathbf{X}}(\tilde{x}_1, \tilde{x}_2, \dots, \tilde{x}_P) \in \mathbb{C}^P$ is the complex transmitted vector of dimension P , whose elements are members of a squared M -dimension Quadrature Amplitude Modulation (M -QAM) constellation. It is assumed that the channel coefficients matrix, $\tilde{\mathbf{H}} \in \mathbb{C}^{P \times Q}$, which is comprised of i.i.d $\mathcal{CN}(0, 1)$ entries, can be estimated accurately at the receiver. The noise vector comprised of i.i.d $\mathcal{CN}(0, 2\sigma^2)$ entries is presented by $\tilde{\mathbf{N}} \in \mathbb{C}^Q$, where $\sigma^2 = Q\bar{E}_S 10^{-0.1 \text{ SNR}} / 2 \log_2^M$, and \bar{E}_S is the average signal energy of the constellation. A symbol, defined as $\mathbf{S} : x_1 \dots x_p$, is transmitted over P antennas, and $\tilde{\mathbf{Y}} \in \mathbb{C}^Q$, which is given by $\tilde{\mathbf{Y}} = \tilde{\mathbf{H}}\tilde{\mathbf{X}} + \tilde{\mathbf{N}}$, is received.

To obtain a lattice representation of this multiple antenna system, the complex matrix equation is transformed into the real matrix equation as

$$\mathbf{Y} = \mathbf{H}\mathbf{X} + \mathbf{N}, \quad (1)$$

where \mathbf{Y} and \mathbf{N} , similar to \mathbf{X} are obtained through $\mathbf{X} = [\text{real}(\tilde{\mathbf{X}}^T) \text{ imag}(\tilde{\mathbf{X}}^T)]^T$ and $\tilde{\mathbf{H}}$ is transformed to

$$\mathbf{H} = \begin{bmatrix} \text{real}(\tilde{\mathbf{H}}) & -\text{imag}(\tilde{\mathbf{H}}) \\ \text{imag}(\tilde{\mathbf{H}}) & \text{real}(\tilde{\mathbf{H}}) \end{bmatrix} \in \mathbb{R}^{p \times q}, \quad (2)$$

where for easier notation, $p = 2P$ and $q = 2Q$.

The remainder of this paper is organized as follows. Section 2 describes sphere decoding and SE-SD algorithm, briefly. The initial radius and complexity of the algorithm is discussed through simulation results over a wide range of SNRs and channel sizes in Section 3. Section 4 goes into the ideas of stopping criteria for the algorithm. In Section 5 a new low-complexity algorithm is introduced. Finally, Section 6 draws the conclusion.

2. Sphere Decoding

A finite lattice can be defined as $\Lambda = \{\mathbf{H}\mathbf{X} : \mathbf{X} \in \mathbb{Z}^P\}$ where \mathbf{H} is the generator matrix of the lattice and \mathbf{X} contains the coordinates of lattice points. The ML estimates \mathbf{X}_{ML} that minimizes the Euclidean distance between \mathbf{Y} and \mathbf{X}_{ML} , as follows:

$$\mathbf{X}_{ML} = \arg \min_{\mathbf{X} \in \mathbb{Z}_\Omega^p} \|\mathbf{Y} - \mathbf{H}\mathbf{X}\|^2, \quad (3)$$

where $\|\cdot\|^2$ represents the vector norm and $\mathbb{Z}_\Omega^p = \{a + jb \mid a, b \in \{-\sqrt{M} + 1, -\sqrt{M} + 3, \dots, \sqrt{M} - 3, \sqrt{M} - 1\}\}$ represents the set of points of the M -QAM constellation.

As mentioned earlier, SD searches the lattice through a given set of points bounded by a sphere with the received point as center and a specific initial radius. Whenever a point is found inside the sphere, the radius is reduced to the value of the distance between the new and the received point. Under assumption of $p = q$, the channel matrix can be transformed into $\mathbf{H} = \mathbf{Q}\mathbf{R}$ by performing QR-decomposition. \mathbf{R} is an upper triangular matrix, and \mathbf{Q} is an orthogonal matrix. Therefore, the ML problem will be simplified to find the lattice point that satisfies the following condition:

$$C_0^2 \geq \|\hat{\mathbf{Y}} - \mathbf{R}\mathbf{X}\|^2, \quad (4)$$

where $\hat{\mathbf{Y}} = \mathbf{Q}^* \mathbf{Y}$ and $(\cdot)^*$ represents Hermitian matrix transposition. The inequality can be rewritten and then expanded as

$$C_0^2 \geq \sum_{i=1}^p \left(\hat{y}_i - \sum_{j=i}^p r_{i,j} x_j \right)^2 = \left(\hat{y}_p - r_{p,p} x_p \right)^2 + \left(\hat{y}_{p-1} - r_{p-1,p} x_p - r_{p-1,p-1} x_{p-1} \right)^2 + \dots, \quad (5)$$

where $r_{i,j}$ denotes the (i, j) entry of \mathbf{R} . The previous inequality results in p different inequalities. By taking advantage of the upper triangular property of \mathbf{R} the first term of right-hand side of (5) depends only on x_p and thus it belongs to the following interval:

$$\left[\frac{-C_0 + \hat{y}_p}{r_{p,p}} \right] \leq x_p \leq \left[\frac{C_0 + \hat{y}_p}{r_{p,p}} \right], \quad (6)$$

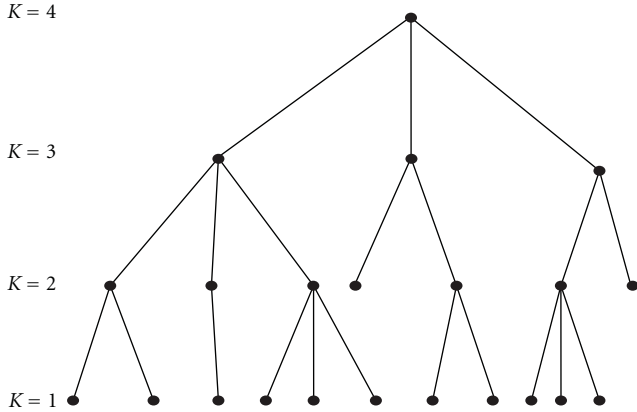


FIGURE 1: The possible searching paths in a tree for $P = 3$ and 4—QAM.

where $\lceil \cdot \rceil$ and $\lfloor \cdot \rfloor$ denote rounding to the nearest larger and smaller element in the set of numbers that spans the lattice, respectively. The intervals for $x_{p-1}, x_{p-2}, \dots, x_1$ are found in a similar fashion, in which x_i is a function of only j , $j = i, \dots, p$. Generally speaking, all possible candidates for x_i should be searched within a sphere with radius C_0 and dimension $p - i + 1$.

The first candidate for x_i , namely, \hat{x}_i , is:

$$\hat{x}_i = \left\lceil \frac{1}{r_{i,i}} \left(\hat{y}_i - \sum_{j=i+1}^p r_{i,j} x_j \right) \right\rceil. \quad (7)$$

By SE enumeration, the candidates are spanned in a zigzag order, starting from the midpoint. Hence, at each level i , the SE enumeration will produce this sequence of candidates for x_i : $\{\hat{x}_i, \hat{x}_i + 1, \hat{x}_i - 1, \hat{x}_i + 2, \hat{x}_i - 2, \dots\}$ if $\hat{y}_i - \sum_{j=i+1}^p r_{i,j} x_j - r_{i,i} \hat{x}_i < 0$ and otherwise $\{\hat{x}_i, \hat{x}_i - 1, \hat{x}_i + 1, \hat{x}_i - 2, \hat{x}_i + 2, \dots\}$.

A full search can be depicted as a search tree, like Figure 1, which its root is the P th entries of the possible symbol and each node in the i th level shows one of the possible values for the i th entry of the symbol. The search starts from the root down to the 1st level (leaf node), where at the i th level, all possible $(i - 1)$ entries are found so that the symbol lies in the sphere. When the search reaches the leaf node, all the entries of the symbol are discovered. Therefore, each path through the tree corresponds to a possible symbol. As a result, SD can be viewed as a pruning algorithm on this tree from which, based on violation of the constraint given by (4), a branch can be removed at any level.

The work of [17] proposed an algorithm with 6 recursive steps to implement SE-SD algorithm. After initialization, leading to start from the highest level of the tree and set C_0 , the algorithm begins with step 2, by offering the first candidate for the root of the tree. The testing node at each level is offered by steps 2 and 6 through SE enumeration. By using the lattice boundary (maximum and minimum of \mathbb{Z}_Q^p) in steps 2 and 6, the algorithm works with only the finite square M -QAM constellation. Step 3 examines the constraint given by (5) which may lead to two cases.

- (1) If the candidate is valid and a leaf node is reached ($i = 1$), the symbol is recorded as the ML solution, the radius is updated in step 5, and the algorithm restarts from ($i = 2$). But if the valid candidate is found in other levels, the search proceeds in a lower level.
- (2) If the candidate is not valid, the algorithm will go to step 4. If the algorithm is in the top level, it means that there is no valid symbol in the sphere. Thus, the algorithm terminates. Otherwise, the algorithm will go up to $i + 1$ and the next candidate of that level will be tested.

This paper uses the SE-SD algorithm introduced in [20] which is the modified version of the proposed algorithm in [17] which does not consider any point outside the finite lattice through lattice boundary awareness. This algorithm is preferred because of the lower complexity without any performance degradation.

3. Initial Radius of SE-SD Algorithm

Several approaches have been proposed to find an appropriate initial radius. Because of the advantages of the Schnorr-Euchner enumeration, the conventional methods choose the positive infinity as the initial radius. Obviously, this approach avoids declaring an empty sphere. It is also clear that the first point found with $C_0 = \infty$ corresponds to the Babai point [16]. Thus, a more suitable choice for C_0 is to use the distance between the Babai point and \mathbf{Y} , since this radius guarantees the existence of at least one lattice point inside the sphere. Generally, it is not clear whether this choice of initial radius leads to too many lattice points lying inside the sphere [18]. In [21] through some examples it is shown that this sphere contains at least one point, if the radius is computed exactly. However, in practice, due to rounding errors introduced by floating-point computation, this radius cannot be calculated exactly. It offers an upper bound for the computational error of C_0 and defines $C_0 + 2\mu(\sqrt{q}\|\mathbf{H}\|^2\|\mathbf{X}\|^2)$ as the initial radius, where μ is the unit of round-off. The work of [22] mentions that this method is useful when the noise variance is relatively small. The work of [23] proposes a method that utilizes the result of QR decomposition and reordering of \mathbf{H} to obtain Babai point and defines the initial radius as the distance between the received signal and the lattice point mapped by the suboptimal solution.

Another case for C_0 is the covering radius of the lattice, defined to be the smallest radius of spheres centered at the lattice points that covers the entire space [24]. This is clearly the smallest radius that guarantees the existence of a point inside the sphere for any \mathbf{Y} . The problem with this choice of C_0 is that determining the covering radius for a given lattice is itself NP-hard [25].

Some works consider a small fixed number as C_0 for all cases, which is increased if no lattice point is found in the sphere. The work of [26] sets the initial radius to the distance between the lattice point mapped by Minimum Mean Square Error (MMSE) solution and the received signal. In general,

the approaches that use the suboptimal solutions to find C_0 contribute to higher complexity.

A useful approach is to choose C_0 according to the noise distribution, so (3) can be helpful to determine the desired C_0 . $\|\mathbf{Y} - \mathbf{H}\mathbf{X}\|^2 = \|\mathbf{N}\|^2$ is a Chi-square random variable with q degrees of freedom. Therefore, a radius may be chosen to be a scaled variance of the noise [18]:

$$C_0^2 = Kq\sigma^2. \quad (8)$$

In such a way, a lattice point can be found inside the sphere with a high probability:

$$\int_0^{0.5kq} \frac{\lambda^{0.5q-1}}{\Gamma(0.5q)} e^{-\lambda} d\lambda = 1 - \epsilon, \quad (9)$$

where the integrand is the probability density function of the Chi-square random variable with q degrees of freedom, and ϵ is set to a value close to 1. If the point is not found, the probability will be increased and a new C_0 is calculated; consequently, the searching will be restarted considering the new radius.

It is important to note that the radius is chosen based on the statistics of the noise and not H . Making the choice based on H quickly leads us to NP hard problems (such as determining the covering radius). Moreover, as noted in [1], selection of the radius based on the noise has a beneficial effect on the computational complexity. The work of [27] proposes an empirical definition for K in special situations (64 and 16-QAM) in a small SNR range.

To investigate the behavior of the algorithm, we find the average number of flops, a measure for the complexity, and Bit Error Rate (BER) of the SE-SD algorithm for various ρ , M and p through computer simulations. Our experimental setup corresponds to the transmission of M -QAM constellations over a multiple antenna flat Rayleigh fading channel, which is reasonable for many communication problems. The channel matrix \mathbf{H} , changes randomly after transmitting 100 symbols. In order to plot BER or complexity versus initial radius for certain ρ , M , and p , a set of 100 initial radii are examined, and 10^8 random symbols per any particular C_0 , are tested. Note that only the flops of the search process are counted without considering the cost of QR decomposition. In practice, at least one lattice point should be found by the algorithm, and if C_0 does not contain any point the initial radius is multiplied by 1.5 and the algorithm is restarted.

The work of [17] investigates the effect of C_0 on the average complexity of SE-SD algorithm for a 16-QAM constellation at a range of $\rho = 15$ to 25 dB and it is shown that for $\rho > 20$ dB, the complexity is less insensitive to the initial radius than the original SD. However, the relationship between the computational complexity and the initial radius does not discussed in [17].

Although (9) implies that the probability of finding lattice point inside the sphere changes as initial radius changes, there are no known paper on the effect of C_0 on the performance of SE-SD for finite lattices. Figure 2 illustrates the significant effect of initial radius on the performance of the algorithm. It shows BER as a function of initial radius for $P = 4$ and $M = 64$ when $\rho = 18.4, 21.46,$ and

24 dB ($\sigma^2 = 0.203, 0.1,$ and 0.056). A particular C_0 that leads to the lowest BER calling ‘‘the best performance initial radius’’, C_{0BP} , can be seen in each subfigure of Figure 2. For instance, when $\rho = 18.4$ dB, BER of $C_0 = C_{0BP}$ is 21% less than that of $C_0 = 70$. The average Babai Radius is depicted by a line in Figure 2, and this figure shows that C_{0BP} is close to C_{ba} but not exactly equal to it.

A huge number of figures that show the complexity versus C_0 have been obtained from simulations when $P = 4$, $M = 64$ and ρ is choosing from 7.5 dB to 30 dB with the step of 0.5 dB, which is the typical SNR range for wireless communication applications. In this paper only 6 examples of these simulation results are depicted in Figures 3 and 4 due to the limited space. These figures depict the complexity of SE-SD algorithm as a function of initial radius for $\rho = 7.5, 11.4, 13.3, 18.4, 24,$ and 30 dB. All of the simulated curves follow a similar pattern and can be fitted to a rational function of two fourth-order polynomials [28].

For any C_0 less than C_{0LC} , as the initial radius decreases, the complexity soars. Because the smaller spheres force the algorithm to restart several times, this contributes to huge computational complexity. The curves show that the complexity gets its lowest value when C_0 is near C_{ba} . This C_0 can be defined as the ‘‘lowest complexity initial radius’’, C_{0LC} . There is three cases related to ρ and C_0 .

- (1) The curves related to low ρ (Figures 3(a) and 3(b)) are smoother, and for any C_0 bigger than C_{ba} the complexity seems almost constant, so, in this case a big initial radius should be chosen to have low complexity however, it should be small enough (second-order value) not to degrade the performance noticeably (noting Figure 2). For example $C_0 = 60$ is suitable for the case of $P = 4$, $M = 64$, and $\rho = 10$ to 5 dB.
- (2) Moderate ρ results can be seen in Figures 4(a) and 3(c). In this curve the lowest complexity is obtained when C_0 is around C_{ba} and it grows considerably when C_0 increases. For instance, the complexity grows about 40% as $C_0 = 70$ is chosen for $\rho = 11.4$ dB. Therefore, in this case the most suitable C_0 should be chosen slightly less than C_{ba} .
- (3) High ρ makes the complexity of the algorithm less sensitive to any C_0 (greater than C_{ba}), as Figures 4(b) and 4(c) illustrate. Although the raise in the complexity can be neglected for high C_0 , the performance degradation is significant. It comes to the conclusion that an initial radius greater than C_{ba} and less than 1 can be acceptable in this situation to comprise between the performance and the complexity.

From Figures 3 and 4 it is obvious that decreasing of ρ leads to decline in C_{0LC} and also smoothing the curves which supports the theory in [18] that recommends choosing C_0 according to the noise variance.

Simulation results that depict the average complexity and BER of SE-SD algorithm as a function of C_0 when $P = 4$, $\sigma^2 = 0.203$, and $M = 4, 16, 64,$ and 128 show that not only C_{0LC} but also C_{0BP} does not change as the constellation’s size grows. It comes to the conclusion that the

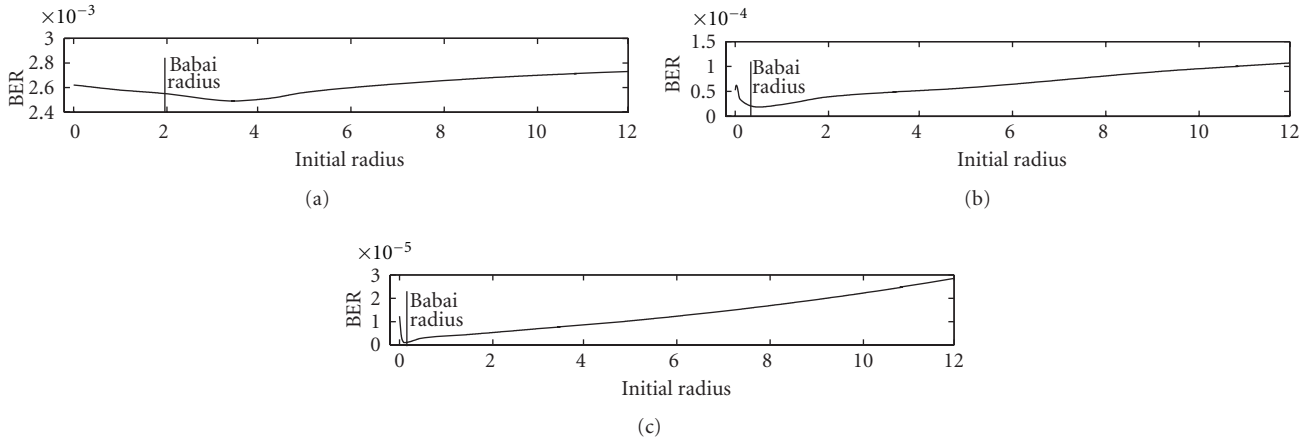


FIGURE 2: BER versus initial radius of SE-SD algorithm when $P = 4$, $M = 64$. (a) $\rho = 18.4$ dB, (b) $\rho = 21.46$ dB, (c) $\rho = 24$ dB.

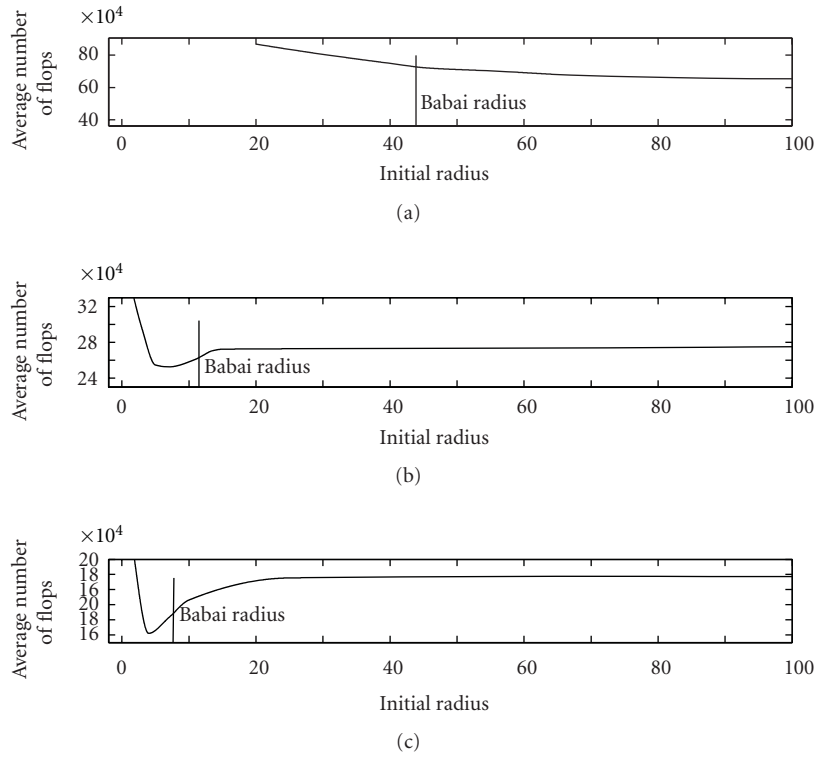


FIGURE 3: The average number of flops versus initial radius of SE-SD algorithm when $P = 4$, $M = 64$. (a) $\sigma^2 = 2.49$ ($\rho = 7.5$ dB), (b) $\sigma^2 = 1.02$ ($\rho = 11.4$ dB), (c) $\sigma^2 = 0.65$ ($\rho = 13.3$ dB).

size of constellation does not affect the performance and the complexity of SE-SD.

While an approach is to choose C_{ba} as the initial radius [16, 17], Figures 2, 3, and 4 show that neither C_{OLC} nor C_{OBP} is exactly equal to C_{ba} . Using C_{ba} as the initial radius in some practical scenarios causes a noticeable increase in BER and the complexity due to the rounding problem. In addition, calculating C_{ba} costs extra complexity which cannot be negligible in some scenarios.

Figure 5 shows C_{ba} and the proper C_0 (which is obtained from a compromise between performance and complexity) of

SE-SD algorithm as a function of number of transmit antennas when $M = 64$ and $\sigma^2 = 0.65, 0.203$, and 0.05 . As it can be seen from Figures 5(b) and 5(c), for a low σ^2 scenario in spite of C_{ba} , the number of transmit antennas does not affect the suitable C_0 and it remains almost constant for any number of antennas. Thus, in this case, finding suitable C_0 for small problem size (low P) concludes to solving the initial radius problem for the big one (high P). Since the complexity of calculating C_{ba} for scenarios with small number of antennas is considerably less than the big one, the cost of finding suitable initial radius reduces significantly.

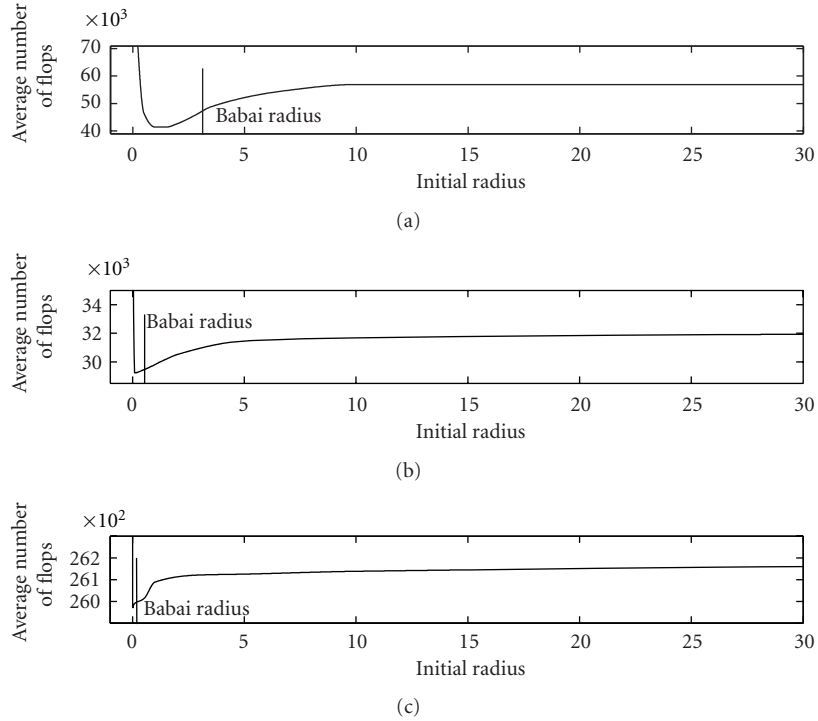


FIGURE 4: The average number of flops versus initial radius of SE-SD algorithm when $P = 4$ and $M = 64$. (a) $\sigma^2 = 0.203$ ($\rho = 18.4$ dB), (b) $\sigma^2 = 0.056$ ($\rho = 24$ dB), and (c) $\sigma^2 = 0.014$ ($\rho = 30$ dB).

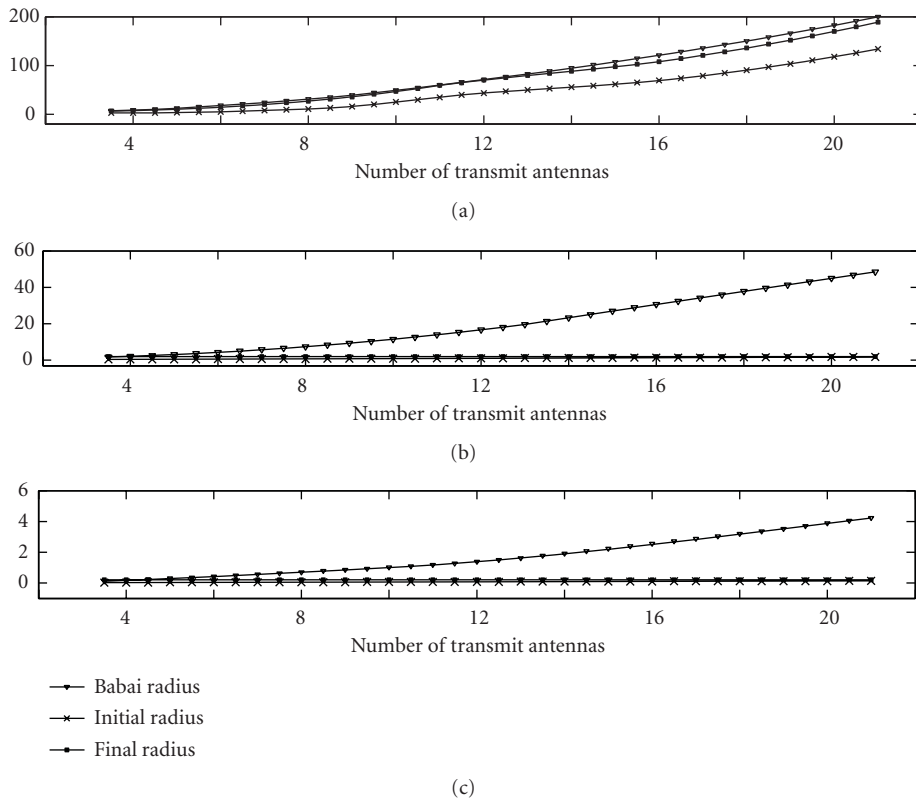


FIGURE 5: C_f , the proper C_0 , and C_{ba} of SE-SD versus the number of antennas for 64QAM. (a) $\sigma^2 = 0.65$, (b) $\sigma^2 = 0.203$, and (c) $\sigma^2 = 0.05$.

However, as it can be seen from Figure 5(a), high σ^2 scenario needs calculating of Babai radius to use as initial radius. Because of the rounding problem for any scenarios with $\sigma^2 > 0.5$, the suitable C_0 is approximately 8% smaller than C_{ba} .

4. Stopping Criteria for SE-SD Algorithm

Stopping criterion is a potential mean for saving computational complexity in iterative algorithms like SE-SD. The work of [29] suggests that if an enumerated lattice point is found to be at a distance less than half the length of shortest lattice vector (packing radius) from \mathbf{Y} , it is clearly a nearest lattice point and thus the enumeration process can be terminated right away. The work of [29] utilizes a lower bound on the packing radius as a stopping test. The work of [30] introduces a parameter, V_{th} , based on the target symbol error rate and σ^2 , and the proposed probabilistic search stops when \hat{x} is within it.

The idea of [31] is to first run a lattice reduction-aided SIC detector. If this results in a valid vector, with all elements within the symbol alphabet, the algorithm stops. Otherwise, it proceeds by running the sphere decoder.

It was mentioned that when the algorithm finds a symbol in the sphere, calculates a new radius for the sphere and when the algorithm reaches its convergence radius, it still tries to find a symbol inside the new sphere, but it does not succeed, because there is no one. Of course, the attempts to find a new symbol after reaching the convergence radius cause significant extra calculations. Thus, if SE-SD algorithm terminates as soon as it reaches the convergence radius, the huge amount of unnecessary computations can be prevented. Consequently, the complexity of the algorithm will be reduced considerably.

Finding the convergence radius is itself really complicated. Through the computer simulations of SE-SD for each scenario we recorded the average *Final Radius*, C_f , the radius of the last sphere in which the algorithm cannot find any lattice point after a huge amount of calculations. Figure 5 shows C_f , C_{ba} , and the proper C_0 of SE-SD algorithm as a function of the number of transmit antennas when $M = 64$ and $\sigma^2 = 0.65, 0.203, \text{ and } 0.05$. It seems that the final radius, similar to Babai radius, increases as the number of antennas grows. This growth in low σ^2 scenarios is negligible (Figures 5(b) and 5(c)) but for high σ^2 it cannot be ignored (Figure 5(a)). The distance between the final radius and Babai radius for high σ^2 seems to be a function of the number of antennas and the noise variance. When suitable C_0 is chosen 8% less than C_{ba} for high σ^2 is the final radius empirically found to be approximately equal to

$$C_f = C_{ba} - \frac{\sigma^2 \times P}{3}. \quad (10)$$

So, in this case calculating C_{ba} results in not only a proper initial radius but also the final one.

When a new sphere radius is calculated in step 5 of the algorithm, it should be compared to the estimated C_f , and when it is found to be less than C_f , the SE-SD algorithm

terminates to avoid extra useless calculations after reaching the convergence radius. This technique can be defined as *Early terminated SE-SD*.

Although the problem of finding suitable C_f can be solved easily using C_{ba} and (10), yet there is a question about the cost of calculating C_{ba} . To find out the complexity growth, we take into account the complexity of three types of performing SE-SD:

SE-SD with $C_0 = C_{ba}$,

SE-SD which C_0 is chosen through previous section's recommendation, namely, proposed initiated SE-SD (PSE-SD),

early terminated PSE-SD (EPSE-SD).

Table 1 indicates the percentage reduction in the complexity of these three types of SE-SD in comparison with the case of C_0 equal to a certain rough value like 20, when $M = 64, P = 20, 12, 10, 6, 4$, and $\sigma^2 = 0.203$. The negative number in the table means the increasing in the complexity.

According to Table 1 if P is greater than 10, the complexity declines by at least 9% via $C_0 = C_{ba}$ compared to the case that $C_0 = 20$. The reduction soars to at least 16% using PSE-SD. In addition, utilization of EPSE-SD results in a substantial decrease (more than 27%) in the complexity. Therefore, the slight additional complexity entailed by calculating C_{ba} leads to significant reduction in the total complexity of SE-SD.

However, if $P < 10$, the number of flops of calculating C_{ba} is comparable to the overall SE-SD complexity and the complexity reduction of EPSE-SD seems to be negligible. For example, Figure 4(a) indicates that for the case of $\sigma^2 = 0.203$ and $P = 4 < 10$ the average number of flops for decoding a burst of 100 symbols is around 48000, and so, 14600 flops of calculating C_{ba} is comparable to the SE-SD complexity.

Table 2 demonstrates a comparison between the three techniques, SE-SD with $C_0 = C_{ba}$, PSE-SD and EPSE-SD, when $M = 64, P = 4$, and $\sigma^2 = 2.49, 1.14, 1.02, 0.203$, and 0.056. In this table the percentage reduction of the complexity of the three types of SE-SD reflects the apparent discrepancy between $\sigma^2 \leq 1.02$, and $\sigma^2 > 1.02$. On one hand, EPSE-SD causes a significant fall in complexity when $\sigma^2 \leq 1.02$; on the other hand, calculating C_{ba} increases the number of flops of PSE-SD dramatically when $\sigma^2 > 1.02$.

In fact the noticeable beneficial effect of allocating C_f as a criterion for early termination of SE-SD is evident in the case of high noise variance or big problem size. For instance the complexity declines by 52% in the case of $M = 64, P = 4$, and $\sigma^2 = 2.49$.

5. Proposed TF-Based Algorithm

As a result of the presented discussion, EPSE-SD seems not to be the efficient decoding algorithm for some cases; a criterion should be introduced to help us to choose one of the initiation and termination techniques of SE-SD. We propose the TF-based algorithm performing different

TABLE 1: Reduction in complexity corresponding the number of transmit antennas.

Number of transmit antennas	SE-SD complexity reduction (%) when $C_0 = C_{ba}$	PSE-SD complexity reduction (%)	EPSE-SD complexity reduction (%)
20	30	40	58
12	15	21	33
10	9	16	27
6	-5	-2	4
4	-13	-7	1

TABLE 2: Reduction in complexity corresponding noise variance.

Noise variance	SE-SD Complexity reduction (%) when $C_0 = C_{ba}$	PSE-SD complexity reduction (%)	EPSE-SD complexity reduction (%)
2.49	20	30	52
1.14	3	8	22
1.02	-2	3	13
0.203	-13	-7	1
0.056	-32	-30	-27

decoding techniques via a Threshold Factor (TF). TF of this algorithm is defined as a function of P and σ^2 :

$$TF \triangleq 10 \times P \times (\sigma^2)^2. \quad (11)$$

There are four major cases according to the value of TF. First, when TF is greater than 300, the TF-based algorithm only performs SIC decoding. For instance, if $P = 4$ and σ^2 is greater than 2.74, $TF > 300$, SE-SD leads to a huge amount of computational complexity, and its performance is more or less identical to SIC decoding.

In the second case when TF is between 3.2 and 300, the algorithm initially performs SIC decoding to find C_{ba} and consequently calculates suitable C_0 and C_f using C_{ba} and then performs SE-SD algorithm. According to Tables 1 and 2, if $P \geq 10$ and $\sigma^2 = 0.204$, or in a case of $P = 4$ and $0.283 \leq \sigma^2 < 2.74$, so $3.2 \leq TF < 300$, the PESE-SD can make an acceptable performance with a reasonable complexity.

In the third case, when TF is between 0.4 and 3.2, the algorithm only performs SE-SD with $C_0 = 1$. Because the complexity of finding C_{ba} is comparable to SE-SD, it is not logical to use either PSE-SD or EPSE-SD. Based on Figures 2 and 4, when $P = 4$ and $0.1 \leq \sigma^2 < 0.283$, $0.4 < TF < 3.2$, a certain C_0 equal to 1 can make a sensible complexity without any performance degradation.

Finally, the fourth case is when TF is less than 0.4 and the algorithm performs SE-SD with $C_0 = 0.5$. In this case SE-SD can find the closest lattice point quickly which costs a quiet small number of flops. The proposed algorithm can be summarized as Algorithm 1.

- (1) Calculate TF
 - (2) If $TF > 300$ Then Do SIC algorithm
 - (3) If $3.2 < TF < 300$ Then Do SIC decoding, Calculate C_{ba} , C_f . Do EPSE-SD
 - (4) If $0.4 < TF < 3.2$ Then let $C_0 = 1$. Do SE-SD
 - (5) If $TF < 0.4$ Then let $C_0 = 0.5$. Do SE-SD

ALGORITHM 1: TF-Based algorithm.

6. Conclusion

In order to make SE-SD feasible for real applications, some techniques should be utilized to decrease the complexity of this algorithm. We presented new methods of initiation and termination of the SE-SD algorithm that can contribute to achieve the goal of having a reasonable complexity.

We showed that for a high number of transmit antennas, using Babai distance as initial radius leads to considerable performance degradation due to the big problem size. The suitable initial sphere radius which results in low complexity and desirable performance in the range of ρ which covers wireless communication applications can be found by the our proposed method. Moreover, this paper offers a technique to estimate the final radius to which SE-SD converges. Utilizing the estimated final radius as a criterion for early terminating of SE-SD is a way of controlling the complexity of the algorithm because it avoids considerable amount of unnecessary calculations. Simulation results show that employing proposed initiation and early termination of SE-SD causes a significant reduction in the complexity. For example, when $M = 64$, $P = 4$, and $\rho = 7.5$ dB, the technique leads to reduction in the complexity by 52%.

To estimate the initial radius and the final one, Babai distance should be found through SIC decoding. Therefore, the presented technique sounds not to be useful for some cases in which the extra complexity of SIC decoding is comparable to that of SE-SD process. This investigation proposed an algorithm that utilizes different techniques according to a threshold factor defined in terms of the number of transmit antennas and noise variance. Using threshold factor, the novel algorithm offers a reasonable complexity without any performance degradation.

Acknowledgments

This work is supported by Developing Research and Strategic Planning Department of Mobile Communication Company of Iran (MCI) as a part of advanced communication systems project. The authors would like to thank Mr. Vahid Sadoughi, the CEO of MCI, for his financial support. They would like to thank Mrs. Samaneh Movassaghi (University of Technology, Sydney) and Mr. Mahyar Shirvani Moghaddam (University of Sydney) for the great help they provided. Also, the authors would like to thank the editor and anonymous reviewers of the International Journal of Antennas and Propagation (IJAP) for their very helpful comments and suggestions which have improved the presentation of the paper.

References

- [1] G. J. Foschini and M. J. Gans, "On limits of wireless communications in a fading environment when using multiple antennas," *Wireless Personal Communications*, vol. 6, no. 3, pp. 311–335, 1998.
- [2] R. Kannan, "Improved algorithms on integer programming and related lattice problems," in *Proceedings of the 15th Annual ACM Symposium on Theory of Computing*, pp. 193–206, 1983.
- [3] J. C. Lagarias, H. W. Lenstra, and C. P. Schnorr, "Korkin-Zolotarev bases and successive minima of a lattice and its reciprocal lattice," *Combinatorica*, vol. 10, no. 4, pp. 333–348, 1990.
- [4] M. Pohst, "On the computation of lattice vectors of minimal length, successive minima and reduced bases with applications," *ACM SIGSAM Bulletin*, vol. 15, pp. 37–44, 1981.
- [5] U. Fincke and M. Pohst, "Improved methods for calculating vectors of short length in a lattice, including a complexity analysis," *Mathematics of Computation*, vol. 44, pp. 463–471, 1985.
- [6] E. Viterbo and J. Boutros, "A universal lattice code decoder for fading channels," *IEEE Transactions on Information Theory*, vol. 45, no. 5, pp. 1639–1642, 1999.
- [7] C. P. Schnorr and M. Euchner, "Lattice basis reduction: improved practical algorithms and solving subset sum problems," *Mathematical Programming*, vol. 66, no. 2, pp. 181–191, 1994.
- [8] W. Zhao and G. B. Giannakis, "Reduced complexity closest point decoding algorithms for random lattices," *IEEE Transactions on Wireless Communications*, vol. 5, no. 1, pp. 101–111, 2006.
- [9] W. Xu, Y. Wang, Z. Zhou, and J. Wang, "A computationally efficient exact ML sphere decoder," in *Proceedings of the IEEE Global Communications Conference*, pp. 2594–2598, December 2004.
- [10] A. Li, W. Xu, Y. Wang, Z. Zhou, and J. Wang, "A faster ML sphere decoder with competing branches," in *Proceedings of the 61st IEEE Vehicular Technology Conference (VTC '05)*, pp. 438–441, June 2005.
- [11] J. W. Choi, B. Shim, A. C. Singer, and N. I. Cho, "Low-complexity decoding via reduced dimension maximum-likelihood search," *IEEE Transactions on Signal Processing*, vol. 58, no. 3, pp. 1–14, 2010.
- [12] W. Zhao and G. B. Giannakis, "Sphere decoding algorithms with improved radius search," *IEEE Transactions on Communications*, vol. 53, no. 7, pp. 1104–1109, 2005.
- [13] R. Gowaikar and B. Hassibi, "Statistical pruning for near-maximum likelihood decoding," *IEEE Transactions on Signal Processing*, vol. 55, no. 6 I, pp. 2661–2675, 2007.
- [14] A. D. Murugan, H. El Gamal, M. O. Damen, and G. Caire, "A unified framework for tree search decoding: rediscovering the sequential decoder," *IEEE Transactions on Information Theory*, vol. 52, no. 3, pp. 933–953, 2006.
- [15] W. K. Ma, T. N. Davidson, K. M. Wong, Z. Q. Luo, and P. C. Ching, "Quasi-maximum-likelihood multiuser detection using semi-definite relaxation with application to synchronous CDMA," *IEEE Transactions on Signal Processing*, vol. 50, no. 4, pp. 912–922, 2002.
- [16] E. Agrell, T. Eriksson, A. Vardy, and K. Zeger, "Closest point search in lattices," *IEEE Transactions on Information Theory*, vol. 48, no. 8, pp. 2201–2214, 2002.
- [17] M. O. Damen, H. E. Gamal, and G. Caire, "On the complexity of ML detection and the search for the closest lattice point," *IEEE Transactions on Information Theory*, vol. 59, no. 10, pp. 2400–2414, 2003.
- [18] B. Hassibi and H. Vikalo, "On the sphere-decoding algorithm I. expected complexity," *IEEE Transactions on Signal Processing*, vol. 53, pp. 2806–2818, 2005.
- [19] J. Jaldén and B. Ottersten, "On the complexity of sphere decoding in digital communications," *IEEE Transactions on Signal Processing*, vol. 53, no. 4, pp. 1474–1484, 2005.
- [20] Y. Wang and K. Roy, "A new reduced-complexity sphere decoder with true lattice—boundary—awareness for multi-antenna systems," in *Proceedings of the IEEE International Symposium on Circuits and Systems (ISCAS '05)*, pp. 4963–4966, May 2005.
- [21] F. Zhao and S. Qiao, "Radius selection algorithms for sphere decoding," in *Proceedings of the Computational Science and Engineering Workshops*, pp. 169–174, Montreal, Canada, 2009.
- [22] S. Qiao, "Integer least squares: sphere decoding and the LLL algorithm," in *Proceedings of the Computational Science and Engineering Workshops*, vol. 273, pp. 23–28, Montreal, Canada, 2008.
- [23] B. Cheng, W. Liu, Z. Yang, and Y. Li, "A new method for initial radius selection of sphere decoding," in *Proceedings of the 12th IEEE International Symposium on Computers and Communications (ISCC '07)*, pp. 19–24, Aveiro, Portugal, July 2007.
- [24] J. H. Conway and N. J. A. Sloane, *Sphere Packings, Lattices and Groups*, Springer, New York, NY, USA, 1988.
- [25] J. H. Conway and N. Sloane, *Sphere Packings, Lattices and Graphs*, Springer, New York, NY, USA, 1993.
- [26] Q. Liu and L. Yang, "A novel method for initial radius selection of sphere decoding," in *Proceedings of the IEEE 60th Vehicular Technology Conference (VTC'04)-Fall*, pp. 1280–1283, September 2004.
- [27] E. Zimmermann, W. Rave, and G. Fettweis, "On the complexity of sphere decoding," in *Proceedings of the International Conference on Wireless Personal and Multimedia Communications (WPMC'04)*, Abano Terme, Italy, 2004.
- [28] F. E. Hosseini and S. S. Moghaddam, "Initial radius selection of sphere decoder for practical applications of MIMO channels," in *Proceedings of the IEEE Conference on Complexity in Engineering (COMPENG'10)*, pp. 61–63, Rome, Italy, February 2010.
- [29] W. H. Mow, "Universal lattice decoding: principle and recent advances," *Wireless Communications and Mobile Computing*, vol. 3, no. 5, pp. 553–569, 2003.
- [30] W. Zhao and G. B. Giannakis, "Reduced complexity closest point decoding algorithms for random lattices," *IEEE Transactions on Wireless Communications*, vol. 5, no. 1, pp. 101–111, 2006.
- [31] Z. Ma, B. Honary, P. Fan, and E. G. Larsson, "Stopping criterion for complexity reduction of sphere decoding," *IEEE Communications Letters*, vol. 13, no. 6, pp. 402–404, 2009.

Research Article

Compact Multiantenna

L. Rudant, C. Delaveaud, and P. Ciaï

CEA-Leti, Minatec Campus, 17 Rue des Martyrs, 38054 Grenoble Cedex 9, France

Correspondence should be addressed to L. Rudant, lionel.rudant@cea.fr

Received 30 July 2011; Accepted 30 October 2011

Academic Editor: Li Yang

Copyright © 2012 L. Rudant et al. This is an open access article distributed under the Creative Commons Attribution License, which permits unrestricted use, distribution, and reproduction in any medium, provided the original work is properly cited.

Planar inverted-f antenna (PIFA) and notch antenna are combined within a compact 2-port MIMO antenna. Electrical and magnetic duality of the two antennas avoids a critical coupling and best performances can be expected for multiple-input multiple-output (MIMO) communication. When excitation of notch antenna is optimized properly, the notch length can be short enough so that the two antennas can be collocated in a single compact volume. This compact multiantenna design is suitable for integration in MIMO handheld terminals. A prototype for broadband network application in 3.4–3.8 GHz frequency band has been characterized in anechoic chamber.

1. Introduction

Modern wireless networks have to meet the increasing needs in terms of throughput and reliability. Broadband communication and multiple-input multiple-output (MIMO) techniques are promising solutions. If multiantenna are widely developed and used at base station and access point side, a key challenge is without a doubt the design of compact and wideband MIMO antennas for small terminals.

Due to small size of modern terminals, multiantenna has to be integrated in restricted volume with respect to the wavelength. When space between antennas is too reduced, diversity must be achieved with an optimization of radiation, that is, pattern shape and electromagnetic field polarization. In addition to classical antenna miniaturization effects on radiation efficiency and bandwidth, multiantenna performances are impacted by high coupling when antennas are very close. In this paper, two radiating elements are collocated in a single electrically small volume with dual polarization and pattern diversity. Bandwidth, radiation efficiency, low coupling, and uncorrelated radiation properties have been optimized despite closeness.

Planar inverted-f antenna (PIFA) and notch antenna are common radiating elements to be integrated at terminal because of small size. Different combinations of PIFA and notch have been reported in [1] for compact MIMO antenna design. When the two elements are combined side by side, a slit

can cut between them in the ground plane to avoid high coupling [2]. In [3], a partial overlap of PIFA and notch has been presented.

Earlier in [4], PIFA and notch have been brought together in collocated multiantenna system. In this paper, PIFA and notch are combined with complete overlap and diversity can be integrated in a single antenna volume. A prototype for broadband MIMO communication is characterized in anechoic chamber.

2. Close Combination of PIFA and Notch

Polarization diversity is commonly performed with linearly polarized radiating elements which are oriented orthogonally. Planar inverted-f antenna (PIFA) is electric-like radiating element and notch antenna is considered as magnetic-like radiating slot [4]. The combination presented in Figure 1 enables achieving complementary electric/magnetic diversity with a compact multiantenna because both elements are quarter-wavelength resonators. One other advantage is that the two combined elements have collinear resonant lengths and multiantenna can fit a thin volume in the terminal.

When notch is fed by coupling with a printed micro-strip line, impedance matching is reached by joint optimization of two parameters: a is relative position of the strip along the notch; p is serial stub length after the notch. In Figure 2, a notch antenna is optimized at 2.5 GHz frequency band with

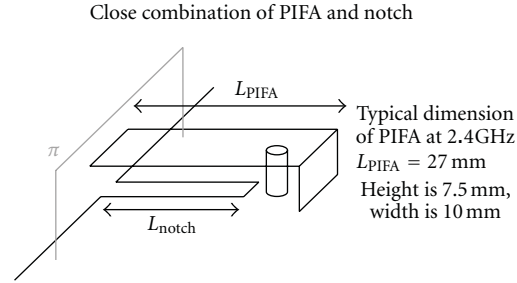


FIGURE 1: Close combination of PIFA and notch with complete overlap.

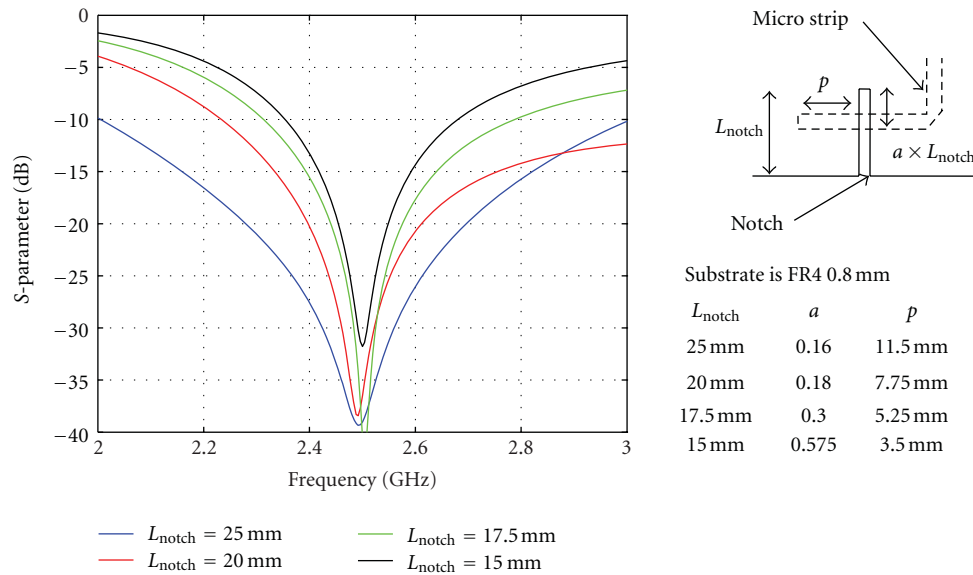


FIGURE 2: Impedance matching of notch with reduced length.

different notch lengths. The notch length can be reduced from quarter-wavelength (~ 25 mm) if coupling strip is closer to open end of the notch and if stub is short. Consequently the notch can be shortened enough to be cut under PIFA with complete overlap according to Figure 1 ($L_{notch} = 15$ mm).

Different placements and orientations of PIFA with respect to combination with notch antenna are investigated by means of simulation (CST microwave studio). The highest coupling level in 2.4–2.5 GHz frequency band is presented in Figure 3. We can observe that best isolation is reached when PIFA and notch are in-line perfectly.

For both PIFA and notch, electrical fields are strong close to open end of the resonators. From Figure 4, we can observe electrical fields in π plane defined in Figure 1. Orientation of strongest fields is orthogonal from one element to the other. In this configuration notch antenna can be cut in the ground plane above the PIFA without critical coupling. Close combination of PIFA and notch provides compact multiantenna for MIMO or diversity application at terminal.

3. Compact Multiantenna Prototype

IEEE 802.16 WiMax terminals are deployed in 3.4–3.8 GHz frequency band with multiple antennas. We design a prototype of PIFA and notch combination for WiMax network access.

3.1. Multiantenna Geometry. Figure 5 shows compact multiantenna geometry. PIFA has dual resonant lengths which have been jointly optimized in order to widen its operating frequency range [5]. The excitation is performed by means of a metallic post. The PIFA has naturally high radiation efficiency since copper is a good conductor and air substrate is used between radiator and ground plane. The notch is etched in ground plane of a compact printed circuit board (PCB) 25 mm \times 35 mm. Radiation efficiency of notch antenna can be significantly reduced by the dielectric losses of the substrate. Therefore, a high performance substrate rogers TMM4 ($\tan \delta = 2_E - 3$) has been used and the notch has been partly hollowed from the substrate material close to

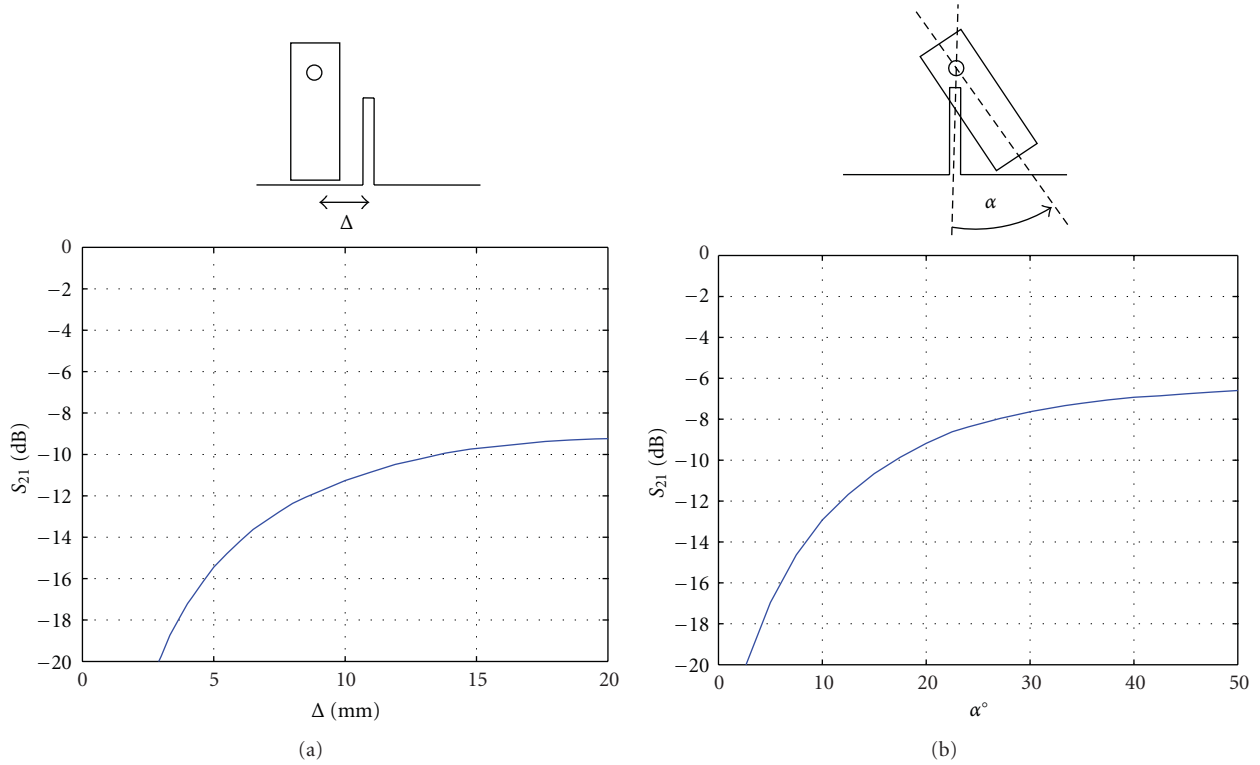


FIGURE 3: Investigation of misplacement or rotation of PIFA.

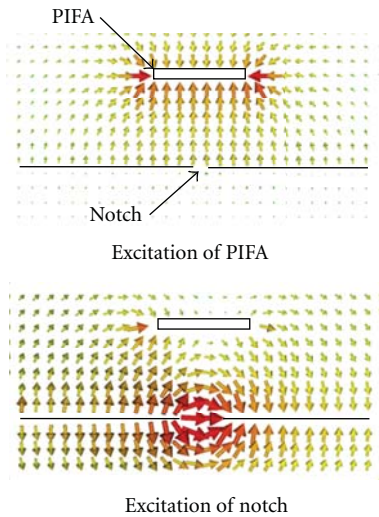


FIGURE 4: Electrical fields in open end (π plane).

open end, where resonant electrical fields are strong. Notch antenna is fed by coupling with a micro-strip line etched on the opposite side of the substrate. Impedance matching is reached keeping a short notch length so that it can be located under PIFA with complete overlap. Finally, main dimensions of the multiantenna system are $19 \text{ mm} \times 10 \text{ mm} \times 8 \text{ mm}$, that is, $0.22 \lambda \times 0.11 \lambda \times 0.09 \lambda$, where λ is the wavelength in free space at 3.4 GHz. Two SMA edge card connectors are mounted on PCB for multiantenna characterization.

3.2. Impedance Matching and Coupling. The scattering parameters of multiantenna prototype are presented in Figure 6. Measurement and CST microwave studio simulation results are, respectively, presented with and without star markers. Ports 1 and 2 are PIFA and notch antenna, respectively. A low reflection coefficient is simultaneously reached at the two ports 3.4–3.6 GHz frequency band. The coupling between the two combined antennas in this bandwidth is low $|S_{ij}|^2 < -20 \text{ dB}$. We obtain a quite good agreement between simulation and measurement; slight differences can be explained with respect to the measurement coaxial cable effect.

3.3. Radiation Performances. Gain patterns of the multiantenna prototype at 3.6 GHz are presented in Figure 7 for three orthogonal cut planes. The reference coordinate system is presented in Figure 7 as well. Measurement and CST microwave studio simulation results are, respectively, presented with and without star markers.

We can clearly observe a polarization duality between the two combined antennas in the three considered cut planes: vertically polarized radiation patterns of the PIFA antenna are like the cross-polarized radiation patterns of the notch antenna and vice versa. Each of the two antennas has multiple polarization properties and an omni directional radiation pattern if we consider the elevation cut planes: the multiantenna system is suitable for different environments and/or orientations [4]. Simulation and measurement are in good agreement. We can observe some slight perturbations of the radiation patterns due to the measurement coaxial cables but polarization duality and maximum gain in each cut plane are not significantly affected.

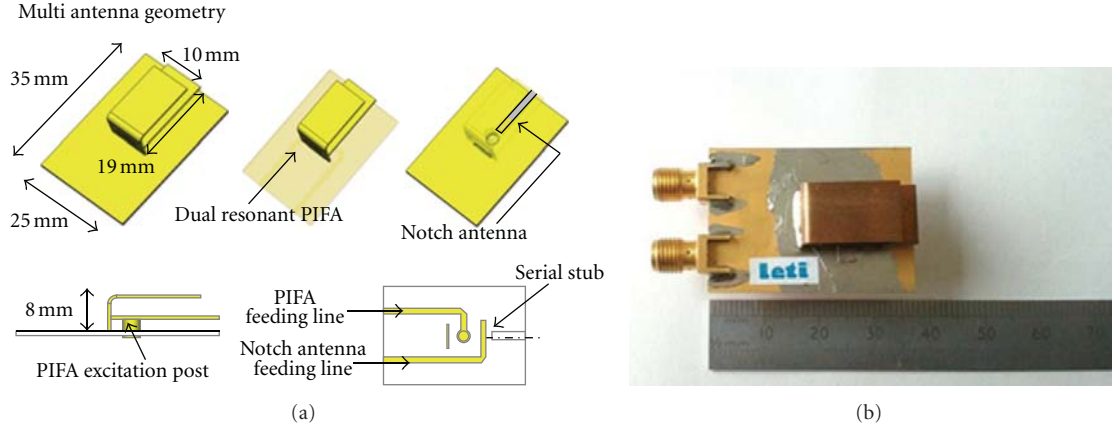


FIGURE 5: Compact multiantenna for WiMax.

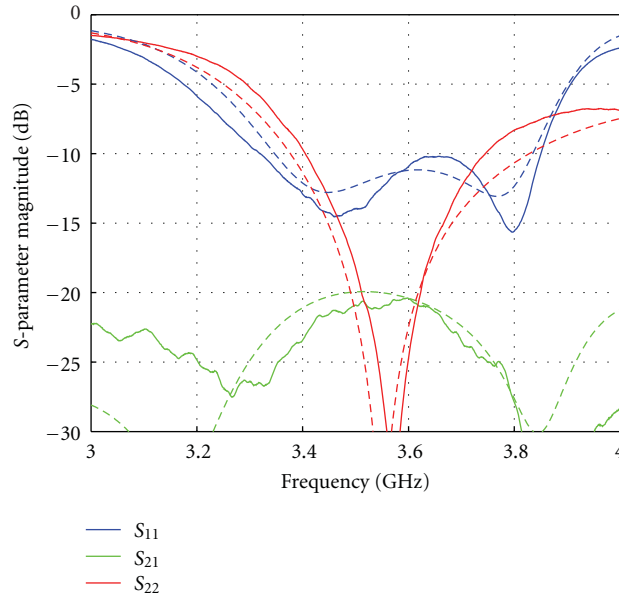


FIGURE 6: Scattering parameters of compact multiantenna prototype. Solid line is measurement, dashed is simulation.

Antenna diversity and MIMO schemes take advantage of uncorrelated radiation properties. The envelop correlation coefficient ρ is computed by means of (1) [6]. If we assume an isotropic environment:

$$\rho = \frac{\iint E_1 \cdot E_2^* d\Omega}{\sqrt{\iint E_1 \cdot E_1^* d\Omega \cdot \iint E_2 \cdot E_2^* d\Omega}}, \quad (1)$$

E_1 and E_2 are radiated electrical far field of PIFA and notch antenna, respectively. Ω is solid angle unit and * denotes complex conjugate.

Table 1 presents computation results of performance figures based on simulation and measurement results. The radiation efficiency of the PIFA (η_1) is high in the 3.4–3.8 GHz frequency band. Also the radiation efficiency of the notch antenna (η_2) is high thanks to the poor losses in the rogers TMM4 substrate and the hollowed portion of the substrate in the slot. The multiantenna system provides two signals with

TABLE 1: Multiantenna performances.

Frequency	Simulation			Measurement		
	η_1	η_2	$ \rho $	η_1	η_2	$ \rho $
3.4 GHz	0.97	0.96	0.04	0.94	0.97	0.05
3.6 GHz	0.98	0.96	0.03	0.94	0.97	0.03

high diversity benefit since the radiation efficiencies are balanced $\eta_1 \cong \eta_2$ and the envelop correlation coefficient is very low $\rho < 0.1$ over the targeted frequency band [6, 7].

4. Conclusion

In this paper, we presented a compact multi antenna. The key concept of this design is heterogeneous combination of antennas. An electric-like PIFA and a magnetic-like notch can

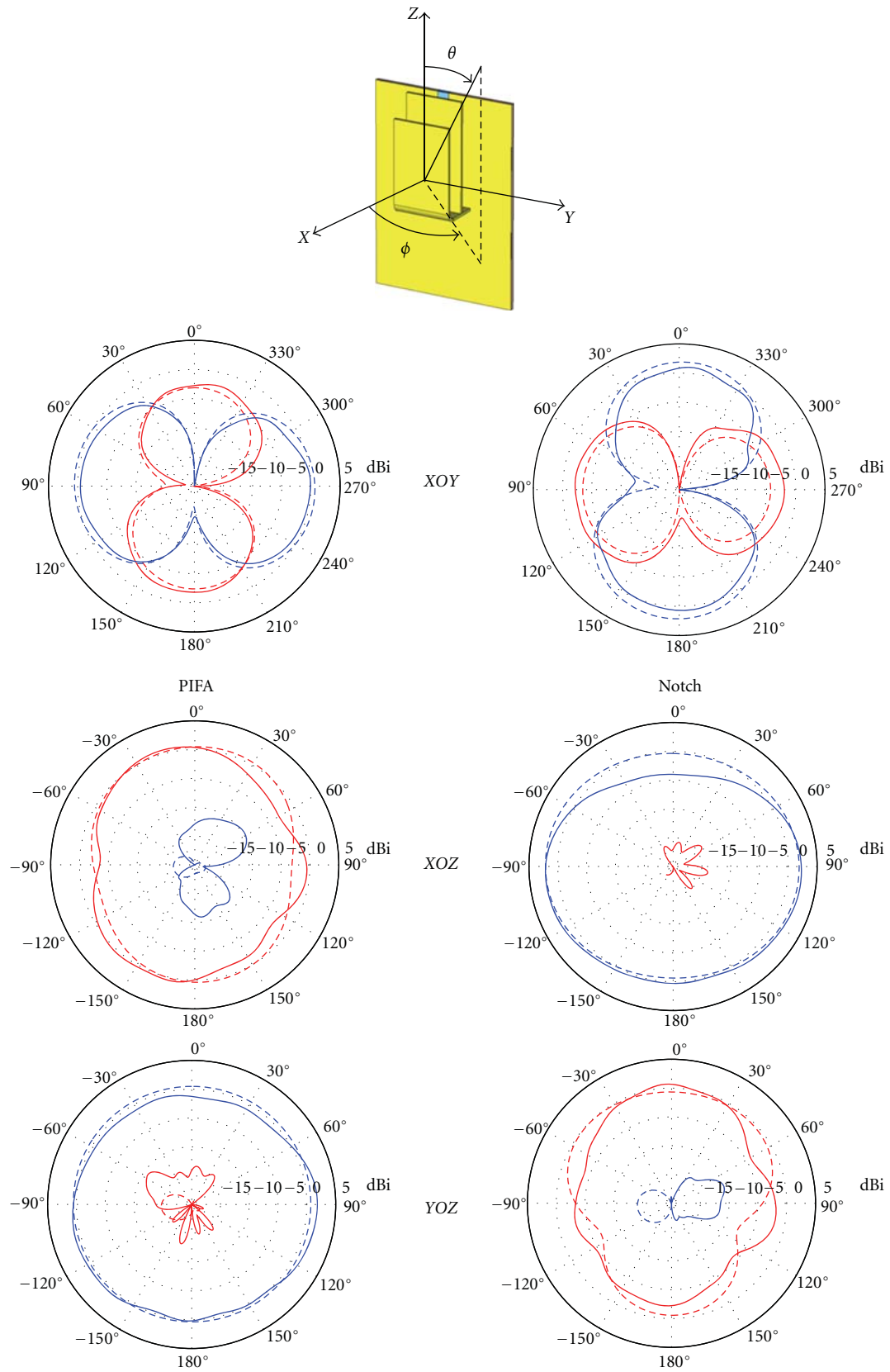


FIGURE 7: Gain patterns of compact multiantenna prototype at 3.6 GHz. Solid line is measurement, dashed is simulation. Vertical polarization is red line, horizontal is blue line.

be colocated in a single volume without strong coupling despite complete overlap. The properties of far-field radiation resulting from duality of combined radiation sources lead to polarization and pattern diversity providing signals weakly correlated. Wideband behavior of this compact antenna system has been demonstrated by designing a prototype optimized for broadband network access in WiMax 3.4–3.8 GHz frequency band. Compact multiantenna system fits in a $0.22 \lambda \times 0.11 \lambda \times 0.09 \lambda$ volume, where λ is the free space wavelength at 3.4 GHz.

Acknowledgments

This work was supported in part by the EU commission in the FP7 ROCKET Project and by the French National Research Agency ANR in the ORIANA Project.

References

- [1] C.-Y. Chiu and R. D. Murch, "Overview of multiple antenna designs for handheld devices and base stations," in *Proceedings of the IEEE International Workshop on Antenna Technology (iWAT '11)*, pp. 74–77, Hong Kong, China, March 2011.
- [2] J. B. Yan, C. Y. Chiu, and R. D. Murch, "Handset 4-port MIMO antenna using slit separated PIFA and quarterwave-slot antenna pair," in *Proceedings of the IEEE International Symposium on Antennas and Propagation*, July 2008.
- [3] C. Y. Chiu, J. B. Yan, R. D. Murch, J. X. Yun, and R. G. Vaughan, "Design and implementation of a compact 6-port antenna," *IEEE Antennas and Wireless Propagation Letters*, vol. 8, Article ID 5159465, pp. 767–770, 2009.
- [4] L. Rudant and C. Delaveaud, "Heterogeneous combination for compact integrated diversity multi-antenna system," in *Proceedings of the 2nd European Conference on Antennas and Propagation (EuCAP '07)*, Edinburgh, UK, 2007.
- [5] R. B. Waterhouse, J. T. Rowley, and K. H. Joyner, "Stacked shorted patch antenna," *Electronics Letters*, vol. 34, no. 7, pp. 612–614, 1998.
- [6] R. Vaughan and J. B. Andersen, *Channels Propagation and Antennas for Mobile Communications*, vol. 50 of *IEE Electromagnetic Waves series*, 2003.
- [7] K. Fujimoto and J. R. James, *Mobile Antenna Systems Handbook*, Artech House Publishers, 3rd edition, 2008.

Research Article

Indoor Off-Body Wireless Communication: Static Beamforming versus Space-Time Coding

Patrick Van Torre,^{1,2} Maria Lucia Scarpello,¹ Luigi Vallozzi,¹ Hendrik Rogier,¹
Marc Moeneclaeys,³ Dries Vande Ginste,¹ and Jo Verhaevert²

¹Department of Information Technology (INTEC), Ghent University, St. Pietersnieuwstraat 41,
9000 Ghent, Belgium

²Faculty of Applied Engineering Sciences (INWE), University College Ghent, Valentin Vaerwyckweg 1, 9000 Ghent, Belgium

³Department of Telecommunications and Information Processing (TELIN), Ghent University, St. Pietersnieuwstraat 41,
9000 Ghent, Belgium

Correspondence should be addressed to Patrick Van Torre, patrick.vantorre@ugent.be

Received 25 July 2011; Revised 20 October 2011; Accepted 22 October 2011

Academic Editor: Yan Zhang

Copyright © 2012 Patrick Van Torre et al. This is an open access article distributed under the Creative Commons Attribution License, which permits unrestricted use, distribution, and reproduction in any medium, provided the original work is properly cited.

The performance of beamforming versus space-time coding using a body-worn textile antenna array is experimentally evaluated for an indoor environment, where a walking rescue worker transmits data in the 2.45 GHz ISM band, relying on a vertical textile four-antenna array integrated into his garment. The two transmission scenarios considered are static beamforming at low-elevation angles and space-time code based transmit diversity. Signals are received by a base station equipped with a horizontal array of four dipole antennas providing spatial receive diversity through maximum-ratio combining. Signal-to-noise ratios, bit error rate characteristics, and signal correlation properties are assessed for both off-body transmission scenarios. Without receiver diversity, the performance of space-time coding is generally better. In case of fourth-order receiver diversity, beamforming is superior in line-of-sight conditions. For non-line-of-sight propagation, the space-time codes perform better as soon as bit error rates are low enough for a reliable data link.

1. Introduction

Reliable wireless data communication is of paramount importance for rescue workers operating in indoor environments. Smart garments for professionals active during emergency situations contain integrated sensors and a transmitting system for sending the collected data to the command center in real time [1].

The indoor environment where interventions are performed exhibits line-of-sight (LoS) as well as non line-of-sight (NLoS) radio propagation conditions. The received signals experience Ricean or Rayleigh fading, often with additional lognormal shadowing, easily producing variations in signal-to-noise ratio (SNR) exceeding 35 dB [2, 3].

1.1. Motivation. Experimental data comparing the performance of beamforming and space-time coding (STC)

transmissions are scarce in literature. In case of off-body communication links, a literature search revealed no experimental results. Theoretically, for LoS conditions, the received signals can be significantly enhanced by using beamforming techniques. However, for off-body communication in an indoor environment, beamforming is not straightforward, especially when relying on flexible textile antennas directly deployed on the human body. In addition to significant multipath effects and shadowing by the human body, many factors influence array performance, such as the proximity of the human body to the wearable antenna elements and movements of the body as well as deformation of the flexible textile array affecting the orientation of the beam. Shadowing by the body can cause blocking of the direct path in the LoS environment, but a large beam width in the azimuth plane will significantly increase the portion of signals received via dominant specular reflections at walls and office equipment.

By performing beamforming using a vertical array, the transmitted power is concentrated in the elevation direction along the direct path between the transmitter and the receiver, resulting in an increased average received signal level and reducing the number of paths contributing to fading. However, the interference between direct and reflected signals can still cause significant fading, which is detrimental to the bit error rate (BER) performance. Additional receiver diversity using maximum-ratio combining (MRC) can mitigate these fading effects. Previous measurements in our indoor environment, documented in [4], confirmed substantial diversity gain for fourth-order receive diversity with two dual-polarized antennas. Beamforming is preferred in the elevation direction only, to accommodate for movements of the rescue worker. For a walking person, the rotation of the array in the elevation plane is minimal, allowing static low-elevation angle beamforming. Beamforming in the azimuth plane is not advised as the actual orientation of the rescue worker in the azimuth plane is assumed to be unpredictable. For NLoS propagation, the rich scattering of the signals in the environment includes waves propagating at higher elevation angles. Therefore, it is interesting to transmit with a wide-elevation coverage. Thanks to their high beamwidth and higher diversity order, transmit diversity techniques such as space-time codes are expected to outperform static beamforming systems [5] for NLoS propagation conditions.

Adaptive beamforming could in principle further enhance the communication as compared to static beamforming but requires continuous feedback of channel information from the receiver to the transmitter [6]. For a rescue worker operating in an indoor environment, the channel response often varies significantly within a fraction of a second [2], therefore, high-rate channel information feedback would be necessary, introducing a large overhead in the communication and requiring more complex hardware.

In terms of implementation complexity and energy consumption, static beamforming is preferred over STC. Static beamforming can be realized by simply using phase shifters, whereas STC requires complex and more power-consuming hardware with dedicated transmit chains for each channel. Additional diversity reception is an important option to further improve the error performance, increasing complexity at the base station but not at the transmitter.

1.2. Previous Work. A very limited set of measurements comparing beamforming to STC is available in literature and the available material covers no body-centric applications, hence, they are not dealing with direct shadowing by the human body. An experimental comparison of MIMO and beamforming schemes is presented in [7, 8]. These papers focus on channel capacity, and the measurements are for an outdoor-to-indoor scenario, with a fixed transmitter and the receiver in a number of fixed positions. Horizontal antenna arrays are used at both the transmitter and receiver. The related propagation conditions are different from those for a walking person with a body-worn vertical antenna array.

The literature study revealed many simulations and analytical results. Space-time codes were studied in combination with beamforming at the receiver for interference rejection in [9]. Alternatively, depending on propagation conditions, a number of transmit beams can be formed, in combination with an appropriately sized space-time code [10–12]. Often the proposed schemes use environment-oriented adaptive beamforming, forming a directive beam pattern toward the impinging waves' directions-of-arrival. This is more appropriate for situations where the angles-of-arrival of the signals are fairly constant [10, 13, 14]. Others propose optimal power allocation for beamforming based on statistical channel information [15–17] or imperfect instantaneous channel state information [18, 19].

A numerical comparison between beamforming and space-time coding is documented in [20, 21], confirming the better performance of space-time codes in NLoS conditions with large feedback delay, because of the higher diversity gain. In [18], the performance of both techniques is compared as a function of the quality of the channel feedback information. In [22], an interesting scheme is proposed with a performance converging to conventional space-time coding with low-rate and erroneous channel estimation feedback and to directional beamforming with high-rate and error-free channel estimation feedback.

However, for wearable applications, systems with low weight, low cost, and low power consumption are desired. The need for a feedback channel often makes the proposed scheme not compatible with these requirements. Note that an off-body system is likely to require a high-rate feedback channel due to the quickly changing channel response for a walking person in an indoor fading environment.

1.3. Own Contributions. In contrast to scenarios in existing literature, the transmit array is flexible and directly deployed on the body of a moving user. Only static beamforming is considered because of the rapidly changing channel conditions experienced by a walking person. The aim of this paper is to experimentally investigate the performance gain realized by confining a transmit beam along zero elevation (for communication with a receiver located on the same floor of the building) by means of a vertically oriented textile antenna array integrated into a firefighter suit, and to compare this beamforming gain with diversity gain realized by means of space-time codes relying on the same array. By creating a relatively broad beam in the azimuth plane, the wearable vertical array also provides some beamforming gain in case of dominant specular reflection, even when the direct path is blocked by the wearer's body.

In the following measurement campaign, static beamforming SISO and 1×4 SIMO systems are compared to space-time coded 4×1 MISO and 4×4 MIMO links, respectively. All measurements are performed in the 2.45 GHz ISM (industrial, scientific, and medical) band. The measurements confirm the better performance of space-time coding in NLoS conditions, similar to the numerical comparison documented in [20, 21].

Our measurements indicate that a degree of diversity is always desirable. Without receiver diversity, the space-time code performs better than beamforming for all acceptable bit error rates, due to the absence of diversity for the latter. With receiver diversity, beamforming is always better in LoS conditions, whereas for NLoS, space-time coding performs better for bit error rates lower than $3.3 \cdot 10^{-3}$.

1.4. Organization of the Paper. Section 2 documents the textile antenna array used for beamforming/transmit diversity. Section 3 discusses the transmit antenna setup, signal format, and receiver operation. Measurement results are presented in Section 4, including signal-to-noise ratios (SNRs), signal correlation coefficients, and bit error characteristics. General conclusions follow in Section 5.

2. Wearable Textile Antenna Array

At the transmit side of the off-body link, we deploy a wearable textile antenna array invisibly integrated into a firefighter suit. A uniform linear array (ULA) topology, composed of four tip-truncated equilateral triangular microstrip patch antennas (ETMPAs), was adopted. For easy low-cost beamforming, the four ETMPAs are equally spaced and fed through a 50Ω coaxial SMA connector, manually soldered. By cutting off a triangle from one of the tips of the patch [23, 24], the size of the ETMPA can be further reduced.

The triangular patch, used as antenna element, provides radiation characteristics similar to a rectangular microstrip antenna while occupying a smaller area and guaranteeing low mutual coupling between adjacent elements. It is frequently used as a microstrip element, microstrip radiator, or for array design on rigid substrates [25], but never before on a textile substrate.

Both the patch and ground plane of the array are made of *Flectron*, a breathable and highly conductive electrotile material, being a copper-plated nylon fabric with a surface resistivity of less than $0.10 \Omega/\text{sq}$.

The array is implemented on a nonconductive textile substrate, being a protective polyurethane foam called “Azzurri,” manufactured by Lion [26]. Geometrical parameters of the patches and dielectric characteristics of the substrates are listed in Table 1 and indicated in Figure 1. The textile array is specifically designed for integration inside a firefighter jacket, and it is vertically positioned on the human torso, as shown in Figure 2.

The distance between patches is chosen to be $(34)\lambda$, where λ is the free-space wavelength, being approximately 122 mm, to minimize mutual coupling between two adjacent elements. The choice of 92 mm between two consecutive feeding points leads to a low-cost array implementation, as it consists of only four patches. Moreover, it is a convenient choice as the complete array, to be positioned vertically, has a large aperture, fully exploiting the size of the human torso. In fact, the design of this vertical array offers limited steering capabilities of the beam maximum in a narrow angular sector of about 10° , centered around the broadside direction, allowing to confine the energy within a narrow beam,

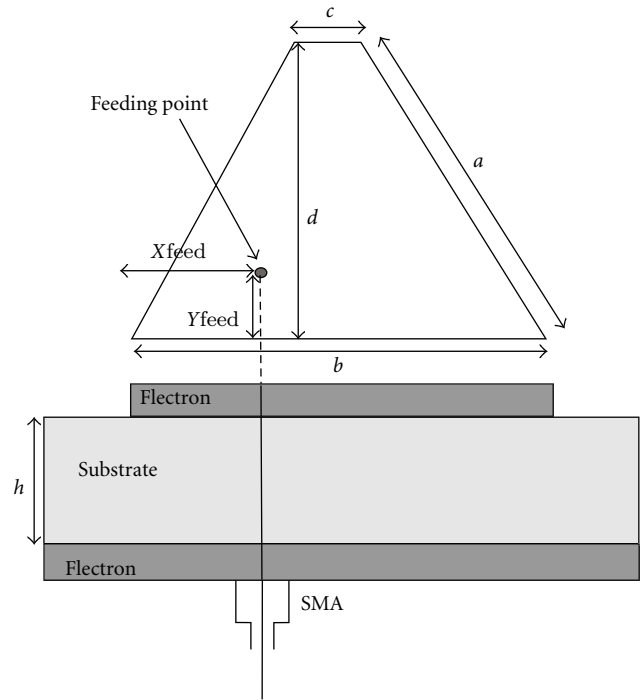


FIGURE 1: Side view of the textile antenna array and its geometrical dimensions.

TABLE 1: Tip-truncated ETMPA on the Azzurri substrate: dielectric properties and patch dimensions.

Patch (mm)		Substrate	
a	60.1	L (mm)	480
b	69	W (mm)	180
c	8.6	h (mm)	3.55
d	52.8		
X_{feed}	27.5	ϵ_r	1.19
Y_{feed}	10	$\tan \delta$	0.003

centered around the azimuth plane. Within this steering range, it does not exhibit grating lobes. The total size of the array and the distance between two feeding points are indicated in Figure 2 and Table 1.

For the array positioned vertically, Table 2 displays the simulated and measured -3 dB beam width of a single-patch antenna and of the array at 2.45 GHz, in the elevation plane (xz -plane) and in the azimuth plane (yz -plane). It is clear that the array is quite directive in the elevation plane, compared to the single-patch element.

The beam width in the azimuth plane is always wide enough to allow for movements of the rescue worker. The beam width in the elevation plane is small, providing a higher gain along the beam maximum at zero elevation. Note that for the space-time code, the elevation beam width for a single-patch is valid.

3. Measurement Setup

3.1. Mobile Rescue Worker: Transmitted Signals. The rescue worker transmits with the vertically mounted textile antenna

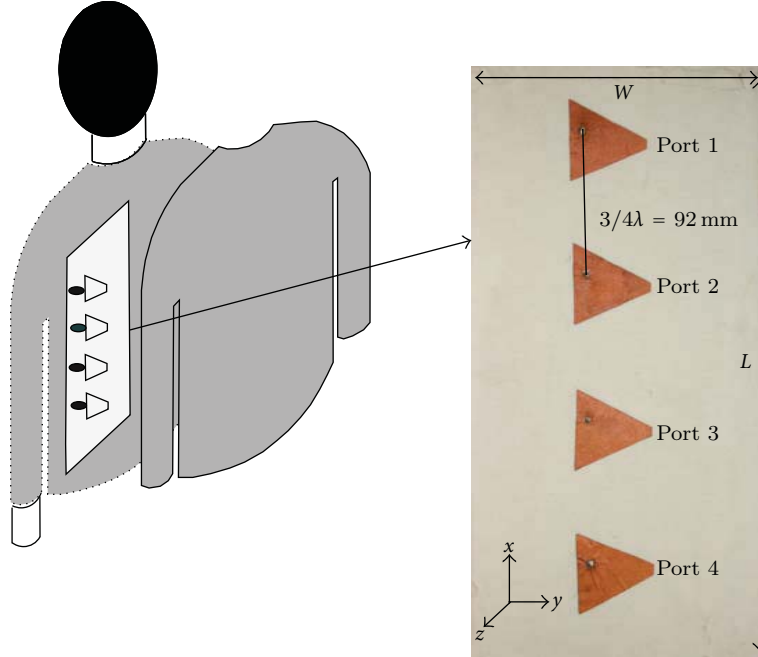


FIGURE 2: Top view of the textile antenna array and its position on the human body. TX1 to TX4 from top to bottom. W and L are the dimensions of the ground plane, as indicated in Table 1. The antenna array is placed on the back of the body, inside the firefighter jacket.

TABLE 2: Simulated and measured -3 dB beam width of a single-patch antenna and of the array, in the elevation plane (xz -plane) and in the azimuth plane (yz -plane).

	Elevation plane (xz -plane)		Azimuth plane (yz -plane)	
	Single patch	Array	Single patch	Array
Simulation	77°	16°	64°	66°
Measurement	76°	18°	57°	65°

array worn on the back, inside the jacket (Figure 2). The same array is used for the beamforming and space-time coding scenarios.

The transmission is performed in frames, transmitting at a rate of 1 Msymbols per second. Each transmitted frame is simultaneously used for both beamforming and space-time coding and consists of the following symbols.

- (i) Binary (BPSK phase shift keyed) pilot symbols for each transmit antenna sent in separate time slots to avoid interference of pilot symbols from different transmit antennas at the receiver. These pilot symbols are exploited at the receiver for estimating symbol timing, carrier frequency offset, and complex channel gains.
- (ii) Quadrature (QPSK phase shift keyed) data symbols encoded according to the 3/4 rate orthogonal space-time code documented in [27, pp 194 (5.143)].
- (iii) Uncoded QPSK symbols, equal on all transmit channels but with phase increments at the antenna terminals in multiples of 15° to generate beams in the $-10^\circ, \dots, +10^\circ$ elevation range.

A guard interval is inserted between consecutive frames. From the signals received during the guard intervals the noise variance is estimated.

Transmitted beams can be steered with main beams oriented along small-elevation angles around broadside, without the generation of grating lobes in the radiation pattern. The elevation angle θ is zero when all array elements are driven in phase. Beams at other elevation angles are produced by driving the subsequent antenna patches of the array with a phase increment $\Delta\varphi = \varphi_2 - \varphi_1 = \varphi_3 - \varphi_2 = \varphi_4 - \varphi_3$, with φ_n denoting the phase rotation applied to the n th transmit antenna ($n = 1, 2, 3, 4$). The relation between the phase angle increment $\Delta\varphi$ and elevation angle θ is given by

$$\Delta\varphi = \frac{2\pi d}{\lambda} \sin(\theta) \approx \frac{2\pi d}{\lambda} \theta. \quad (1)$$

The approximation is valid for small-elevation angles and, with $d = 92$ mm and $\lambda = 122$ mm at 2.45 GHz, results in $\Delta\varphi \approx 4.74 \cdot \theta$. A phase increment of $\Delta\varphi = 15^\circ$ at the antenna terminals, equal to the phase step size applied in the transmission, corresponds to an increment of $\theta \approx 3.2^\circ$ in the main beam's elevation angle. The performance for a beam with a given elevation angle is assessed by

selecting the received symbols that have been transmitted with the corresponding phase increment on subsequent antenna patches.

The transmit power configured for each antenna is +0 dBm for the LoS and +20 dBm for the NLoS measurements in order to compensate for the average path loss experienced in the specific propagation conditions. The signals received in this way are always well above the receiver noise floor but always below the level that causes saturation of the receivers' analog-to-digital converters.

Denoting by $s_n^{(i)}(k)$ the k th signal sample transmitted by the n th antenna during the i th frame, in case of beamforming, we have $s_n^{(i)}(k) = a^{(i)}(k)e^{j\varphi_n}$, where $a^{(i)}(k)$ is a QPSK symbol with

$$E\left[|a^{(i)}(k)|^2\right] = \sigma_a^2. \quad (2)$$

The transmitted energy per information bit is denoted as $E_{b,\text{tr}}$, the total (sum over all antennas) transmitted energy per symbol interval (for QPSK) is $4\sigma_a^2 = 2E_{b,\text{tr}}$, so that $E_{b,\text{tr}} = 2\sigma_a^2$. In case of space-time coding, we consider an orthogonal block code with the following codeword structure [27, pp 194 (5.143)]:

$$\mathbf{C} = \begin{bmatrix} a_1 & -a_2^* & -a_3^* & 0 \\ a_2 & a_1^* & 0 & -a_3^* \\ a_3 & 0 & a_1^* & a_2^* \\ 0 & a_3 & -a_2 & a_1 \end{bmatrix}. \quad (3)$$

The row and column indices refer to the transmit antenna and the time slot, respectively. The nonzero entries of \mathbf{C} are QPSK symbols with variance σ_a^2 . Denoting by $\mathbf{C}^{(i)}(l)$ the l th codeword transmitted during the i th frame, we have $s_n^{(i)}(4l + p) = (\mathbf{C}^{(i)}(l))_{n,p}$ for $p = 0, 1, 2, 3$. The total (sum over all antennas) transmitted energy per symbol interval is $3\sigma_a^2 = (1/4) \cdot 6E_{b,\text{tr}}$, yielding $E_{b,\text{tr}} = 2\sigma_a^2$.

For the space-time code, only three out of four antennas are transmitting in each time slot, reducing the total transmitted power by a factor 3/4 as compared to beamforming. However, since only three information symbols are transmitted in four time slots, the useful symbol rate is also reduced by a factor 3/4. Therefore, the total transmitted energy per information bit $E_{b,\text{tr}}$ is the same for the space-time code and for the beam former.

3.2. Base Station: Receiving System. The receiving antenna array is displayed in Figure 3 and consists of four vertically polarized dipole antennas equally spaced at 32 cm (2.6λ) apart and with its phase center 1.25 m above the floor level. The antenna array is directly connected to a Signalion HaLo 430 MIMO transceiver unit, synchronously sampling the received signals after conversion to baseband. The obtained I and Q samples are stored on a hard disk for later processing.

Based on the stored I and Q samples, carrier frequency offset and timing correction are applied, and matched filter output samples (at the symbol rate) are computed. The

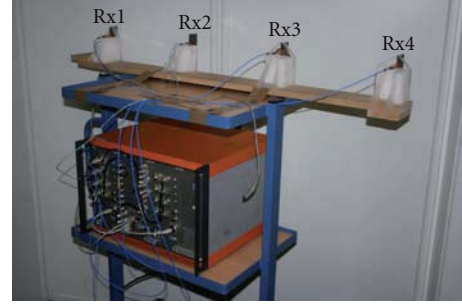


FIGURE 3: The fixed receiving antenna array with four vertical dipoles.

sample corresponding to the m th receive antenna during k th symbol interval in i th frame can be represented by

$$r_m^{(i)}(k) = \sum_{n=1}^4 h_{m,n}^{(i)} s_n^{(i)}(k) + w_m^{(i)}(k), \quad (4)$$

where $h_{m,n}^{(i)}$ denotes the channel gain from the n th transmit antenna to the m th receive antenna, and $w_m^{(i)}(k)$ is a Gaussian noise contribution with

$$E\left[|w_m^{(i)}(k)|^2\right] = N_{0,m}. \quad (5)$$

In the case of beamforming, the detection of the symbol $a^{(i)}(k)$ is based on maximum-ratio combining (MRC) of the samples $r_m^{(i)}(k)$, $m = 1, \dots, 4$. The resulting SNR at the input of the detector corresponding to the i th frame is given by

$$\text{SNR}_{\text{Beam}}^{(i)} = \sum_{m=1}^4 \text{SNR}_{\text{Beam},m}^{(i)}, \quad (6)$$

where

$$\text{SNR}_{\text{Beam},m}^{(i)} = \frac{\sigma_a^2}{N_{0,m}} \left| \sum_{n=1}^4 h_{m,n}^{(i)} e^{j\varphi_n} \right|^2 \quad (7)$$

is the ratio of signal power to noise power in $r_m^{(i)}(k)$.

In the case of space-time coding, the detection of an information symbol contained in the codeword $\mathbf{C}^{(i)}(l)$ is based on the MRC of the samples $r_m^{(i)}(4l + p)$, $m = 1, \dots, 4$, $p = 0, \dots, 3$. The resulting SNR at the input of the detector corresponding to the i th frame is given by

$$\text{SNR}_{\text{STC}}^{(i)} = \sum_{m=1}^4 \text{SNR}_{\text{STC},m}^{(i)}, \quad (8)$$

where

$$\text{SNR}_{\text{STC},m}^{(i)} = \frac{\sigma_a^2}{N_{0,m}} \sum_{n=1}^4 |h_{m,n}^{(i)}|^2 \quad (9)$$

is the ratio of signal power to noise power after the proper combining of $r_m^{(i)}(4l + p)$, $p = 0, \dots, 3$.

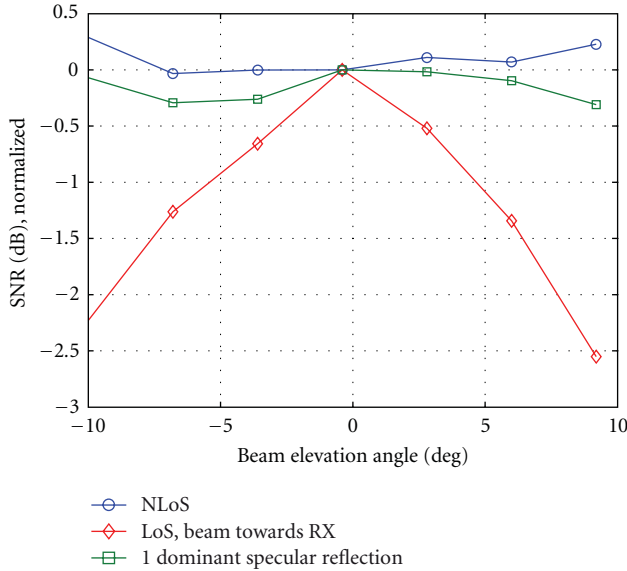


FIGURE 5: Average SNR as a function of the beam elevation angle, in the LoS environment, with the main beam directed towards and away from the receiver, as well as in the NLoS environment. The SNR is normalized to 0 dB for the 0° elevation beam.

4.1.2. *LoS, Beam towards the Receiver.* The measured SNR demonstrates the correct implementation of the beamforming. The zero-elevation beam clearly provides the highest SNR. Note that the values in Table 2 are for anechoic conditions, whereas the LoS curve in Figure 5 is measured in the actual indoor environment. The measured beamwidth is larger, probably due to ground and ceiling reflections.

4.1.3. *A Single Dominant Specular Reflection.* With the beam oriented away from the receiver, the propagation is assumed to predominantly occur via a single reflection in the indoor environment. The difference in SNR for different beam angles is smaller but the zero-elevation beam still provides the strongest signal.

4.2. *Line-of-Sight Path.* For the measurements along the LoS path, the rescue worker walks between the points marked A and B in the floor plan, Figure 4. The plots in Figures 6 and 7, displaying the E_b/N_0 per frame for the LoS scenario, correspond to the walk sequence ABABA. Clearly, shadowing effects by the human body cause an additional attenuation of the signal when the antenna array is oriented away from the receiver. Note that, as the antenna array is worn on the back, the beam is oriented away from the receiver when the test person approaches the base station (from A to B). A steep change in E_b/N_0 , by more than 15 dB, is noticed each time the rescue worker turns around, reorienting the beam.

4.2.1. *Reception without Receiver Diversity.* Without receiver diversity, the E_b/N_0 recorded for the beamforming results from a constructive addition of the received electromagnetic fields generated by each transmit antenna n (see (7)). For

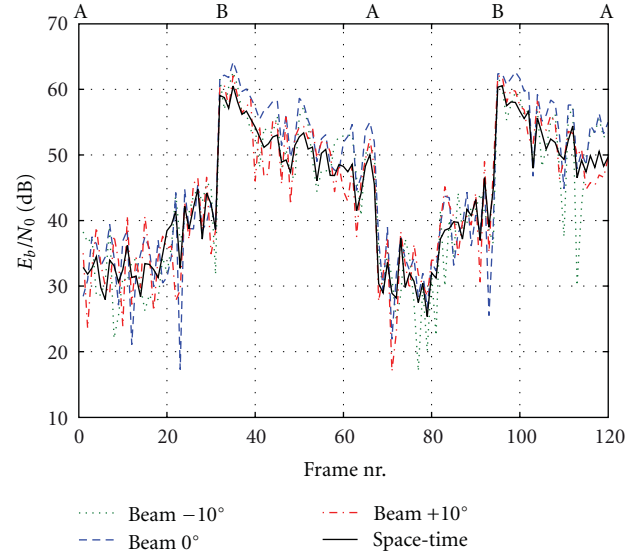


FIGURE 6: E_b/N_0 along the line-of-sight path, without receiver diversity (no MRC) for -10° , 0° , and $+10^\circ$ beams and for the space-time code. Labels on top indicate locations on the floor plan.

the space-time code, the E_b/N_0 results from the addition of the powers received from each transmit antenna n (see (9)). The results for reception in LoS conditions without receiver diversity are displayed in Figure 6.

- (i) Line-of-sight (beam towards RX).
 - (a) The beamforming achieves E_b/N_0 values that are a few dB larger compared to using the space-time code. If the receive antennas were located at zero-elevation angle and assuming identical additive white Gaussian noise (AWGN) channels between the transmit and receive antennas, the difference in E_b/N_0 between beamforming and space-time coding would amount to 6 dB, which corresponds to the difference between the constructive addition of the received electromagnetic fields at the receive antenna elements along the main beam direction of the array (beamforming) and the addition of the powers in case of transmit diversity (by means of space-time coding).
 - (b) The zero-elevation beam concentrates the transmitted power towards the receiver. The azimuth angle is much wider (Table 2), allowing considerable rotation of the body in the azimuth plane while maintaining a good communication link.
- (ii) A single dominant specular reflection (beam away from RX).
 - (a) The beam and the space-time code approximately exhibit equal performance, when considering average E_b/N_0 over all received frames.

The measured behavior, with the zero-elevation beam providing the strongest signal compared to beams with other elevations, indicates the presence of low-elevation reflections of the transmitted beam on vertical surfaces such as walls and metal closets.

- (b) The variance of the signal level is larger for the beamforming case, known to cause a worse BER for the same average E_b/N_0 . No transmit diversity is present in the beamforming case whereas fourth-order transmit diversity is achieved by the space-time code. In Figure 6, less signal fading occurs for the space-time coded transmission, especially with the beam oriented away from the receiver.

4.2.2. Reception with Fourth-Order Receiver Diversity. The results for reception in LoS conditions with fourth-order receiver diversity are displayed in Figure 7.

- (i) Line-of-sight (beam towards RX).
 - (a) The E_b/N_0 values for the zero-elevation beam are now often 6 dB higher than for the space-time code.
 - (b) Thanks to the receiver diversity, the transmission relying on beamforming suffers less degradation due to fading. The signal dips in Figure 7 are less deep than in Figure 6.
- (ii) A single dominant specular reflection (beam away from RX).
 - (a) Even with the beam oriented away from the receiver, zero-elevation beamforming still performs better (in terms of average E_b/N_0) than space-time coding, since the propagation in LoS conditions predominantly occurs by means of a small number of low-elevation angle reflections at walls and office equipment.
 - (b) The beam transmission corresponds to a 1×4 MIMO link and the space-time code to a 4×4 MIMO system. Therefore, less signal fading occurs for the space-time coded transmission, especially with the beam oriented away from the receiver.

4.3. Non-Line-of-Sight. For the NLoS measurements, the rescue worker walks back and forth between the points marked A and C in the floor plan, Figure 4. The measurement results are displayed in Figures 8 and 9. As the propagation link is composed of a sum over an ensemble of nondominant multipaths created by reflection/transmission/diffraction, the E_b/N_0 varies dramatically for subsequent frames. Note that 20 dB extra transmit power is used to compensate for the associated signal attenuation.

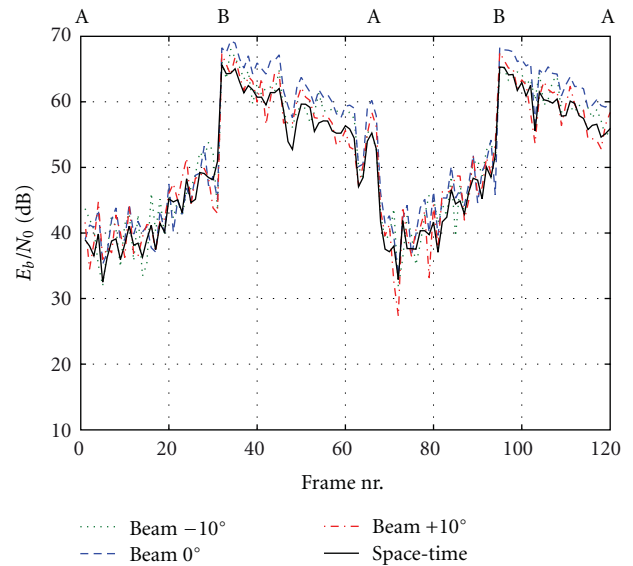


FIGURE 7: E_b/N_0 along the line-of-sight path, with receiver diversity (MRC) for -10° , 0° , and $+10^\circ$ beams and for the space-time code. Labels on top indicate locations on the floor plan.

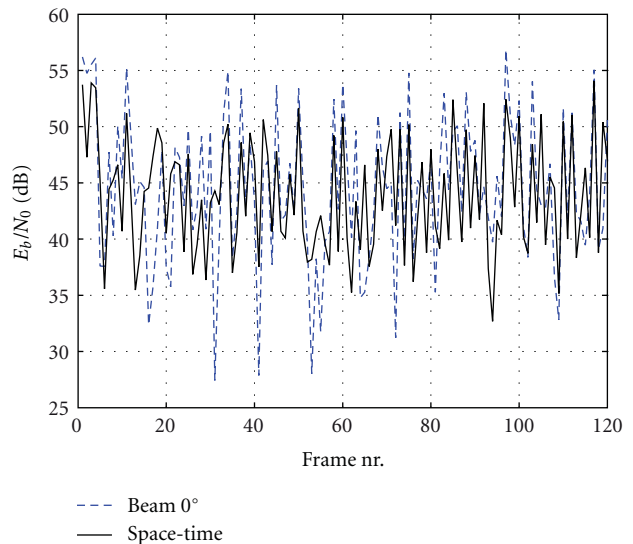


FIGURE 8: E_b/N_0 in non-line-of-sight conditions, without receiver diversity (no MRC). NLoS transmissions performed at 20 dB extra power compared to LoS transmissions.

4.3.1. No Receiver Diversity. The results for beamforming in NLoS conditions without receiver diversity are displayed in Figure 8. Without receiver diversity the beamforming performs clearly worse than the space-time code. Deep fades occur due to the lack of transmit diversity, gain for the static beamforming case. The space-time code realizes fourth-order transmit diversity, decreasing the fluctuation in E_b/N_0 .

4.3.2. Fourth-Order Receiver Diversity. The results for beamforming in NLoS conditions with fourth-order receiver diversity are displayed in Figure 9. With receiver diversity, the

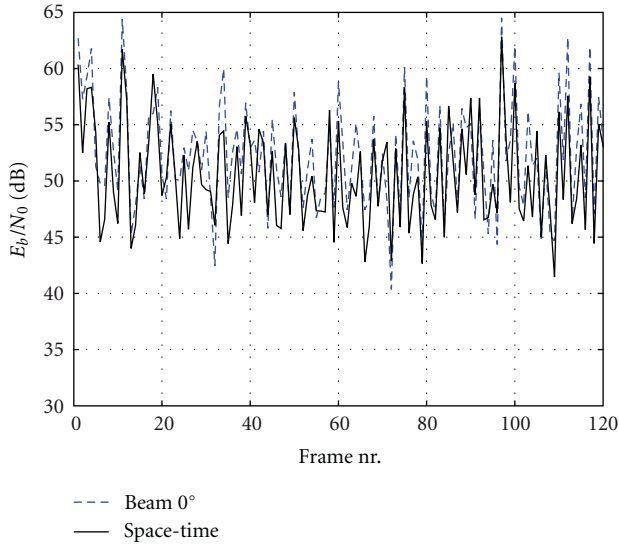


FIGURE 9: : E_b/N_0 in non-line-of-sight conditions, with receiver diversity (MRC). NLoS transmissions performed at 20 dB extra power compared to LoS transmissions.

variation of E_b/N_0 caused by fading is reduced, also for the beamforming case.

4.4. Minimum, Average, and Maximum E_b/N_0 . The minimum, average, and maximum E_b/N_0 values recorded for each measurement are listed in Table 3. The beamforming always achieves higher average received E_b/N_0 values (the associated power gain is listed in the last column of Table 3), indicating the important contribution of signals reflected or scattered at low-elevation angles in the indoor propagation environment. Simulation results in [5] also indicated that beamforming maximizes the received SNR.

The minimum E_b/N_0 values are generally higher for the space-time code especially in absence of receive diversity gain. Lower minimum E_b/N_0 values indicate more severe fading, resulting in a higher BER for a given average E_b/N_0 value. Higher maximum E_b/N_0 values always result for the beamforming case, caused by concentrating the transmitted power in a range of low-elevation angles. However, the average BER is mostly determined by the lowest E_b/N_0 values occurring.

The results indicate that some degree of diversity is always beneficial, even in LoS conditions. MRC of 4 signals, received on separate antennas, provides array gain and additional diversity gain. The average measured total additional gain by receiving on 4 antennas using MRC varies between 5.9 and 6.8 dB for all measured cases in Table 3.

4.5. BER Characteristics. For QPSK, the BER for the i th frame is given by

$$\text{BER}^{(i)} = Q\left(\sqrt{\left(\frac{2E_b}{N_0}\right)^{(i)}}\right), \quad (10)$$

where $Q(x)$ is the tail area (from x to ∞) of the zero-mean univariate Gaussian distribution, and $(E_b/N_0)^{(i)}$ is the E_b/N_0 value at the input of the detector corresponding to the i th frame, which equals $(1/2) \cdot \text{SNR}_{\text{Beam}}^{(i)}$ or $(1/2) \cdot \text{SNR}_{\text{STC}}^{(i)}$ depending on the transmit scenario. The displayed BER is the average of $\text{BER}^{(i)}$ over the frame index i . The detailed procedure for calculating measurement-based BER characteristics for a range of average E_b/N_0 values is outlined in [2]. In case of fourth-order receiver diversity, we obtain receive array gain (which equals 6 dB in case of identical powers on each receive antenna), with an additional diversity gain. The bit error rate represented allows a performance comparison of our experimental transmissions for beamforming and space-time coding with or without receiver diversity. Note that beamforming and space-time coding transmissions are performed within the same transmission frame, hence with equal momentary propagation conditions.

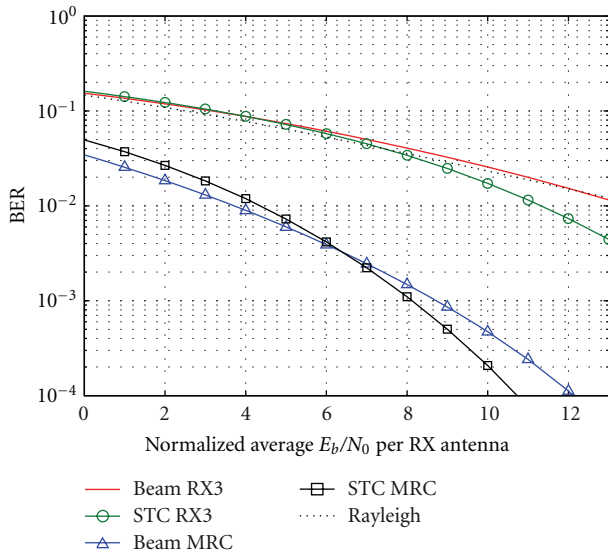
To obtain a fair comparison of the BER produced by beamforming versus space-time coding, we consider an equal total transmitted energy per information bit $E_{b,\text{tr}}$ for both scenarios. Therefore, we introduce the notion of normalized average E_b/N_0 , which equals either the average E_b/N_0 at the detector output (in the case of STC) or the average E_b/N_0 at the detector output minus the beamforming power gain from Table 3 (in the case of beamforming). This way displaying BER curves as a function of the normalized E_b/N_0 includes the power gain associated with coherent beamforming.

4.5.1. Non-Line-of-Sight. Figure 10 lists the BER characteristics for the measurements along the NLoS path. Due to the absence of diversity, the curve in case of beamforming, as received on RX3, approaches the theoretical curve for Rayleigh fading. Without receiver diversity, relying only on RX3, at higher E_b/N_0 the BER decreases more quickly for links relying on the space-time code than for the beamforming link thanks to the inherent transmit diversity of the former. For the beamforming, there is no diversity at all in this case, hence we are comparing fourth and first order diversity systems. Space-time coding performs better than beamforming when the $\text{BER} < 8.6 \cdot 10^{-2}$.

With receiver diversity, the curves for the space-time code also decrease faster than for the beamforming case, thanks to the higher diversity order. However, the difference is not so large for low-to-moderate E_b/N_0 values, as we are now comparing a 4×4 MIMO link with a 1×4 SIMO system. They exhibit 16th- and fourth-order diversity, respectively, and the additional performance gain associated to increasing the diversity order from 4 to 16 is not that large anymore. The space-time code performs better than beamforming when the $\text{BER} < 3.3 \cdot 10^{-3}$. To achieve a $\text{BER} = 10^{-4}$, the space-time code requires 1.4 dB less transmit energy per information bit. Measurements documented in [7], although focused on channel capacity, also indicated the better performance of space-time coding at higher SNR levels. Note that beamforming is also more sensitive to movements of the rescue worker, as bending of the body will point the beam upward or downward.

TABLE 3: E_b/N_0 for STC and beamforming; beamforming power gain.

	STC (dB)	Beamforming (dB)	Beamforming power gain (dB)
NLoS, no receive diversity			
min.	29.7	25.9	
avg.	43.7	45.5	1.8
max.	51.1	53.8	
NLoS, fourth-order receive diversity			
min.	38.4	36.5	
avg.	50.2	52.2	2.0
max.	59.8	62.5	
LoS, no receive diversity			
min.	43.1	38.6	
avg.	49.9	53.3	3.4
max.	57.5	60.5	
LoS, fourth-order receive diversity			
min.	49.7	51.9	
avg.	56.6	60.1	3.5
max.	62.0	65.5	
A single dominant specular reflection, no receive diversity			
min.	22.3	13.1	
avg.	33.4	34.9	1.5
max.	40.2	42.9	
A single dominant specular reflection, fourth-order receive diversity			
min.	29.5	29.7	
avg.	39.3	41.0	1.7
max.	45.3	49.0	

FIGURE 10: BER as a function of the normalized average E_b/N_0 per receive antenna, recorded along the NLoS path, for transmissions at equal total $E_{b,tt}$.

4.5.2. *Line-of-Sight.* The BER characteristics for the LoS path are calculated separately for the frames where the

beam is oriented towards the receiver and those with the beam directed away from it. Figure 11 displays the BER characteristics for the frames recorded in LoS, with the beam oriented towards the receiver. The curve for beamforming without diversity is now better than the theoretical curve for Rayleigh fading. The signal propagation, composed of a strong LoS component and some reflected signals, produces a large power gain for the transmission relying on beamforming. BER curves for the set of frames measured with the beam oriented towards the receiver display a considerable performance improvement in case of transmit beamforming with receiver diversity. Concentrating the transmitted power along the low-elevation angles creates a significantly stronger signal at the receiver. To achieve a $BER = 10^{-4}$, the beamforming requires 2.3 dB less transmit energy per information bit.

4.5.3. *A Single Dominant Specular Reflection.* The BER curves in Figure 12 correspond to the set of frames measured along the LoS path, with the beam oriented away from the receiver. The characteristic for beamforming without diversity approaches the theoretical Rayleigh fading characteristic, indicating the blockage of the direct signal path by the human body. Additionally, the antenna array's main beam is now directed away from the receiver. The performance of beamforming with receiver diversity is always slightly

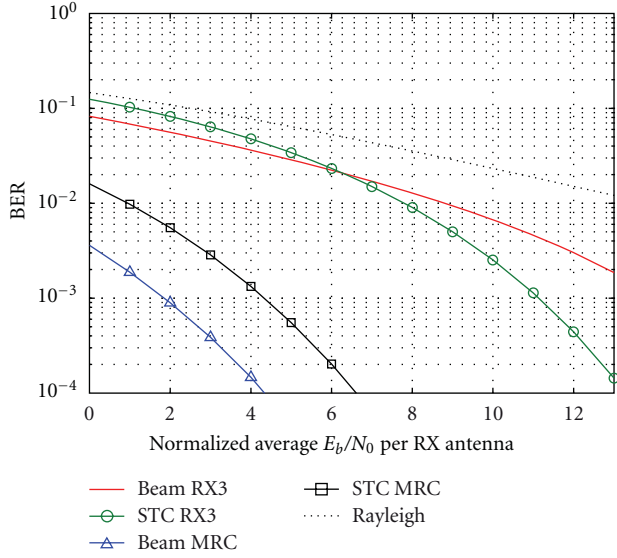


FIGURE 11: BER as a function of the normalized received E_b/N_0 per antenna, recorded along the LoS path with the transmit antenna array oriented towards the receiver, for transmissions at equal total $E_{b,tr}$.

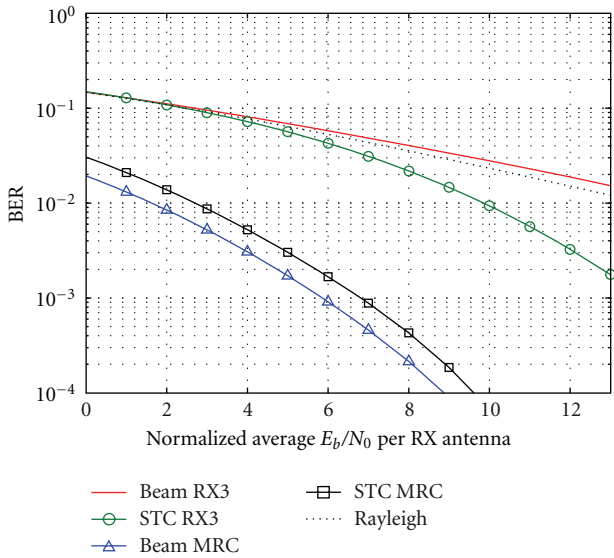


FIGURE 12: BER as a function of the normalized received E_b/N_0 per antenna, for communication via a single dominant specular reflection and transmissions at equal total $E_{b,tr}$.

better than for space-time coding. The propagation is mainly realized through one dominant specular reflection, occurring at a low-elevation angle. To achieve a $BER = 10^{-4}$, the beamforming requires 0.7 dB less transmit energy per information bit, with the beam oriented away from the receiver.

TABLE 4: Signal envelope correlation of the received signals.

	RX1	RX2	RX3	RX4
NLoS, zero-elevation beam				
RX1	1	0.49966	0.46488	0.37184
RX2	0.49966	1	0.49911	0.51818
RX3	0.46488	0.49911	1	0.58911
RX4	0.37184	0.51818	0.58911	1
LoS, zero-elevation beam				
RX1	1	0.64439	0.64289	0.64433
RX2	0.64439	1	0.53591	0.54072
RX3	0.64289	0.53591	1	0.55964
RX4	0.64433	0.54072	0.55964	1
A dominant specular reflection, zero-elevation beam				
RX1	1	0.55218	0.43311	0.19448
RX2	0.55218	1	0.58084	0.42663
RX3	0.43311	0.58084	1	0.58893
RX4	0.19448	0.42663	0.58893	1

4.6. *Signal Envelope Correlation.* The normalized correlation coefficients of the signal envelopes are given by

$$\rho_{X,Y} = \frac{E[X \cdot Y] - E[X]E[Y]}{\sqrt{[E[X^2] - (E[X])^2][E[Y^2] - (E[Y])^2]}}. \quad (11)$$

For the transmit correlation, as seen from antenna RX3, we set $X = |h_{3,n_1}|$ and $Y = |h_{3,n_2}|$, with n_1 and n_2 the indices of the corresponding TX antennas. The used channel estimation values $h_{i,j}$ are based on the received pilot symbols. For the receive correlation, X and Y are the magnitudes of the zero-elevation beam symbols as received on the corresponding RX antennas.

4.6.1. *Correlation Coefficients of the Received Signals.* Table 4 lists the correlation coefficients for the received signals, for reception of the zero-elevation beam. A significant diversity gain may be realized when the envelope correlation coefficient is lower than 0.7 [28], which is the case for all receive correlation values. MRC reception with multiple antennas will produce array and diversity gain in all cases. An interesting observation is the decreasing correlation for receive antennas spaced further apart in the NLoS and specular reflection cases (Figure 3 shows the RX antenna positions). For the LoS case, as expected for a beam directed towards the receiver along a LoS path, the correlation is higher and more constant as a function of RX antenna separation.

4.6.2. *Correlation Coefficients of the Transmitted Signals.* Table 5 displays the correlation coefficients for the signals transmitted by different patches of the off-body array. The values are rather high for all cases, due to the proximity of the human body. Remarkably, the correlation is the lowest for the upper two patches (TX1 and TX2) in the array. This value is below 0.7 for all cases and allows a significant transmit

TABLE 5: Signal envelope correlation of the transmitted signals

	TX1	TX2	TX3	TX4
NLoS, as received by RX3				
TX1	1	0.60868	0.73301	0.76079
TX2	0.60868	1	0.84735	0.86725
TX3	0.73301	0.84735	1	0.99728
TX4	0.76079	0.86725	0.99728	1
LoS, as received by RX3				
TX1	1	0.66085	0.67815	0.72005
TX2	0.66085	1	0.85092	0.87672
TX3	0.67815	0.85092	1	0.99662
TX4	0.72005	0.87672	0.99662	1
A dominant specular reflection, as received by RX3				
TX1	1	0.56683	0.74630	0.76840
TX2	0.56683	1	0.83224	0.84849
TX3	0.74630	0.83224	1	0.99781
TX4	0.76840	0.84849	0.99781	1

diversity gain [28] for the space-time code. The other signals will also provide some diversity but in a minor way. The correlation is very high for the lower two patches (TX3 and TX4). As the array is perfectly symmetrical, we assume that this is an effect of the proximity to the floor.

5. Conclusions

Experimentally comparing static beamforming and transmit diversity techniques based on space-time codes for a wearable vertical textile, antenna array consisting of four radiating patches worn on the back of a firefighter walking in an indoor environment leads to the following conclusions.

While the measured average E_b/N_0 values at the input of the detector are always higher for the beamforming system, the variation of the signal level is more severe due to the limited diversity, resulting in worse bit error characteristics.

Without receiver diversity, the bit error rate curves indicate that, for any bit error rate of practical use ($BER < 2.1 \cdot 10^{-2}$), space-time coding performs best for line-of-sight as well as for non-line-of-sight conditions. In the indoor environment, some degree of diversity, is desired to combat the severe fading that is present on the signals.

With fourth-order receiver diversity in line-of-sight conditions, beamforming always performs better than space-time coding. The presence of both transmit beamforming and receive diversity results in a higher average received E_b/N_0 while the effects of fading are also reduced. In non-line-of-sight conditions, however, space-time coding is better as soon as $BER < 3.3 \cdot 10^{-3}$. The relative advantage of space-time coding for higher SNR levels was also observed in [7].

An important aspect to take into account is that the beamforming system is more sensitive to body movements, such as bending over, changing the elevation angle of the main beam. Switching to space-time coding results in a larger beam width in the elevation plane.

Static beamforming, however, can be realized by using phase shifters, whereas space-time coding requires expensive and more power-consuming hardware with dedicated transmit chains for each channel.

Further research will involve an extension of the system presented in this contribution, deploying two textile antenna arrays, worn at the front and the back of the human body, realizing a significant additional improvement by countering the effect of shadowing by the human body. Also, a hybrid system that combines static beamforming and space-time coding will be studied experimentally.

Acknowledgment

This work was supported by the fund for Scientific Research-Flanders (FWO-V) by project ‘‘Advanced space-time processing techniques for communication through multi-antenna systems in realistic mobile channels.’’

References

- [1] D. Curone, E. L. Secco, A. Tognetti et al., ‘‘Smart garments for emergency operators: the ProeTEX project,’’ *IEEE Transactions on Information Technology in Biomedicine*, vol. 14, no. 3, pp. 694–701, 2010.
- [2] P. Van Torre, L. Vallozzi, C. Hertleer, H. Rogier, M. Moeneclae, and J. Verhaevert, ‘‘Dynamic link performance analysis of a rescue worker’s off-body communication system using integrated textile antennas,’’ *IET Science, Measurement and Technology*, vol. 4, no. 2, pp. 41–52, 2010.
- [3] S. Cotton and W. Scanlon, ‘‘An experimental investigation into the influence of user state and environment on fading characteristics in wireless body area networks at 2.45 GHz,’’ *IEEE Transactions on Wireless Communications*, vol. 8, no. 1, Article ID 4786471, pp. 6–12, 2009.
- [4] L. Vallozzi, P. Van Torre, C. Hertleer, H. Rogier, M. Moeneclae, and J. Verhaevert, ‘‘Wireless communication for firefighters using dual-polarized textile antennas integrated in their garment,’’ *IEEE Transactions on Antennas and Propagation*, vol. 58, no. 4, Article ID 5398858, pp. 1357–1368, 2010.
- [5] C. van Rensburg and B. Friedlander, ‘‘Transmit diversity for arrays in correlated Rayleigh fading,’’ *IEEE Transactions on Vehicular Technology*, vol. 53, no. 6, pp. 1726–1734, 2004.
- [6] L. Chu, J. Yuan, and Z. Chen, ‘‘A coded beamforming scheme for frequency-flat MIMO fading channels,’’ *IET Communications*, vol. 1, no. 5, pp. 1075–1081, 2007.
- [7] C. Hermosilla, R. A. Valenzuela, L. Ahumada, and R. Feick, ‘‘Empirical comparison of MIMO and beamforming schemes for outdoor-indoor scenarios,’’ *IEEE Transactions on Wireless Communications*, vol. 8, no. 3, Article ID 4801460, pp. 1139–1143, 2009.
- [8] C. Hermosilla, R. Feick, R. Valenzuela, and L. Ahumada, ‘‘Improving MIMO capacity with directive antennas for outdoor-indoor scenarios,’’ *IEEE Transactions on Wireless Communications*, vol. 8, no. 5, Article ID 4927423, pp. 2177–2181, 2009.
- [9] X. Chen, Y. Gong, and Y. Gong, ‘‘Suppression of directional interference for STBC MIMO system based on beamforming,’’ in *Proceedings of the International Conference on Communications, Circuits and Systems, (ICCCAS’06)*, pp. 983–987, June 2006.

- [10] L. Min, Y. Luxi, and Y. Xiaohu, "Adaptive transmit beamforming with space-time block coding for correlated MIMO fading channels," in *Proceedings of the IEEE International Conference on Communications, (ICC'07)*, pp. 5879–5884, June 2007.
- [11] L. Ping, L. Zhang, and H. So, "On a hybrid beamforming/space-time coding scheme," *IEEE Communications Letters*, vol. 8, no. 1, pp. 15–17, 2004.
- [12] G. Jongren, M. Skoglund, and B. Ottersten, "Combining beamforming and orthogonal space-time block coding," *IEEE Transactions on Information Theory*, vol. 48, no. 3, pp. 611–627, 2002.
- [13] C. Sun and N. Karmakar, "Environment-oriented beamforming for space-time block coded multiuser MIMO communications," in *Proceedings of the Antennas and Propagation Society International Symposium*, pp. 1744–1747, IEEE, June 2004.
- [14] K. Lin, Z. Hussain, and R. Harris, "Adaptive transmit eigen-beamforming with orthogonal space-time block coding in correlated space-time channels," in *Proceedings of the IEEE International Conference on Acoustics, Speech, and Signal Processing*, pp. V-817–V-820, May 2004.
- [15] X. Cai and G. B. Giannakis, "Differential space-time modulation with eigen-beamforming for correlated MIMO fading channels," *IEEE Transactions on Signal Processing*, vol. 54, no. 4, pp. 1279–1288, 2006.
- [16] L. Liu and H. Jafarkhani, "Application of quasi-orthogonal space-time block codes in beamforming," *IEEE Transactions on Signal Processing*, vol. 53, no. 1, pp. 54–63, 2005.
- [17] H. Kim and J. Chun, "MIMO structure which combines the spatial multiplexing and beamforming," in *Proceedings of the 59th IEEE Vehicular Technology Conference, (VTC'04)*, pp. 108–112, May 2004.
- [18] C. Lin, V. Raghavan, and V. Veeravalli, "To code or not to code across time: space-time coding with feedback," *IEEE Journal on Selected Areas in Communications*, vol. 26, no. 8, Article ID 4641968, pp. 1588–1598, 2008.
- [19] Y. G. Kim and N. Beaulieu, "On MIMO beamforming systems using quantized feedback," *IEEE Transactions on Communications*, vol. 58, no. 3, Article ID 5426515, pp. 820–827, 2010.
- [20] Y. Ko, Q. Ma, and C. Tepedelenlioglu, "Comparison of adaptive beamforming and orthogonal STBC with outdated feedback," *IEEE Transactions on Wireless Communications*, vol. 6, no. 1, pp. 20–25, 2007.
- [21] M. Kobayashi, G. Caire, and D. Gesbert, "Transmit diversity versus opportunistic beamforming in data packet mobile downlink transmission," *IEEE Transactions on Communications*, vol. 55, no. 1, pp. 151–157, 2007.
- [22] S. Ekbatani and H. Jafarkhani, "Combining beamforming and space-time coding using noisy quantized feedback," *IEEE Transactions on Communications*, vol. 57, no. 5, pp. 1280–1286, 2009.
- [23] S. S. Karimabadi, Y. Mohsenzadeh, A. R. Attari, and S. M. Moghadasi, "Bandwidth enhancement of single-feed circularly polarized equilateral triangular microstrip antenna," in *Proceedings of the Progress in Electromagnetic Research Symposium*, pp. 147–150, Hangzhou, China, March 2008.
- [24] C. L. Tang, J. H. Lu, and K. L. Wong, "Circularly polarised equilateral-triangular microstrip antenna with truncated tip," *Electronics Letters*, vol. 34, no. 13, pp. 1277–1278, 1998.
- [25] Y. S. Jawad and G. Debatosh, "Applications of triangular microstrip patch: circuit elements to modern wireless antennas," *Mikrotalasna Revija*, vol. 13, no. 1, pp. 8–11, 2007.
- [26] Lion International (LDH group), 2011, <http://lion-frankreich.lhd-gruppe.de/company.html>.
- [27] C. Oestges and B. Clerckx, *MIMO Wireless Communications: From Real-World Propagation to Space-Time Code Design*, Academic Press, 2007.
- [28] S. M. Alamouti, "A simple transmit diversity technique for wireless communications," *IEEE Journal on Selected Areas in Communications*, vol. 16, no. 8, pp. 1451–1458, 1998.

Research Article

Tetraband Small-Size Printed Strip MIMO Antenna for Mobile Handset Application

Qinghao Zeng,¹ Yuan Yao,¹ Shaohua Liu,¹ Junsheng Yu,¹ Peng Xie,¹ and Xiaodong Chen²

¹ School of Electronic Engineering, Beijing University of Posts and Telecommunications, Beijing 100876, China

² School of Electronic Engineering and Computer Science, Queen Mary University of London, London E1 4NS, UK

Correspondence should be addressed to Qinghao Zeng, hankszeng@163.com

Received 31 August 2011; Accepted 10 October 2011

Academic Editor: Li Yang

Copyright © 2012 Qinghao Zeng et al. This is an open access article distributed under the Creative Commons Attribution License, which permits unrestricted use, distribution, and reproduction in any medium, provided the original work is properly cited.

A compact printed multiple-input multiple-output (MIMO) antenna for tetraband (GSM900/1800/1900/UMTS) mobile handset application is presented. The proposed MIMO antenna, which consists of two coupled-fed loop antennas with symmetrical configuration, was printed on a $120 \times 60 \times 0.8 \text{ mm}^3$ Fr-4 substrate of relative permittivity of 4.4, loss tangent 0.02. Each element antenna requires only a small area of $22.5 \times 25 \text{ mm}^2$ on the circuit board. The edge-to-edge spacing between the two elements is only $0.03\lambda_0$ of 920 MHz. A slot and a dual-inverted-L-shaped ground branch were added in the ground plane to decrease the mutual coupling between the antenna elements. The measured isolation of the proposed antenna is better than 15 dB among the four operating frequency bands. The simulated 3D radiation patterns at 900 MHz and 1900 MHz of both antenna elements show that two loop antennas in general cover complementary space regions with good diversity performance. Detailed antenna impedance matching performance comparisons were done to evaluate the benefit of using different decoupling technology. The envelop correlation coefficient is calculated to represent the diversity performance of the MIMO antenna.

1. Introduction

Multiple-input and multiple-output (MIMO) technology which seemed as a key technology for long-term evolution (LTE) has attracted significant attention [1–3]. Theoretical and experimental investigations have revealed substantial improvements in channel capacity and reliability in rich scattering environments when multiple transmitter and receiver antennas are deployed [4, 5]. There are more limitations for engineers to design a qualified MIMO antenna for handset applications than a MIMO antenna for base station applications such as the extremely small size and the mutual coupling between the element antennas [6, 7]. The correlation coefficient is directly related to the mutual coupling between the element antennas. The higher the isolation was, the higher the data transmission speed could be obtained [8].

Many studies have been carried out to reduce the mutual coupling between the multiple antenna elements. A corrugated ground plane with $\lambda/4$ slot was used to reduce the interference of a current flowing in the common ground

plane [9]. In [10], the protruded T-shaped stub and L-shaped stub at ground plane are used to reduce the mutual coupling between two element antennas. The polarization diversity technique [11] and defected ground structure [12] are adopted to improve the separation between the element antennas. Various MIMO antennas for laptop or mobile handset applications were provided during these years. The majority of them are designed for laptop operating at WLAN (2.4–2.48 GHz, 5.2 GHz) and WiMAX band [13–15]. MIMO antennas for mobile terminal have drawn more and more research interest nowadays, and more and more designs are presented. Most of MIMO antennas for handset applications are designed to resonate at high frequencies such as GSM1800/1900/UMTS [9–12]. However, fewer researches were carried out to design MIMO antennas resonating at lower frequencies such as GSM850/900/LTE 700 or to design MIMO antennas resonating at both lower frequencies and higher frequencies. In [16, 17], two articles of MIMO antennas for only LTE 700 application were provided.

In this paper, we present a promising small-size on-board printed multiple-input and multiple-output

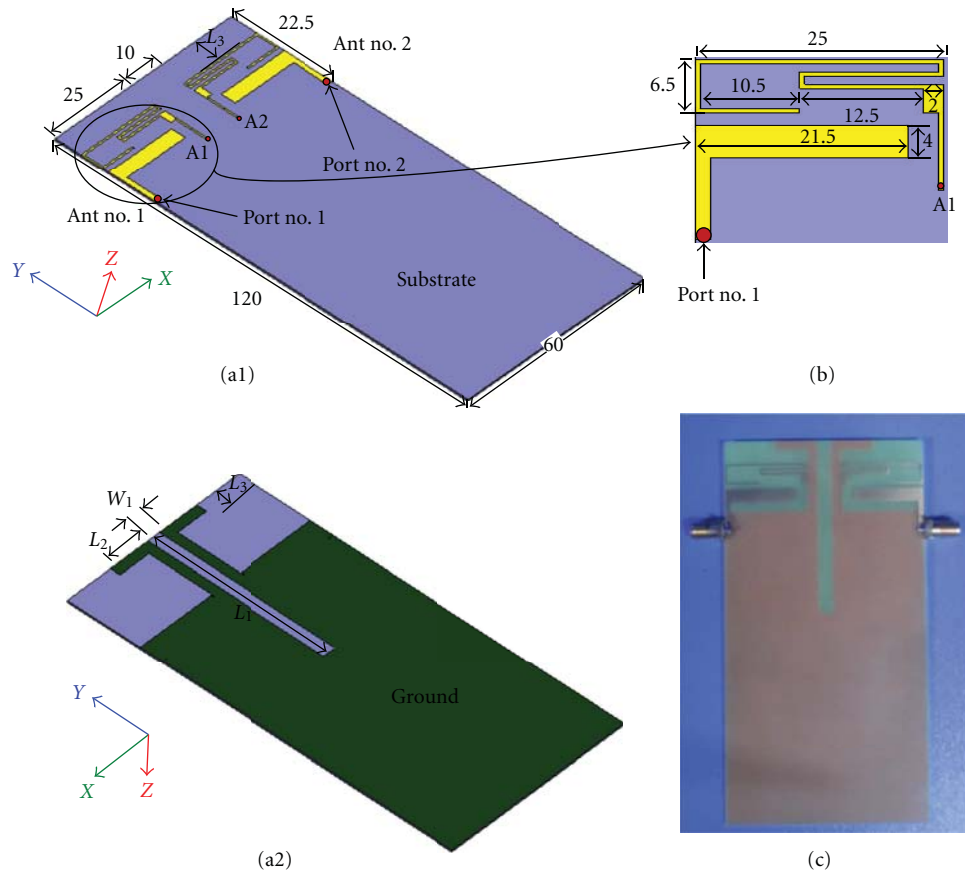


FIGURE 1: Geometry of the proposed MIMO antenna: (a1) and (a2) 3D view of the proposed MIMO antenna, (b) element antenna structure, and (c) fabricated MIMO antenna.

antenna for tetraband wireless communication applications (GSM900/1800/1900/UMTS). The proposed antenna, which consists of two coupled-fed loop antennas with symmetric configuration, was printed on a $120 \times 60 \times 0.8 \text{ mm}^3$ FR-4 substrate of relative permittivity of 4.4, loss tangent 0.02. Two coupled-fed strip antennas were etched on the top layer of the substrate. The grounds with a 4 mm-width slot and dual-inverted-L-shaped ground branches were etched on the bottom layer of the substrate. The loop antenna is formed by a loop strip with end terminal short-circuited to the ground plane and its front section capacitively coupled to a feeding strip which is also an efficient radiator to contribute a resonant mode for the antenna's upper band to cover 1710–2170 MHz. Through the coupling excitation, the antenna can also generate a qua-wavelength loop resonant mode to form the antenna's lower band to cover the 880–960 MHz [18]. The isolation between the two antenna elements highly improved when a slot and a dual-inverted-L were added on the ground. The slot on the ground also generates a resonance at about 900 MHz that broaden the antenna's lower operating band.

2. Antenna Design

The geometry of the proposed MIMO antenna is shown in Figure 1. Two element antennas and ground were etched

on the top layer and bottom layer, respectively. Figure 1(a1) depicts the layout of the two coupled-fed loop antennas; the edge-to-edge spacing is 10 mm. The detailed dimension of the element antenna is shown in Figure 1(b). Each element antenna occupies a footprint of $22.5 \times 25 \text{ mm}^2$. The element antenna is formed by a 0.5 mm-width loop strip and a feeding strip. The end terminal of the loop strip is short-circuited to the ground via pin A1 and A2. A $2 \times 4 \text{ mm}^2$ rectangular matching piece was added to improve the impedance matching performance. The front section of the loop strip is capacitively coupled to the feeding strip which starts from a shot section of 50Ω microstrip. The feeding strip also generates a resonant mode for GSM1800/1900/UMTS.

The ground of the proposed antenna is shown in Figure 1(a2). The substrate extends its length by $L_3 = 7.5 \text{ mm}$. A slot with length $L_1 = 55 \text{ mm}$ and width $W_1 = 4 \text{ mm}$ was laid in the middle of the ground plane. A dual-inverted-L-shaped ground branch with strip width $W_2 = 3 \text{ mm}$ and x -direction end section length $L_2 = 15 \text{ mm}$ was laid on the left and right sides of the slot.

Figure 1(c) is the photograph of the fabricated MIMO antenna. Port no. 1 and port no. 2 were connected with two SMA female connectors for S-parameter measurements and radiation patterns measurements.

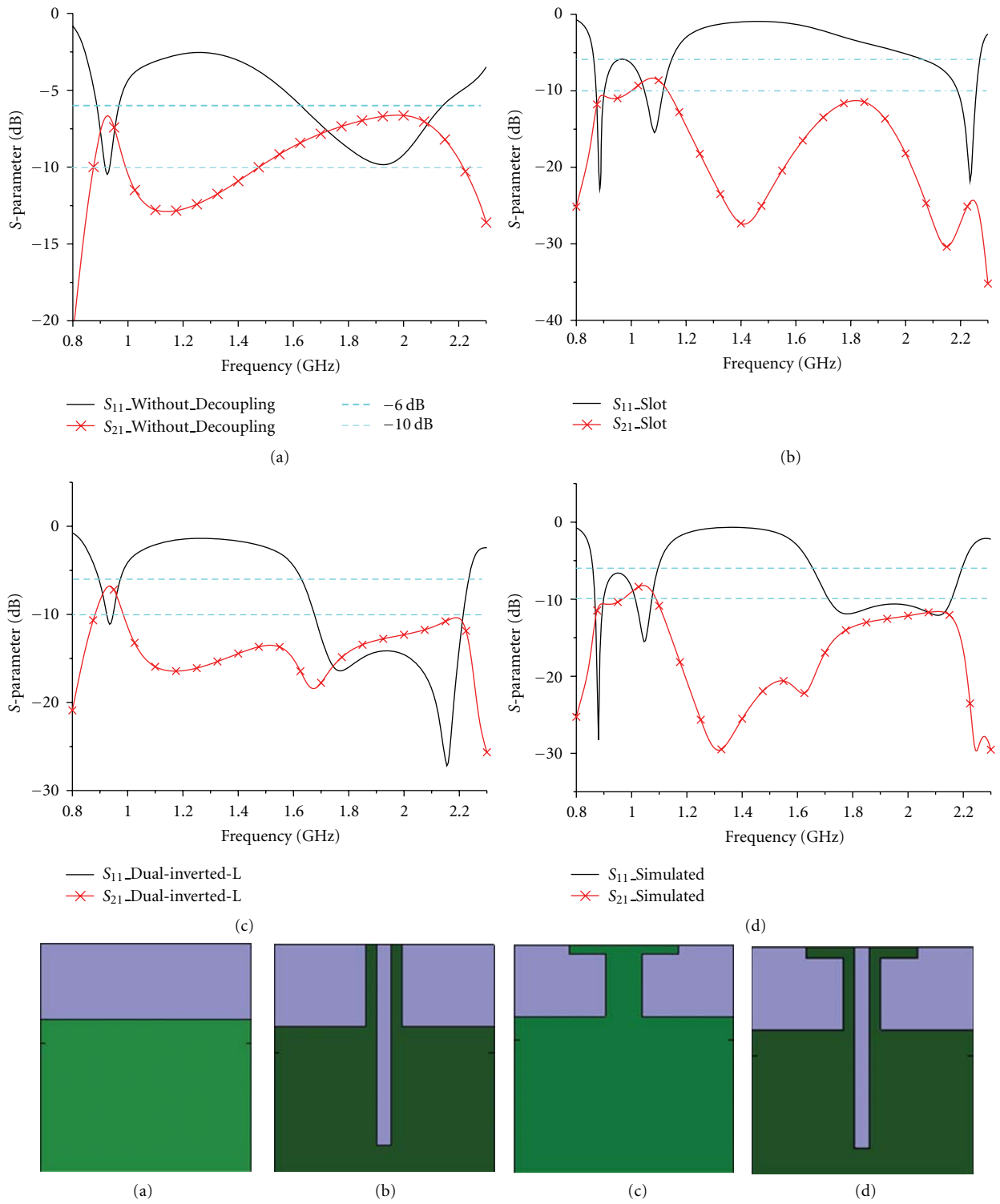


FIGURE 2: Simulated S_{11} and S_{21} curves: (a) simulated S -parameter curves of the antenna without slot on ground plane and ground branch, (b) simulated S -parameter curves of antenna with slot on the ground plane, (c) simulated S -parameter of antenna with dual-inverted-L shaped ground branch, (d) simulated S -parameter of antenna with both slot and ground branch.

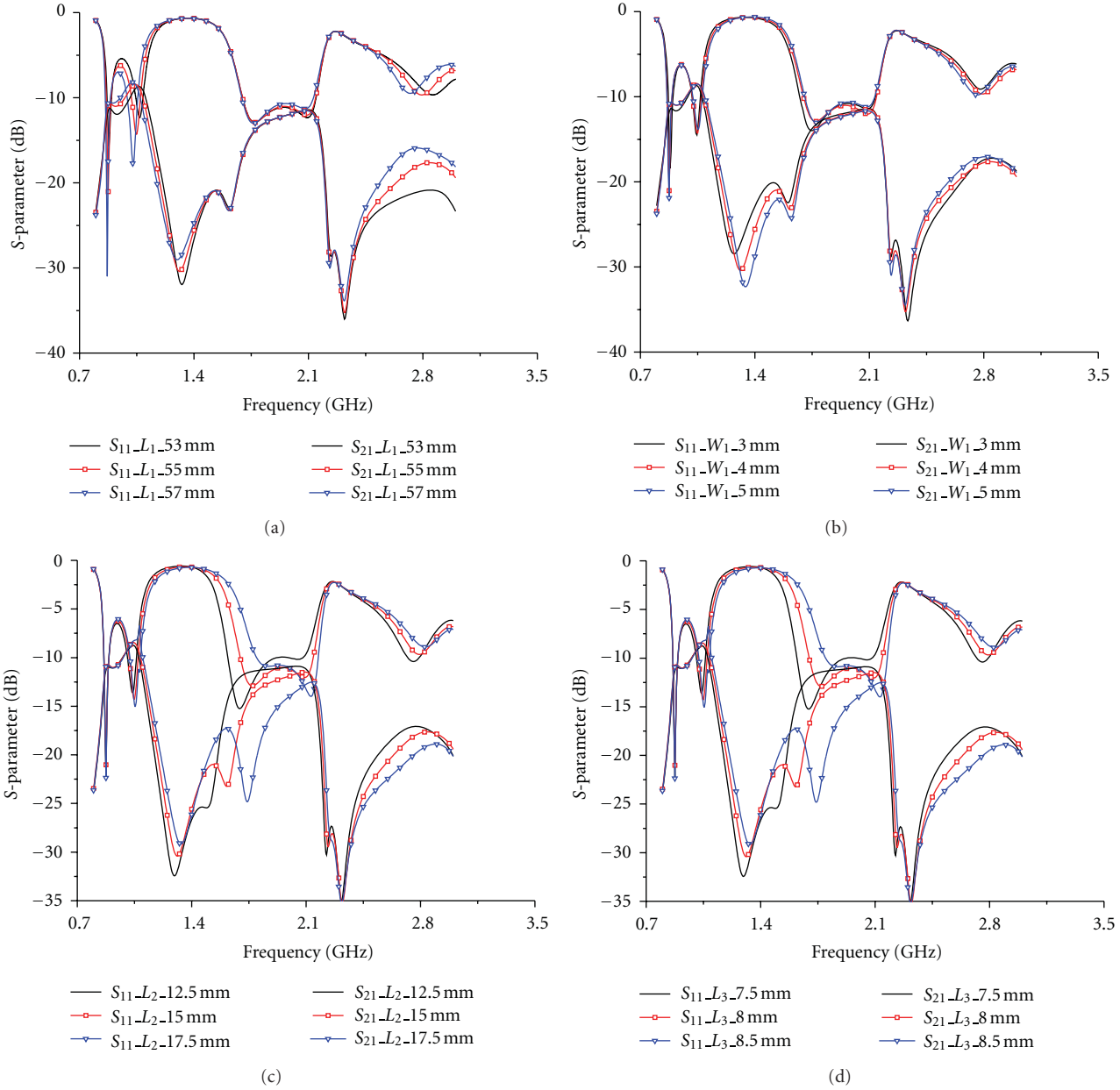


FIGURE 3: Parameter studies of $L_1/W_1/L_2$ and L_3 ; the nominal values of the dimensions are $L_1 = 55$ mm/ $W_1 = 4$ mm/ $L_2 = 15$ mm/ $L_3 = 8$ mm.

3. Simulation Analysis

The antenna was simulated and optimized with 3D full-wave EM simulation software Ansoft HFSS (High Frequency Structure Simulator) V11 [19]. Various simulations were carried out to verify different decoupling techniques, and simulation results were obtained. S_{11} & S_{22} or S_{21} & S_{12} are the same because of the absolutely symmetrical structure. Figure 2 shows the simulated S_{11} and S_{21} curves of antenna with different ground planes. Figure 2(a) is the simulated S_{11} and S_{21} curves of antenna without decoupling structure. Both the lower and upper frequency bands can merely satisfy the impedance matching bandwidth requirement that

$S_{11} < -6$ dB frequency band should cover 880–960 MHz and 1710–2170 MHz. However, the S_{21} values are larger than -7 dB at both GSM900 and GSM1800/1900/UMTS bands. Figure 2(b) shows the S -parameters of the antenna with a slot in the middle of the ground plane to decrease the mutual coupling between the two element antennas. The isolation at both lower and higher frequency bands improved to 10 dB, but the upper resonant mode shifted to 2.2 GHz with only about 150 MHz $S_{11} < -6$ dB bandwidth. Additionally, the inserted slot on the ground plane contributes to a new resonance at 1.05 GHz which could be shifted to lower frequency and broaden the lower frequency operating bandwidth by adjusting the length of the slot (L_2). Impedance matching

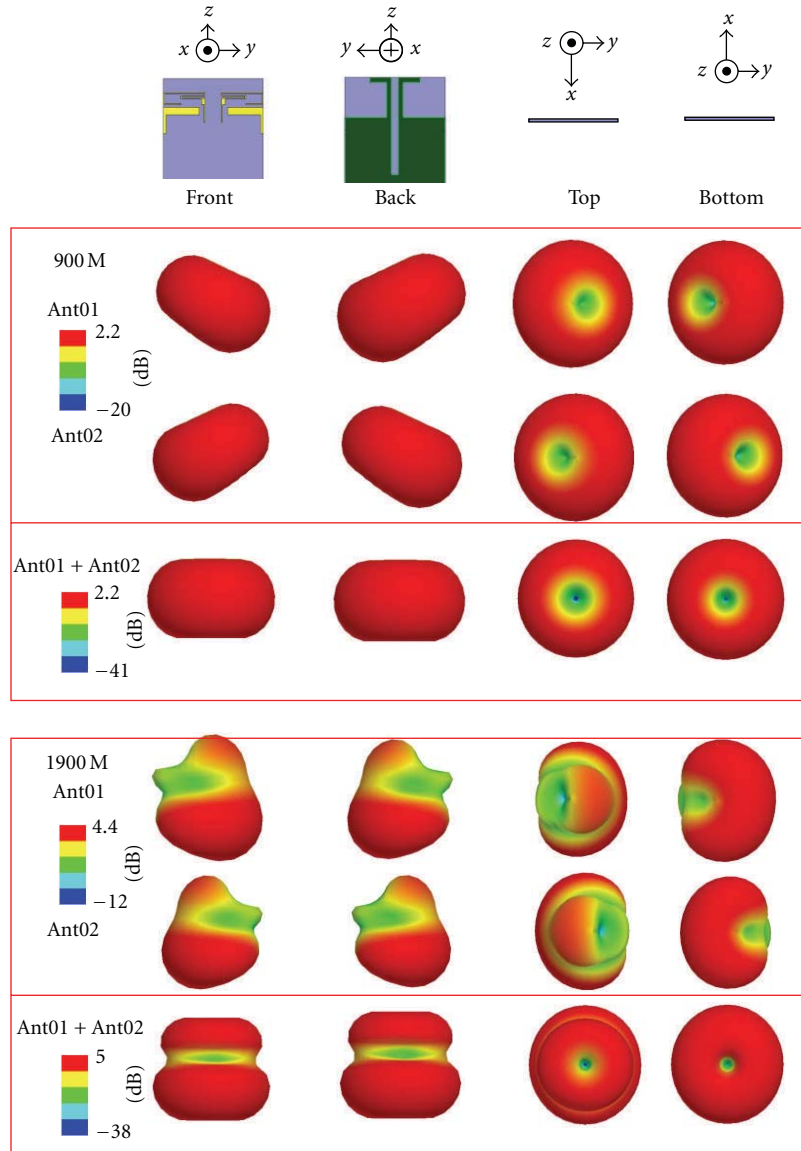


FIGURE 4: Simulated total power 3D radiation pattern of antenna no. 1 and antenna no. 2 at 900 MHz and 1900 MHz.

performance of antenna with dual-inverted-L ground branch is depicted in Figure 2(c). Both the Return Loss and Isolation satisfy the requirements at upper frequency band when dual-inverted-L ground branch was added in the ground. But the dual-inverted-L ground branch structure does not improve Isolation at the lower frequency band. The Isolation maintains 7 dB at about 900 MHz. The Isolation and Return Loss satisfied the requirements at both the upper and lower frequency when two decoupling techniques combined. Figure 2(d) shows the simulated S_{11} and S_{21} curves of the antenna with both slot and dual-inverted-L-shaped ground branch. The $S_{11} < -6$ dB frequency bandwidth covers from 865 MHz to 1100 MHz at lower frequency band and from 1650 MHz to 2190 MHz at upper frequency band. The $S_{21} < -10$ dB frequency band spans from 800 MHz to 965 MHz at lower frequency band and the entire upper frequency band.

All the dimensions that may affect the return Loss and isolation performances of the antenna are examined. Figure 1(a2) shows the dimensions that influence the antenna's return loss and isolation performances. L_1 is the length of the slot, and W_1 is the width of the slot. L_2 is the length of the inverted-L stub's x -direction end section. L_3 represents the extended length of the PCB. Figure 3 shows how all the four dimensions above affect the S -parameters of the antenna while other dimensions did not vary. The nominal values of the four dimensions are $L_1 = 55$ mm/ $L_2 = 15$ mm/ $L_3 = 7.5$ mm/ $W_1 = 4$ mm. It is difficult to choose a set of dimensions to meet the antenna's requirements because S_{11} and S_{21} curves interact with each other at the lower frequency band. A set of dimensions were obtained after studying all the dimensions, $L_1 = 55$ mm/ $L_2 = 15$ mm/ $L_3 = 7.5$ mm/ $W_1 = 4$ mm.

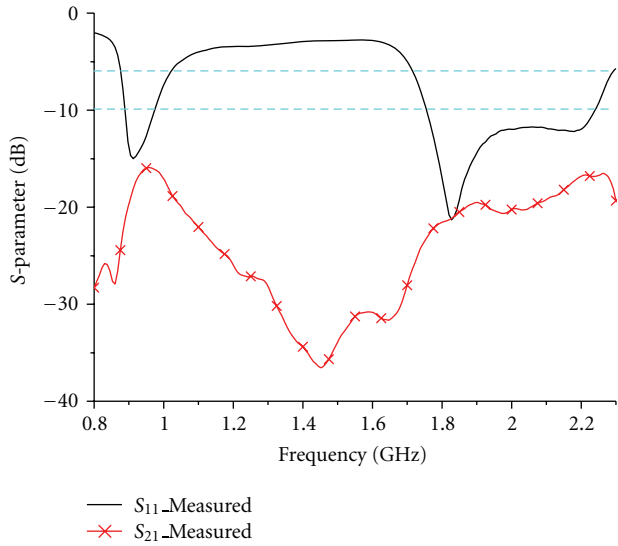


FIGURE 5: Measured S11 and S21 Curves.

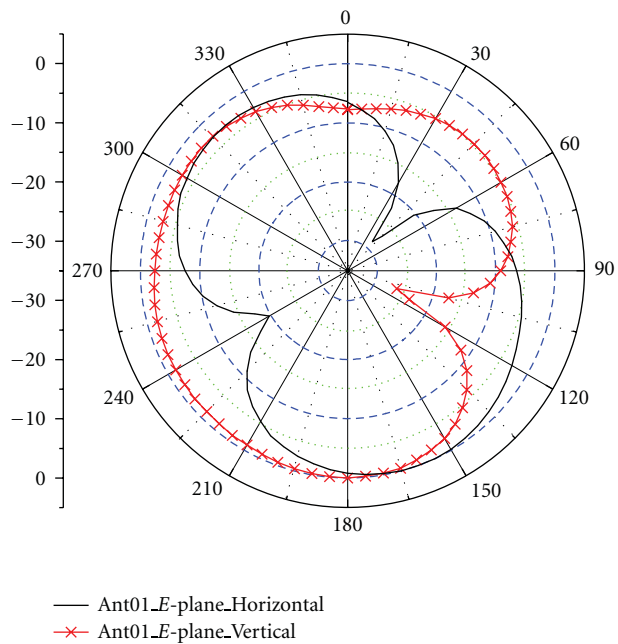


FIGURE 6: Measured E-Plane radiation pattern of antenna no. 1 at 900 MHz.

The simulated three-dimensional (3D) total power radiation patterns at 900 MHz and 1900 MHz of the proposed small-size MIMO antenna are plotted in Figure 4. The radiation patterns are seen from four different directions (front, back, top, and bottom) considering the cases of element antennas work respectively and two element antennas work together. For the lower frequency at 900 MHz, each element antenna generates an oblique dipole-like radiation pattern with the center axes orthogonal to each other. Two bolique dipole-like radiation patterns combined to a unique dipole-like radiation patterns with it center axis directly oriented toward z-axis. The same diversity performance could also be

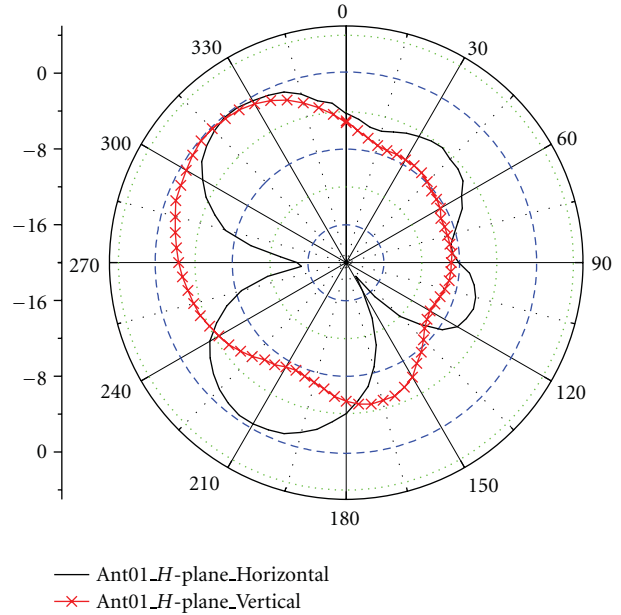


FIGURE 7: Measured H-Plane radiation pattern of antenna no. 1 at 900 MHz.

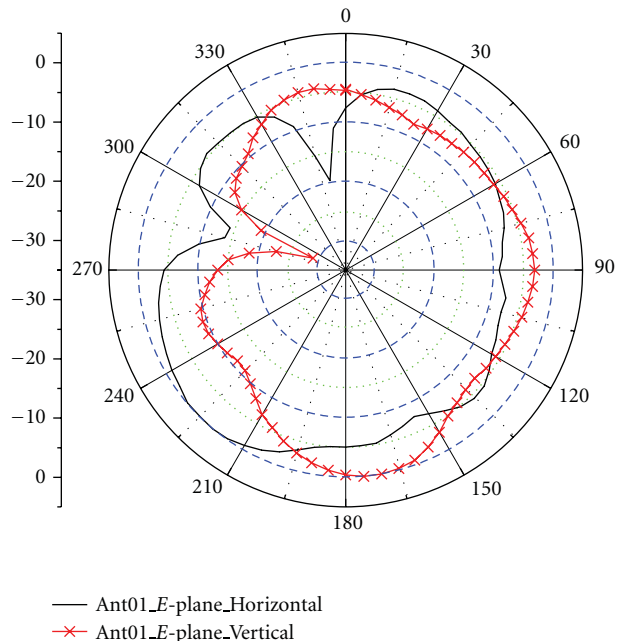


FIGURE 8: Measured E-Plane radiation pattern of antenna no. 1 at 1900 MHz.

seen from the radiation pattern at 1900 MHz. Two radiation patterns with dips and nulls combined to a dual-circle dipole-like radiation pattern with the axis toward z-axis. The diversity characteristic enables the proposed MIMO antenna a promising design for mobile handset applications. The simulated peak gains of the element antennas are about 2.2 dBi at 900 MHz and 4.4 dBi at 1900 MHz.

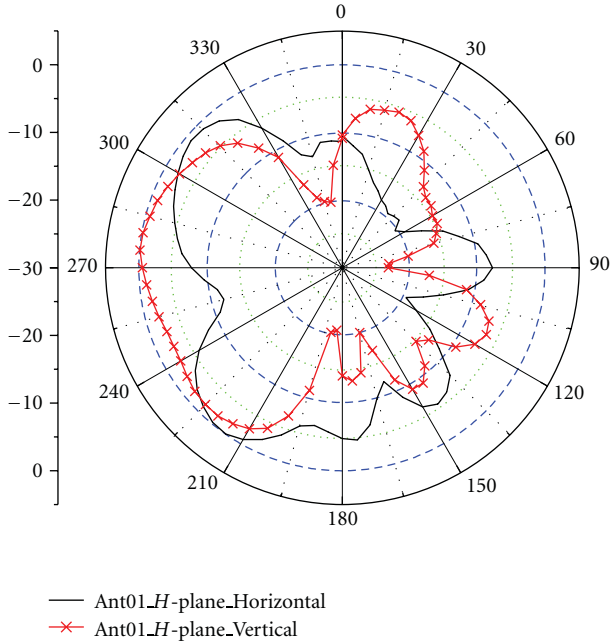


FIGURE 9: Measured H -Plane radiation pattern of antenna no. 1 at 1900 MHz.

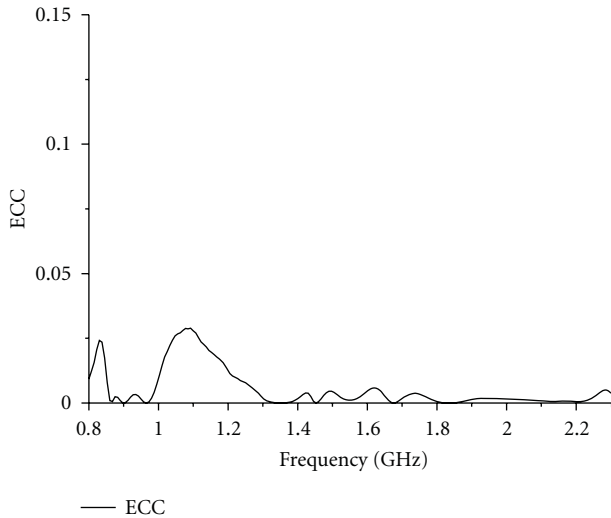


FIGURE 10: Calculated ECC Curve.

4. Measurement Result

The antenna was fabricated and tested in the school of Electronic Engineering of Beijing University of Posts and Telecommunications (BUPT). The S -parameters were measured by a Vector Network Analyzer, and the radiation pattern measurement is carried out inside an anechoic chamber.

The measured S_{11} and S_{21} curves of the antenna are plotted in Figure 5. The $S_{11} < -6$ dB frequency bandwidth covers from 870 MHz to 1010 MHz at lower frequency band and from 1710 MHz to 2290 MHz at higher frequency band. The measured S_{21} values of the MIMO antenna are smaller

than -15 dB over the entire frequency band of 800 MHz–2300 MHz. The return loss and isolation of the antenna fully satisfies the requirement of MIMO antenna operation at GSM900/1800/1900/UMTS.

The 900 MHz and 1900 MHz measured radiation patterns of antenna no. 1 are depicted in Figures 6, 7, 8, and 9. The measured E -Plane and H -Plane radiation patterns of antenna no. 2 are consistent with radiation patterns of antenna no. 1 except a 180-degree rotation because of the exactly symmetrical configuration. Each figure shows the radiation pattern at one frequency including H -plane's (x - y plane)/ E -plane's (x - z plane) horizontal radiation pattern and vertical radiation pattern.

The ECC (envelope correlation coefficient) is usually used to evaluate the diversity capability of a multiantenna system and should ideally be computed using the 3D radiation pattern [20]. Assuming that the antennas will operate in a uniform multipath environment, it can be alternatively calculated by using the scattering parameters. The ECC of two antennas is given by (1) [21]. The calculated envelope correlation coefficient (ECC) curve is plotted in Figure 10 to evaluate the performance of the MIMO antenna. The ECCs of the two element antennas are always below 0.05 over the whole frequency band. This leads to perfect performance in terms of diversity:

$$\rho_{12} = \frac{|S_{11}^* S_{12} + S_{12}^* S_{22}|}{(1 - |S_{11}|^2 - |S_{21}|^2)(1 - |S_{22}|^2 - |S_{12}|^2)}. \quad (1)$$

5. Conclusion

A dual-element small-size printed strip multiple-input and multiple-output (MIMO) antenna was proposed in this paper. The edge-to-edge spacing between the two elements is only $0.03 \lambda_0$ of 920 MHz. A ground plane with a slot and dual-inverted-L-shaped stub were used to decrease the mutual coupling between the element antennas. Antenna performances of with- and without-decoupling techniques were listed. Prototypes were fabricated and measured after parameter optimizations. The measured -6 dB bandwidth are 870 MHz to 1010 MHz and 1710 MHz to 2290 MHz. The isolations are better than 15 dB covering all the frequency band. The simulated and measured radiation patterns of the antenna show good diversity characteristic. The calculated ECCs are below 0.05 over the whole band. The features above proved that the proposed antenna is a promising product for mobile terminals.

The $S_{11} < -6$ dB frequency bandwidth covers from 870 MHz to 1010 MHz at lower frequency band and from 1710 MHz to 2290 MHz at higher frequency band.

Acknowledgment

This work was supported in part by the Fundamental Research Funds for the Central Universities, the National Natural Science Foundation of China under Grant nos.

60703036 and 41040040, and China Important National Science and Technology Specific Project with no. 2009ZX03007-003-01.

References

- [1] Wikipedia, <http://en.wikipedia.org/wiki/LTE>.
- [2] Wikipedia, <http://en.wikipedia.org/wiki/4G>.
- [3] Wikipedia, <http://en.wikipedia.org/wiki/MIMO>.
- [4] J. W. Wallace, M. A. Jensen, A. L. Swindlehurst, and B. D. Jeffs, "Experimental characterization of the MIMO wireless channel: data acquisition and analysis," *IEEE Transactions on Wireless Communications*, vol. 2, no. 2, pp. 335–343, 2003.
- [5] S. C. K. Ko and R. D. Murch, "Compact integrated diversity antenna for wireless communications," *IEEE Transactions on Antennas and Propagation*, vol. 49, no. 6, pp. 954–960, 2001.
- [6] G. J. Foschini and M. J. Gans, "On limits of wireless communications in a fading environment when using multiple antennas," *Wireless Personal Communications*, vol. 6, no. 3, pp. 311–335, 1998.
- [7] Y. Gao, X. Chen, Z. Ying, and C. Parini, "Design and performance investigation of a dual-element PIFA array at 2.5 GHz for MIMO terminal," *IEEE Transactions on Antennas and Propagation*, vol. 55, no. 12, pp. 3433–3441, 2007.
- [8] A. Derneryd and G. Kristensson, "Signal correlation including antenna coupling," *Electronics Letters*, vol. 40, no. 3, pp. 157–159, 2004.
- [9] M. Karakoikis, C. Soras, G. Tsachtsiris, and V. Makios, "Compact dual-printed inverted-F antenna diversity systems for portable wireless devices," *IEEE Antennas and Wireless Propagation Letters*, vol. 3, no. 1, pp. 9–14, 2004.
- [10] Y. Ding, Z. Du, K. Gong, and Z. Feng, "A novel dual-band printed diversity antenna for mobile terminals," *IEEE Transactions on Antennas and Propagation*, vol. 55, no. 7, pp. 2088–2096, 2007.
- [11] S. B. Yeap, X. Chen, J. A. Dupuy, C. C. Chiau, and C. G. Parini, "Low profile diversity antenna for MIMO applications," *Electronics Letters*, vol. 42, no. 2, pp. 69–71, 2006.
- [12] M. Salehi, A. Motevasselian, A. Tavakoli, and T. Heidari, "Mutual coupling reduction of microstrip antennas using defected ground structure," in *Proceedings of the 10th IEEE Singapore International Conference on Communications Systems (ICCS '06)*, pp. 1–5, November 2006.
- [13] C. Y. Chiu, C. H. Cheng, R. D. Murch, and C. R. Rowell, "Reduction of mutual coupling between closely-packed antenna elements," *IEEE Transactions on Antennas and Propagation*, vol. 55, no. 6, pp. 1732–1738, 2007.
- [14] A. C. K. Mak, C. R. Rowell, and R. D. Murch, "Isolation enhancement between two closely packed antennas," *IEEE Transactions on Antennas and Propagation*, vol. 56, no. 11, pp. 3411–3419, 2008.
- [15] S. Zhang, S. N. Khan, and S. He, "Reducing mutual coupling for an extremely closely-packed tunable dual-element PIFA array through a resonant slot antenna formed in-between," *IEEE Transactions on Antennas and Propagation*, vol. 58, no. 8, Article ID 5466048, pp. 2771–2776, 2010.
- [16] H. Bae, F. J. Harackiewicz, M. J. Park et al., "Compact mobile handset MIMO antenna for LTE700 applications," *Microwave and Optical Technology Letters*, vol. 52, no. 11, pp. 2419–2422, 2010.
- [17] M. Han and J. Choi, "Small-size printed strip MIMO antenna for next generation mobile handset application," *Microwave and Optical Technology Letters*, vol. 53, no. 2, pp. 348–352, 2011.
- [18] K. L. Wong, W. Y. Chen, and T. W. Kang, "On-board printed coupled-fed loop antenna in close proximity to the surrounding ground plane for penta-band WWAN mobile phone," *IEEE Transactions on Antennas and Propagation*, vol. 59, no. 3, pp. 751–757, 2011.
- [19] Ansoft Corporation HFSS [online], <http://www.ansoft.com/products/hf/hfss>.
- [20] I. Salonen and P. Vainikainen, "Estimation of signal correlation in antenna arrays," in *Proceedings of the 12th International Symposium Antennas*, vol. 2, pp. 383–386, July 2002.
- [21] S. Blanch, J. Romeu, and I. Corbella, "Exact representation of antenna system diversity performance from input parameter description," *Electronics Letters*, vol. 39, no. 9, pp. 705–707, 2003.

Research Article

Virtual Antenna Array Analysis for MIMO Synthetic Aperture Radars

Wen-Qin Wang

*School of Communication and Information Engineering, University of Electronic Science and Technology of China (UESTC),
Chengdu 611731, China*

Correspondence should be addressed to Wen-Qin Wang, wqwang@uestc.edu.cn

Received 17 July 2011; Revised 9 October 2011; Accepted 18 October 2011

Academic Editor: Wenhua Chen

Copyright © 2012 Wen-Qin Wang. This is an open access article distributed under the Creative Commons Attribution License, which permits unrestricted use, distribution, and reproduction in any medium, provided the original work is properly cited.

Multiple-input multiple-output (MIMO) synthetic aperture radar (SAR) that employs multiple antennas to transmit orthogonal waveforms and multiple antennas to receive radar echoes is a recently proposed remote sensing concept. It has been shown that MIMO SAR can be used to improve remote sensing system performance. Most of the MIMO SAR research so far focused on signal/data models and corresponding signal processing algorithm. Little work related to MIMO SAR antenna analysis can be found. One of the main advantages of MIMO SAR is that the degrees of freedom can be greatly increased by the concept of virtual antenna array. In this paper, we analyze the virtual antenna array for MIMO SAR high-resolution wide-swath remote sensing applications. The one-dimensional uniform and nonuniform linear antenna arrays are investigated and their application potentials in high-resolution wide-swath remote sensing are introduced. The impacts of nonuniform spatial sampling in the virtual antenna array are analyzed, along with a multichannel filtering-based reconstruction algorithm. Conceptual system and discussions are provided. It is shown that high operation flexibility and reconfigurability can be obtained by utilizing the virtual antenna arrays provided by the MIMO SAR systems, thus enabling a satisfactory remote sensing performance.

1. Introduction

Multiple-input multiple-output radar has received much attention in recent years [1–3]; however, little work about MIMO synthetic aperture radar (SAR) has been investigated [4–6]. Note that the MIMO SAR discussed in this paper is different from the general MIMO radars in that aperture synthesis is employed in the MIMO SAR, but no aperture synthesis is employed in general MIMO radars [7]. Although SAR is a well-proven remote sensing application which obtains its high range resolution by utilizing the transmitted wide-band waveform and high azimuth resolution by exploiting the relative motion between the imaged target and the radar platform, current single-antenna SARs cannot provide some specific remote sensing performance, for example, simultaneously high-resolution and wide-swath (the width of the ground area covered by the radar beam) imaging [8, 9]. MIMO SAR provides a solution to resolving these problems.

MIMO ideas are not new, their origin in control systems can be traced back to 1970s [10]. The early 1990s saw an emergence of MIMO ideas into the field of communication systems. More recently, the ideas of MIMO appears in sensor and radar systems. Given that MIMO SAR is in its infancy, there is no clear definition of what it is. It is generally assumed that independent signals are transmitted through different antennas, and these signals, after propagating through the environment, are received by multiple antennas. Unlike conventional phased array radars [11], in MIMO SARs each antenna transmits a unique waveform, orthogonal to the waveforms transmitted by other antennas. In the MIMO SAR receiver, a matched filter-bank is used to extract the orthogonal waveform components. When the orthogonal signals are transmitted from different antennas, the returns of each orthogonal signal will carry independent information about the remote sensing targets. The phase difference caused by different transmitting antennas along with the phase differences caused by different receiving

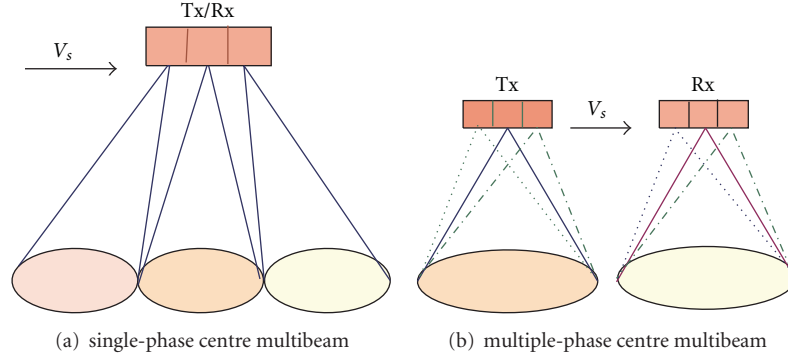


FIGURE 1: Geometry mode of the MIMO SAR antennas.

antennas can form a new virtual antenna array steering vector. With optimally designed antenna array positions, we can create a very long array steering vector with a small number of antennas [12–14]. More importantly, this provides high flexibility and reconfigurability in antenna configuration, thus enabling a flexible and reconfigurable SAR remote sensing performance.

Most of the MIMO SAR research so far focused on signal/data models and corresponding signal processing algorithm [15–17]. Little work related to MIMO radar antenna can be found. The antenna effects on a monostatic MIMO radar for direction estimation were studied in [18] by analyzing the Cramer-Rao low bound (CRLB). Two different uniform linear antenna arrays, one narrowband and the another wideband, were investigated by exploring the CRLB. An iterative algorithm was proposed in [19] to design sparse MIMO radar transmit arrays to approximate a desired transmit beampattern response. Additionally, several minimum redundancy MIMO radars were proposed by other authors [14, 20–22]. In fact, one of the main advantages of MIMO SAR is that the degrees of freedom can be greatly increased by the concept of virtual array provided by the multiple antennas. In this paper, we analyze the virtual antenna array design for MIMO SAR high-resolution wide-swath remote sensing, which has not been investigated in the literature.

The remaining sections are organized as follows. The system principle of the MIMO SAR is described in Section 2. The one-dimensional uniform and nonuniform linear antenna arrays are designed in Section 3. Their application potentials in high-resolution wide-swath remote sensing are also introduced. Next, Section 4 analyzes the impacts of nonuniform spatial sampling in the virtual antenna arrays. Finally, conceptual design system and discussions are provided in Section 5. This paper is concluded in Section 6.

2. MIMO SAR Virtual Antenna Array

There are two kinds of MIMO SAR configuration, as shown in Figure 1. The operation mode of the single phase centre multibeam (SPCM) MIMO SAR system is shown in Figure 1(a). A distinct channel is associated with each of the receive beams, and, hence, the data are split according to azimuth angular position or, equivalently, instantaneous

Doppler frequency centre in the azimuth direction. As a result, given knowledge of the relative squint angles of each beam (hence the Doppler center frequency for each beam) and assuming suitable isolation between the beams, each channel can be sampled at a Nyquist rate appropriate to the bandwidth covered by each narrow beam, instead of that covered by the full beamwidth. This arrangement enables correct sampling of the azimuth spectrum with a pulse repetition frequency (PRF) fitting the total antenna azimuth length, which is significantly smaller than the general PRF requirement.

The multiple phase centre multibeam (MPCM) MIMO SAR system also synthesizes multiple receive beams in the azimuth direction, as shown in Figure 1(b); however, the operating mode of this system is quite different from that of the previous one. In this case, the system transmits multiple broad beams and receives the radar returns in multiple beams which are displaced in the along-track direction. The motivation is that multiple independent sets of target returns are obtained for each transmitted pulse if the distance between phase centres is suitably set. This method basically implies that we may broaden the azimuth beam from the diffraction-limited width, giving rise to improved resolution, without having to increase the system operating PRF.

As noted previously, one of the main advantages of MIMO SAR is that the degrees of freedom can be greatly increased by the concept of virtual array [23]. Figure 2 illustrates a MIMO SAR system. Consider the MIMO SAR system with a transmit array equipped with M colocated antennas and a receive array equipped with N colocated antennas. Suppose both the transmit and receive arrays are close to each other in space (possibly the same array) so that they see targets at same directions.

The MIMO SAR received signal at each receiving antenna is the weighted summation of all the transmitted waveform

$$r_n(t) = \sum_{m=1}^M a_{n,m} s_m(t), \quad m \in [1, 2, \dots, M], \quad (1)$$

$$n \in [1, 2, \dots, N],$$

where $r_n(t)$ is the received signal at the n th antenna, $s_m(t)$ is the transmitted waveform at the m th antenna, and $a_{n,m}$ is the channel coefficient with the m th antenna as input and the

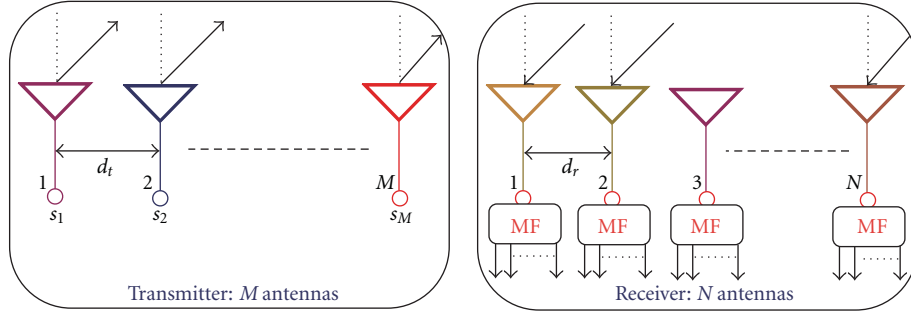


FIGURE 2: Illustration of an example MIMO SAR system.

n th antenna as output. When the transmitted waveforms are designed to be orthogonal

$$\int s_m(t)s_{m'}^*(t)dt = \begin{cases} \delta(t), & m = m', \\ 0, & m \neq m', \end{cases} \quad (2)$$

where $()^*$ denotes a conjugate operator. At each receiving antenna, these orthogonal waveforms can then be extracted by M matched filters. There are a total of $M \times N$ extracted signals. Compared to the traditional phased-array SAR where the same waveform is used at all the transmitting antennas and a total of N coefficients are obtained for the matched filtering, the MIMO SAR gives more coefficients and, therefore, provides more degrees of freedom.

Suppose there are K point targets, the received MIMO SAR signals can be written in a vector form

$$\mathbf{x}(t) = \sum_{k=1}^K \sigma_k (\mathbf{a}^T(\theta_k) \mathbf{s}(t)) \mathbf{b}(\theta_k) + \mathbf{n}(t), \quad (3)$$

where θ_k is the target direction, σ_k is the complex-valued reflection coefficient of the focal point θ_k for the k th point target, $()^T$ is a transpose operator, $\mathbf{n}(t)$ is the noise vector, $\mathbf{a}(\theta_k)$ and $\mathbf{b}(\theta_k)$ are the actual transmit and actual receive steering vectors associated with the direction θ_k . Without loss of generality, we ignore the noise in the following discussions. The SAR returns due to the m th transmitted waveform can be extracted by matched filtering the received signal to each of the waveforms $s_m(t)$

$$\mathbf{x}_m = \int \mathbf{x}(t) s_m^*(t) dt. \quad (4)$$

The $MN \times 1$ virtual target signal vector can then be written as

$$\mathbf{y} = \sigma_s \mathbf{a}(\theta_s) \otimes \mathbf{b}(\theta_s), \quad (5)$$

where \otimes and θ_s denote the Kronker product and the target direction, respectively. Note that here perfect waveform orthogonality is assumed. This equation can be represented by

$$\mathbf{y} = \sigma_s \mathbf{v}(\theta_s), \quad (6)$$

where

$$\mathbf{v}(\theta_s) = \mathbf{a}(\theta_s) \otimes \mathbf{b}(\theta_s) \quad (7)$$

is the $MN \times 1$ steering vector associated with an virtual array of MN sensors.

Suppose the transmitter has M antennas, whereas the receiver has N antennas, (7) means that a virtual antenna array with utmost number of MN nonoverlapped virtual transmitting/receiving elements can be obtained to take full advantages of the MIMO antenna array. Since different antenna array configurations have different spatial sampling characteristics and signal processing complexity, the MIMO SAR antenna array configuration should be optimally designed.

3. Linear Virtual Antenna Array

3.1. Signal Models. Consider a linear transmitting array with M antenna elements and a linear receiving array with N antenna elements. Without loss of any generality, suppose the transmitting and the receiving arrays are parallel and colocated. The m th transmitting antenna is located at $x_{T,m} = (\lambda/2)u_m$ and the n th receiving antenna is located at $x_{R,n} = (\lambda/2)v_n$, where λ is the wavelength. Consider a far-field point target, the transmitter and receiver steering vectors can be represented, respectively, by

$$\begin{aligned} \mathbf{a}(\theta_s) &= [e^{ju_1\pi \sin \theta_s}, e^{ju_2\pi \sin \theta_s}, \dots, e^{ju_M\pi \sin \theta_s}]^T, \\ \mathbf{b}(\theta_s) &= [e^{jv_1\pi \sin \theta_s}, e^{jv_2\pi \sin \theta_s}, \dots, e^{jv_N\pi \sin \theta_s}]^T. \end{aligned} \quad (8)$$

From (7), we can get

$$\mathbf{v}(\theta_s) = \begin{bmatrix} e^{j(v_1+u_1)\pi \sin \theta_s} & e^{j(v_1+u_2)\pi \sin \theta_s} & \dots & e^{j(v_1+u_M)\pi \sin \theta_s} \\ e^{j(v_2+u_1)\pi \sin \theta_s} & e^{j(v_2+u_2)\pi \sin \theta_s} & \dots & e^{j(v_2+u_M)\pi \sin \theta_s} \\ \vdots & \vdots & \dots & \vdots \\ e^{j(v_N+u_1)\pi \sin \theta_s} & e^{j(v_N+u_2)\pi \sin \theta_s} & \dots & e^{j(v_N+u_M)\pi \sin \theta_s} \end{bmatrix}. \quad (9)$$

Note that the amplitude of the signal reflected by the target has been normalized to unity. That is, the target response in the m th matched filtering output of the n th receiving antenna is expressed as

$$v_{m,n}(\theta_s) = e^{j(v_n+u_m)\pi \sin \theta_s}. \quad (10)$$

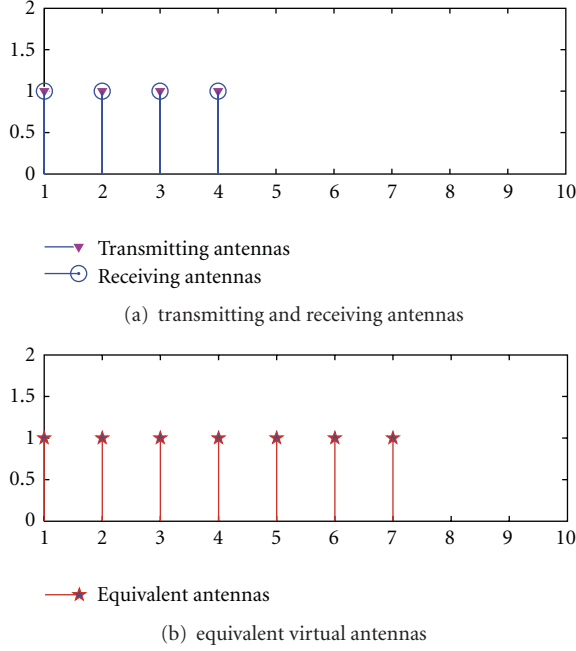


FIGURE 3: Virtual phase centres of the uniform linear array.

It can be noticed that the phase differences are created by both the transmitting antenna locations and the receiving antenna locations. The target response expressed in (11) is the same as the target response received by a receiving array with MN antenna elements located at

$$\{x_{T,m} + x_{R,m}\}, \quad m \in [1, 2, \dots, M], \quad n \in [1, 2, \dots, N]. \quad (11)$$

The phase differences are created by both transmitting and receiving antenna locations. This MN -element array is just the virtual antenna array. An utmost number of MN -element virtual array can be obtained by using only $M + N$ physical antenna elements. It is as if we have a receiving array of MN elements. The virtual antenna array can be seen as a way to sample the electromagnetic wave in the spatial domain. This degree-of-freedom can greatly increase the design flexibility of the MIMO SAR systems.

3.2. Effective Phase Centres. To investigate the effective phase centre caused by the virtual antenna array, in this section we consider several typical linear array configurations for MIMO SAR systems.

3.2.1. Transmitter Is Same to Receiver: $M = N = L$. If the transmitting array and the receiving array are uniform linear arrays, we assume that the first element of $\mathbf{a}(\theta_s)$ and $\mathbf{b}(\theta_s)$, respectively, is the reference element. From (8) and (9), we have

$$\mathbf{a}(\theta_s) = \mathbf{b}(\theta_s) = [1, e^{j\pi \sin \theta_s}, e^{j2\pi \sin \theta_s}, \dots, e^{j(M-1)\pi \sin \theta_s}]^T. \quad (12)$$

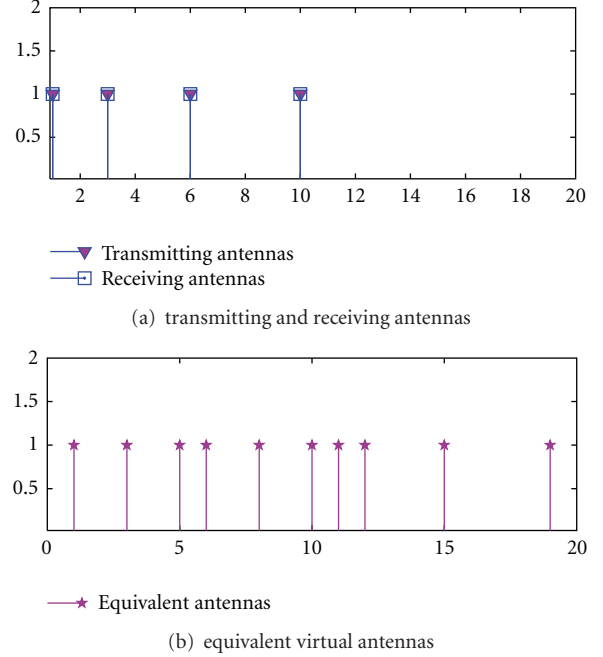


FIGURE 4: Virtual phase centres of the nonuniform linear array.

The equation (11) can then be reexpressed as

$$\mathbf{v}(\theta_s) = \begin{bmatrix} 1 & e^{j\pi \sin \theta_s} & \dots & e^{j(L-1)\pi \sin \theta_s} \\ e^{j\pi \sin \theta_s} & e^{j2\pi \sin \theta_s} & \dots & e^{jL\pi \sin \theta_s} \\ \vdots & \vdots & \dots & \vdots \\ e^{j(L-1)\pi \sin \theta_s} & e^{jM\pi \sin \theta_s} & \dots & e^{j(2L-3)\pi \sin \theta_s} \end{bmatrix}. \quad (13)$$

In this case, the number of effective virtual phase centres is $2L - 1$ with the biggest virtual aperture of $2L - 2$. Suppose $M = N = 4$, Figure 3 shows the corresponding virtual arrays.

If the transmitting array and the receiving array are nonuniform linear array, we can express the steering vector as

$$\mathbf{a}(\theta_s) = \mathbf{b}(\theta_s) = [e^{ju_1\pi \sin \theta_s}, e^{ju_2\pi \sin \theta_s}, \dots, e^{ju_M\pi \sin \theta_s}]^T. \quad (14)$$

In this case, (11) can then be reexpressed as

$$\mathbf{v}(\theta_s) = \begin{bmatrix} e^{j(2u_1)\pi \sin \theta_s} & e^{j(u_1+u_2)\pi \sin \theta_s} & \dots & e^{j(u_1+u_M)\pi \sin \theta_s} \\ e^{j(u_2+u_1)\pi \sin \theta_s} & e^{j(u_2+u_2)\pi \sin \theta_s} & \dots & e^{j(u_2+u_M)\pi \sin \theta_s} \\ \vdots & \vdots & \dots & \vdots \\ e^{j(u_M+u_1)\pi \sin \theta_s} & e^{j(u_M+u_2)\pi \sin \theta_s} & \dots & e^{j(2u_M)\pi \sin \theta_s} \end{bmatrix}. \quad (15)$$

It can be proved that the utmost number of effective virtual phase centres is $L(L+1)/2$. Suppose also $M = N = 4$; Figure 4 shows the corresponding virtual arrays.

3.2.2. Transmitter and Receiver Have No Overlapped Elements. Suppose $M + N = L$; the utmost number of effective virtual phase centres can be determined by $L_v = N(L - N) \leq L^2/4$. For $M = 3, N = 4$, Figure 5 shows two typical virtual arrays, one is uniform linear array and the other is nonuniform linear array.

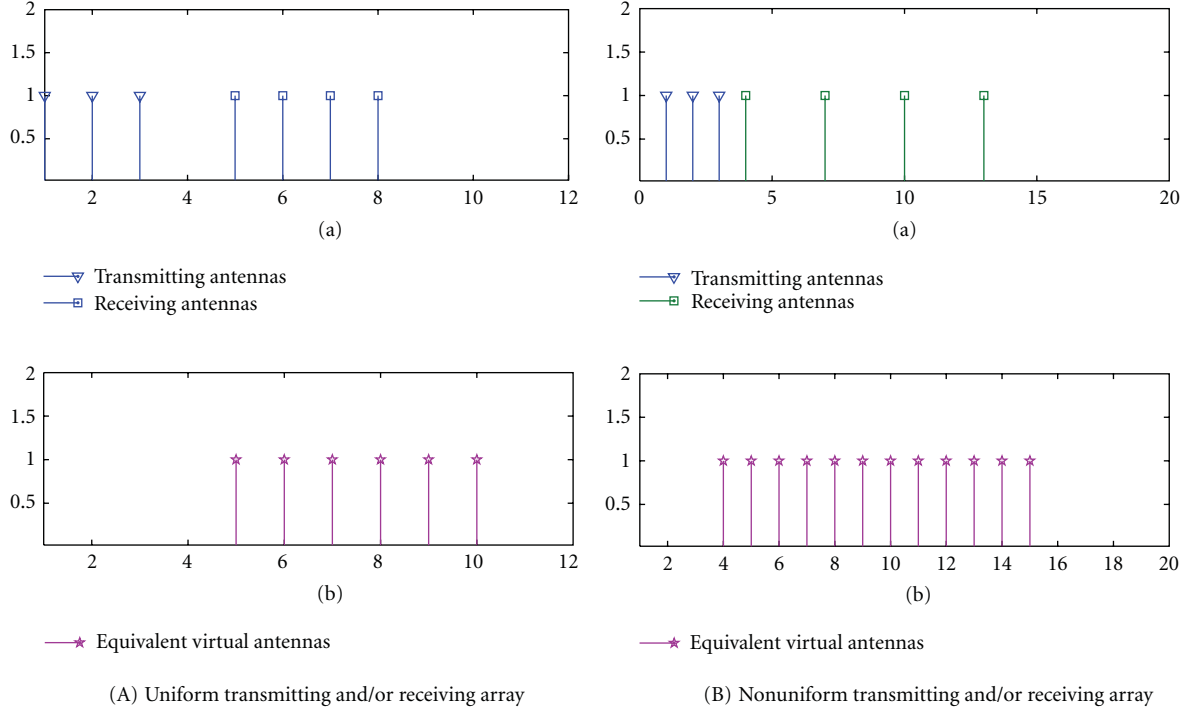


FIGURE 5: The azimuth-variant Doppler characteristics: Case A: using spaceborne transmitter, Case B: using airborne transmitter.

3.2.3. *Transmitter and Receiver Have Overlapped Elements.* Suppose the transmitter and receiver have N_{ov} overlapped elements, the utmost number of effective virtual phase centres is determined by

$$L_v \leq \frac{N_{ov}(N_{ov} + 1)}{2} + (M - N_{ov})(N - N_{ov}). \quad (16)$$

Suppose also $M = 4$, $N = 3$; Figure 6 shows the corresponding virtual arrays.

Comparing the three cases discussed above, we can concluded that the minimum redundant array is obtained when the transmitting array and/or the receiving array are nonuniform linear array.

3.3. *System Performance Analysis.* Future SAR will be required to produce high-resolution imagery over a wide area of surveillance. However, the minimum antenna area constraint makes it a contradiction to simultaneously obtain both unambiguous high azimuth resolution and wide-swath. As well as consideration of antenna beam-width, the actual achievable resolution and swath for a SAR is subject to a number of restrictions imposed by various operating factors. The details can be found in [24, 25]. A basic limitation is the minimum antenna area constraint, which can be represented by

$$A_a \geq \frac{4v_s \lambda R_c \tan \eta}{c_0}, \quad (17)$$

where v_s is the velocity of SAR platform, R_c is the slant range from radar to mid-swath, η is the incidence angle, and c_0

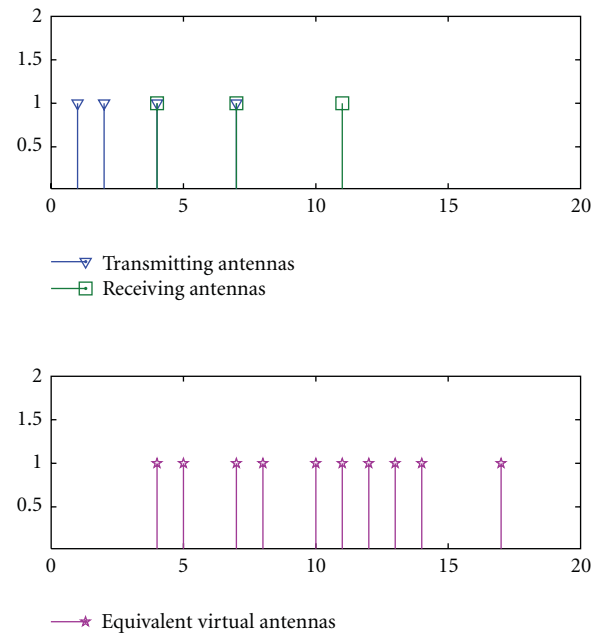


FIGURE 6: Virtual phase centres of the nonuniform linear array.

is the speed of light. This requirement arises because the illuminated area of the ground must be restricted so that the radar does not receive ambiguous returns in range or/and Doppler. In this respect, a high operating PRF is desired for suppressing azimuth ambiguity. But the magnitude of the operating PRF is limited by the range ambiguity requirement.

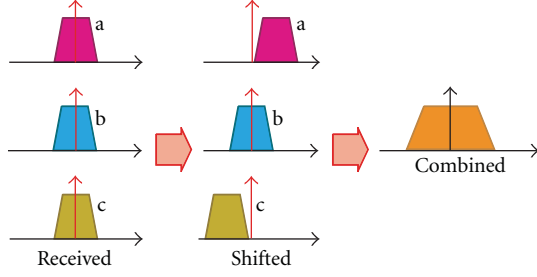


FIGURE 7: Azimuthal spectra synthesis for multichannel subsampling. Here three channels are assumed. It is for illustration only.

The attainment of wide-swath will become increasingly difficult if higher spatial resolution is required, due to the requirement of increased PRF. The MIMO SAR can overcome the minimum antenna area. The virtual effective phase centres enable correct sampling of the azimuth spectrum with a PRF fitting the total antenna azimuth length, which is L_v times smaller than the general PRF requirement. Correspondingly, the area of each antenna is restricted by

$$A_a \geq \frac{4v_s \lambda R_c \tan \eta}{c_0} \cdot \frac{1}{L_v}. \quad (18)$$

Clearly the minimum antenna area is L_v -times smaller than the respective area of a monostatic SAR. Thereafter, the displaced phase center antenna (DPCA) technique [26, 27] can be used to gain additional samples along the synthetic aperture which enables an efficient suppression of azimuth ambiguities, that is, the multiple beams in azimuth allow for the division of a broad Doppler spectrum into multiple narrow-band subspectra with different Doppler centroids. A coherent combination of the subspectra will then yield a broad Doppler spectrum for high azimuth resolution, as shown in Figure 7 [28]. Thus this approach is especially attractive for high-resolution SAR imaging that uses a long antenna for unambiguous wide-swath remote sensing.

For a given range and azimuth antenna pattern, the PRF must be selected such that the total ambiguity noise contribution is enough small relative to the signal. Alternately, given a PRF or range of PRFs, the antenna dimensions should be enough small such that the ambiguity-to-noise ratio specification is met. Thus, the MIMO SAR system performance can be evaluated by the azimuth ambiguity to signal ratio (AASR), which is defined as [29]

$$AASR \approx \frac{\sum_{m=-\infty, m \neq 0}^{\infty} \int_{-0.5B_d}^{0.5B_d} G^2(f + m \cdot PRF) df}{\int_{-0.5B_d}^{0.5B_d} G^2(f) df}, \quad (19)$$

where B_d is the SAR correlator azimuth processing bandwidth, $G(f)$ is the equivalent azimuth transmit-receive antenna pattern, and PRF is the value of PRF.

As an example, we consider only the MIMO SAR configuration in which the transmitter is same to the receiver, for example, the configuration illustrated in Figure 3. Suppose the transmitting antennas synchronize perfectly with the

receiving antennas, the k th antenna beam can be represented by

$$G_k(\theta) = \sin^2 \left(\frac{\pi L_{as} \cos(k \cdot \theta_a)}{\lambda} \sin(\theta - k \cdot \theta_a) \right), \quad (20)$$

where L_{as} is the subantenna length, θ is the antenna beam-width in elevation, and θ_a is the antenna beam-width in azimuth. Note that here the central antenna element is assumed as the reference element. As the 3 dB beam-width can be approximately determined by

$$\theta \approx \frac{\lambda}{2v_s} f, \quad \theta_a = k_a \frac{\lambda}{L_{as}} \quad (21)$$

with k_a a given constant, we can get

$$\begin{aligned} AASR_k(PRF) &= \left\{ \sum_{m=-\infty, m \neq 0}^{\infty} \left[\int_{(i-0.5)B_{ds}}^{(i+0.5)B_{ds}} G_k^2(f + m \cdot PRF) df \right. \right. \\ &\quad \left. \left. + \sum_{j \neq k} \int_{(i-0.5)B_{ds}}^{(i+0.5)B_{ds}} G_k(f + m \cdot PRF) G_j \right. \right. \\ &\quad \left. \left. \times (f + m \cdot PRF) df \right] \right\} \\ &\cdot \left\{ \int_{(i-0.5)B_{ds}}^{(i+0.5)B_{ds}} G_k^2(f) df + \sum_{j \neq k} \int_{(i-0.5)B_{ds}}^{(i+0.5)B_{ds}} G_k(f) G_j(f) df \right\}^{-1}, \end{aligned} \quad (22)$$

where B_{ds} is the Doppler bandwidth of each subantenna.

4. Impacts of Nonuniform Spatial Sampling

As investigated previously, different array configurations have different spatial sampling characteristics and signal processing complexity. A uniform array is desired, so that the complexity of signal processing can be reduced, and the ultimate MIMO SAR image quality can be ensured. To reach this aim, the optimum PRF must be satisfactory with

$$PRF_{uni} = \frac{2v_s}{L_v d_a}, \quad (23)$$

where d_a is azimuth separation between the virtual array elements. This imposes a stringent requirement on the system as it states that to ensure equal spacing between all samples in azimuth the PRF has to be chosen such that the SAR platform moves just one half of its antenna length between subsequent radar pulses. This optimum PRF yields a data array equivalent to that of a single-aperture system operating with $L_v \cdot PRF$. In reverse, any deviation from the relation will result in a nonequally sampled data array along the synthetic aperture that is no longer equivalent to a monostatic signal and cannot be processed by conventional monostatic algorithms without performance degradation.

To analyze the impact of nonuniform displaced phase centre sampling, we consider the received radar returns

$$s_i(t, \tau) \approx \sigma_i [h_0(t) *_{\tau} h_{1,i}(t, \tau)], \quad i = 1, 2, \dots, N, \quad (24)$$

where t is the range fast time, τ is the azimuth slow time, and \ast_t is a convolution operator on the variable t . $h_0(t)$ and $h_{1,i}(t, \tau)$ denote, respectively, the range reference function and azimuth reference function

$$h_0(t) = w_r(t) \cdot \exp(-j\pi k_r t^2), \quad (25)$$

$$h_{1,i}(t, \tau) = \exp\left\{-j\frac{2\pi}{\lambda}\left[R_c(\tau) + R_c\left(\tau + i\frac{d_a}{v_s}\right)\right]\right\} \times w_a(\tau) \cdot \delta\left[\tau - \frac{R_c(\tau) + R_c(\tau + id_a/v_s)}{c_0}\right], \quad (26)$$

where $R_c(t)$ is the equivalent slant range and k_r is the chirp rate of the transmitted waveforms. Note that perfect orthogonal frequency division multiplexing (OFDM) linearly frequency modulation (LFM) waveforms are assumed in this paper. $w_r(t)$ and $w_a(\tau)$ denote the antenna pattern in range dimension and azimuth dimension, respectively. Since

$$R_c(\tau) + R_c\left(\tau + i\frac{d_a}{v_s}\right) \approx 2R_c\left(\tau + i\frac{d_a}{2v_s}\right), \quad (27)$$

we then have

$$s_i(t, \tau) \approx \sigma_i \left[h_0(t) \otimes_i h_1\left(t, \tau + i\frac{d_a}{2v_s}\right) \right]. \quad (28)$$

with

$$h_1\left(t, \tau + i\frac{d_a}{2v_s}\right) = w_a\left(\tau + i\frac{d_a}{2v_s}\right) \cdot \exp\left\{-j\frac{4\pi}{\lambda}R_c\left(\tau + i\frac{d_a}{2v_s}\right)\right\} \cdot \left[\tau - \frac{2R_c(\tau + i(d_a/2v_s))}{c_0}\right]. \quad (29)$$

Equivalently, the nonuniform PRF can be considered as azimuth time drift

$$\tau_{er} = \frac{d_a}{2v_s} - \frac{1}{L_v \cdot \text{PRF}}. \quad (30)$$

After matched filtering and range mitigation correction, we can get

$$\begin{aligned} s_i\left(k\frac{1}{L_v \cdot \text{PRF}}\right) &= w_a\left(k\frac{1}{L_v \cdot \text{PRF}} + i \cdot \tau_{er}\right) \\ &\times \exp\left\{-j\left[2\pi f_d\left(\frac{1}{L_v \cdot \text{PRF}} + i \cdot \tau_{er}\right) + \pi k_a\left(k\frac{1}{L_v \cdot \text{PRF}} + i \cdot \tau_{er}\right)^2\right]\right\}, \end{aligned} \quad (31)$$

where k is an integer, f_d is the Doppler frequency centroid, and k_a is the Doppler chirp rate. It is noticed that the signals are periodic nonuniform with the period of $1/\text{PRF}$. This information is particularly important for developing nonuniform reconstruction algorithms. The impacts of

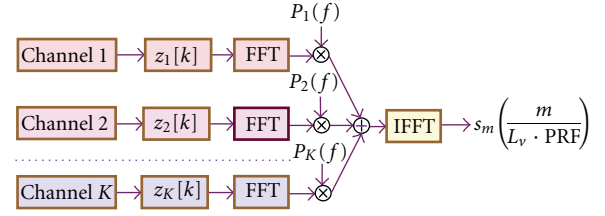


FIGURE 8: Reconstruction filtering for multichannel subsampling in case of three channels.

nonuniform spectral sampling can be evaluated by the following expression [8]:

$$\begin{aligned} s_i(\tau) &= w_a(\tau) \exp(-j\pi k_a \tau^2) \\ &\times \left\{ J_0(2\pi f_d \tau_{er} b_n) \right. \\ &\quad - j2\pi k_d \tau_{er} b_n J_0(2\pi f_d \tau_{er} b_n) \tau \sin\left(\frac{2\pi\tau}{L_v \cdot \text{PRF}}\right) \\ &\quad \left. - 2jJ_1(2\pi f_d \tau_{er} b_n) \sin\left(\frac{2\pi\tau}{L_v \cdot \text{PRF}}\right) \right\}. \end{aligned} \quad (32)$$

The ambiguous Doppler spectrum of a nonuniformly sampled SAR signal can be recovered unambiguously by applying a system of reconstruction filters. The algorithm illustrated in Figure 8 is based considering the data acquisition in the MIMO SAR as a linear system with multiple receiver channels, each is described by a linear filter. The reconstruction consists essentially of multiple linear filters which are individually applied to the subsampled signals of the receiver channels and then combined coherently. The details can be found in [30, 31].

Therefore, the optimal MIMO SAR configuration should have a uniform virtual linear array along the azimuth dimension. Consider a MIMO SAR with an M -element p -spaced transmitting uniform linear array and an N -element q -spaced receiving uniform linear array. According to the proposition discussed in [32]. The virtual array is an effective uniform linear array if and only if $1 \leq \gamma \leq N$ with the ratio coefficient $\gamma = p/q$ or $1 \leq \gamma_0 \leq M$ with $\gamma_0 = 1/\gamma$. Moreover, the virtual array is a nonoverlapped MN -element uniform linear array if and only if $\gamma = N$ or $\gamma = 1/M$.

5. Conceptual System Design and Discussions

To further evaluate the quantitative performance, an example MIMO SAR system is considered. The MIMO SAR operates in X-band with a center frequency of 10 GHz. The geometric ground-range and azimuth resolution are set to $\rho_r = 0.2m$ and $\rho_a = 0.2m$, respectively. To calculate the system performance, an overall loss factor $L_f = 3$ dB, a fixed flying height of 30 km, and a receiver noise figure of $F = 3$ dB are assumed. It is further assumed that the signal bandwidth is adjusted for varying angle of incidence such that the ground-range resolution is constant across the swath. One example system design is provided in Table 1. We can notice that, for the incidence angle given in Table 1 a swath of 18 km

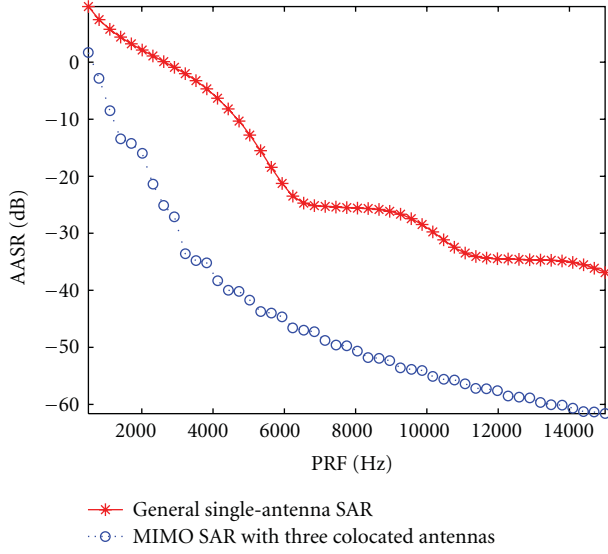


FIGURE 9: Comparative AASR results between conventional single-antenna SAR as a function of PRF.

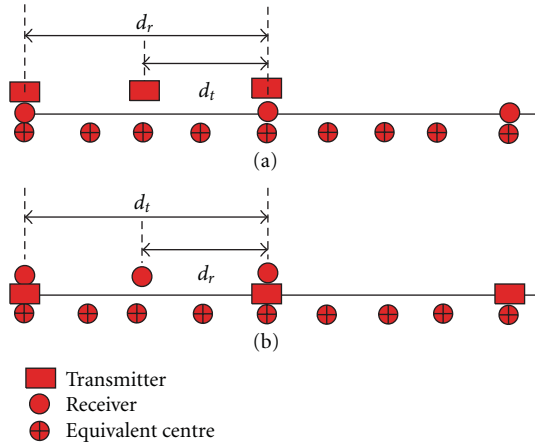


FIGURE 10: Two general linear antenna configurations for MIMO SAR systems.

and a noise equivalent sigma zero (NESZ) of -48 dB can be obtained with a total antenna size not larger than that of current systems. Note that the NESZ is defined as the target radar cross section for which the final SAR image SNR is equal to one (i.e., $\text{SNR}_{\text{image}} = 0$ dB).

It is also worthwhile to compare its AASR performance to conventional single-aperture SAR. Consider again the system parameters listed in Table 1; Figure 9 gives the comparative AASR performance as a function of PRF. In SAR remote sensing applications, AASR is typically specified to be on the order of -20 dB, but a lower AASR is desired. It can be noticed from Figure 9 that the AASR is typically below -20 dB with a low operating PRF requirement. This means that a wider swath can be obtained.

The equivalent virtual antenna pattern can be impacted by the different antenna configurations, even for the same number of equivalent virtual antenna array. Figure 10 shows

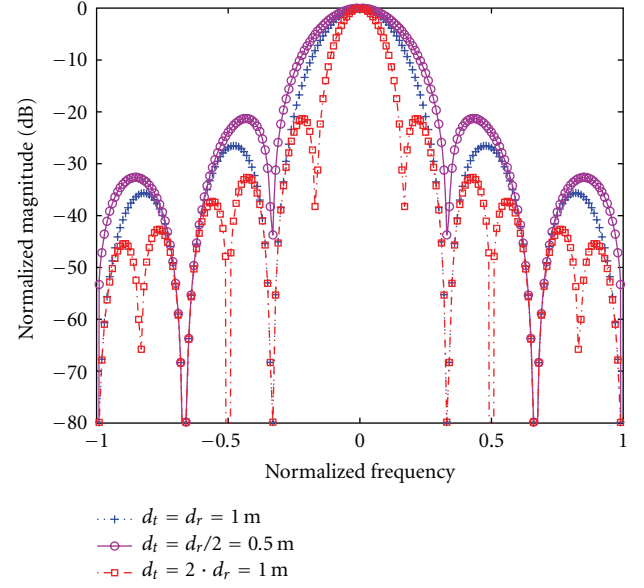


FIGURE 11: Equivalent antenna pattern of the MIMO SAR configurations.

TABLE 1: Performance parameters of an example MIMO SAR system.

Parameters	Variables	Values
Mean transmit power	P_{avg}	10 W
Number of transmitting antennas	M	3
Number of receiving antennas	N	3
Transmit/receive antenna length	L_{as}	0.9 m
Platform altitude	h_s	30 km
Platform velocity	v_s	500 m/s
Incidence angle	η	30°
Antenna width	H_a	0.1 m
Swath width	W_s	12 km
Radiometric resolution	NESZ	-51.16 dB
Incidence angle	η	45°
Antenna width	H_a	0.1 m
Swath width	W_s	18 km
Radiometric resolution	NESZ	-48.52 dB
Incidence angle	η	45°
Antenna width	H_a	0.2 m
Swath width	W_s	9 km
Radiometric resolution	NESZ	-54.54 dB

two general linear antenna configurations, where d_t and d_r denote the distance separation between two neighboring antennas for the transmitter and the receiver, respectively. Figure 11 shows the comparative equivalent antenna patterns for the two antenna configurations. It can be noticed that different equivalent MIMO SAR antenna patterns can be obtained by choosing different array configurations. This provides a potential to develop new GMTI or remote sensing approaches.

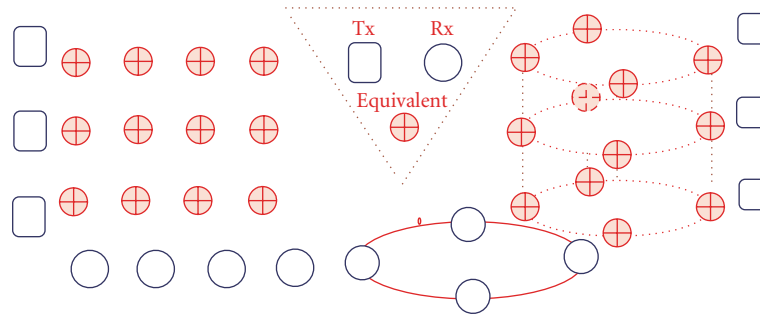


FIGURE 12: Example two-dimensional planar virtual array and three-dimensional cylindrical virtual array.

Another note is that, in this paper, we considered only the one-dimensional linear array. Two-dimensional and three-dimensional phantom element array can also be synthesized midway between each transmitter-receiver pair. Figure 12 shows an example two-dimensional, planar array and a three-dimensional cylindrical array. Note that many other forms of two-dimensional three-dimensional arrays can be obtained in a similar way.

6. Conclusion

MIMO SAR is a recently proposed remote sensing concept. It has been shown that MIMO SAR can be used to improve remote sensing system performance. One of the main advantages of MIMO SAR is that the degrees of freedom can be greatly increased by the concept of virtual antenna array. In this paper, we investigated the virtual linear antenna array for MIMO SAR high-resolution wide-swath remote sensing applications. The impacts of nonuniform spatial sampling in the virtual antenna array are analyzed, along with a multichannel filtering-based reconstruction algorithm. The virtual high-dimensional antenna arrays are also investigated. Conceptual design system is provided, along with the system performance. It is shown that high operation flexibility and reconfigurability can be obtained by utilizing the virtual antenna arrays provided by the MIMO SAR systems, thus enabling a satisfactory remote sensing performance. High-dimensional virtual antenna arrays including two-dimensional planar array and three-dimensional cylindrical array are also discussed, with an aim for further investigations. In a subsequent work, we plan to further investigate the MIMO SAR sparse antenna array design and the corresponding signal processing algorithms to resolve the spatial nonuniform sampling problems.

Acknowledgments

This work was supported in part by the National Natural Science Foundation of China under Grant no. 41101317, the Fundamental Research Funds for the Central Universities under Grant no. ZYGX2010J001, the First Grade of 49th Chinese Post-Doctor Research Funds under Grant no. 20110490143, and the Open Funds of the State Laboratory of Remote Sensing Science, Institute of Remote Sensing

Applications, Chinese Academy of Sciences under Grant no. OFSLRSS201011.

References

- [1] J. Li and P. Stoica, *MIMO Radar Signal Processing*, John Wiley & Sons, New York, NY, USA, 2008.
- [2] J. Li and P. Stoica, "MIMO radar with colocated antennas," *IEEE Signal Processing Magazine*, vol. 24, no. 5, pp. 106–114, 2007.
- [3] A. M. Haimovich, R. S. Blum, and L. J. Cimini, "MIMO radar with widely separated antennas," *IEEE Signal Processing Magazine*, vol. 25, no. 1, pp. 116–129, 2008.
- [4] X. Zhuge and A. G. Yarovoy, "A sparse aperture MIMO-SAR-based UWB imaging system for concealed weapon detection," *IEEE Transactions on Geoscience and Remote Sensing*, vol. 49, no. 1, pp. 509–518, 2011.
- [5] D. Cristallini, D. Pastina, and P. Lombardo, "Exploiting MIMO SAR potentialities with efficient cross-track constellation configurations for improved range resolution," *IEEE Transactions on Geoscience and Remote Sensing*, vol. 49, no. 1, pp. 38–52, 2011.
- [6] W.-Q. Wang, "Space-time coding MIMO-OFDM SAR for high-resolution imaging," *IEEE Transactions on Geoscience and Remote Sensing*, vol. 49, no. 8, pp. 3094–3104, 2011.
- [7] W.-Q. Wang, "Applications of MIMO technique for aerospace remote sensing," in *Proceedings of Aerospace Remote Sensing*, Big Sky, Mont, USA, March 2007.
- [8] W.-Q. Wang, *Multi-Antenna Synthetic Aperture Radar Imaging Theory and Practice*, National Defense Industry Press, Beijing, China, 2010.
- [9] W.-Q. Wang, *Near-Space Remote Sensing: Potential and Challenges*, Springer, Berlin, Germany, 2011.
- [10] R. K. Mehra, "Optimal inout signals for parameter estimation in dynamic systems—survey and new results," *IEEE Transactions on Automatic Control*, vol. 19, no. 6, pp. 753–768, 1974.
- [11] M. Bachmann, M. Schwerdt, and B. Bräutigam, "Accurate antenna pattern modeling for phased array antennas in SAR applications—demonstration on TerraSAR-X," *International Journal of Antennas and Propagation*, vol. 2009, Article ID 492505, 9 pages, 2009.
- [12] D. R. Fuhrmann, J. P. Browning, and M. Rangaswamy, "Signaling strategies for the hybrid MIMO phased-array radar," *IEEE Journal on Selected Topics in Signal Processing*, vol. 4, no. 1, pp. 66–78, 2010.
- [13] A. Hassanien and S. A. Vorobyov, "Phased-mimo radar: a tradeoff between phased-array and mimo radars," *IEEE*

- Transactions on Signal Processing*, vol. 58, no. 6, pp. 3137–3151, 2010.
- [14] C. Y. Chen and P. P. Vaidyanathan, “Minimum redundancy MIMO radars,” in *Proceedings of IEEE International Symposium on Circuits and Systems (ISCAS ’08)*, pp. 45–48, Seattle, Wash, USA, May 2008.
- [15] Y. Lin, B. Zhang, W. Hong, Y. Wu, and Y. Li, “MIMO SAR processing with azimuth nonuniform sampling,” in *Proceedings of IEEE International Geoscience and Remote Sensing Symposium (IGARSS ’10)*, pp. 4652–4655, Honolulu, Hawaii, USA, 2010.
- [16] W.-Q. Wang, Q. Peng, and J. Cai, “Diversified MIMO SAR waveform analysis and generation,” in *Proceedings of the 2nd IEEE Asian-Pacific Conference on Synthetic Aperture Radar (APSAR ’09)*, pp. 270–273, Xi’an, China, October 2009.
- [17] V. K. Ithapu, A. K. Mishra, and R. K. Panigrahi, “Diversity employment into target plus clutter SAR imaging using MIMO configuration,” in *Proceedings of Indian Antenna Week on Advanced Antenna Technology (AAT ’10)*, pp. 1–4, Puri, India, June 2010.
- [18] X. H. Wu, A. A. Kishk, and A. W. Glisson, “Antenna effects on a monostatic MIMO radar for direction estimation, a Cramèr-Rao lower bound analysis,” *IEEE Transactions on Antennas and Propagation*, vol. 59, no. 6, pp. 2388–2395, 2011.
- [19] W. Roberts, L. Xu, J. Li, and P. Stoica, “Sparse antenna array design for MIMO active sensing applications,” *IEEE Transactions on Antennas and Propagation*, vol. 59, no. 3, pp. 846–858, 2011.
- [20] J. Dong, Q. Li, and W. Guo, “A combinatorial method for antenna array design in minimum redundancy MIMO radars,” *IEEE Antennas and Wireless Propagation Letters*, vol. 8, pp. 1150–1153, 2009.
- [21] G. Liao, M. Jin, and J. Li, “A two-step approach to construct minimum redundancy MIMO radars,” in *Proceedings of International Radar Conference-Surveillance for a Safer World*, pp. 1–4, Bordeaux, France, 2009.
- [22] M. Jin, G. Liao, J. Li, and W. Li, “Direction finding using minimum redundancy MIMO radar,” in *Proceedings of IET International Radar Conference*, pp. 1–4, Guilin, China, 2009.
- [23] D. W. Bliss and K. W. Forsythe, “Multiple-input multiple-output (MIMO) radar and imaging: degrees of freedom and resolution,” in *Proceedings of the 37th IEEE Asilomar Conference on Signals, Systems, and Computers*, pp. 54–59, Pacific Grove, Calif, USA, November 2003.
- [24] A. Currie and M. A. Brown, “Wide-swath SAR,” *IEE Proceedings, Part F*, vol. 139, no. 2, pp. 122–135, 1992.
- [25] P. Capece, “Active SAR antennas: design, development, and current programs,” *International Journal of Antennas and Propagation*, vol. 2009, Article ID 796064, 11 pages, 2009.
- [26] A. Bellettini and M. A. Pinto, “Theoretical accuracy of synthetic aperture sonar micronavigation using a displaced phase-center antenna,” *IEEE Journal of Oceanic Engineering*, vol. 27, no. 4, pp. 780–789, 2002.
- [27] P. Lombardo, F. Colone, and D. Pastina, “Monitoring and surveillance potentialities obtained by splitting the antenna of the COSMO-SkyMed SAR into multiple sub-apertures,” *IEE Proceedings: Radar, Sonar and Navigation*, vol. 153, no. 2, pp. 104–116, 2006.
- [28] W.-Q. Wang, “Near-space wide-swath radar imaging with multiaperture antenna,” *IEEE Antennas and Wireless Propagation Letters*, vol. 8, pp. 461–464, 2009.
- [29] F. K. Li and W. T. K. Johnson, “Ambiguities in spaceborne synthetic aperture radar systems,” *IEEE Transactions on Aerospace and Electronic Systems*, vol. 19, no. 3, pp. 389–397, 1983.
- [30] N. Gebert, G. Krieger, and A. Moreira, “SAR signal reconstruction from non-uniform displaced phase centre sampling in the presence of perturbations,” in *Proceedings of IEEE Geoscience and Remote Sensing Symposium*, pp. 1034–1037, Seoul, Korea, 2005.
- [31] G. Krieger, N. Gebert, and A. Moreira, “Unambiguous SAR signal reconstruction from nonuniform displaced phase center sampling,” *IEEE Geoscience and Remote Sensing Letters*, vol. 1, no. 4, pp. 260–264, 2004.
- [32] L. Wang, J. Xu, S. Peng, J. Yuan, and X. Ma, “Optimal linear array configuration and DOF tradeoff for MIMO-SAR,” *Chinese Journal of Electronics*, vol. 20, no. 2, pp. 380–384, 2011.

Research Article

Novel Compact Multiband MIMO Antenna for Mobile Terminal

Cheng Yang,¹ Yuan Yao,¹ Junsheng Yu,¹ and Xiaodong Chen²

¹ School of Electronic Engineering, Beijing University of Posts and Telecommunications, Xi Tu Cheng Road No.10, Haidian District, Beijing 100876, China

² School of Electronic Engineering and Computer Science, Queen Mary, University of London, Mile End Road, London E1 4NS, UK

Correspondence should be addressed to Cheng Yang, chengyang0565@126.com

Received 30 August 2011; Revised 9 October 2011; Accepted 18 October 2011

Academic Editor: Wenhua Chen

Copyright © 2012 Cheng Yang et al. This is an open access article distributed under the Creative Commons Attribution License, which permits unrestricted use, distribution, and reproduction in any medium, provided the original work is properly cited.

A novel compact MIMO antenna for personal digital assistant (PDA) and pad computer is proposed. The proposed antenna is composed by two multipatch monopole antennas which are placed 90° apart for orthogonal radiation. To strengthen the isolation, a T-shaped ground branch with proper dimension is used to generate an additional coupling path to lower the mutual coupling (below -15 dB), especially at GSM850/900 band. The proposed MIMO antenna is fabricated and tested, both the simulated and the measured results are presented, and some parametric studies are also demonstrated. In addition, there are some advantages about the proposed antenna such as simple structure, easy fabrication, and low cost.

1. Introduction

With the rapid development of wireless communication, high data rate is required to improve the quality of information. However, the channel capacity of the conventional single-input, single-output (SISO) communication system is limited according to the Shannon's theorem. To solve this problem and reduce the signal fading in the rich scattering environment without any extra expenditure in power or spectrum, the multiple-input multiple-output (MIMO) communication system has been well developed in the past a few years [1, 2].

The printed monopole antennas are widely used in the MIMO communication systems for their advantages of low cost, easy fabrication, and good performance. To obtain the predicted high signal capacity, the mutual coupling between the antennas in the MIMO communication systems should be low enough, and the high isolation makes uncorrelated signals among the antennas [3]. Usually, low coupling can be obtained by separating the antennas at a distance of half a wavelength or more, but this is impractical in the mobile terminals, so a lot of methods have been studied to reduce the mutual coupling between the closely spaced monopole antennas.

Now many different MIMO antennas consisted of printed monopole antennas have been reported. In [4, 5], a quarter wavelength slot and its deformation are used to reduce the mutual coupling. In [6], parasitic elements are proposed for high isolation. In [7–9], different kinds of ground branches are reported to create an additional coupling path to cancel the original coupling. In [10–13], neutralization technique between antennas is proposed which can neutralize the current of two antennas. In [14, 15], decoupling networks based on lumped elements are adopted to strengthen the isolation between antennas. In [16], metamaterials are used to generate low correlation between antennas. Most of these MIMO antennas are worked at PCS, DCS, UMTS, or WLAN 2.4/5.2 bands with high isolation, but few of them can work at GSM 850/900 band with a strong isolation (below -15 dB) for mobile terminal.

In this paper, we present a novel compact multiband MIMO antenna with isolation enhancement using a T-shaped ground branch for mobile terminal, such as PDA and pad computer. It is consisted of two symmetric printed monopole antennas and covers the GSM850/900, DCS, PCS, UMTS, and LTE2500 band with mutual coupling low enough (below -15 dB). Both the simulated and the measured results

are represented, and the influence of the T-shaped ground branch on the isolation is analyzed.

2. Antenna Design

Figure 1 shows the geometry of the proposed multi-band MIMO antenna printed on a substrate of dimension $125 \times 100 \text{ mm}^2$, which can represent the circuit board of the mobile terminal, such as PDA and pad computer. The substrate of the proposed antenna was chosen as low cost FR-4 material with a thickness of 0.8 mm, 4.4 of dielectric constant, and 0.02 of loss tangent. Ansoft High-Frequency Structure Simulator (HFSS) was used to simulate and optimize the parameters of the proposed antenna.

The antenna is consisted of two orthogonal monopole antennas printed on the top layer of the substrate. The distance between the two monopole antennas is 36 mm which is only about 0.1λ at 850 MHz. The radiated element of the monopole antenna is consisted of a rectangular patch with a folded slot inserted and a parasitic patch. The dimension of the rectangular patch is $33 \times 11 \text{ mm}^2$. The folded slot divides the rectangular patch into two patches, and the inner patch (patch 2) is circled by the outer patch (patch 1). Patch 1 starts from the feed point and follows the folded slot to the open end of the slot while patch 2 starts from feed point to the end of inner patch circled by the folded slot, so the length of patch 1 is much longer than the length of patch 2 which makes patch 1 generate much lower operating band (GSM850/900) compared to the operating band (DCS, PCS, and UMTS) generated by patch 2. To enlarge the high band, a parasitic patch (patch 3) is introduced which works at the LTE2500 band. By adjusting the lengths of the three patches properly, the desired operating bands can be obtained. The lengths of three patches are less than a quarter free wavelength of their own operating bands; this is mainly caused by the effect of the FR-4 substrate which decreases the resonant length of the radiating patches.

A 50 ohm microstrip is used to feed the monopole antenna, which is also printed on the top layer of the substrate. Good impedance match can be obtained without any other match circuit.

The main ground plate of the MIMO antenna is about $85 \times 100 \text{ mm}^2$ and there is a T-shaped branch extending from the main ground plate between the two monopole antennas. Both the T-shaped branch and the main ground plate are printed on the bottom layer of the substrate. The T-shaped branch is consisted of a vertical subbranch and a horizontal subbranch; the widths of the two subbranches are same to simplify the design of the proposed MIMO antenna. To obtain a high isolation, the dimensions of the two subbranches should be properly selected.

3. Simulation and Experimental Results

The proposed antenna shown in Figure 1 was fabricated and measured. The photo of the fabricated antenna is shown in Figure 2.

The simulated and experimental S_{11} and S_{21} parameters which were obtained using an Agilent 8753ES network

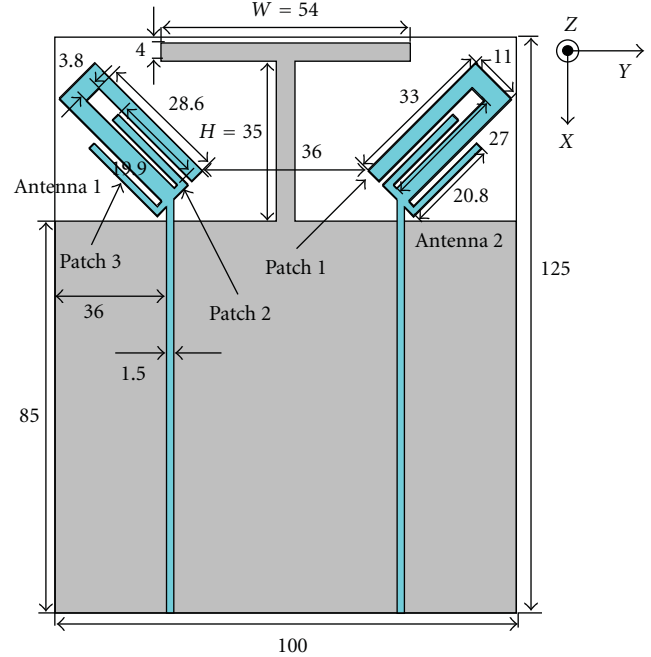


FIGURE 1: Geometry of the proposed multi-band MIMO antenna. (Unit: mm).

analyzer are shown in Figures 3 and 4, respectively. Because of the symmetry of the MIMO antenna, there are only S_{11} and S_{21} shown. The measured results have some discrepancy compared to the simulated results which is probably caused by the manufactured and the measured tolerance. The S_{11} bandwidth of the lowest band determined by VSWR 3:1 is from 0.81 GHz to 1.02 GHz which covers the GSM850 (824–894 MHz)/900 (880–960 MHz) band, and the bandwidth of the middle band is from 1.45 GHz to 2.2 GHz and covers the DCS (1710–1880 MHz), PCS (1850–1990 MHz), and UMTS (1920–2170 MHz) band. On the other hand, the bandwidth of high band caused by the parasitic patch is from 2.39 GHz to 2.8 GHz and satisfies the requirement of LTE2500 (2500–2690 MHz) band. The measured S_{21} parameter in all of these bands is below -15 dB and this value is low enough for mobile terminal. From Figure 4 it can be seen that the isolation between two ports is worse in the lower band than in the higher band, this is mainly because the normalized distance by wavelength between the ports is shorter in the lower band.

The simulated 3D radiation patterns of antenna 1 and antenna 2 at 0.9 GHz, 1.9 GHz, and 2.5 GHz are shown in Figures 5, 6 and 7, respectively. From the results it can be seen that the radiation patterns of the two antennas are orthogonal to each other, so the dual-element MIMO antenna shows good pattern diversity characteristic to overcome the multipath fading and enhance the system performance. The simulated gain in all the bands is high than 0 dB, and the value of the gain has a little difference between antenna 1 and antenna 2. The far field measurements were carried out in an anechoic chamber. When one antenna was measured, the other one was terminated by a 50 ohm load. Figures 8, 9 and 10 show the radiation patterns in the yoZ plane and in the xoZ

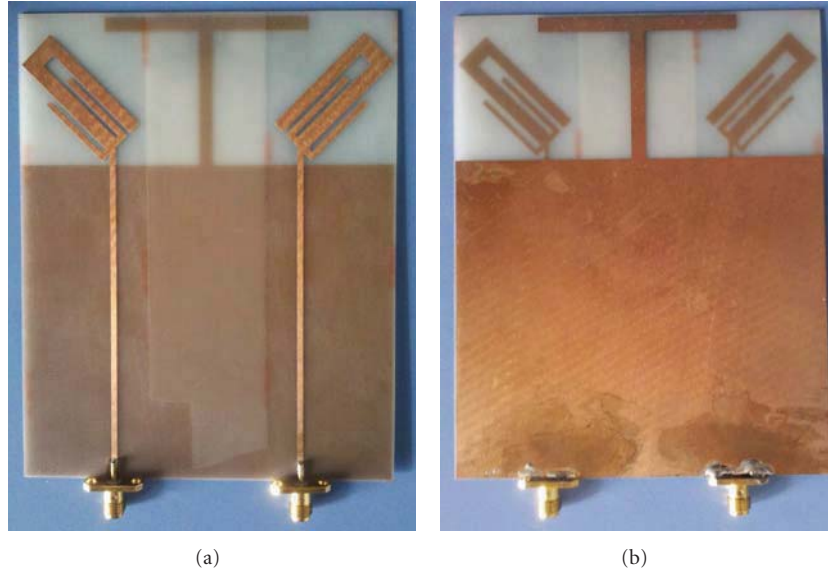


FIGURE 2: Photographs of the fabricated MIMO antenna.

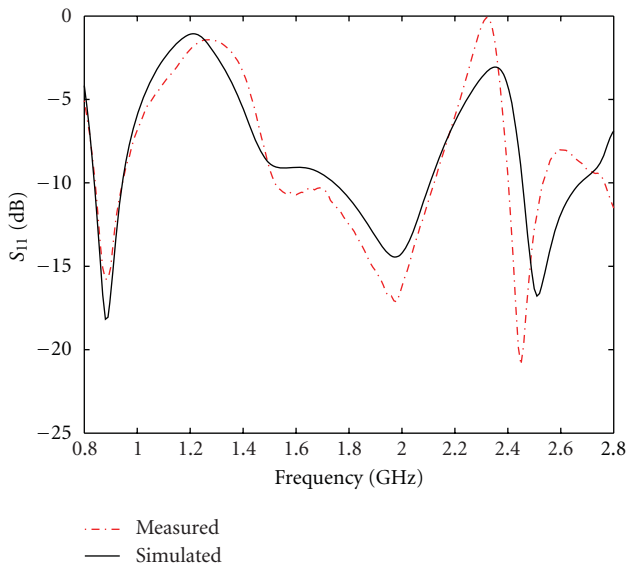


FIGURE 3: Measured and simulated S_{11} of the proposed antenna.

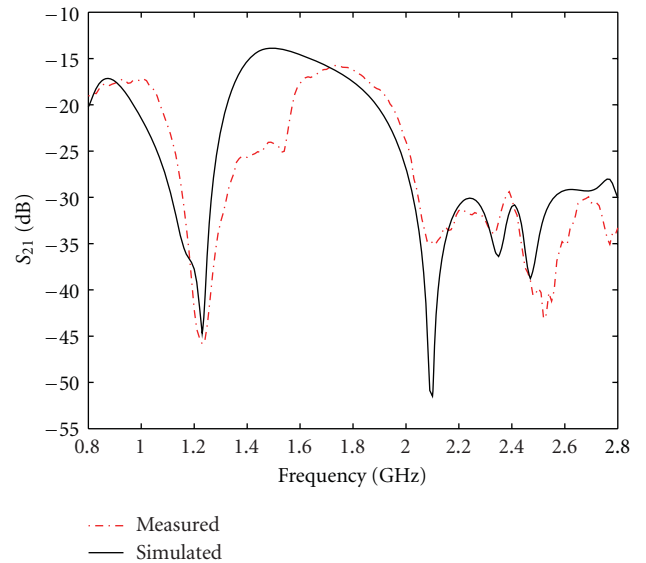


FIGURE 4: Measured and simulated S_{21} of the proposed antenna.

plane at 0.9, 1.9, and 2.5 GHz, respectively. The results also show that the radiation fields of the antenna 1 and antenna 2 are orthogonal. The discrepancy of the patterns between the two antennas is mainly caused by the manufactured and the measured aberration.

Usually, the envelope correlation coefficient is an important parameter to evaluate the diversity characteristic of a multi-antenna system [17]. Low envelope correlation coefficient means high diversity gain. Generally speaking, this value should be less than 0.5 to get a good characteristic of diversity for the mobile terminal application [18]. The envelope

correlation coefficient computed from the measured S parameters is shown as follows [19]:

$$\rho_e = \frac{|S_{11}^* S_{12} + S_{21}^* S_{22}|^2}{[1 - (|S_{11}|^2 + |S_{21}|^2)][1 - (|S_{22}|^2 + |S_{12}|^2)]}. \quad (1)$$

From the measured S parameters, the envelope correlation coefficient was calculated, which is shown in Figure 11. In the GSM850/900 band, the maximum coefficient is 0.005, on the other hand, the maximum coefficients in the middle bands and the LTE2500 band are 0.0127 and 0.001, respectively. The obtained envelope correlation coefficient shows that the proposed antenna is hopeful for MIMO application.

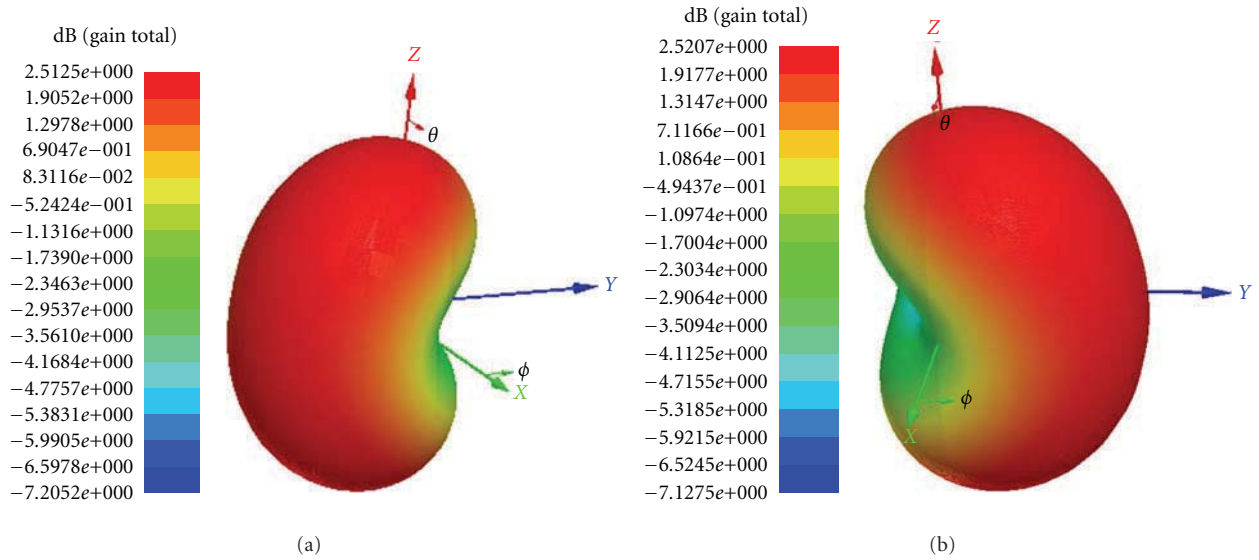


FIGURE 5: Simulated 3D radiation pattern at 0.9 GHz. (a) Antenna 1 excited. (b) Antenna 2 excited.

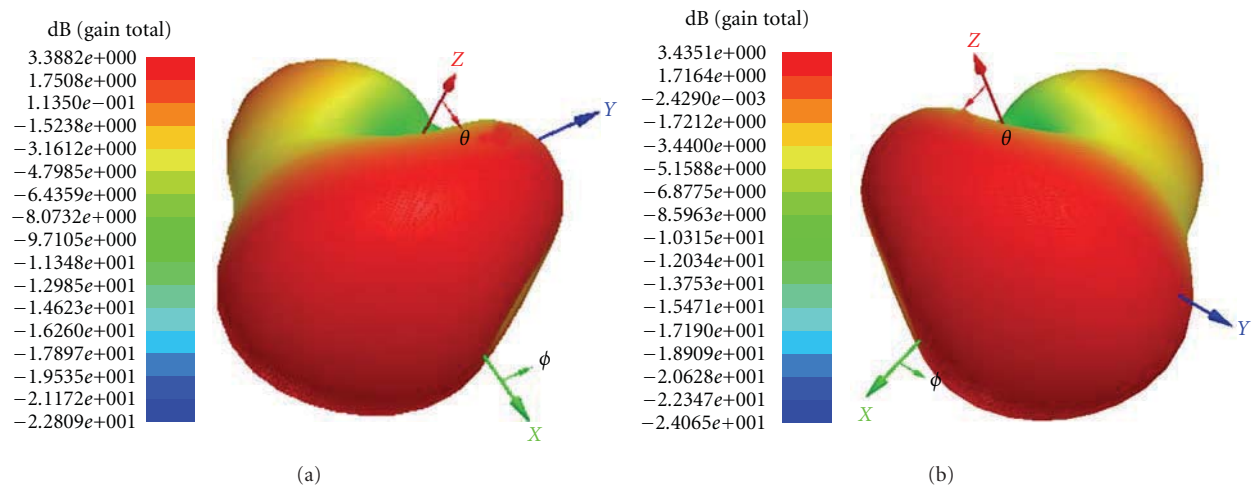


FIGURE 6: Simulated 3D radiation pattern at 1.9 GHz. (a) Antenna 1 excited. (b) Antenna 2 excited.

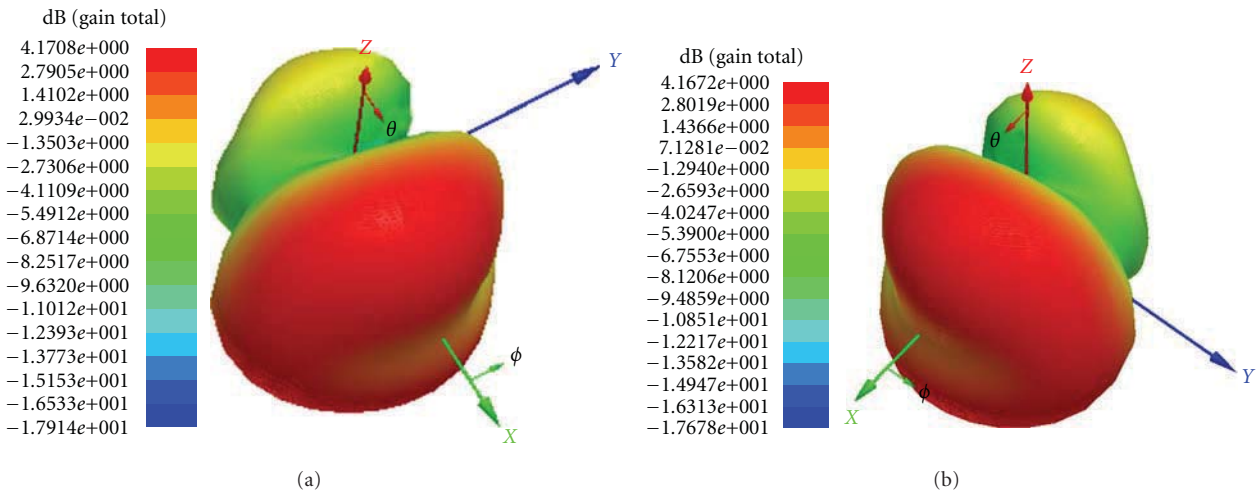


FIGURE 7: Simulated 3D radiation pattern at 2.5 GHz. (a) Antenna 1 excited. (b) Antenna 2 excited.

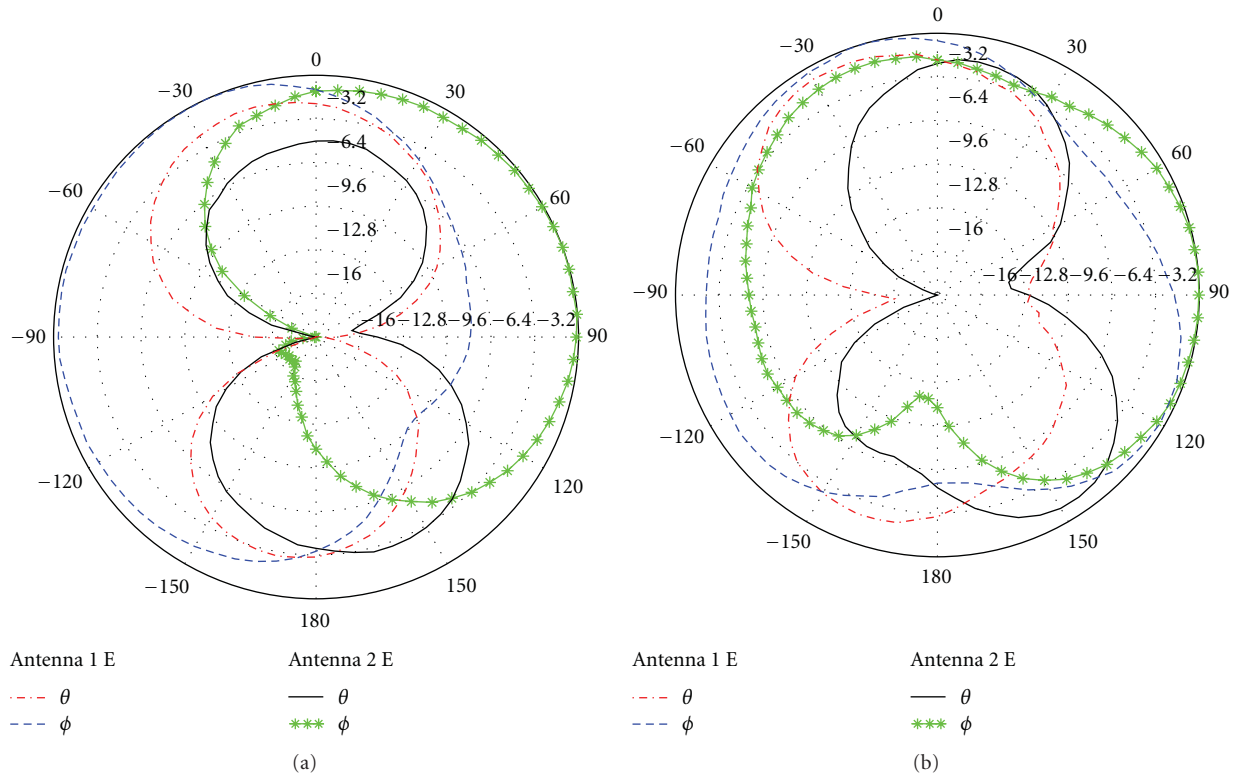


FIGURE 8: Measured radiation pattern at 0.9 GHz. (a) The yoz plane. (b) The xoz plane.

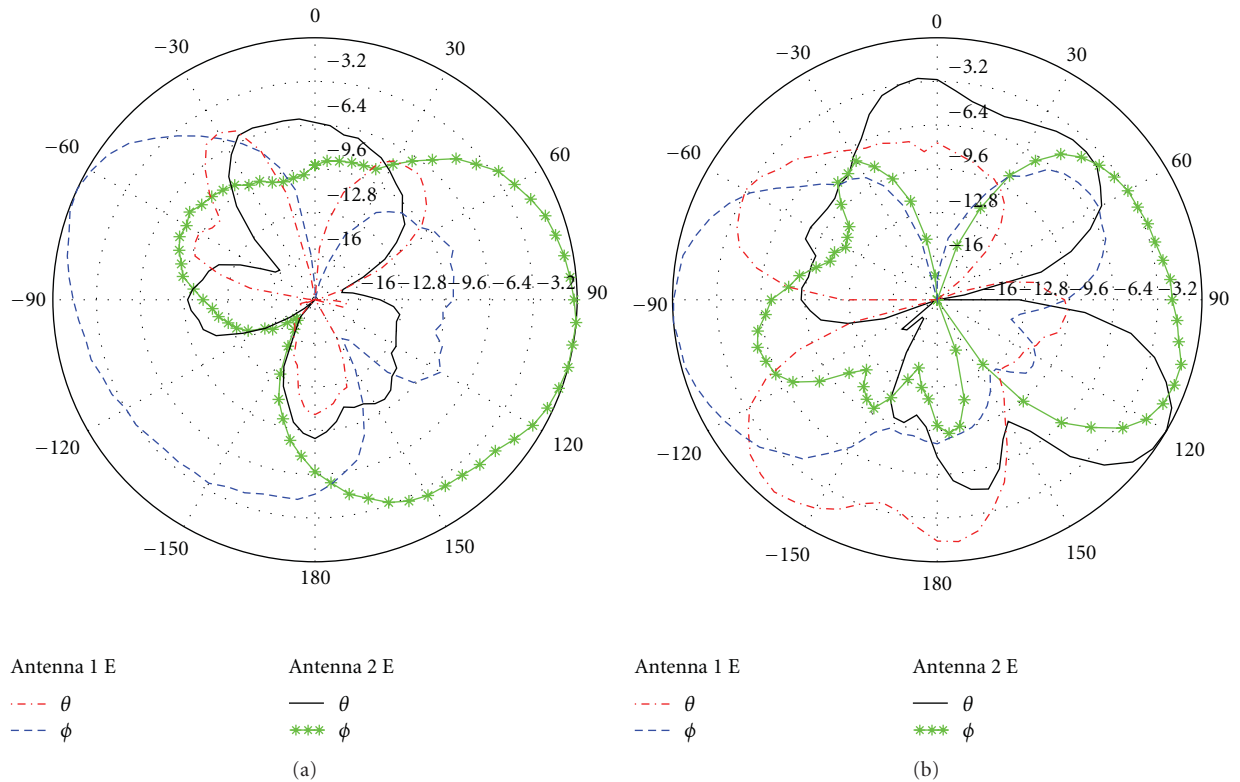


FIGURE 9: Measured radiation pattern at 1.9 GHz. (a) The yoz plane. (b) The xoz plane.

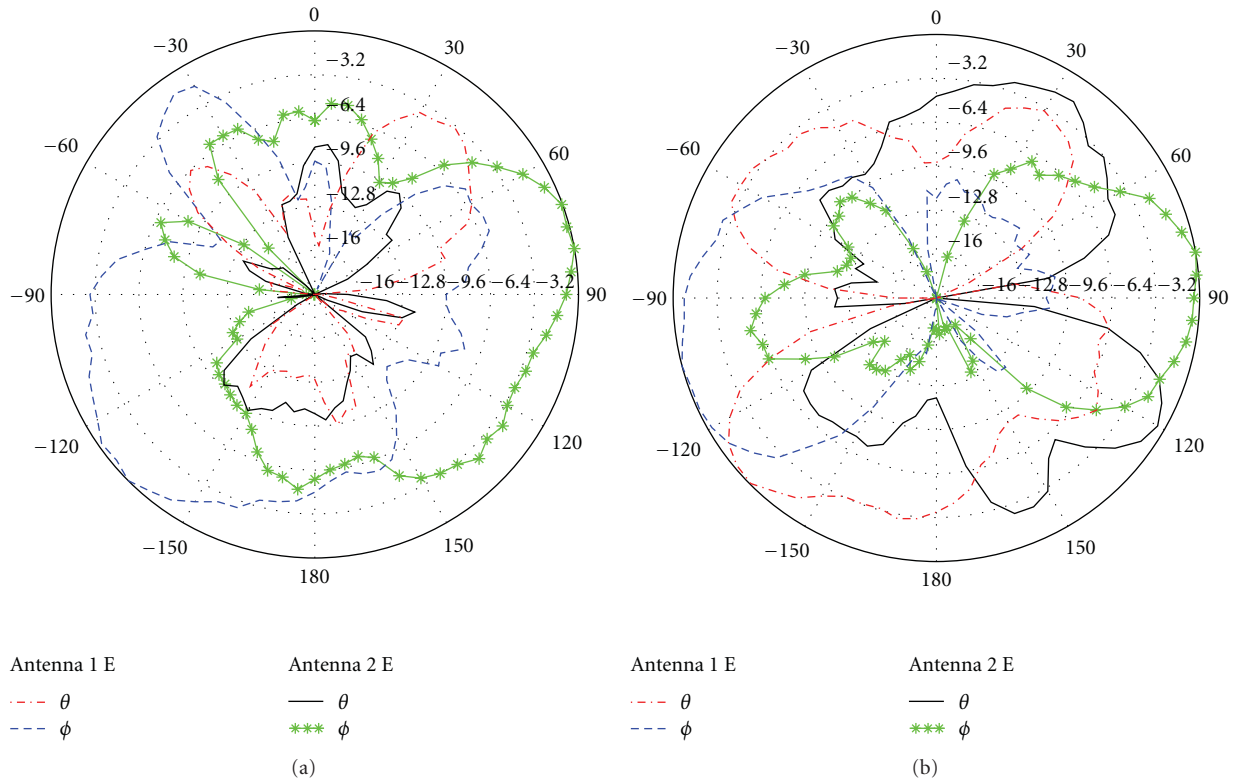


FIGURE 10: Measured radiation pattern at 2.5 GHz. (a) The yoz plane. (b) The xoz plane.

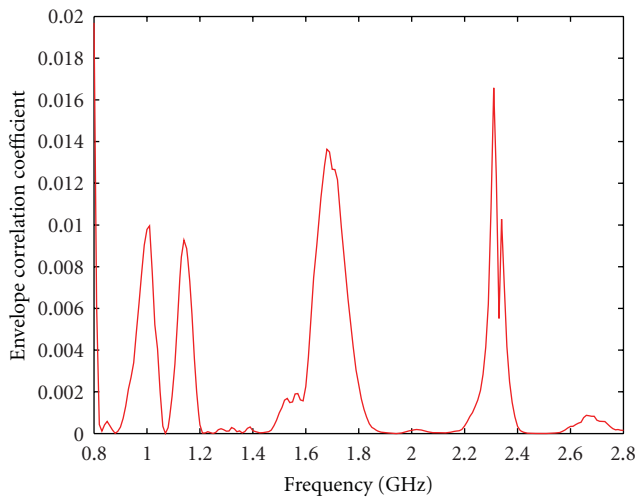


FIGURE 11: Envelope correlation coefficient computed from the measured S parameters.

4. Parametric Studies on Decoupling Element

To further demonstrate the operation of the decoupling element, we have made some parametric studies on the T-shaped ground branch and show the current distribution on the MOMO antenna.

Figure 12 shows the simulated results of the S_{21} parameter of the MIMO antenna with the T-shaped branch or not.

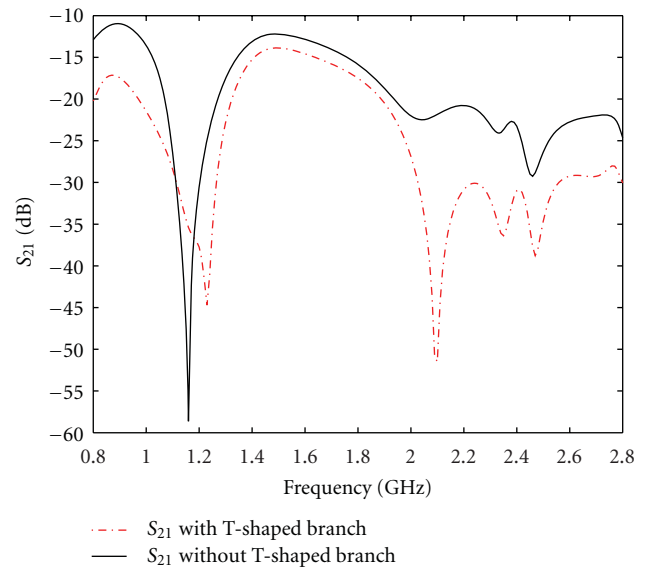


FIGURE 12: Simulated results of S_{21} of the antenna with the T-shaped branch or not.

From the result it can be seen that the mutual coupling between antenna 1 and antenna 2 is greatly improved. With the T-shaped branch, the maximum S_{21} at the GSM 850/900 band is from -11 dB to -17 dB, at the middle band is from -14 dB to -16 dB, and at the LTE2500 band is from -22 dB to -29 dB. With the T-shaped ground branch, the isolation

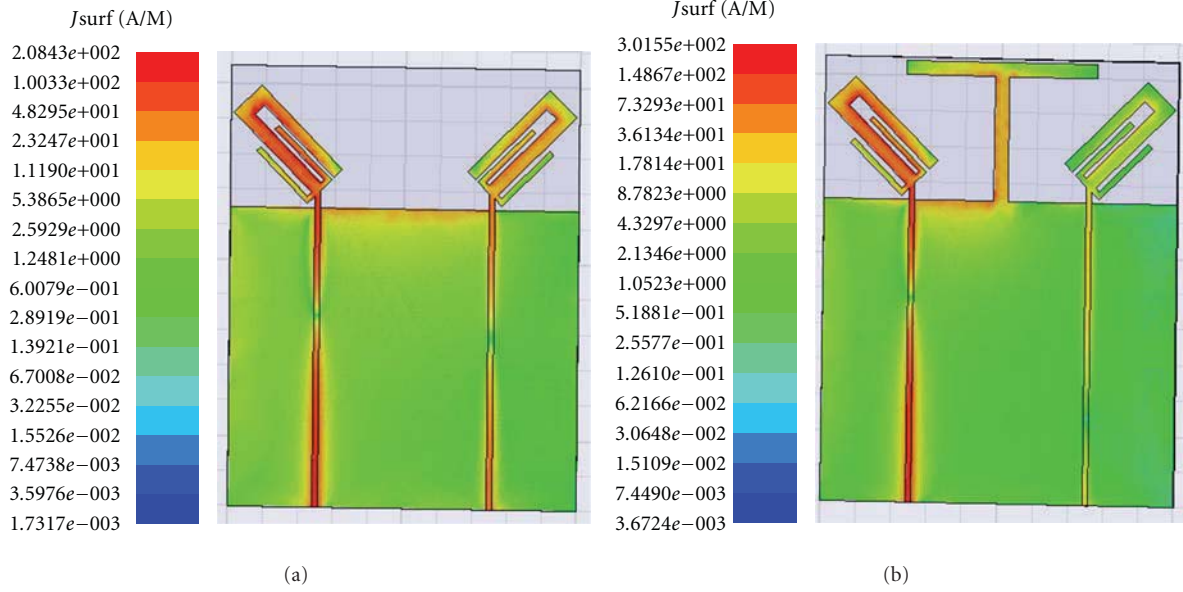


FIGURE 13: Simulated surface current distribution at 0.9 GHz. (a) Without the T-shaped branch. (b) With the T-shaped branch.

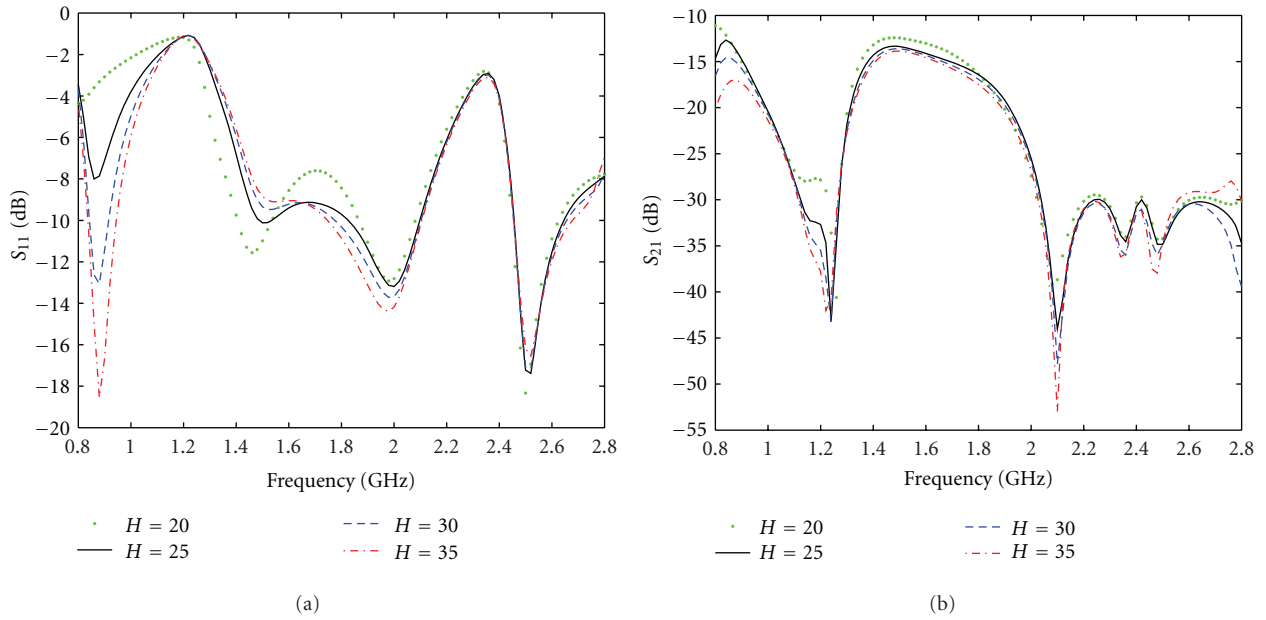


FIGURE 14: Simulated results of S parameters when parameter H varied (Unit: mm). (a) S_{11} . (b) S_{21} .

between the two monopole antennas is strong enough for mobile terminal.

To explain how the T-shaped ground patch reduces the mutual coupling, the surface current distribution is shown. Figure 13(a) shows the surface current distribution on the entire element without the T-shaped branch while antenna 1 is excited. In this case, the surface current induced on the antenna 2 is strong, so the mutual coupling is high. At Figure 13(b), when the T-shaped branch is added to the ground plate, the induced surface current on the antenna 2 is much weaker where the antenna 1 is excited as before, so the mutual coupling is much lower. The reason is that the

antenna 1 induces coupling current on the T-shaped branch and the antenna 2, respectively, and the T-shaped branch also induces coupling current on the antenna 2 where the two induced coupling currents on the antenna 2 are reverse, so the isolation is strengthened.

Figure 14 shows the effect of various values of the parameter H which is shown in Figure 1 on the simulated S_{11} and S_{21} parameters for the proposed MIMO antenna while other parameters are fixed. From the picture it can be seen that the impedance matching is improved and the isolation between the two antennas is strengthened when the value of the parameter H increases, especially at the lower bands. Besides

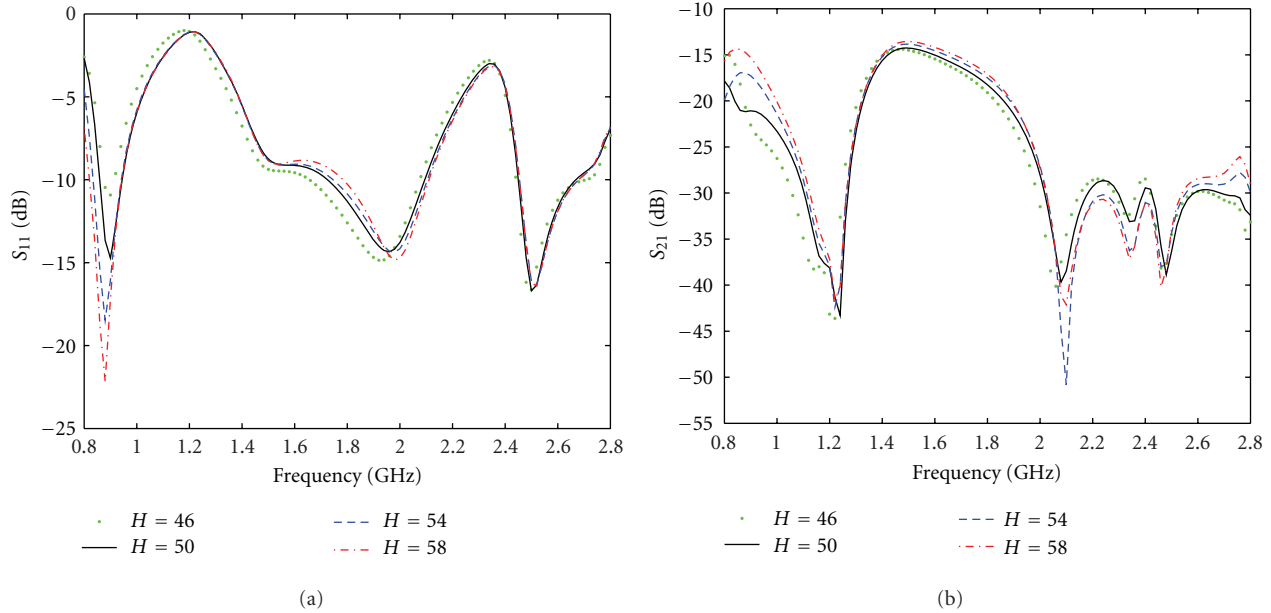


FIGURE 15: Simulated results of S parameters when parameter W varied (Unit: mm). (a) S_{11} . (b) S_{21} .

these, the resonant frequencies are not changed much when the parameter H varies. So the parameter $H = 35$ mm was chosen for the proposed antenna.

The effect of various values of the parameter W on the simulated S_{11} and S_{21} parameters is shown in Figure 15; other parameters are fixed. From the results we can see that the impedance matching is improved when the value of the parameter W increases. For the isolation, there exists an optimal value of W . In this study, when $W = 50$ mm, the mutual coupling between the antennas is lowest in the desired bands. But in this situation, the S_{11} band at GSM850 band is not wide enough, so a trade-off between the bandwidth and the isolation should be made, and we chose $W = 54$ mm for our design.

5. Conclusion

In this paper, a novel compact MIMO antenna for GSM850/900, PCS, DCS, UMTS, and LTE2500 bands has been proposed and studied. The MIMO antenna is consisted of two orthogonal monopole antennas and the monopole antenna is formed by three patches with different lengths. To strength the isolation between the two ports, a T-shaped ground branch between the two monopoles is adopted. Furthermore, the decoupling mechanism of the T-shaped ground branch is proposed, and some parametric studies on the branch have been made to make a good impedance matching and a high isolation. The prototypes of the proposed MIMO antenna have been successfully implemented and good antenna performances have been observed. The return loss (S_{11}) is below -6 dB and the isolation characteristic (S_{21}) is less than -15 dB in all the desired frequency bands, especially at GSM850/900 band. Both the simulated and the measured patterns are given and the orthogonal radiation characteristic

is observed. Moreover, the envelope correlation coefficient of this MIMO antenna is far less than 0.5 which leads to a good diversity characteristic to overcome the multipath fading. The design is simple and constructed with a low cost which is promising for mobile terminal such as PDA and pad computer.

Acknowledgment

The authors wish to acknowledge the support of the Fundamental Research Funds for the Central Universities.

References

- [1] R. D. Murch and K. Ben Letaief, "Antenna systems for broadband wireless access," *IEEE Communications Magazine*, vol. 40, no. 4, pp. 76–83, 2002.
- [2] J. W. Wallace, M. A. Jensen, A. L. Swindlehurst, and B. D. Jeffs, "Experimental characterization of the MIMO wireless channel: data acquisition and analysis," *IEEE Transactions on Wireless Communications*, vol. 2, no. 2, pp. 335–343, 2003.
- [3] T. Svantesson and A. Ranheim, "Mutual coupling effects on the capacity of multielement antenna systems," in *Proceedings of the IEEE International Conference on Acoustics, Speech, and Signal Processing (ICASSP '01)*, pp. 2485–2488, May 2001.
- [4] K. J. Kim and K. H. Ahn, "The high isolation dual-band inverted F antenna diversity system with the small N-section resonators on the ground plane," *Microwave and Optical Technology Letters*, vol. 49, no. 3, pp. 731–734, 2007.
- [5] G. A. Mavridis, J. N. Sahalos, and M. T. Chryssomallis, "Spatial diversity two-branch antenna for wireless devices," *Electronics Letters*, vol. 42, no. 5, pp. 266–268, 2006.
- [6] Z. Li, Z. Du, and K. Gong, "A dual-slot diversity antenna with isolation enhancement using parasitic elements for mobile handsets," in *Proceedings of the Asia Pacific Microwave Conference (APMC '09)*, pp. 1821–1824, December 2009.

- [7] A. C. K. Mak, C. R. Rowell, and R. D. Murch, "Isolation enhancement between two closely packed antennas," *IEEE Transactions on Antennas and Propagation*, vol. 56, no. 11, pp. 3411–3419, 2008.
- [8] Y. Ding, Z. Wu, K. Gong, and Z. Feng, "A novel dual-band printed diversity antenna for mobile terminals," *IEEE Transactions on Antennas and Propagation*, vol. 55, no. 7, pp. 2088–2096, 2007.
- [9] H. Chung, Y. Jang, and J. Choi, "Design of a multiband internal antenna for mobile application," in *Proceedings of the IEEE International Symposium on Antennas and Propagation and USNC/URSI National Radio Science Meeting (APSURSI '09)*, pp. 1–4, June 2009.
- [10] Q. Luo, J. R. Pereira, and H. M. Salgado, "Reconfigurable dual-band C-shaped monopole antenna array with high isolation," *Electronics Letters*, vol. 46, no. 13, pp. 888–889, 2010.
- [11] Q. Luo, H. M. Salgado, and J. R. Pereira, "Printed C-shaped monopole antenna array with high isolation for MIMO applications," in *Proceedings of the IEEE International Symposium on Antennas and Propagation and CNC-USNC/URSI Radio Science Meeting*, pp. 1–4, July 2010.
- [12] I. Dioum, A. Diallo, C. Luxey, and S. M. Farsi, "Dual-band monopole MIMO antennas for LTE mobile phones," in *Proceedings of the ICECom Conference*, pp. 1–4, 2010.
- [13] G. Park, M. Kim, T. Yang, J. Byun, and A. S. Kim, "The compact quad-band mobile handset antenna for the LTE700 MIMO application," in *Proceedings of the IEEE International Symposium on Antennas and Propagation and USNC/URSI National Radio Science Meeting (APSURSI '09)*, pp. 1–4, June 2009.
- [14] S. C. Chen, Y. S. Wang, and S. J. Chung, "A decoupling technique for increasing the port isolation between two strongly coupled antennas," *IEEE Transactions on Antennas and Propagation*, vol. 56, no. 12, pp. 3650–3658, 2008.
- [15] C. Y. Lui, Y. S. Wang, and S. J. Chung, "Two nearby dual-band antennas with high port isolation," in *Proceedings of the IEEE International Symposium on Antennas and Propagation and USNC/URSI National Radio Science Meeting (APSURSI '08)*, pp. 1–4, July 2008.
- [16] C. C. Hsu, K. H. Lin, H. L. Su, H. H. Lin, and C. Y. Wu, "Design of MIMO antennas with strong isolation for portable applications," in *Proceedings of the IEEE International Symposium on Antennas and Propagation and USNC/URSI National Radio Science Meeting (APSURSI '09)*, pp. 1–4, June 2009.
- [17] S. C. K. Ko and R. D. Murch, "Compact integrated diversity antenna for wireless communications," *IEEE Transactions on Antennas and Propagation*, vol. 49, no. 6, pp. 954–960, 2001.
- [18] R. G. Vaughan and J. B. Andersen, "Antenna diversity in mobile communications," *IEEE Transactions on Vehicular Technology*, vol. 36, no. 4, pp. 149–172, 1987.
- [19] S. Blanch, J. Romeu, and I. Corbella, "Exact representation of antenna system diversity performance from input parameter description," *Electronics Letters*, vol. 39, no. 9, pp. 705–707, 2003.

Research Article

Measurement-Based Analysis of Transmit Antenna Selection for In-Cabin Distributed MIMO System

Yan Zhang,^{1,2} Zhenghui Li,^{2,3} Fengyu Luan,^{1,2} Limin Xiao,² Shidong Zhou,¹ and Jing Wang²

¹Department of Electronic Engineering, Tsinghua University, Beijing 100084, China

²Tsinghua National Laboratory for Information Science and Technology, Tsinghua University, Beijing 100084, China

³Department of Communication Engineering, Xiamen University, Xiamen 361005, China

Correspondence should be addressed to Yan Zhang, yanz@tsinghua.edu.cn

Received 31 August 2011; Accepted 10 October 2011

Academic Editor: Yuan Yao

Copyright © 2012 Yan Zhang et al. This is an open access article distributed under the Creative Commons Attribution License, which permits unrestricted use, distribution, and reproduction in any medium, provided the original work is properly cited.

Aircraft seems to be the last isolated island where the wireless access is still not available. In this paper, we consider the distributed multiple-input multiple-output (D-MIMO) system application based on measurements in aircraft cabin. The channel response matrices of in-cabin D-MIMO system are collected by using a wideband channel sounder. Channel capacities with optimum transmit antenna selections (TASs) are calculated from the measured data at different receiver positions. Then the optimum capacity results are compared to those without selection in different transmit SNR. It is shown that the TAS can lead obvious capacity gain, especially in the front and back of cabin. The capacity gain represents a decreasing trend with the transmit SNR increasing. The optimal transmit antenna subset is closely related to the transmit SNR. With the SNR increasing, more transmit antennas will be chosen for higher performance. The subset of those transmit antennas near the receiver is a reasonable choice in practical application of D-MIMO system.

1. Introduction

With the rapid development of wireless communications, subscribers require more convenient access service at any time. Aircraft seems to be the last remaining frontier where the wireless access is still not available [1, 2]. Passengers want to use mobile phones and laptops to meet their business and entertainment requirements in flight. To realize the in-cabin wireless access, one basic work is to investigate the propagation model in the aircraft. Some measurements have been carried out in cabin scenario to analyze the coverage and capacity of wireless systems [2–6]. MIMO (multi-input-multi-output) technology, which can improve the capacity gain and frequency efficiency, has been widely studied. However, only a little research work has been conducted for the in-cabin application of MIMO technique. In [5, 6], the capacity gain has been proved for the in-cabin centralized MIMO system. In this presented paper, we will focus on the distributed MIMO (D-MIMO) channel characteristics. Compared with traditional centralized MIMO system, D-MIMO system can provide higher energy

efficiency and fairer coverage [7, 8]. Especially in cabin scenario, the D-MIMO system could offer the passengers equal wireless service with low power consumption. To our best knowledge, there is still no measurement-based research work on the in-cabin D-MIMO channel.

In practice, access point with more antennas has to employ more radio frequency (RF) units. Then the cost of RF equipments and the complexity of the signal processing will increase too, which limit the MIMO system application. To solve this problem, antenna selection technology is proposed. In MIMO systems, antenna selection is to choose an optimum subset of antennas for communication. It can be classified as transmit (Tx) and receive (Rx) antenna selections. The latter one can reduce receive antenna number and signal processing complexity. Meanwhile, some receive energy will be lost, and the channel rank will not be improved. Thus, the receive antenna selection is unable to lead capacity gain of total MIMO system [9].

In this presented paper, we will emphasize the transmit antenna selection (TAS) impacts on D-MIMO system's capacity in cabin scenario. For D-MIMO channel, because the

transmit antennas are placed with distances, different links suffer diverse shades. Then the TAS can be useful with utilization of the macrodiversity gain. In order to validate the TAS's effect based on measured results, measurement campaigns are carried out in cabin to collect MIMO channel-impulse-response (CIR) matrices. Based on the collected data, the capacities under different antenna selection schemes with fixed total transmit power are analyzed and compared. The results show that, besides the reduction of the complexity and cost, the TAS will lead capacity gain in cabin scenario. The relationship between the signal-to-noise ratio (SNR) and antenna selection scheme is also discussed. Then we present a simple near-optimum selecting way for practical application.

The rest of this paper is organized as follows. In Section 2, the channel sounder and measurement setup are introduced. The D-MIMO channel capacity with TAS is characterized in Section 3. In Section 4, the measurement results are shown to evaluate the TAS performance. Finally, our conclusions are presented in Section 5.

2. Experimental Setup

2.1. THU Channel Sounder. The Tsinghua University (THU) MIMO channel sounder [10] was used to collect raw measured data. It worked at the center frequency of 3.52 GHz with 40 MHz bandwidth, supporting both centralized and distributed MIMO channel measurements. During the in-cabin measurements, the transmitter employed a signal generator to periodically output a linear frequency modulated (LFM) sequence. A microwave switch was used to connect the signal generator with seven transmit antenna ports. Tx antennas were connected to the switch through cables and were distributed in the cabin.

At the receiver side, seven antennas constituted a uniform linear array (ULA) with half-wavelength interelement spacing. The received signal was input to one RF tunnel via another 7-way switch. Then a 7-input 7-output system was realized by adopting this fast time-division-multiplexed switching (TDMS) scheme. The microwave switches were controlled to scan all possible antenna combinations by a synchronization unit.

The major configurations of the THU channel sounder were shown in Table 1. The test signal length t_p was 12.8 μ s. A guard interval t_g was also inserted between adjacent transmission to protect the test signal from the delay spread infection. Then one total snapshot interval was $7 \times 7 \times 2t_p = 1254.4 \mu$ s. The real-time measured data was stored in a server. To obtain the channel parameters of interest, the data processing was finished off line.

2.2. Measurement Environment. Our measurement campaigns are carried out in an MD-82 aircraft. The MD-82 [11] is a short-haul aircraft with 149 seats arranged in 33 rows. The first three rows are the business class and the other rows are the economy class. The dimensions of the cabin are 30.5 m length, 3.34 m width, and 2.05 m height, respectively. The aisle width is 0.5 m, and the distance between rows is 0.7 m. The seat height is 1.16 m above the floor.

TABLE 1: The configurations of THU MIMO channel sounder.

Parameter	Range
Carrier frequency	3.52 GHz
Bandwidth	40 MHz
Tx signal length	12.8 μ s
Snapshot interval	1.2544 ms
Antenna configuration	7×7
Antenna type	Omnidirectional with 4 dBi gain
Polarization	Vertical

As illustrated in Figure 1, seven transmit antennas (Tx1–Tx7) were fixed at different positions. The Tx antenna height was 1.68 m above the floor, and the distance between adjacent Tx antennas was 2.9 m.

The cross-section of the measurement environment was shown in Figure 2. The receiver with centralized antenna array was placed on a dining car. The receiver height was 1.37 m. There are seven Rx antennas (Rx1–Rx7) at the receiver, but in the following analysis only three of them were used. Other elements were used as dummy elements, and their responses were discarded.

During the measurements, the receive array's position was changed along the aisle from the 4th row to the 27th row of the economic class, as the pentagrams shown in Figure 1. At each position, receiver was moved in an 8λ interval back and forth, in order to collect channel data with independent small-scale fading.

3. D-MIMO Capacity with Transmit Antenna Selection

3.1. Distributed MIMO Channel Model. In D-MIMO system, each base station has N distributed antenna ports, each port with V microdiversity antennas. The mobile station's antenna number is M , and then this D-MIMO system can be noted by (N, V, M) [12].

This (N, V, M) D-MIMO channel can be described as

$$\mathbf{H} = [\mathbf{H}_1(d_1), \mathbf{H}_2(d_2), \dots, \mathbf{H}_N(d_N)]_{M \times NV}, \quad (1)$$

where d_i ($i = 1, \dots, N$) is the distance between the i th antenna port to the mobile station. $\mathbf{H}_i(d_i)$ is the $M \times V$ CIR matrix of i th antenna port. If $N = 1$, it becomes a traditional centralized system, and if $V = 1$ a star-shaped D-MIMO. As introduced in Section 2, our channel sounder is a $(7, 1, 7)$ star-shaped D-MIMO system.

3.2. D-MIMO Capacity with Transmit Antenna Selection. Consider a channel is unknown at the transmitter. The capacity of a D-MIMO channel with equally allocated transmit power can be calculated as [9]

$$C = \log_2 \det \left(\mathbf{I}_M + \frac{P_t}{N\sigma^2} \mathbf{H}\mathbf{H}^H \right). \quad (2)$$

Here, \mathbf{H} is the $M \times N$ CIR matrix, whose elements include the pathloss, shade fading, and small-scale fading effects.

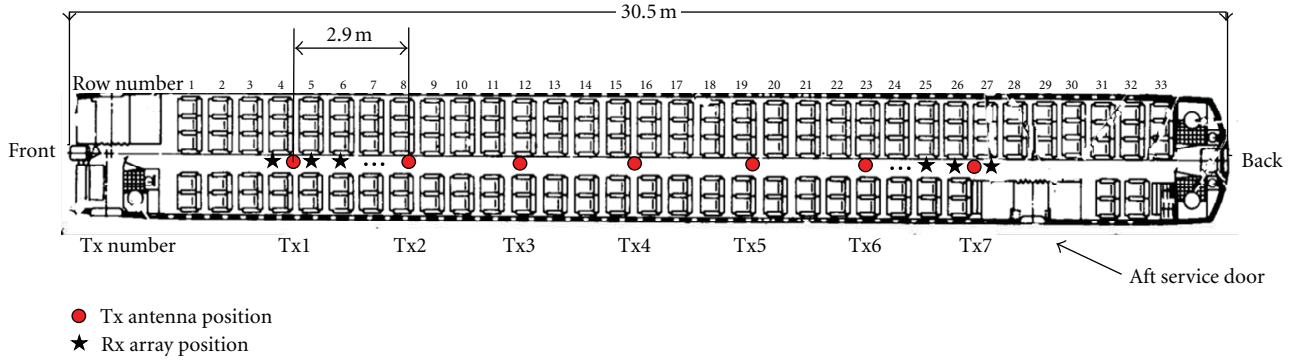


FIGURE 1: Interior arrangement of the measurement environment.

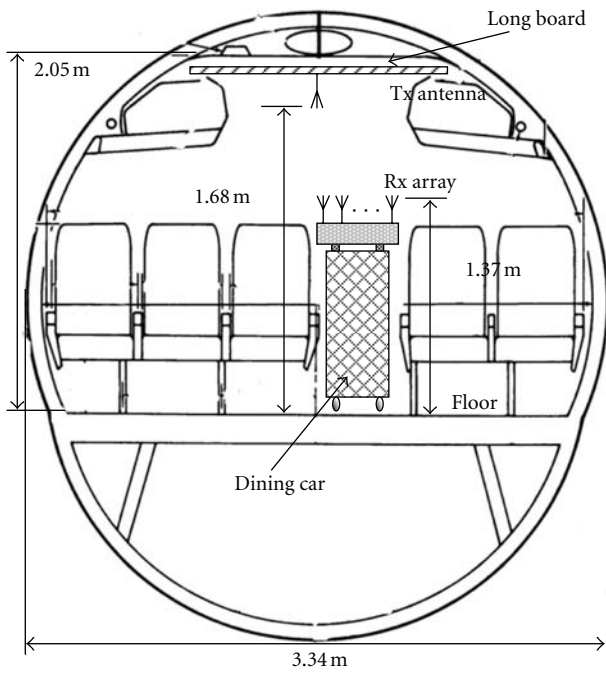


FIGURE 2: Cross-section of the measurement environment.

Then it is not a normalized matrix. N and M are the transmit and receive antenna numbers, respectively. \mathbf{I}_M is an $M \times M$ identity matrix. P_t is the total transmit power and σ^2 is the noise power. Then $\rho_t = P_t/\sigma^2$ is the transmit SNR. Superscript $(\cdot)^H$ denotes the Hermitian transpose.

Two metrics including ergodic capacity and outage capacity are usually used to evaluate MIMO system's performance. The ergodic capacity is corresponding to the average capacity of random channel and will be considered in the following analysis. The ergodic capacity can be computed by

$$C_{\text{ergodic}} = E_{\mathbf{H}} \left\{ \log_2 \det \left(\mathbf{I}_M + \frac{P_t}{N\sigma^2} \mathbf{H}\mathbf{H}^H \right) \right\}. \quad (3)$$

$E_{\mathbf{H}}(\cdot)$ is the average operator. It means that independent channel realizations are needed to obtain the ergodic capacity. For each Rx position's data processing, we consider both

the spatial realizations in 8λ and the frequency realizations in 40 MHz bandwidth.

The objective of TAS is to choose an optimum antenna subset including L antennas to maximize capacity given by

$$C_{\text{sel}} = \max_{\tilde{\mathbf{H}} \in \mathbf{H}} \{C\} = \log_2 \det \left(\mathbf{I}_M + \frac{P_t}{L\sigma^2} \tilde{\mathbf{H}}\tilde{\mathbf{H}}^H \right), \quad (4)$$

where $\tilde{\mathbf{H}}$ is an $M \times L$ subblock matrix of \mathbf{H} .

The capacity gain with antenna selection can be defined as

$$G = \frac{C_{\text{opt}} - C_{\text{no.sel}}}{C_{\text{no.sel}}}. \quad (5)$$

Here, C_{opt} is the ergodic capacity with optimum selection subset. $C_{\text{no.sel}}$ is the capacity without antenna selection; that is, all transmit antennas are employed to send equal power.

4. Measurement Results

4.1. Antenna Selection Effect on Channel Capacity. As mentioned above, the channel sounder is a star-shaped D-MIMO system with seven distributed transmit antennas. The receiver also employs seven Rx antennas as a centralized array. In future wireless systems, limited to the size and cost requirements, three or fewer antennas are practicable for most mobile terminals (e.g., mobile phones). So we only select three receive antennas (Rx3, Rx4, and Rx5) for following analysis. These three antennas are located at the center of the array, and one-wavelength array size is approximately a mobile phone's length. Then we will focus on a (3, 7, 1) D-MIMO system's performance with TAS.

According to (3), firstly the ergodic capacities without antenna selection are extracted from the measured data at 24 different positions. Then the max capacity with TAS is computed by searching all possible antenna selection schemes. To keep the comparison justice, the total transmit power of all Tx antennas is set to be equal for a fair comparison. If less antennas are used, each antenna will radiate more power. As illustrated in Figure 3, TAS can lead obvious capacity gain. Here the transmit SNR is 87 dB, which is corresponding to about 20 dB average receive SNR. For all receiver positions, the gains are between 3% and 14%.

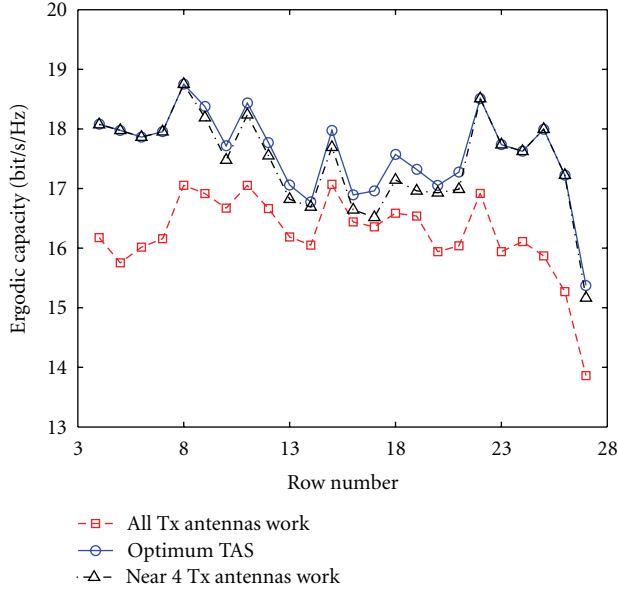


FIGURE 3: Ergodic capacities with different TAS schemes at 24 Rx positions.

This capacity gain is related to the Rx locations. In this cabin scenario, the distributed Tx antennas are arranged in a line. When all transmit antennas work together with equal power, some of them are far from the receiver and energy from these antennas are small. Thus, the receive SNR is lower than that with TAS. For example, at the front and back of the cabin, antennas at the other side are far from the receiver, so the capacity with TAS can be 10% more than that without selection. In the middle of cabin, because the distances between receiver and different Tx antennas are similar, the capacity gain brought by TAS is relatively smaller.

Moreover, in the front or back of the cabin, the macro diversity is smaller than that in the middle. In our previous work [13], we have proved that when Rx is placed in the cabin back (e.g., the 25th row), the signals sent from Tx1 and Tx2 would undergo similar reflection and scattering, which leads to strong spatial correlation between Tx1 and Tx2. Similar thing occurs when receiver is located in the front of cabin. Then the microdiversity effects led by distributed Tx antennas are not large in the front or back of cabin. Comparatively, in the middle the Tx correlations are smaller. Selecting more Tx antennas will increase the channel rank obviously and make the eigenvalues more uniform.

Equation (2) can be rewritten as

$$C = \sum_{j=1}^{\text{rank}(\mathbf{H})} \log_2 \left(1 + \frac{P_t}{N\sigma^2} \lambda_j \right), \quad (6)$$

where $\text{rank}(\mathbf{H})$ is the rank of the CIR matrix \mathbf{H} . λ_j is the j th eigenvalue. According to (6), the improvement of channel rank and min eigenvalue can partly counteract the receive energy loss. Thus, the gap between the two curves is not large when Rx is in the middle.

The capacities measured at the 26th and 27th rows are lower than others. It may be led by the energy leakage because

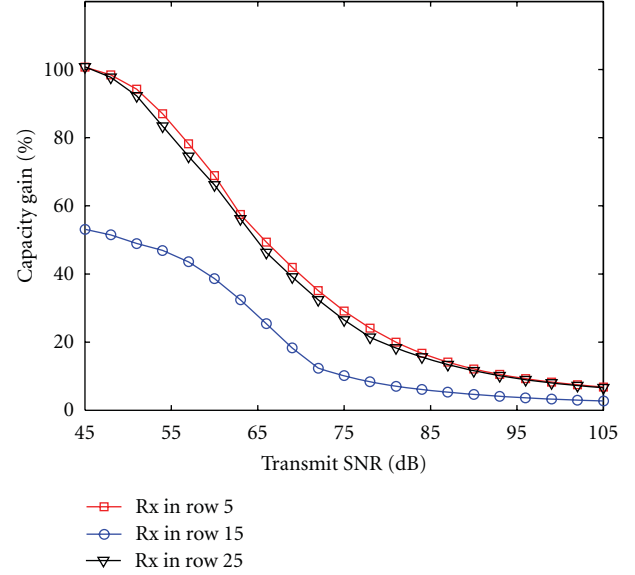


FIGURE 4: TAS capacity gains with different transmit SNRs using Rx3, Rx4, and Rx5.

the Aft service door was always open during measurement campaigns.

In Figure 4, the capacity gains with TAS at different SNRs are illustrated. It can be seen that capacity gain falls with the increase of transmit SNR. Similarly, selecting more transmit antennas will improve the CIR matrix rank. According to (6), with high transmit SNR, larger CIR matrix rank and more uniform eigenvalues can increase the channel capacity without TAS. For practical communication systems, the receive SNR is usually from -5 dB to 20 dB, approximately corresponding to the transmit SNR from 60 dB to 85 dB. In this range, the capacity gain is visible. Also, it can be seen that the capacity gain at the middle is smaller than those at the edges of the cabin.

4.2. Optimum Transmit Antenna Selection Scheme. With different transmit SNRs, the proportions of the optimal antenna number at all 24 positions are shown in Figure 5. It can be seen that with very low SNR, for example, lower than 50 dB, at most positions only one antenna is needed to reach the largest capacity. With the increase of transmit SNR, the smallest eigenvalue of CIR matrix becomes bigger, and then more antennas can provide better performance by leading larger multiplexing effect. In this situation, more antennas can do that. Then the capacity will become larger. However, even with very high SNR, the probability of selecting six or more antennas is very small. In the application of the D-MIMO system, it means that all transmit antennas are not necessary for one passenger's service. Considering the practical receive SNR, the number of the transmitter RF devices can be reduced. In most cases, receiver with three antennas only needs from 2 to 4 transmit antennas.

Then another question is which antenna subset is the optimum one. For seven transmit antennas, there are totally 127 selection schemes. Searching all combinations will

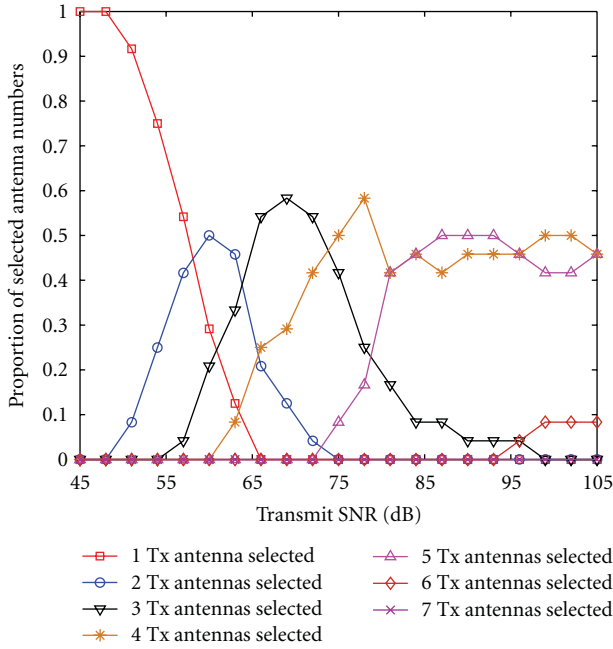


FIGURE 5: The antenna number of optimal TAS subset.

lead high processing complexity. According to the former analysis, we notice that the access distance is quite important for D-MIMO system. Then one near-optimum scheme is to select transmit antennas near the receiver. As an example, in Figure 3 we give the results when using about four transmit antennas. The black dot-dash with triangle marker is corresponding to the ergodic capacity at this case. It can be seen that this TAS scheme's performance is quite close to the optimum one. Then in practical application, we can just select the nearest 2 to 4 antennas to serve the passengers in different rows.

4.3. Results with Larger Receive Array. In the analysis above, we choose Rx3, Rx4, and Rx5 to form a small-size (one-wavelength) receive array. Small array means that there exist high correlations among receive antennas in the long and narrow cabin. The CIR matrix has low rank, and the eigenvalues distribute nonuniformly, especially at the ends of the cabin. In (6), it means that the SNR is the deterministic factor to the channel.

If we consider a larger receive array, including Rx1, Rx4, and Rx7. This array is 3-wavelength long, which is corresponding to a laptop's size. Then Rx correlations are smaller. Choosing more transmit antennas will make the eigenvalues distribute more uniform, which can partly eliminate the loss of energy. Thus in this situation, the capacity gain with TAS will be lower. The measured results also prove that, as shown in Figure 6. Compared with Figure 4, the capacity gain is not larger than 40%. The differences between the middle and edges are not so large as that in Figure 4.

5. Conclusion

The TAS effects on channel capacity of in-cabin D-MIMO system were analyzed by using measured data. The optimum

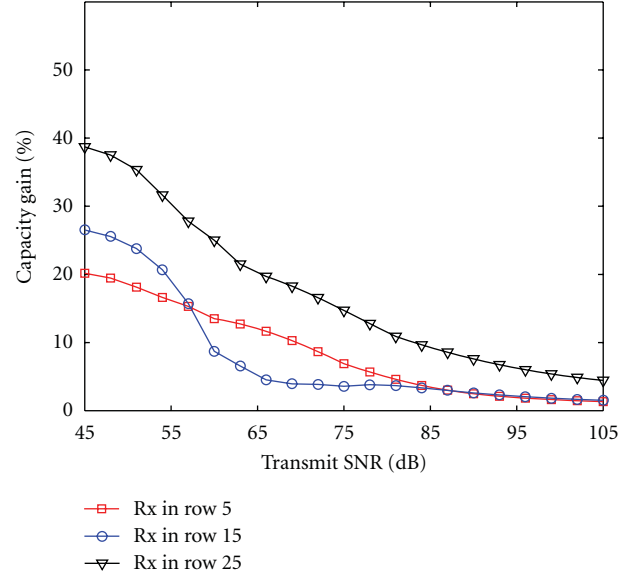


FIGURE 6: TAS capacity gain with different transmit SNR using Rx1, Rx4, and Rx7.

TAS subsets at different Rx positions were found out by searching all possible schemes. Then the ergodic capacity with optimum TAS was compared with that without selection. The results showed that the TAS could lead visible capacity gain, especially in the front and back of the cabin. With the increase of the transmit SNR, the capacity gain decreased. The selected antenna number in the optimum subset also depended on the transmit SNR. With low SNR only few antennas were needed to provide better performance, while in high SNR condition more antennas would lead larger capacity. And in most cases, the optimum selected number was smaller than 5. One practical selection scheme was to choose the Tx antennas near the receiver. For receiver with larger array size, the effects of TAS would become smaller. These results provided practical references to the future distributed MIMO system applications in cabin.

Acknowledgments

This work was partially supported by National Basic Research Program of China (2012CB316002), Tsinghua University Initiative Scientific Research Program (20111081025), China's Major Project (2009ZX03007-003-02), China's 863 Project (2009AA011501), PCSIRT, Tsinghua-Qualcomm Joint Research Program, and China Postdoctoral Science Foundation.

References

- [1] A. Jahn, M. Holzbock, J. Müller et al., "Evolution of aeronautical communications for personal and multimedia services," *IEEE Communications Magazine*, vol. 41, no. 7, pp. 36–43, 2003.
- [2] N. Moraitis, P. Constantinou, F. P. Fontan, and P. Valtr, "Propagation measurements and comparison with EM techniques

- for in-cabin wireless networks,” *Eurasip Journal on Wireless Communications and Networking*, vol. 2009, Article ID 784905, 13 pages, 2009.
- [3] N. R. Díaz and J. E. J. Esquitino, “Wideband channel characterization for wireless communications inside a short haul aircraft,” in *Proceedings of the IEEE 59th Vehicular Technology Conference (VTC '04-Spring)*, pp. 223–228, Milan, Italy, May 2004.
 - [4] A. Kaouris, M. Zaras, M. Revithi, N. Moraitis, and P. Constantinou, “Propagation measurements inside a B737 aircraft for in-cabin wireless networks,” in *Proceedings of the IEEE 67th Vehicular Technology Conference-Spring, VTC*, pp. 2932–2936, Singapore, May 2008.
 - [5] J. R. Nagel, A. M. Richards, S. Ananthanarayanan, and C. M. Furse, “Measured multi-user MIMO capacity in aircraft,” *IEEE Antennas and Propagation Magazine*, vol. 52, no. 4, Article ID 5638282, pp. 179–184, 2010.
 - [6] R. Bhagavatula, R. W. Heath Jr, and S. Vishwanath, “Optimizing MIMO antenna placement and array configurations for multimedia delivery in aircraft,” in *Proceedings of the IEEE 65th Vehicular Technology Conference (VTC2007-Spring)*, pp. 425–429, Dublin, Ireland, April 2007.
 - [7] M. Alatossava, A. Taparugssanagorn, V. Holappa, and J. Ylitalo, “Measurement based capacity of distributed MIMO antenna system in Urban microcellular environment at 5.25 GHz,” in *Proceedings of the IEEE Vehicular Technology Conference (VTC Spring 2008)*, pp. 430–434, May 2008.
 - [8] X. Hu, Y. Zhang, Y. Jia, S. Zhou, and L. Xiao, “Power coverage and fading characteristics of indoor distributed antenna systems,” in *Proceedings of the 4th International Conference on Communications and Networking in China (CHINACOM '09)*, pp. 1–4, Xian, China, August 2009.
 - [9] S. Sanayei and A. Nosratinia, “Capacity of MIMO channels with antenna selection,” *IEEE Transactions on Information Theory*, vol. 53, no. 11, pp. 4356–4362, 2007.
 - [10] Y. Zhang, X. Hu, Y. Jia, S. Zhou, X. Chen, and J. Wang, “A novel coupling-based model for wideband MIMO channel,” in *Proceedings of the Global Telecommunications Conference (GLOBECOM '09)*, pp. 1–6, Honolulu, Hawaii, USA, 2009.
 - [11] <http://www.boeing.com/commercial/airports/m80.htm>.
 - [12] J.-K. Lain, “Joint transmit/receive antenna selection for MIMO systems: a real-valued genetic approach,” *IEEE Communications Letters*, vol. 15, no. 1, pp. 58–60, 2011.
 - [13] Z. H. Li, F. Y. Luan, Y. Zhang, L. M. Xiao, L. F. Huang, and S. D. Zhou, “Capacity and spatial correlation measurements for wideband distributed MIMO channel in aircraft cabin environment,” in *Proceedings of the IEEE Wireless Communications and Networking Conference (WCNC '12)*, Paris, France, 2012.

Research Article

Channel Parameter Estimation for Scatter Cluster Model Using Modified MUSIC Algorithm

Jinsheng Yang, Xuzhao Wu, and Qing Wang

School of Electronic and Information Engineering, Tianjin University, Tianjin 300072, China

Correspondence should be addressed to Jinsheng Yang, jsyang@tju.edu.cn

Received 29 August 2011; Accepted 2 October 2011

Academic Editor: Yan Zhang

Copyright © 2012 Jinsheng Yang et al. This is an open access article distributed under the Creative Commons Attribution License, which permits unrestricted use, distribution, and reproduction in any medium, provided the original work is properly cited.

Recently, the scatter cluster models which precisely evaluate the performance of the wireless communication system have been proposed in the literature. However, the conventional SAGE algorithm does not work for these scatter cluster-based models because it performs poorly when the transmit signals are highly correlated. In this paper, we estimate the time of arrival (TOA), the direction of arrival (DOA), and Doppler frequency for scatter cluster model by the modified multiple signal classification (MUSIC) algorithm. Using the space-time characteristics of the multiray channel, the proposed algorithm combines the temporal filtering techniques and the spatial smoothing techniques to isolate and estimate the incoming rays. The simulation results indicated that the proposed algorithm has lower complexity and is less time-consuming in the dense multipath environment than SAGE algorithm. Furthermore, the estimations' performance increases with elements of receive array and samples length. Thus, the problem of the channel parameter estimation of the scatter cluster model can be effectively addressed with the proposed modified MUSIC algorithm.

1. Introduction

It is important to estimate the spatial/temporal parameters, such as directions of arrival (DOAs), path delays, frequencies, and so forth, embedded in the receive signals in radar, sonar, and wireless communication systems. It also finds applications in source localization, accident reporting, cargo tracking, and intelligent transportation. For example, a precise estimation of DOAs and frequencies of rays in wireless communication channels can helpfully provide better channel information so as to enhance the performance in terms of coverage, capacity, and quality of service (QoS) considerably and increase resistance against interferences. On the other hand, an effective channel model must rely on a realistic characterization of the probability distribution of the relevant channel parameters. So the validation of channel parameter is a prerequisite to ensure that these models reproduce the critical features of the propagation environment, that is, in delay, direction, Doppler, and polarization.

Recently, various high-resolution methods have been proposed in mobile channel to estimate some of the parameters of impinging plane waves, that is, their complex amplitude,

relative delay, incidence azimuth, incidence elevation, and Doppler's frequency. These methods can be grouped into three of the categories [1]: spectral estimation, parametric subspace-based estimation (PSBE), and maximum likelihood estimation (ML). The first mentioning category is the MUSIC (multiple signal classification) algorithm [2]. The ESPRIT (estimation of signal parameter via rotational invariance techniques) [3] and unitary ESPRIT [4] methods are included in the PSBE techniques. Among the ML methods, the expectation-maximization (EM) algorithm and the SAGE (space-alternating generalized EM) algorithm [5] have perfect performance. Especially, SAGE algorithm has been applied for joint delay and azimuth estimation in time-invariant environments as well as for joint delay, azimuth, and Doppler's frequency estimation in time-variant environments.

Unfortunately, the computational burden of the SAGE algorithm is high due to the necessity of nonlinear and multidimensional optimization procedure. Since Swindlehurst proposed several computational efficient algorithms for the estimation of the delays of a multiray channel and solved the spatial signatures (or DOAs) as a least square problem [6],

many algorithms which can estimate the channel parameters by a 2D searching on the DOA-delay domain or DOA-frequency domain have been proposed such as JADE-MUSIC algorithm [7], TST-MUSIC algorithm [8], FSF-MUSIC algorithm [9].

With the development understanding of the wave propagation phenomena, the ray model is not suitable to interpret the parameter estimation results of a channel parameter estimator. This is due to the limited resolution of any wireless channel system. A number of radio channel models based on scatter clusters have been proposed in the literature. Many such models which are referred to as cluster delay line (CDL) models simplify the scattering environment and thereby precisely evaluate the performance of the communication system.

However, the SAGE algorithm did not work for the scatter cluster model because the transmit signals are highly correlated. In this paper, we present a low-complexity, yet high-accuracy, MUSIC-based algorithm, which combines the techniques of temporal filtering and of joint DOA and frequency with two-dimensional (2D) searching. Except for this, there are several other advantages of modified MUSIC algorithm compared with SAGE algorithm, such as the reduction of computation, reduced complexity.

This paper is organized as follows. Section 2 introduces the system model of the fading multiray channels, which assumes the propagation rays to be scatter cluster. In Section 3, we present modified MUSIC algorithm and some related issues. In Section 4, simulation results are presented to verify the performance of the proposed approach. Section 5 comes to the conclusions.

2. System Model

We consider a wireless communication system with M closely spaced receive antennas (Rx), which is equipped with a uniform linear arrays (ULAs), and all the elements are omnidirectional; the interelement spacing at the receive antennas is half a wavelength. Suppose that the signals have a common center frequency of f_0 , then the corresponding wavelength is $\lambda = c/f$, where c is the speed of propagation. Generally, the radio channel in a wireless communication system is often characterized by a multiray propagation model. According to 3GPP SCM model [10], the received signal at the MS consists of D time-delayed multipath replicas of the transmitted signal. These D paths are defined by the same delays which are caused by scatter clusters, and each path consists of K_i ($i = 1, 2, \dots, D$) subpaths. Each subpath represents real ray. The total ray is $K = K_1 + K_2 + \dots + K_D$. So, the output of the each element at the receive antennas (Rx) can be written as

$$x(t) = \sum_{d=1}^D \sum_{k=1}^{K_d} \alpha(\theta_{dk}) e^{j2\pi f_{dk} t} s(t - \tau_d), \quad (1)$$

where $\alpha(\theta_{dk}) = \exp\{j2\pi d_m \sin(\theta_{dk})/\lambda\}$ denotes the m th receive antenna response to the ray from θ_{dk} , in which θ_{dk} is the DOA of the k th subpath of the d th path. f_{dk} denotes Doppler's frequency of the k th subpath of the d th path. If

a narrow-band transmit signal and a slow-fading environment are considered, we can assume that the signals are block fading; that is, $s(t - \tau_d)$ remains unchanged in a short period and fades independently from block to block. After appending T time samples at the m th receive antennas, we can obtain the block signals in matrix:

$$X(t) = A(\theta) \text{diag}(s(t - \tau)) B^T(f) + N(t). \quad (2)$$

Using the general relation, $\text{vec}(A \text{diag}[b]C) = (A \diamond CT)b$, yields

$$X(t) = A(\theta) \diamond B(f_k) \cdot S(t - \tau) + N(t), \quad (3)$$

where $X(t) = [x(t_m), x(t_m + T_s), \dots, x(t_m + (T - 1)T_s)]$, with T_s denoting the sampling period and $x(t_m) = [x_1(t_m), \dots, x_M(t_m)]^T$. Then the Khatri-Rao product $A(\theta) \diamond B(f) \in C^{ML \times K}$, and $N(t)$ is an additive noise process, assumed to be a zero-mean Gaussian noise vector with covariance $\sigma^2 I$. The receive array response matrix $A(\theta) = [A_1(\theta), \dots, A_D(\theta)]$, $A_d(\theta) = [\alpha_1(\theta), \dots, \alpha_{K_i}(\theta)]$, where $\alpha(\theta_i)$ denotes the array response vector of the i th ray:

$$\alpha(\theta_i) = [1, \exp\{j\pi \sin(\theta_i)\}, \dots, \exp\{j\pi(M - 1) \sin(\theta_i)\}]^T. \quad (4)$$

The frequency array response matrix $B(f)$ is L frequency samples in a short period, with f_s denoting the sampling rate, $B(f) = [B(f_1), \dots, B(f_{DK})]$:

$$B(f_k) = \left[1, \exp\left(\frac{j2\pi f}{f_s}\right), \dots, \exp\left(\frac{j2\pi(L - 1)f}{f_s}\right) \right]^T, \quad (5)$$

where $S(t - \tau) = [s(t - \tau_1), \dots, s(t - \tau_D)]^T$ denotes the transmit signal which has a delay τ .

3. Modified MUSIC Algorithm

Because the rank of correlation matrix is the number of cluster and not the number of ray, the conventional MUSIC algorithm does not work for scatter cluster model directly. So we make some modification based on the conventional MUSIC algorithm. The flow chart of the modified MUSIC algorithm is illustrated in Figure 1.

3.1. The Temporal Filter Method. Despite the conventional MUSIC algorithm constructs a spatial correlation matrix, the proposed algorithm is based on the decomposition of the theoretical temporal correlation matrix R^t into a signal subspace E_s and a noise subspace E_N :

$$R^t = E \{X^H(t) \cdot X(t)\} = S^H B_S S + \sigma^2 I. \quad (6)$$

Note that the number of the incoming paths is assumed to be known a priori; otherwise, we may estimate D by thresholding the magnitude of the eigenvalues of the covariance matrices involved or by using the AIC and the MDL

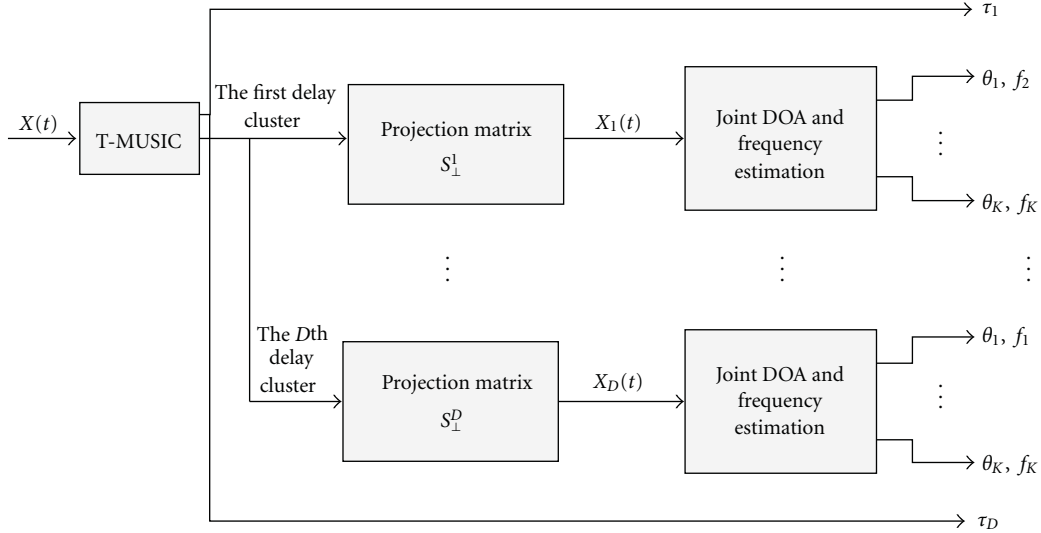


FIGURE 1: The flow chart of the our modified MUSIC algorithm.

detection methods [11], then the next step is similar to the conventional MUSIC algorithm:

$$R^t = V_s^t \Lambda_s^t V_s^{tH} + V_n^t \Lambda_n^t V_n^{tH}. \quad (7)$$

The column vectors of V_s^t are the eigenvectors that span the signal subspace R_s , respectively, corresponding to the D largest eigenvalues. The column vectors of V_n^t spanned by the rest of the and T - D eigenvectors of R^t are the orthogonal complement of the column vectors of V_s^t .

Using the orthogonality property between the signal and the noise subspaces, the T-MUSIC algorithm estimates the path delays by

$$\hat{\tau} = \arg \min_{\tilde{s}(\tau)} \tilde{s}(\tau)^H (I - V_s^t V_s^{tH}) \tilde{s}(\tau). \quad (8)$$

After searching τ over the range of interest, the spectrum of the T-MUSIC is, respectively, defined as

$$P_{\text{MUSIC}}^t(\tau) = \frac{1}{\tilde{s}(\tau)^H (I - V_s^t V_s^{tH}) \tilde{s}(\tau)}. \quad (9)$$

By applying the T-MUSIC, the resulting delays are estimated. Based on the delay estimates, we define the temporal filtering matrices as

$$S_{\perp} = I - s(\tau) \cdot (s(\tau)^H s(\tau))^{-1} \cdot s(\tau)^H. \quad (10)$$

Note that S_{\perp} is the complement project matrix of $s(\tau)$ with $s(\tau)^H \cdot S_{\perp} = 0^T$; with these facts, the modified MUSIC algorithm postmultiplies S_{\perp} to $X(t)$, which is referred to as the temporal filtering process to separate the rays with different delays. Then the output of the d th temporal filter is given by

$$X_d(t) = X(t) \prod_{i=1, i \neq d}^D S_{\perp}^i. \quad (11)$$

3.2. Spatial Smoothing (SS) Method. After applying the temporal filter, we can jointly estimate DOAs and Doppler frequencies of each delay cluster. However, the signals included a delay cluster are coherent, the matrix becomes singular, so that some of its eigenvalues are zero. This means that part of the signal subspace is indistinguishable from the noise subspace. As a result, the observed noise subspace is no longer orthogonal to the signal subspace and the MUSIC algorithm fails. So, to overcome these problems, we use a technique called spatial smoothing (SS) to allow the MUSIC algorithm to be applied to the coherent signal case [12].

The basic idea is to form covariance matrices from subsets of the array, which is equivalent to partitioning the original covariance matrix. If there are P subarrays, each subarray is of size $L = M - P + 1$ and the output of forward subarray is denoted by $X_p^f(t)$ with elements $[x_p(t), \dots, x_{p+L-1}(t)]$.

Then we can jointly estimate DOAs and frequencies in one delay cluster by the spatial correlation matrix R^s , where

$$R^s = \frac{1}{P} E \{ X_p^f(t) X_p^f(t)^H \}. \quad (12)$$

Similarly, after eigen decomposition of R^s , the eigenvectors can be divided into two groups: eigenvectors corresponding to the largest K eigen values are called signal eigenvectors and the subspace they span is called signal subspace. Utilizing the theory of orthogonality, we can obtain the spectrum:

$$P_{\text{MUSIC}}(\theta, f) = \frac{1}{(a(\theta) \otimes b(f))^H (I - V_s^t V_s^{tH}) (a(\theta) \otimes b(f))}. \quad (13)$$

4. Simulation Analysis

In this section, we conduct simulations to assess the proposed MUSIC algorithm. Assume narrow-band signals that

are transmitted through 7 rays and received by a ten-element ($M = 10$) uniform linear array, the spacing of two elements is half a wavelength. The 7 rays are divided into two groups: 4 rays have the same delay of $20 \mu\text{s}$, the remains are $40 \mu\text{s}$ delay; the first delay cluster: $(80^\circ, 30 \text{ kHz})$, $(60^\circ, 60 \text{ kHz})$, $(40^\circ, 90 \text{ kHz})$, $(50^\circ, 90 \text{ kHz})$ and the second delay cluster: $(20^\circ, 120 \text{ kHz})$, $(45^\circ, 30 \text{ kHz})$, $(15^\circ, 60 \text{ kHz})$. We sample the receive signal T times, $T = 512$. In each short sample, we also have $L = 3$ frequency samples, each signal's SNR is set to be 20 dB, and the additive Gaussian white noise (AWGN) is considered.

Figure 2 indicates the two delay clusters estimation of the synthetic channel. Each spectrum peak means Each delayed scatter cluster. The different cluster with $20 \mu\text{s}$ and $40 \mu\text{s}$ delay can be isolated directly. Figure 3 only shows the joint DOA and frequency estimation of the first delay cluster. Each spectrum peak indicates each incoming ray which is included the first delayed cluster with the delay of $20 \mu\text{s}$. All of the group and the single ray can be isolated by the temporal filtering process and the spatial smoothing process during the procedure of the proposed algorithm.

As illustrated in Figures 2 and 3, the modified MUSIC algorithm we proposed could fulfill estimation with high resolving capability for the scatter cluster models.

4.1. Complexity Analysis. In this part, we hereby make a brief comparison for the algorithmic costs in contrast with the modified MUSIC algorithm and SAGE algorithm. Table 1 gives the comparison of complexity for these algorithms.

When the number of ray estimated is small, it is proved that the SAGE algorithm can achieve coverage within 6–10 iterations through simulation analysis. The complexity of SAGE algorithm is less than that of the modified MUSIC algorithm.

On the contrary, the SAGE algorithm achieves coverage within 20 iterations when the wireless scatter environment is dense multipath. So, the complexity of SAGE algorithm is larger than that of the modified MUSIC algorithm.

From Table 1, it is clearly indicated that modified MUSIC algorithm can be optimal in the dense multipath wireless environment among the methods that we have investigated.

4.2. RMSE Analysis for Specular Model. To compare the estimation performance of both algorithms, we present 300 Monte Carlo's simulations to assess the angle estimation performance of our algorithm in specular model and define root mean squared error (RMSE) as

$$\frac{1}{K} \sum_{k=1}^K \sqrt{\frac{1}{300} \sum_{n=1}^{300} (\hat{\theta}_{k,n} - \theta_k)^2}, \quad (14)$$

where $\theta_{k,n}$ is the estimate of DOA θ_k of the n th Monte Carlo trial. Figure 4 shows the DOA estimation performance comparison with modified MUSIC algorithm and SAGE algorithm in specular models. It is indicated that the performances of angle estimation are nearly the same with modified MUSIC algorithm and SAGE algorithm. However,

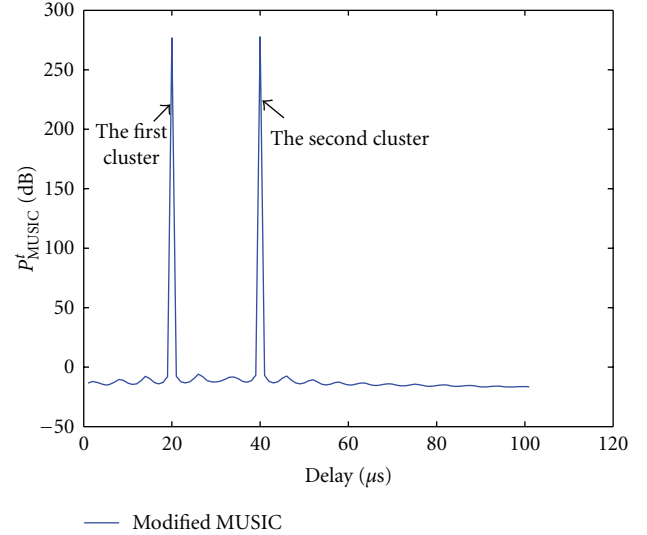


FIGURE 2: Delay clusters estimation using our algorithm.

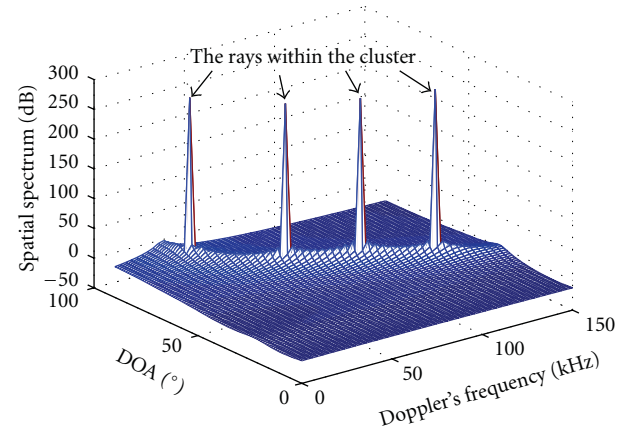


FIGURE 3: Joint DOA and Doppler's frequency estimation of first cluster using our algorithm.

the modified MUSIC algorithm takes less time than the SAGE algorithm in dense multipath environment.

4.3. RMSE Analysis for Cluster Model. Through the simulation, it is found that the iteration step shows sharp fluctuation for scatter cluster model using the SAGE algorithm. The major reason which leads to the failure of SAGE algorithm in the scatter clusters model is the searching procedure in the M step of SAGE algorithm that does not identify the peak caused by the signals which have same delays.

As mentioned above, the modified MUSIC algorithm is proved to be applied for the cluster models. However, the estimation performance depends on the mean of correlation matrix which substitutes for the expect of the correlation matrix in the practice. So, the number of receive antennas and sample length make a great part in the accuracy of estimation.

Figure 5 illustrates the DOA estimation performance comparison with different elements of receive array. It is

TABLE 1: The complexity for algorithms.

Algorithm	Complexity
Modified MUSIC algorithm	$T^2 \times N \times L + O(T^2) + T \times O(T) + (N \times L)^2 \times T + O((N \times L)^2) + n1 \times n2 \times ((N \times L)^2 + (P \times L))$
SAGE algorithm	The number of iteration \times the number of ray estimated $\times (T \times N \times T + n1 \times N \times T + n2 \times N \times T)$

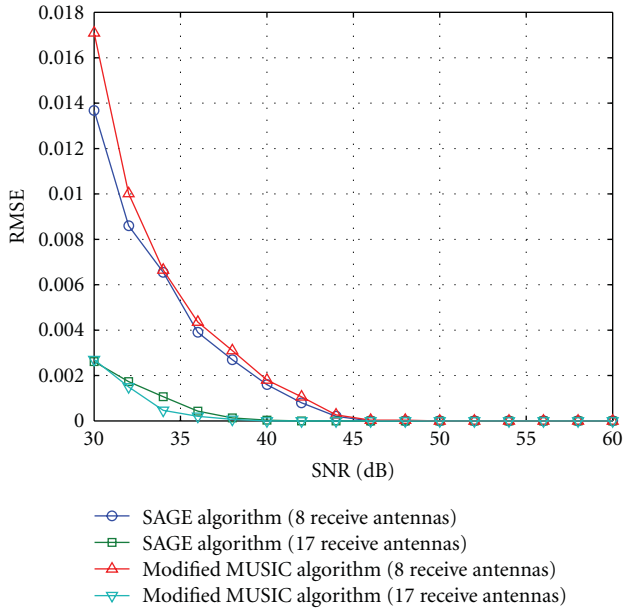


FIGURE 4: The RMSE of DOA estimation performance with Modified MUSIC algorithm and SAGE algorithm in specular models.

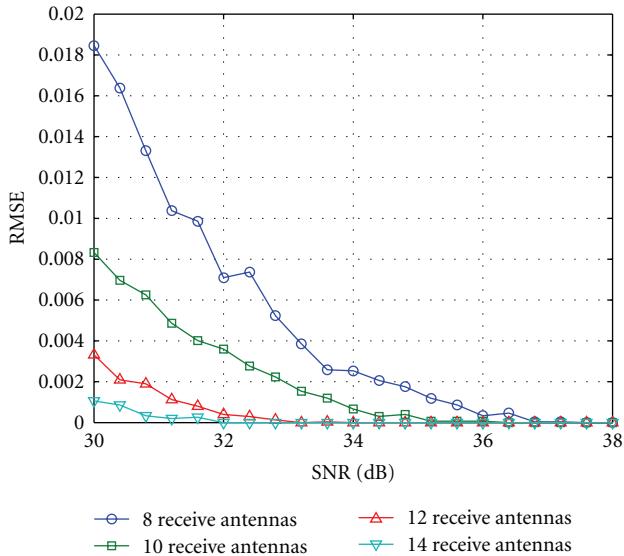


FIGURE 5: The DOA estimation performance with different elements of receive array.

clearly shown that the angle estimation performance of our algorithm is gradually improving with the number of antennas increasing. Multiple antennas improve the estimation performance because of diversity gain. Figure 6 shows the DOA estimation performance comparison with different

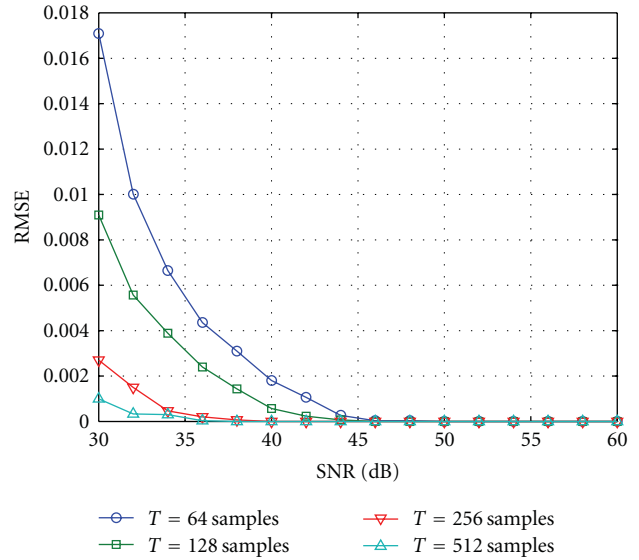


FIGURE 6: The DOA estimation performance with different samples.

samples. The element of receive array of 8-elements was assumed in this simulation. We confirm that the performance of angles estimation becomes better in collaboration with the increasing samples rate.

5. Conclusions

As to the conventional SAGE algorithm does not work for these scatter cluster models, in this paper a modification channel parameter method was proposed which combines the temporal filtering techniques and the spatial smoothing techniques based on the conventional MUSIC algorithm. The synthetic channel was then adopted in simulation to evaluate its performance. We come to a conclusion that the modified MUSIC algorithm takes less time than the SAGE algorithm and has less complexity than the SAGE algorithm in dense multipath environment. The results indicated that this method could fulfill parameter estimation with high resolving capability. It is demonstrated that the estimation performance grows with the number of array elements and the sample rate.

Acknowledgments

This work is supported by the National Science and Technology Major Project of the Ministry of Industry and Information of China (2009ZX03007-003) and the National Natural Science Foundation of China (61101223).

References

- [1] H. Krim and M. Viberg, "Two decades of array signal processing research: the parametric approach," *IEEE Signal Processing Magazine*, vol. 13, no. 4, pp. 67–94, 1996.
- [2] R. O. Schmidt, "Multiple emitter location and signal parameter estimation," *IEEE Transactions on Antennas and Propagation*, vol. 34, no. 3, pp. 276–280, 1986.
- [3] R. Roy and T. Kailath, "ESPRIT—estimation of signal parameters via rotational invariance techniques," *IEEE Transactions on Acoustics, Speech, and Signal Processing*, vol. 37, no. 7, pp. 984–995, 1989.
- [4] M. Haardt and J. A. Nossek, "Unitary ESPRIT: how to obtain increased estimation accuracy with a reduced computational burden," *IEEE Transactions on Signal Processing*, vol. 43, no. 5, pp. 1232–1242, 1995.
- [5] X. Yin, L. Liu, D. K. Nielsen, T. Pedersen, and B. H. Fleury, "A SAGE algorithm for estimation of the direction power spectrum of individual path components," in *Proceedings of the 50th Annual IEEE Global Telecommunications Conference (GLOBECOM '07)*, pp. 3024–3028, November 2007.
- [6] A. L. Swindlehurst, "Time delay and spatial signature estimation using known asynchronous signals," *IEEE Transactions on Signal Processing*, vol. 46, no. 2, pp. 449–462, 1998.
- [7] I. Jaafar, R. Amara, H. Boujemâa, and M. Siala, "Joint angle and delay estimation of point sources," in *Proceedings of the 12th IEEE International Conference on Electronics, Circuits and Systems (ICECS '05)*, pp. 1–5, December 2005.
- [8] Y. Y. Wang, J. T. Chen, and W. H. Fang, "TST-MUSIC for joint DOA-delay estimation," *IEEE Transactions on Signal Processing*, vol. 49, no. 4, pp. 721–729, 2001.
- [9] J. D. Lin, W. H. Fang, Y. Y. Wang, and J. T. Chen, "FSF MUSIC for joint DOA and frequency estimation and its performance analysis," *IEEE Transactions on Signal Processing*, vol. 54, no. 12, pp. 4529–4542, 2006.
- [10] 3GPP, "Spatial channel model for multiple input multiple output MIMO simulations," Technical Specification Group Radio Access Network TR25.996 v6.1.0, 3GPP, September 2003.
- [11] B. Nadler, "Nonparametric detection of signals by information theoretic criteria: performance analysis and an improved estimator," *IEEE Transactions on Signal Processing*, vol. 58, no. 5, pp. 2746–2756, 2010.
- [12] J. S. Thompson, P. M. Grant, and B. Mulgrew, "Performance of spatial smoothing algorithms for correlated sources," *IEEE Transactions on Signal Processing*, vol. 44, no. 4, pp. 1040–1046, 1996.

Research Article

A Novel Dual-Band MIMO Antenna with Lower Correlation Coefficient

Jian Zhang, Jun OuYang, Kai Zhi Zhang, and Feng Yang

Department of Microwave Engineering, University of Electronic Science and Technology of China (UESTC), Chengdu 610054, China

Correspondence should be addressed to Jun OuYang, antenna_ou@163.com

Received 18 August 2011; Revised 14 September 2011; Accepted 28 September 2011

Academic Editor: Yuan Yao

Copyright © 2012 Jian Zhang et al. This is an open access article distributed under the Creative Commons Attribution License, which permits unrestricted use, distribution, and reproduction in any medium, provided the original work is properly cited.

This paper demonstrates a novel dual-band operated MIMO antenna which consisted of planar monopole (main antenna) and 3D slot element (auxiliary antenna). The main antenna is printed on a 1.6 mm thick FR4 board, while the auxiliary antenna is fabricated with gold-coated copper. A lumped impedance network is applied to enhance matching effect at port1. From simulations by commercial software, it can be found that the proposed antenna is able to cover GSM800, GSM900 (lower band), and LTE/WiMAX/WLAN (higher band) quite well. Good agreements between simulations and measurements are obtained. Corresponding measured results, antenna efficiency, peak gain, and radiation patterns, are presented at the same time. By equipping a passive decoupling element, the coupling power on the ground is radiated into free space, and great enhancement of isolation between antenna elements, especially for lower band, is achieved.

1. Introduction

With the prompt development of wireless communication these years, plenty of excellent multimedia services are desirable for users, such as video online or web surfing. So, it is a great challenge worldwide for mobile network operators to accommodate these higher data rates services with current communication systems which possess small channel capacity and poor reliability. Fortunately, it is found that the MIMO (multiple input multiple output) antenna system can be a good candidate to effectively solve this problem. However, it is troublesome that the mutual coupling among closely packed antenna elements will always lead to severe performance deterioration of MIMO systems. In this case, improving the isolation between antenna elements has become a hot topic in the MIMO field, while much effort has been made into studying the technologies for this purpose by antenna experts and scholars.

In order to reduce mutual coupling between MIMO antennas, protruded T-shaped ground plane [1] and corrugated ground plane with $\lambda/4$ slot [2] are utilized, and modified PIFA with a small local ground plane is proposed in [3]. Chung and Yoon have fabricated a MIMO antenna in which

a ground wall and a connecting line are introduced, and it exhibits favorable isolation level [4]. Pairs of slits are etched onto the ground plane of MIMO terminals to avoid current sharing between antenna ports through ground, and significant isolation improvement is obtained compared to conventional ground plane due to the filter effect of etched ground plane [5]. In addition, [6] provides us an different approach for closely packed antennas which consists of a compact integrated diversity antenna with two feed ports. In [7], a MIMO antenna using a T-shaped common grounding element is presented. The proposed MIMO antenna consists of two radiating elements for Mobile-WiMAX service. The structure of T-shaped common grounding element was added between the two modified inverted-L radiating elements to improve the isolation characteristic. To realize the good isolation performance for a small separation, a suspended strip is used to connect the two monopoles together [8], and it forms an effective filter with the ground plane at the required frequency band.

Although there has been many methods to reduce the mutual coupling of MIMO antenna system, just like what we have mentioned above, most of MIMO antennas can only work in a single band, from 1.88 GHz to 2.6 GHz (LTE/

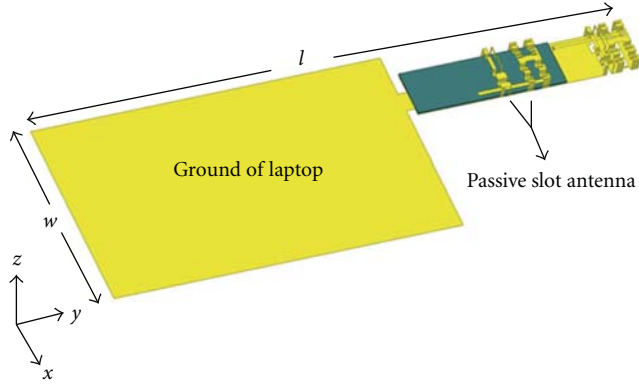


FIGURE 1: Total view of the proposed MIMO antenna with the existence of laptop.

WiMAX/WLAN), and rarely reach to the lower operation bands, such as GSM800 and GSM900, which are still popular bands for our mobile communication at present.

In this paper, a novel USB dongle MIMO antenna with lower correlation coefficient is presented. This MIMO antenna which takes a relative small volume compared with other terminal MIMO antennas consisted of planar monopole and a novel 3D slot element which is meandered in both vertical and horizontal direction [9]. At the same time, for the sake of radiating the coupling power on the ground into free space and thus decreasing the mutual coupling, a passive 3D slot element with separate slots which are responsible for low frequency and high frequency, respectively, is installed in the middle of ground plane. Later, we use the full wave commercial numerical simulation software package to simulate this MIMO antenna and the parameters such as location of the passive antenna, and space between these separate slots have been optimized. It is found that the proposed MIMO antenna works quite well with S_{11} below -6 dB both in lower band (880 MHz–960 MHz) and higher band (1880 MHz–2600 MHz). Significantly, the isolation for these two antenna ports meets the requirements of handset MIMO system, and especially for lower band, reaches about -11 dB. At last, the fabricated MIMO antenna is measured in anechoic chamber (SATIMO StarLab), and good agreements have been obtained. Further, to verify the effect of mutual coupling reduction of the decoupling passive slot antenna, some comparisons have been made. It is demonstrated that the proposed terminal MIMO antenna could be an ideal candidate for application in GSM800, GSM900, and LTE/WiMAX/WLAN.

2. Proposed MIMO Antenna Geometry

The geometry of the proposed two-channel MIMO antenna is shown in Figure 1. Because ground plays an important role in the performance of the antenna, it has been taken into account for our design.

The details for MIMO antenna are illustrated in Figure 2.

As shown in Figure 2, the grey part is the FR4 board with the thickness h_2 , and the yellow part denotes the copper. The proposed MIMO antenna system comprises planar

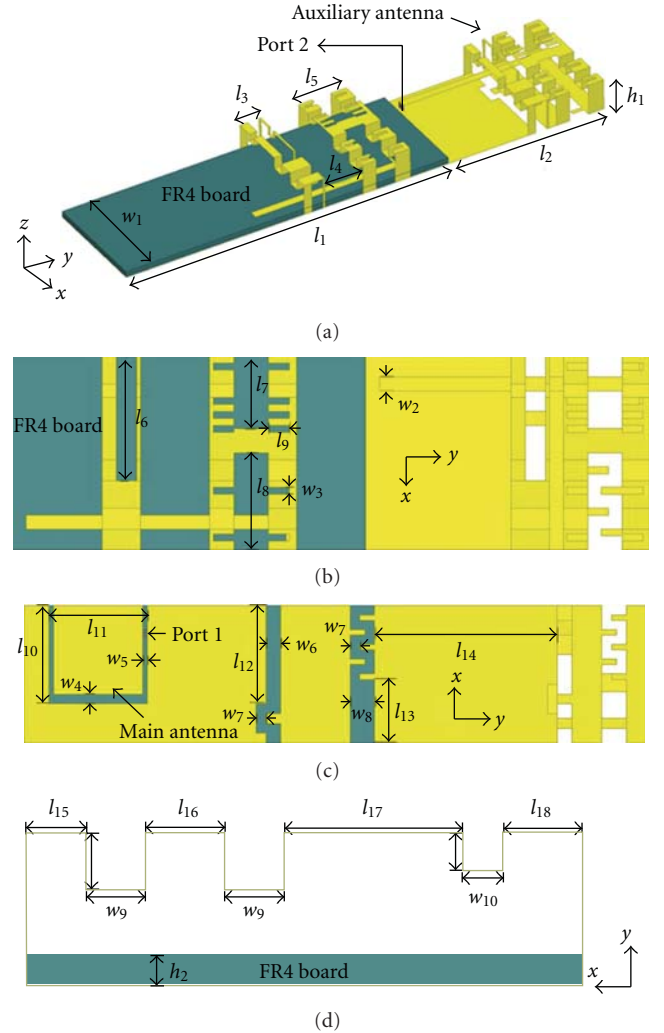


FIGURE 2: (a) MIMO antenna structure. (b) Details of the proposed structure (top view). (c) Details of the proposed structure (bottom view). (d) Details of the proposed structure (front side view).

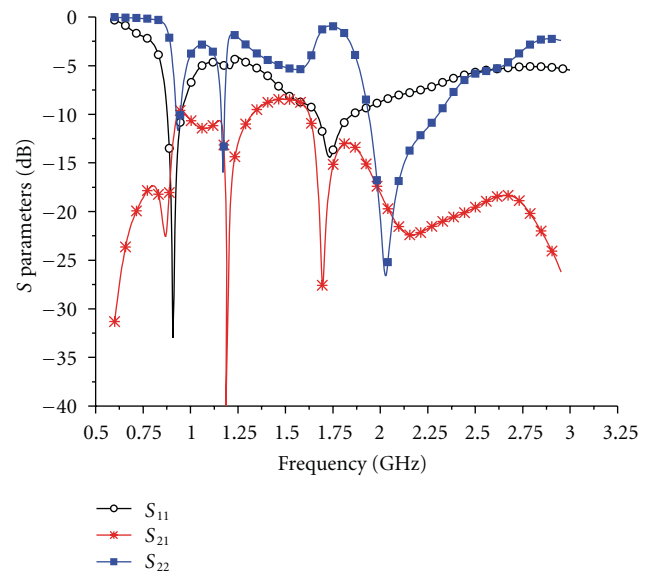


FIGURE 3: Simulated S parameters.

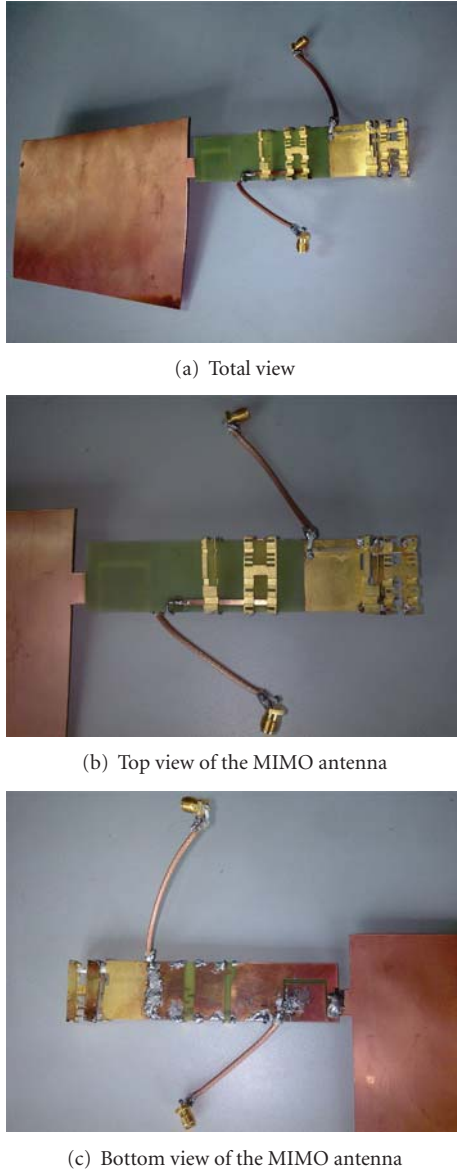


FIGURE 4: Photography of the fabricated MIMO antenna.

TABLE 1: Values of the lumped components.

Series-capacitance	4 pF
Parallel-capacitance	7 pF
Parallel-inductance	0.5 nH

monopole as main antenna and a novel 3D slot element as auxiliary antenna [9]. The main antenna is printed on the PCB board with the dimensions of $l_{10} \times l_{11}$. The auxiliary antenna located at right side consisted of two horizontally and vertically meandered slots with different resonate lengths; meanwhile, it can be noted that an array of short stubs are placed along these slots to minish the antenna size [10]. A microstrip line with no substrate is used to couple the power to the slots of the auxiliary antenna as feedline. In order to achieve good matching effect, a lumped impedance

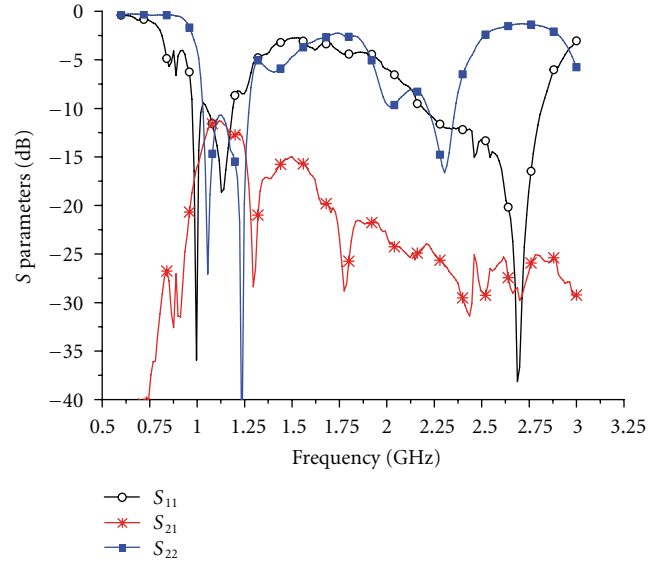


FIGURE 5: Measured S parameters.

network is introduced at Port1 in this design, and the values of the lumped components are given in Table 1.

For multiantenna systems applied in mobile terminals, the mutual coupling between antenna elements is quite severe and mainly caused by ground surface current sharing, especially for low frequency due to relative small space compared to the wavelength. Therefore, to improve the isolation, the preceding 3D slot element is employed between main antenna and auxiliary antenna to radiate the coupling power on the ground into free space. Finally, for a better performance, the passive 3D slot element is divided into two parts, and the separated slots cover lower band and higher band independently. All the parameters of the antenna structure have been optimized and listed in Table 2.

3. Simulation and Measured Results

3.1. Simulation Results. The MIMO antenna model is firstly simulated by the commercial full wave simulation software package-Ansoft HFSS version 13.0, and the simulated S parameters are depicted in Figure 3.

Apparently, from the simulated results, it is found that both main antenna and auxiliary antenna can work well for dual-band operation with reflection (S_{11} and S_{22}) lower than -6 dB, which is acceptable for the applications of miniaturized terminal. Moreover, the MIMO antenna system possess a good isolation level about -10 dB for lower band (880 MHz–960 MHz) and average -20 dB for higher band (1880 MHz–2600 MHz).

3.2. Measured Results. The fabricated antenna is shown in Figure 4, and the copper thickness is 0.5 mm.

We measured this antenna in the anechoic chamber (SATIMO StarLab). The measured data, including efficiency, peak gain, and radiation patterns, are obtained by feeding one port while the other one terminated with a 50 Ohms load.

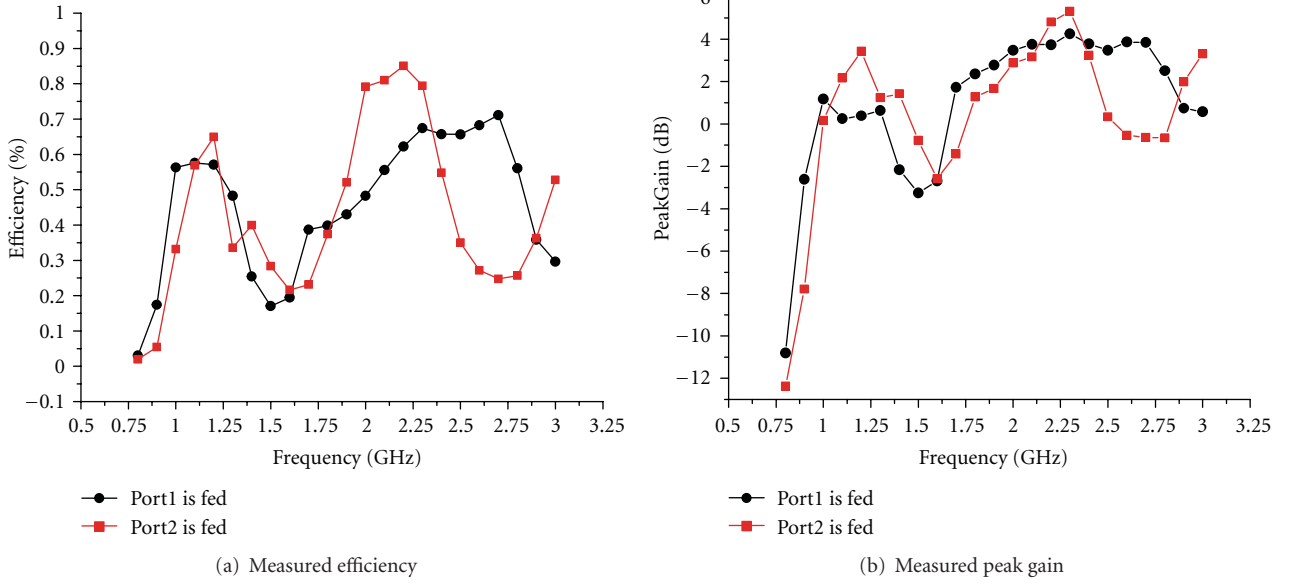


FIGURE 6: Measured efficiency and peak gain.

TABLE 2: Parameters of the antenna structure.

l	331 mm	l_5	12.5 mm	l_{10}	20 mm	l_{15}	3 mm	w_1	28 mm
l_1	85 mm	l_6	21.5 mm	l_{11}	20 mm	l_{16}	4 mm	w_2	2 mm
l_2	41 mm	l_7	10.5 mm	l_{12}	20 mm	l_{17}	9 mm	w_3	1 mm
l_3	5.5 mm	l_8	14 mm	l_{13}	13 mm	l_{18}	4 mm	w_4	2 mm
l_4	10 mm	l_9	3 mm	l_{14}	37 mm	w	120 mm	w_5	1 mm
w_6	3 mm	w_7	2 mm	w_8	5 mm	w_9	3 mm	w_{10}	2 mm
h_1	8 mm	h_2	1.6 mm						

Comparing Figures 3 and 5, even though the resonant point of auxiliary antenna shifts a little higher due to the error which comes from fabrication and installation, it cannot be denied that there is good agreement between simulation and measurement ($S_{11}, S_{22} < -6$ dB, $S_{21} < -11$ dB).

Figure 6 demonstrates that the proposed MIMO antenna operates quite efficiently, at least 40% for lower band and peak efficiency appearing within higher band, is approximately 88%. The peak gains of the antenna are also

qualified to the desired applications. Radiation patterns for lower and higher band are drawn in Figures 7 and 8.

3.3. Correlation Coefficients. In order to further investigate whether these two channels are independent enough, we use the following formula to compute the correlation coefficients of the proposed MIMO antenna:

$$\rho_c = \frac{\left(\oint \oint (XPR \cdot E_{1\theta}(\theta, \phi) \cdot E_{2\theta}^*(\theta, \phi) \cdot \mathcal{A} + E_{1\phi}(\theta, \phi) \cdot E_{2\phi}^*(\theta, \phi) \cdot \mathcal{B}) \cdot \sin \theta \cdot d\theta d\phi \right)^2}{\oint \oint (XPR \cdot G_{1\theta}(\theta, \phi) \cdot \mathcal{A} + G_{1\phi}(\theta, \phi) \cdot \mathcal{B}) \cdot \sin \theta \cdot d\theta d\phi \cdot \oint \oint (XPR \cdot G_{2\theta}(\theta, \phi) \cdot \mathcal{A} + G_{2\phi}(\theta, \phi) \cdot \mathcal{B}) \cdot \sin \theta \cdot d\theta d\phi}, \quad (1)$$

where \mathcal{A} denotes $P_\theta(\theta, \phi)$ and \mathcal{B} denotes $P_\phi(\theta, \phi)$.

In the formula above, $G_\theta = E_\theta(\theta, \phi) \cdot E_\theta^*(\theta, \phi)$, $G_\phi = E_\phi(\theta, \phi) \cdot E_\phi^*(\theta, \phi)$; $E_{1\theta}(\theta, \phi)$ and $E_{2\theta}(\theta, \phi)$ are plural radiation patterns of main antenna and auxiliary antenna, respectively, for vertical polarization situation; $E_{1\phi}(\theta, \phi)$ and $E_{2\phi}(\theta, \phi)$ are for horizontal polarization case; $P_\theta(\theta, \phi)$ and $P_\phi(\theta, \phi)$ denote power probability distributions of two incident wave with different polarizations, also the distributions

vary with various communication networks and operation circumstance of antennas. On the other hand,

$$\begin{aligned} P_\theta(\theta, \phi) &= P_\theta(\theta) \cdot P_\phi(\phi), \\ P_\phi(\theta, \phi) &= P_\phi(\theta) \cdot P_\theta(\phi), \end{aligned} \quad (2)$$

$P_\theta(\theta)$ and $P_\phi(\theta)$ refer to power probability distributions of incident wave in vertical direction, and $P_\theta(\phi)$ and $P_\phi(\phi)$

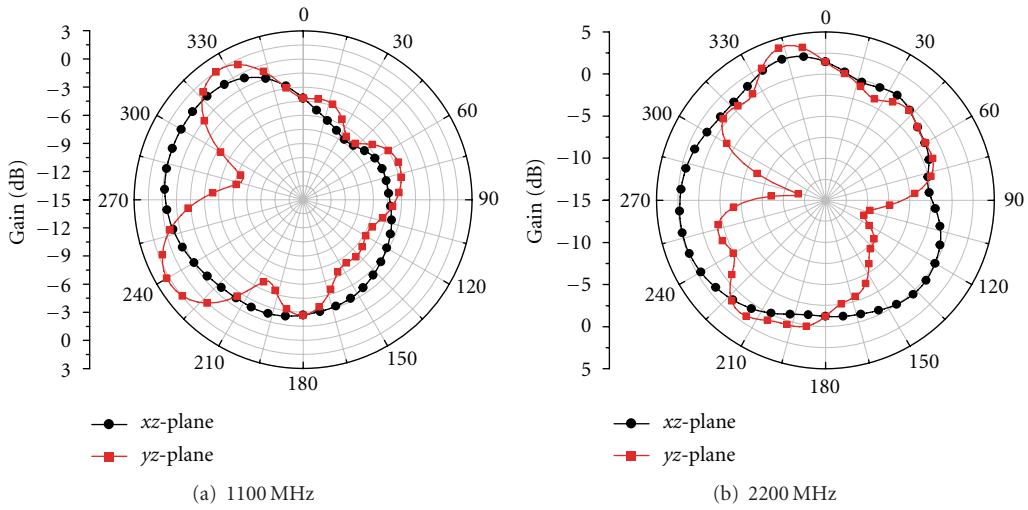


FIGURE 7: Port1 stimulated.

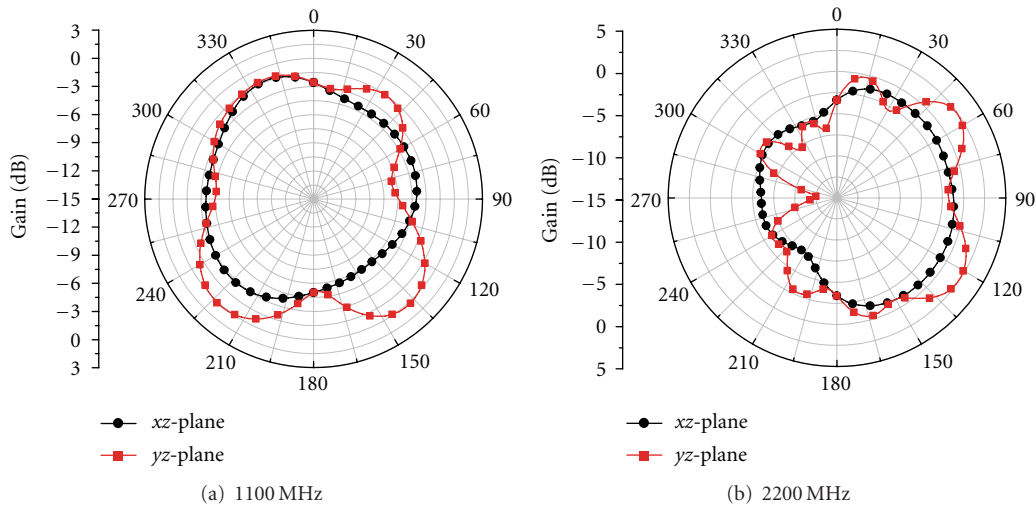


FIGURE 8: Port2 stimulated.

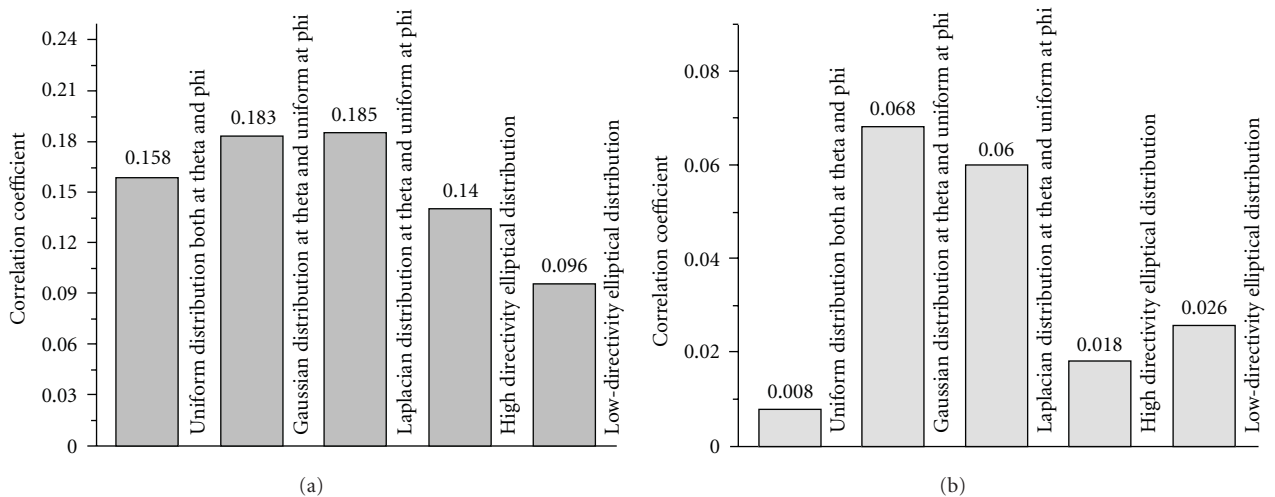


FIGURE 9: Correlation coefficient: (a) (1100 MHz); (b) (2200 MHz).

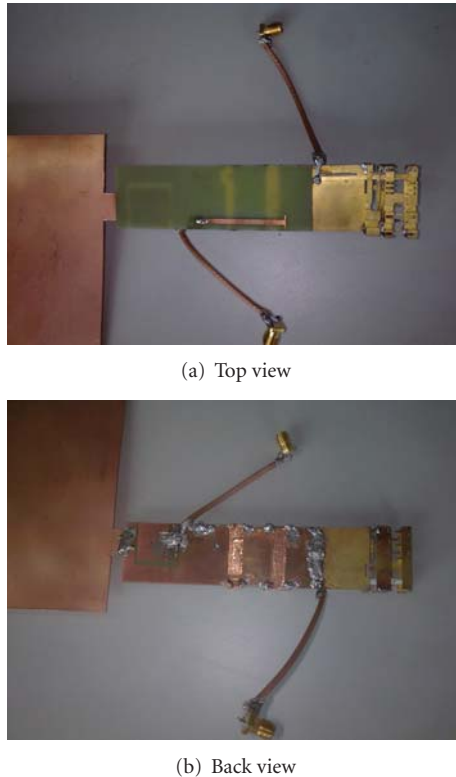
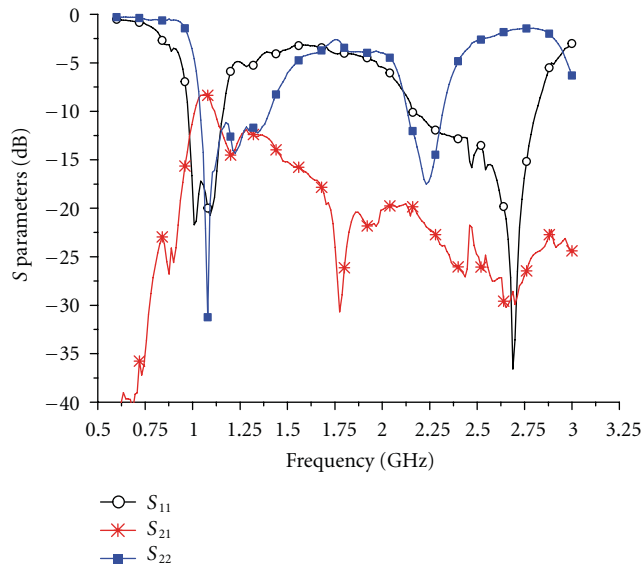


FIGURE 10: Transformed MIMO antenna.

FIGURE 11: Measured S parameters of transformed MIMO antenna.

refer to power probability distributions of incident wave in horizontal direction.

The calculated correlation coefficients of these two antenna elements are diagramed in Figure 9.

Five different correlation coefficients are calculated with five distinct distributions, which are uniform distribution both at theta and phi, Gaussian distribution at theta and uniform at phi, Laplacian distribution at theta and uniform at

phi, high-directivity elliptical distribution, and low-directivity elliptical distribution, respectively. The corresponding equations of those probability distributions are provided in [11].

No matter which kind of distributions is chosen, the calculated correlation coefficients are extremely low here, particularly for higher operation band, all of which are below 0.07, and even the maximal one is merely 0.068. Therefore, these two antenna elements can be reasonably regarded as independent channels to provide better channel capacity.

3.4. Verifying the Effect of the Passive Decoupling Element. To verify the effect of the passive decoupling element, the passive decoupling element is removed away from the proposed MIMO antenna. The transformed antenna is shown in Figure 10.

As illustrated in Figure 10, the decoupling passive 3D slot element has been removed away and the original slot etched on the antenna ground is covered by copper foil. The measured S parameters for this case are demonstrated in Figure 11.

It can be easily found that a deterioration of isolation of the antenna elements occurs comparing with Figure 5, especially for lower band of which the worst point climbs to about -7.5 dB from -11 dB. The correlation coefficient of the transformed MIMO antenna has also increased to a high level, from the original 0.096 to 0.2535 at 1100 MHz with the low-directivity elliptical probability distribution. Thus, we can get to the conclusion that the passive decoupling element is capable of greatly reducing the mutual couple for MIMO antenna.

4. Conclusions

A novel dual-band operated MIMO antenna consisted by planar monopole and 3D slot element is presented in this paper. As a lumped impedance network is introduced in port1, both main antenna and auxiliary antenna matches very well no matter lower band or higher band. Since the coupling power on the ground is radiated into free space by a passive decoupling element, great enhancement of the isolation between antenna elements is obtained. This novel MIMO antenna is a good candidate for the mobile terminal application on GSM800, GSM900, and LTE/WiMAX/WLAN.

Acknowledgments

This work was supported by the postdoctoral Science Foundation of China (no. 20090461325 and no. 201003690), the Natural Science Foundation of China (no. 61001029 and no. 10876007), and the Fundamental Research Funds for the Central Universities (no. 103.1.2 E022050205).

References

- [1] T. Y. Wu, S. T. Fang, and K. L. Wong, "Printed diversity monopole antenna for WLAN operation," *Electronics Letters*, vol. 38, no. 25, pp. 1625–1626, 2002.

- [2] M. Karakoikis, C. Soras, G. Tsachtsiris, and V. Makios, "Compact dual-printed inverted-F antenna diversity systems for portable wireless devices," *IEEE Antennas and Wireless Propagation Letters*, vol. 3, no. 1, pp. 9–13, 2004.
- [3] Y. Gao, C. C. Chiau, X. Chen, and C. G. Parini, "Modified PIFA and its array for MIMO terminals," pp. 255–259.
- [4] K. Chung and J. H. Yoon, "Integrated MIMO antenna with high isolation characteristic," *Electronics Letters*, vol. 43, no. 4, pp. 199–201, 2007.
- [5] C. Y. Chiu, C. H. Cheng, R. D. Murch, and C. R. Rowell, "Reduction of mutual coupling between closely-packed antenna elements," *IEEE Transactions on Antennas and Propagation*, vol. 55, no. 6, pp. 1732–1738, 2007.
- [6] S. C. K. Ko and R. D. Murch, "Compact integrated diversity antenna for wireless communications," *IEEE Transactions on Antennas and Propagation*, vol. 49, no. 6, pp. 954–960, 2001.
- [7] J. Kwon, D. Kim, Y. Lee, and J. Choi, "Design of a MIMO antenna for USB dongle application using common grounding," in *Proceedings of the 13th International Conference on Advanced Communication Technology (ICACT '11)*, pp. 313–316, Seoul, South Korea, 2011.
- [8] Z. Li, M. -S. Han, X. Zhao, and J. Choi, "MIMO antenna with isolation enhancement for wireless USB dongle application at WLAN band," in *Proceedings of the Asia-Pacific Microwave Conference Proceedings (APMC '10)*, pp. 758–761, Yokohama, Japan, December 2010.
- [9] J. OuYang, J. Zhang, K. Z. Zhang, and F. Yang, "Compact folded dual-band slot antenna for wireless communication USB dongle application," *Journal of Electromagnetic Waves and Applications*, vol. 25, no. 8-9, pp. 1221–1230, 2011.
- [10] N. Behdad and K. Sarabandi, "Bandwidth enhancement and further size reduction of a class of miniaturized slot antennas," *IEEE Transactions on Antennas and Propagation*, vol. 52, no. 8, pp. 1928–1935, 2004.
- [11] V. Plicanic, *Antenna diversity studies and evaluation*, M.S. thesis, Master of Science Thesis Vanja Plicanic in Cooperation with Ericsson Mobile Communications AB, 2004.

Research Article

Spatial Correlation and Ergodic Capacity of MIMO Channel in Reverberation Chamber

Xiaoming Chen

Department of Signals and Systems, Chalmers University of Technology, 41296 Gothenburg, Sweden

Correspondence should be addressed to Xiaoming Chen, xiaoming.chen@chalmers.se

Received 27 July 2011; Accepted 26 September 2011

Academic Editor: Li Yang

Copyright © 2012 Xiaoming Chen. This is an open access article distributed under the Creative Commons Attribution License, which permits unrestricted use, distribution, and reproduction in any medium, provided the original work is properly cited.

It has previously been shown that a reverberation chamber can conveniently be used to measure ergodic multiple-input multiple-output (MIMO) capacity for over-the-air (OTA) tests. However, the MIMO channel in the reverberation chamber has not been fully studied before. In this paper, the spatial correlation of the MIMO channel in the chamber is studied by comparing the measured channel with two popular MIMO channel models. It is shown that the models can accurately predict the ergodic MIMO capacity of the channel in the reverberation chamber, but not the outage capacity (especially at high signal-to-noise regime). It is verified that the capacity estimation error is due to the fact that the measured MIMO channel in the chamber does not satisfy multivariate normality (MVN), which causes the capacity error increases additively with MIMO size and multiplicatively with signal-to-noise (SNR).

1. Introduction

Multiple-input multiple-output (MIMO) systems have drawn considerable popularity, over the past decade, due to their performance-enhancement capability in multipath environments [1]. Lots of work has been carried out for measuring MIMO capacity in real-life (outdoor and indoor) multipath environments [2–6]. As opposite to the real-life measurements, the reverberation chamber is being considered as a strong candidate for standardization of over-the-air (OTA) measurements for characterization of MIMO terminals due to its fast, repeatable, and economical measurements. The ergodic MIMO capacity can be measured in reverberation chambers [7–11]. While most of the reverberation chamber works have been focused on characterizing multipoint antennas, the MIMO channel in the chamber has not been fully studied yet.

The aim of this paper is to study the measured channel in the chamber by comparing it with two well-known channel models, (i.e., Kronecker model and full-correlation model [1]) and physically explain the models' discrepancies with measurements. Some different properties of reverberation chamber and real-life multipath environments are also

discussed. Most previous real-life measurements only used Kronecker model to compare with measurements [2–6]. Although there exist other sophisticated models, it is well known that the full-correlation model offers the best accuracy at the expense of the most complexity. Therefore, we include both Kronecker model and the full-correlation model in this paper. It is found that both models have the same performance in terms of capacity estimation, which is a bit surprising. The reasons for this are discussed in Section 4. It is also found that, although both models can well predict the ergodic capacity (with only slight overestimation at high SNR regime), they fail to estimate the outage capacity, or the cumulative distribution function (CDF) of the capacity. Moreover, instead of capacity underestimations as indicated by real-life measurements [4], the present paper shows that Kronecker model tends to overestimate capacities based on measurements in a reverberation chamber. The reasons for this are discussed in Section 5.

This work is of particular interest for OTA characterization of MIMO terminals in reverberation chambers, because it helps to understand the channel conditions under which the passive and/or active MIMO measurements have been conducted in the chamber.

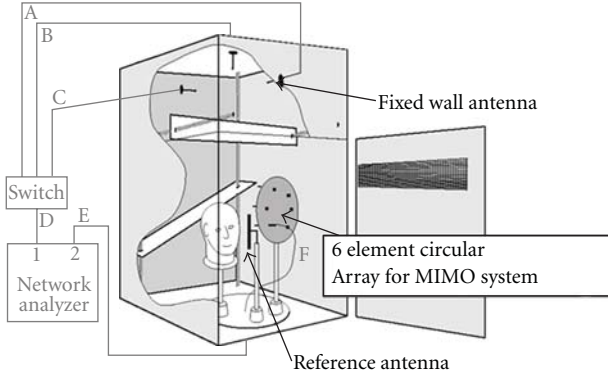


FIGURE 1: Drawing of the Bluetest RC with two mechanical plate stirrers, platform, three wall antennas, and six-monopole array.

2. Measurement Description

It has been shown that the ergodic MIMO capacity of a multiantenna system can be easily determined based on the reverberation chamber measurement [7, 9–11]. The reverberation chamber is basically a metal cavity with many excited modes that are stirred to create a Rayleigh-fading environment [12]. The chamber used in the present paper is Bluetest HP reverberation chamber with a size of $1.75 \times 1.25 \times 1.8 \text{ m}^3$ (see Figure 1). It has two plate mode stirrers, a turn-table platform, and three antennas mounted on three different walls (referred to as wall antennas thereafter). The wall antennas are actually wideband half-bow-tie (or triangular sheet) antennas. In the measurements, the platform (with a radius of 0.3 m), on which the MIMO terminal under test was mounted, was moved to 20 positions equally spaced by 18° , and, for each platform position, the two plates simultaneously moved to 10 positions (equally spanned on the total distances that they can move along the walls). All the mechanical (stepwise) moves were controlled by a computer. At each stirrer position and for each wall antenna, a full frequency sweep was performed by the vector network analyzer (VNA), during which the channel transfer functions at different frequencies were sampled. The frequency step was set to 1 MHz always. Therefore, for each transmit and receive antenna element pair, there are 200 channel transfer function samples per frequency point.

In order to calibrate out the long-term fading, or attenuation, in the chamber (so that only short-term fading came into play) [1], a reference measurement needed to be performed first, where the average power transfer function was measured using a reference antenna with known radiation efficiency. The reference level, P_{ref} , was obtained by dividing the average power function by the radiation efficiency of the reference antenna. Then, the multipoint antenna under test, in this case a six-monopole array (see also Figure 1), was measured (actually this procedure was repeated for each of the monopole while the others are terminated with 50 ohm). During this measurement, the three wall antennas were assumed to be the transmit antenna elements; the monopole array was assumed to be the receive antenna. The monopoles have physical length of 8.3 cm

(resonating at around 900 MHz). The ground plane has a radius of 14 cm. The monopoles are uniformly mounted on the ground plane in a circle, where adjacent monopoles have a separation of 4.6 cm. The small separation is necessary to have reasonably large correlations, in order to effectively compare different channel models [4].

The resulting channel matrix $\mathbf{H}_{6 \times 3}$ is a function of frequency and stirrer positions. For convenience, we introduce the following notation for the normalized measured channel matrix

$$\mathbf{H}_{\text{meas}} = \frac{\mathbf{H}_{6 \times 3}}{\sqrt{P_{\text{ref}}}}, \quad (1)$$

where the reference level, P_{ref} , is described above. Note that the total radiation efficiency of the wall antenna is also calibrated out by (1).

Assume that the receiver has perfect channel state information and that transmitted power is equally allocated among transmitting antenna elements, the ergodic MIMO capacity can be computed from the measured channel matrices by [1]

$$C = E \left\{ \log_2 \left[\det \left(\mathbf{I} + \frac{\gamma}{M_T} \mathbf{H}_{\text{meas}} \mathbf{H}_{\text{meas}}^H \right) \right] \right\}, \quad (2)$$

where γ is signal-to-noise ratio (SNR) and the expectation E can be approximated by averaging over all channel samples.

3. MIMO Channel

3.1. Channel Characterization. Wireless channel that can be assumed as wide-sense stationary uncorrelated scattering (WSSUS) [13] is usually characterized by its coherence bandwidth, coherence time, and coherence distance, or equivalently by their reciprocal counterparts: delay spread, Doppler spread, and angular spread, respectively [1]. Since the channel was sampled (by the VNA) stepwisely, that is, in static condition at each stirrer position, the Doppler spread of the channel is negligible. The angular distribution in the chamber is shown to be three-dimensional (3D) uniform, that is, isotropic [14]. The coherence bandwidth of the channel at the frequency of interest is around 1–2 MHz [15]. In practice, wireless channels are seldom WSSUS. Fortunately, most of them can be assumed as quasi-WSSUS, that is, the channel statistics do not change within certain time and frequency intervals. These intervals are defined in [16] as stationarity time and stationarity bandwidth. Since channel was sampled under static condition, its stationarity time is infinite. Under the assumption of correlation underspread, the stationarity bandwidth is larger than 20 MHz (i.e., at least 10 times larger than the coherence bandwidth). In the reverberation chamber, every subchannel (for each transmit and receive antenna element pair) is assumed to have the same time-frequency statistics.

Note that different fading-type environments can be emulated involving reverberation chamber. Holloway [17] showed that loading the chamber with electromagnetic-absorbing objects can generate Rician fading. It was shown in [10] that two cascaded reverberation chambers can be

used to emulate double-Rayleigh (key-hole) fading. More outdoor-like fading can be generated by connecting a reverberation chamber to an anechoic chamber [18]. As pointed out in [19], for MIMO channels, the most important aspect is the spatial correlation of the channel. Therefore, the main focus of this paper will be on the spatial correlation of the channel and its effects on capacity in an unloaded (with little electromagnetic-absorbing objects) reverberation chamber.

3.2. Channel Models. Assume a single-user narrow band MIMO system, consisting of M_T transmit antennas and M_R receive antennas, in a frequency flat Rayleigh-fading environment. The $M_R \times 1$ output vector of the MIMO system can be expressed as

$$\mathbf{y} = \mathbf{H}\mathbf{x} + \mathbf{n}, \quad (3)$$

where \mathbf{H} is the $M_T \times M_R$ channel matrix, \mathbf{x} is $M_T \times 1$ vector of transmit signals, and \mathbf{n} is $M_R \times 1$ zero mean white Gaussian noise vector. This paper will focus on narrowband models only, knowing that they can be readily extended to wideband model by assuming channel taps with different delays (with each tap modeled as a narrowband channel) [13].

A general, so-called, full-correlation channel model is given by [1]

$$\text{vec}(\mathbf{H}_{\text{full}}) = \mathbf{R}^{1/2} \text{vec}(\mathbf{H}_w), \quad (4)$$

where \mathbf{H}_w is independent and identically distributed (i.i.d.) zero mean spatially white $M_R \times M_T$ channel matrix, $\text{vec}(\mathbf{H})$ is the operator stacking the matrix \mathbf{H} into a vector columnwise, $\mathbf{R}^{1/2}(\mathbf{R}^{1/2})^H = \mathbf{R}$, and \mathbf{R} is the covariance matrix that can be expressed as

$$\mathbf{R} = E[\text{vec}(\mathbf{H}) \text{vec}(\mathbf{H})^H], \quad (5)$$

where superscript H is Hermitian operator. \mathbf{H}_w is normalized so that its Frobenius norm satisfies $E[\|\mathbf{H}_w\|_F^2] = M_T M_R$. This normalization has the same physical meaning as (1), that is, path loss calibration. The full-correlation model is acknowledged as the most accurate model. However, it suffers from huge covariance matrix size and analytical intractability.

The Kronecker model assumes separable \mathbf{R} , that is,

$$\mathbf{R} = \mathbf{R}_t \otimes \mathbf{R}_r, \quad (6)$$

where \otimes denotes Kronecker product and \mathbf{R}_t and \mathbf{R}_r are covariance matrices at the transmit and receive sides, respectively. The superscript T is transpose operator. Under this assumption, \mathbf{H} can be represented using the so-called Kronecker model [1],

$$\mathbf{H}_{\text{Kron}} = \mathbf{R}_r^{1/2} \mathbf{H}_w \mathbf{R}_t^{1/2}. \quad (7)$$

This model has been verified in [2, 3, 5] by real-life measurements. This model is relatively simple and analytically tractable. Furthermore, it allows independent optimizations of transmit and receive MIMO terminals. Therefore, the Kronecker model becomes the most popular MIMO channel

model. However, it was shown in [4, 6] that Kronecker model leads to inaccurate capacity estimation. It was pointed out in [4] that the Kronecker model only rendered correct capacity when the antenna number at either side is no larger than three and that it tends to underestimate capacity otherwise.

4. Measurement Results

From Section 1, it is known that there are only 200 MIMO channel samples at one single frequency, which is too few to support reliable estimation. One simple way of increasing channel samples is to treat the channel samples at different frequencies as different channel realizations (or samples). This methodology has been used in [2] for real-life measurements. In a reverberation chamber, it is usually referred as frequency stirring or electronic stirring [20] (to increase independent samples). However, the frequency stirring bandwidth has to be carefully chosen so that more independent (or less correlated) samples can be included without changing the channel statistics. From Section 3, the coherence bandwidth of the channel is around 1-2 MHz, while the stationarity bandwidth is larger than 20 MHz. In practice, the antenna bandwidth will also affect the channel characteristics, since the (effective) channel also includes the antennas. Hence, the frequency stirring bandwidth should be larger than coherence bandwidth but smaller than stationarity bandwidth and antenna bandwidth. As a result, an empirical frequency stirring bandwidth of 8 MHz (with 1-MHz frequency step) is chosen, which is limited by the monopole bandwidth. As a result, there are 1600 MIMO channel samples for capacity evaluation.

The full channel covariance matrix is estimated from \mathbf{H}_{meas} as

$$\hat{\mathbf{R}} = \frac{1}{N} \sum_{n=1}^N \text{vec}(\mathbf{H}_{\text{meas}}) \text{vec}(\mathbf{H}_{\text{meas}})^H, \quad (8)$$

where $N = 1600$ is the number of samples. Similarly, estimations of the covariance matrices at the transmit and receive sides are, respectively,

$$\hat{\mathbf{R}}_t = \frac{1}{NM_R} \sum_{n=1}^N (\mathbf{H}_{\text{meas}}^H \mathbf{H}_{\text{meas}})^T, \quad (9)$$

$$\hat{\mathbf{R}}_r = \frac{1}{NM_T} \sum_{n=1}^N \mathbf{H}_{\text{meas}} \mathbf{H}_{\text{meas}}^H.$$

Note that covariance matrices calculated using (8) and (9) include both antenna efficiencies and correlation coefficients. The corresponding ergodic capacity of the full-correlation model is

$$\hat{C}_{\text{full}} = \frac{1}{N} \sum_{n=1}^N \left\{ \log_2 \left[\det \left(\mathbf{I} + \frac{\gamma}{M_T} \hat{\mathbf{H}}_{\text{full}} \hat{\mathbf{H}}_{\text{full}}^H \right) \right] \right\}, \quad (10)$$

$$\text{vec}(\hat{\mathbf{H}}_{\text{full}}) = \hat{\mathbf{R}}^{1/2} \text{vec}(\mathbf{H}_w).$$

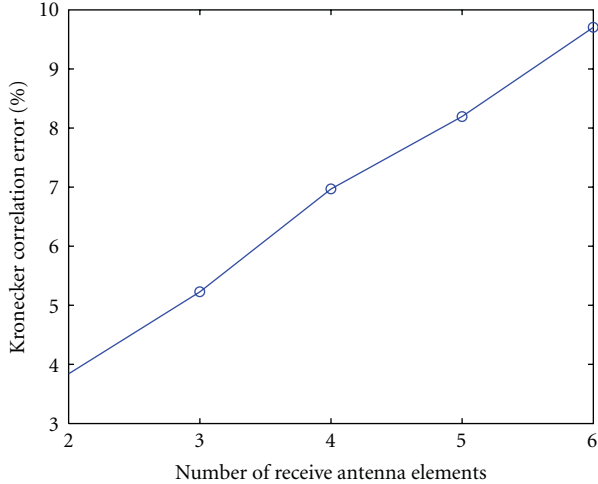


FIGURE 2: Kronecker correlation error as a function of receive monopole number with the three wall antennas fixed as transmit antenna.

Similarly, the corresponding ergodic capacity of the Kronecker model is

$$\hat{C}_{\text{Kron}} = \frac{1}{N} \sum_{n=1}^N \left\{ \log_2 \left[\det \left(\mathbf{I} + \frac{\gamma}{M_T} \hat{\mathbf{H}}_{\text{Kron}} \hat{\mathbf{H}}_{\text{Kron}}^H \right) \right] \right\}, \quad (11)$$

$$\hat{\mathbf{H}}_{\text{Kron}} = \hat{\mathbf{R}}_r^{1/2} \mathbf{H}_w \hat{\mathbf{R}}_t^{1/2}.$$

Apart from comparing capacity, the discrepancy between the full-correlation and Kronecker models can be examined using the Kronecker correlation error defined in [2, 6],

$$\Psi = \frac{\left\| \hat{\mathbf{R}} - \hat{\mathbf{R}}_t \otimes \hat{\mathbf{R}}_r \right\|_F}{\left\| \hat{\mathbf{R}} \right\|_F}. \quad (12)$$

To examine the Kronecker model error as a function of the antenna element number, we fix the three wall antennas and increase the number of monopoles from two to six (the monopoles are always chosen from adjacent ones). The Kronecker correlation errors are then calculated and plotted in Figure 2. It can be seen that the Kronecker correlation model error increases with increasing receive monopole number. Similar result was shown in [2] based on real-life measurements.

From Figure 2, it is tempting to anticipate that the Kronecker model has worse capacity-estimation performance than the full-correlation model for a large antenna element number in a reverberation chamber, just as the cases for real-life multipath environments [4]. However, by comparing capacities based on the Kronecker model, full-correlation model, and measurements in the reverberation chamber (see Figures 3 and 4), it is shown that the Kronecker correlation error obtained in the chamber is a bit misleading in the sense that even when it is as high as 10%, the capacities obtained using both channel models are almost the same, in spite of the deviation from measured ones at high SNR regime.

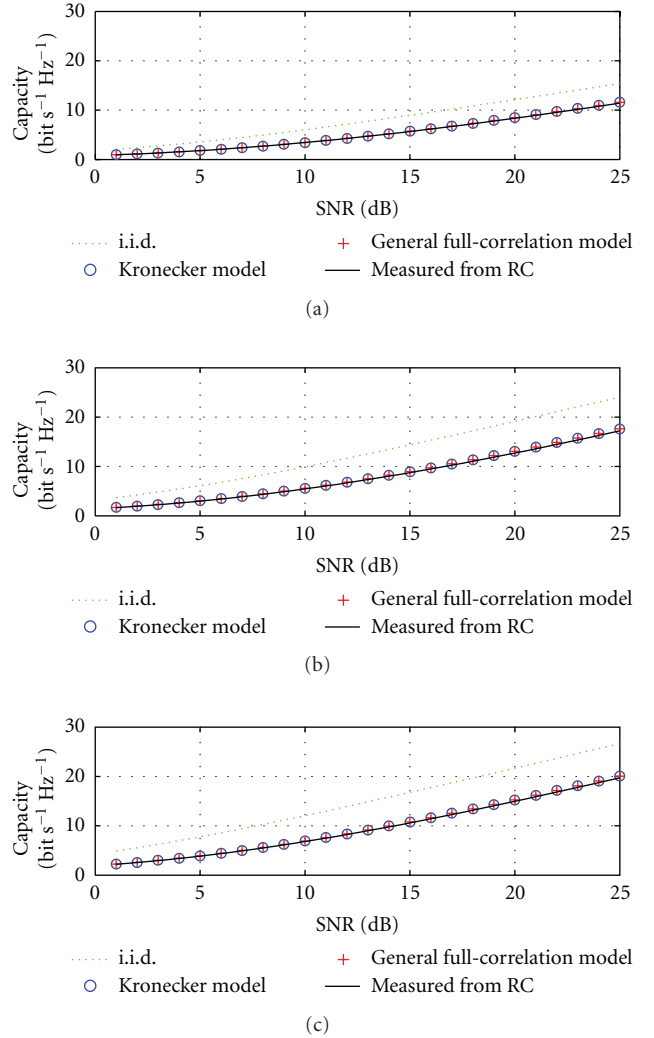


FIGURE 3: Comparison of the Kronecker model and full-correlation model against reverberation chamber measurement of 2×3 (a), 4×3 (b), and 6×3 (c) MIMO ergodic capacities, all at 900 MHz.

Figure 3 shows the comparison of ergodic capacities of the Kronecker and full-correlation models against measurements for the 2×3 (two adjacent monopoles and three wall antennas), 4×3 (four adjacent monopoles and three wall antennas), and 6×3 (all six monopoles and three wall antennas) MIMO systems. As can be seen, the Kronecker model gives almost identical ergodic capacity as the full-correlation model; both models well predict ergodic capacity from measured channel in the chamber. Both Kronecker and full-correlation models slightly overestimate the measured ergodic capacity as the monopole number exceeds three. The ergodic capacity of the corresponding i.i.d. channels are also plotted for each case. The capacity degradation of the measurement from the corresponding i.i.d. channel is due to antenna correlations and efficiencies.

Figure 4 shows the CDFs of the capacities from the Kronecker model, full-correlation model, and measurements for the same 2×3 , 4×3 , and 6×3 MIMO systems with SNRs

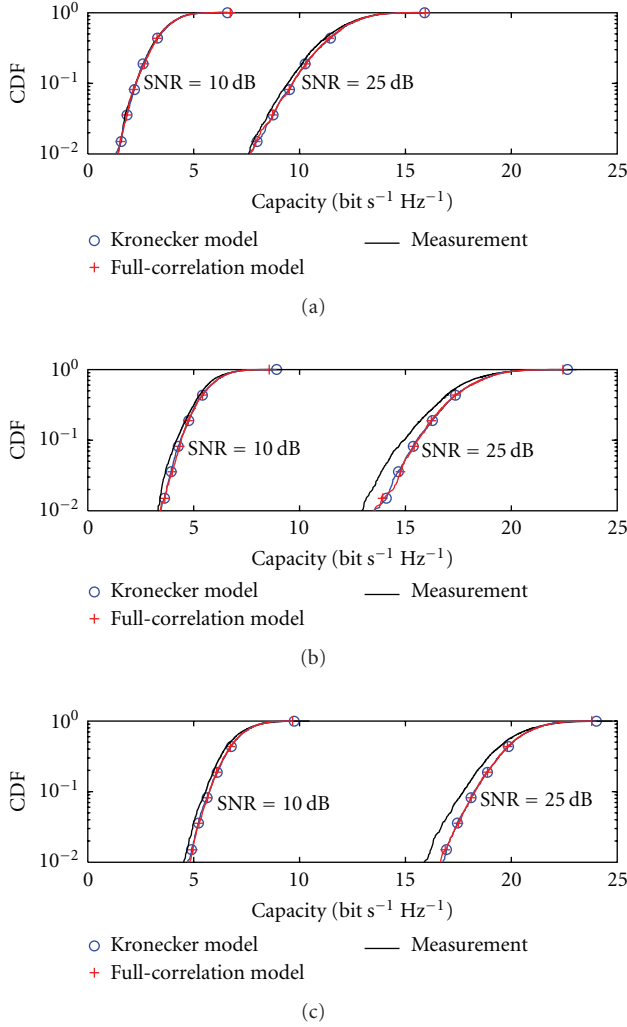


FIGURE 4: Comparison of the Kronecker model and full-correlation model against reverberation chamber measurement of 2×3 (a), 4×3 (b), and 6×3 (c) CDF of MIMO capacities, with SNR = 10 dB and 25 dB, all at 900 MHz.

of 10 dB and 25 dB. For all cases, it is seen that the Kronecker and full-correlation models give almost the same result. However, both models overestimate the measured capacity CDFs for more than three antenna elements, especially at high SNR regime, opposite to the capacity underestimation of the Kronecker model observed in [4] based on real-life measurements. The capacity overestimation of the Kronecker model was also observed in [2] for a 3×3 MIMO system based on real-life measurements. Note that it is shown in [21] that Kronecker model could also overestimate capacity.

It is shown that the Kronecker model has the same performance as the full-correlation model because that multibounce rich scattering property of the chamber makes the correlations at transmit and receive sides separable [22]. And, due to this property, the reverberation chamber can be used to characterize the MIMO performance of a MIMO terminal independent of the other MIMO end, which is highly desired in OTA MIMO terminal tests.

5. Multivariate Normality Test

The good agreement between the Kronecker model and the other two advanced models means that, unlike in real-life multipath environments, the discrepancy of capacity of the Kronecker model with the measured one in the reverberation chamber is not due to the Kronecker structure. Instead, it is probably because the entries of the measured MIMO channel matrix are not jointly Gaussian (or normal). It has been found that the Henze-Zirkeler's test [23] has a good overall power against other alternatives to MVN [6, 24]. Therefore, it is applied to the measured channel matrices in the chamber.

Let $\mathbf{h}_n = \text{vec}(\mathbf{H}_{\text{meas}})$ be the vector of the n th channel sample, then the test statistic is

$$T = \frac{1}{N} \sum_{n,m=1}^N \exp \left[-\frac{\beta^2}{2} (\mathbf{h}_n - \mathbf{h}_m)^H \hat{\mathbf{R}}^{-1} (\mathbf{h}_n - \mathbf{h}_m) \right] - 2(1 + \beta^2)^{-M_T M_R / 2} \times \sum_{n=1}^N \exp \left[-\frac{\beta^2}{2(1 + \beta^2)} (\mathbf{h}_n - \bar{\mathbf{h}})^H \hat{\mathbf{R}}^{-1} (\mathbf{h}_n - \bar{\mathbf{h}}) \right] + N(1 + \beta^2)^{-M_T M_R / 2}, \quad (13)$$

where

$$\beta = \frac{1}{\sqrt{2}} \left[\frac{N(2M_T M_R + 1)}{4} \right]^{1/M_T M_R + 4}, \quad (14)$$

$$\bar{\mathbf{h}} = \frac{1}{N} \sum_n \mathbf{h}_n.$$

The mean and variance of T are, respectively,

$$\mu = 1 - (1 + 2\beta^2)^{-M_T M_R / 2} \times \left[1 + \frac{M_T M_R \beta^2}{1 + 2\beta^2} + \frac{M_T M_R (M_T M_R + 2) \beta^4}{(1 + 2\beta^2)^2} \right], \quad (15)$$

$$\sigma^2 = 2(1 + 4\beta^2)^{-M_T M_R / 2} + 2(1 + 2\beta^2)^{-M_T M_R} \times \left[1 + \frac{2M_T M_R \beta^4}{(1 + 2\beta^2)^2} + \frac{3M_T M_R (M_T M_R + 2) \beta^8}{4(1 + 2\beta^2)^4} \right] - 4w^{-M_T M_R / 2} \times \left[1 + \frac{3M_T M_R \beta^4}{2w} + \frac{M_T M_R (M_T M_R + 2) \beta^8}{2w^2} \right]. \quad (16)$$

Let the null hypothesis be that \mathbf{H}_{meas} is MVN, that is, the test statistic T is approximately lognormally distributed. The probability that the null hypothesis is rejected although it is true is called significance level [25]. If the complementary CDF (CCDF) at T for a lognormal distribution (P value),

$$P = \frac{1}{\sqrt{2\pi\sigma^2}} \int_T^\infty \frac{1}{t} \exp \left[-\frac{(\ln t - \mu)^2}{2\sigma^2} \right] dt, \quad (17)$$

TABLE 1: P value of Henze-Zirkeler's test.

	Number of wall antennas: 1	Number of wall antennas: 2	Number of wall antennas: 3
Number of Monopoles: 1	0.850	0.196	0.000
Number of Monopoles: 2	0.657	0.060	0.000
Number of Monopoles: 3	0.370	0.000	0.000
Number of Monopoles: 4	0.230	0.000	0.000
Number of Monopoles: 5	0.066	0.000	0.000
Number of Monopoles: 6	0.020	0.000	0.000

is no smaller than the significance level, \mathbf{H}_{meas} satisfies MVN. Otherwise, \mathbf{H}_{meas} does not satisfy MVN. A good significance level for Henze-Zirkeler's MVN test is found to be 0.05 [25], which is also used in this paper.

Applying the Henze-Zirkeler's test to the measured channel matrices, it is found that every subchannel coefficient of \mathbf{H}_{meas} is still in (complex) normal distribution, but they are together not jointly normal, that is, \mathbf{H}_{meas} does not satisfy MVN. This finding is a bit surprising, since it is well known the single-input single-output (SISO) channel in a reverberation chamber is in (complex) normal distribution [12]. And it is usually assumed that MIMO channels in the chamber are jointly normal. To find out what is the reason of the non-MVN, the submatrices of \mathbf{H}_{meas} are tested separately. The corresponding P values are listed in Table 1. By comparing the P values with the significant level (0.05), it is found that the subchannel vectors of the monopoles (for one wall antenna) are jointly normal up to five monopole elements, while the subchannel vectors of the wall antennas (for one monopole) are only jointly normal for two wall antennas, that is, the subchannels of the three wall antennas not jointly normal.

It is found that the channels with large MIMO sizes show strong non-MVN and that channels with MIMO small size (e.g., 2×2) approximately satisfy MVN. The different MVN properties for the monopole array and wall antennas are due to the fact that the monopole array is uniformly and circularly distributed (with the same polarization), while the wall antennas are located arbitrarily on three different walls with orthogonal polarizations (which is necessary to keep a desired polarization balance). Thus, the monopole array satisfies antenna stationarity (i.e., antenna correlation depends only on the antenna element separation, not the element positions) [19], while wall antennas do not. The antenna stationarity of an antenna array enables its correlation matrix to converge, which guarantees MVN of the channels seen by the array (cf. weakly converging Gaussian vectors theorem [26]). Note that a well-stirred reverberation chamber is polarization balanced, that is, there is no polarization preference in the chamber. Thus, there is no need to introduce a polarization matrix to the Kronecker model as for the polarization-unbalanced cases [1].

Due to the non-MVN of \mathbf{H}_{meas} , neither of the above-mentioned channel models can estimate the MIMO capacity accurately, because all of them involve \mathbf{H}_w (i.i.d. zero mean complex Gaussian matrix). It can be seen from the MIMO capacity formula (2) that the channel model error is additively increased by MIMO size and multiplicatively

increased by SNR. This explains why the capacity estimation error increases with either increasing MIMO size or increasing SNR. And, therefore, the non-MVN is the main contribution to capacity estimation errors of the channel models in the reverberation chamber. It seems that the only way to circumvent this problem is to give up the MVN assumption in channel modeling. However, the ultimate goal of channel modeling is to find a model that can predict the actual channel correctly and, at the same time, can be used with reasonably low complexity from communication- and information-theoretic viewpoints. Since MVN is virtually the only mathematically tractable multivariate distribution [26], any model giving up the MVN assumption might not be very much useful from communication- and information-theoretic point of views, even though it might offer better estimation accuracy. Therefore, no effort is exerted in finding a model with better accuracy in this paper.

Note that the non-MVN may not be the main contribution for channel model errors for real-life multipath environments, where the full-correlation model can outperform the Kronecker model. The equal performance of all the models for the reverberation chamber measurement is because of the multibounce rich scattering property of the chamber, as discussed in Section 4.

6. Conclusion

In this paper, the MIMO channel in a reverberation chamber is studied by comparing the measurements with different channel models. It is found that both models have the same performance in terms of capacity estimation for the reverberation chamber measurements and that all of them can well predict the ergodic capacity up to six antenna elements with only slight overestimation at high-SNR regime. However, the models fail to predict the CDFs of the capacities for more than three antenna elements, especially at high SNR regime. The reason for this is because of the non-MVN of the MIMO channel in the chamber. Since all the models involves i.i.d. complex Gaussian channel, there will be modeling errors due to the non-MVN of the measured channel. And the channel modeling errors will additively increase with MIMO size and multiplicatively increase with SNR, for MIMO capacity estimations. The equal performance of the Kronecker model and the full-correlation model (for reverberation chamber measurements) implies that the correlations at transmit and receive sides can be treated separately. This is actually very desirable, since it allows characterizing the performance of

a MIMO terminal independently (without the effect of the other MIMO side) by doing an OTA test in the chamber, which in turn allows fair comparisons of different MIMO terminals.

Acknowledgments

This work has been supported by The Swedish Governmental Agency for Innovation Systems (VINNOVA) within the VINN Excellence Center Chase. The author would like to thank Dr. Li Yang and the anonymous reviewers for their helpful comments to increase the quality of this paper.

References

- [1] A. Paulraj, R. Nabar, and D. Gore, *Introduction to Space-Time Wireless Communication*, Cambridge University Press, Cambridge, Mass, USA, 2003.
- [2] K. Yu, M. Bengtsson, B. Ottersten, D. McNamara, P. Carlsson, and M. Beach, "Modeling of wide-band MIMO radio channels based on NLoS indoor measurements," *IEEE Transactions on Vehicular Technology*, vol. 53, no. 3, pp. 655–665, 2004.
- [3] J. P. Kermoal, L. Schumacher, K. I. Pedersen, P. E. Mogensen, and F. Frederiksen, "A stochastic MIMO radio channel model with experimental validation," *IEEE Journal on Selected Areas in Communications*, vol. 20, no. 6, pp. 1211–1226, 2002.
- [4] H. Özcelik, M. Herdin, W. Weichselberger, J. Wallace, and E. Bonek, "Deficiencies of "Kronecker" MIMO radio channel model," *Electronics Letters*, vol. 39, no. 16, pp. 1209–1210, 2003.
- [5] D. Chizhik, J. Ling, P. W. Wolniansky, R. A. Valenzuela, N. Costa, and K. Huber, "Multiple-input-multiple-output measurements and modeling in Manhattan," *IEEE Journal on Selected Areas in Communications*, vol. 21, no. 3, pp. 321–330, 2003.
- [6] T. Svantesson and J. W. Wallace, "Tests for assessing multivariate normality and the covariance structure of MIMO data," in *Proceedings of the IEEE International Conference on Acoustics, Speech, and Signal Processing*, Hong Kong, April 2003.
- [7] K. Rosengren and P.-S. Kildal, "Radiation efficiency, correlation, diversity gain and capacity of a six-monopole antenna array for a MIMO system: theory, simulation and measurement in reverberation chamber," in *Proceedings of the IEEE Microwaves, Optics and Antenna*, vol. 152, pp. 7–16, February 2005.
- [8] J. F. Valdés, M. A. Fernandez, A. M. Gonzalez, and D. A. Hernandez, "The influence of efficiency on receive diversity and MIMO capacity for Rayleigh-fading channels," *IEEE Transactions on Antennas and Propagation*, vol. 56, no. 5, pp. 1444–1450, 2008.
- [9] L. Garcia-Garcia, B. Lindmark, N. Jaldén, and C. Orlenius, "MIMO capacity of antenna arrays evaluated using radio channel measurements, reverberation chamber and radiation patterns," *IET Microwaves, Antennas and Propagation*, vol. 1, no. 6, pp. 1160–1169, 2007.
- [10] O. Delangre, P. de Doncker, M. Lienard, and P. Degauque, "Coupled reverberation chambers for emulating MIMO channels," *Comptes Rendus Physique*, vol. 11, no. 1, pp. 30–36, 2010.
- [11] X. Chen, P.-S. Kildal, J. Carlsson, and J. Yang, "Comparison of ergodic capacities from wideband MIMO antenna measurements in reverberation chamber and anechoic chamber," *IEEE Antennas and Wireless Propagation Letters*, vol. 10, pp. 446–449, 2011.
- [12] J. G. Kostas and B. Boverie, "Statistical model for a mode-stirred chamber," *IEEE Transactions on Electromagnetic Compatibility*, vol. 33, no. 4, pp. 366–370, 1991.
- [13] R. Vaughan and J. B. Andersen, *Channels, Propagation and Antennas for Mobile Communications*, Intelligent Energy Europe, London, UK, 2003.
- [14] D. A. Hill, "Plane wave integral representation for fields in reverberation chambers," *IEEE Transactions on Electromagnetic Compatibility*, vol. 40, no. 3, pp. 209–217, 1998.
- [15] X. Chen, P.-S. Kildal, C. Orlenius, and J. Carlsson, "Channel sounding of loaded reverberation chamber for over-the-air testing of wireless devices: coherence bandwidth versus average mode bandwidth and delay spread," *IEEE Antennas and Wireless Propagation Letters*, vol. 8, pp. 678–681, 2009.
- [16] G. Matz, "Characterization of non-WSSUS fading dispersive channels," in *Proceedings of the International Conference on Communications (ICC '03)*, pp. 2480–2484, Anchorage, Alaska, USA, May 2003.
- [17] C. L. Holloway, D. A. Hill, J. M. Ladbury, P. F. Wilson, G. Koepke, and J. Coder, "On the use of reverberation chamber to simulate a rician radio environment for the testing of wireless devices," *IEEE Transactions on Antennas and Propagation*, vol. 54, no. 11, pp. 3167–3177, 2006.
- [18] H. Fielitz, K. A. Remley, C. L. Holloway, Q. Zhang, Q. Wu, and D. W. Matolak, "Reverberation-chamber test environment for outdoor urban wireless propagation studies," *IEEE Antennas and Wireless Propagation Letters*, vol. 9, Article ID 5406096, pp. 52–56, 2010.
- [19] M. Herdin, *Non-stationary indoor MIMO radio channels*, Ph.D. thesis, Vienna University of Technology, Vienna, Austria, 2004.
- [20] D. A. Hill, "Electronic mode stirring for reverberation chambers," *IEEE Transactions on Electromagnetic Compatibility*, vol. 36, no. 4, pp. 294–299, 1994.
- [21] V. Raghavan, J. H. Kotecha, and A. M. Sayeed, "Why does the Kronecker model result in misleading capacity estimates?" *IEEE Transactions on Information Theory*, vol. 56, no. 10, Article ID 5571876, pp. 4843–4864, 2010.
- [22] A. S. Y. Poon, D. N. C. Tse, and R. W. Brodersen, "Impact of scattering on the capacity, diversity, and propagation range of multiple-antenna channels," *IEEE Transactions on Information Theory*, vol. 52, no. 3, pp. 1087–1100, 2006.
- [23] N. Henze and B. Zirkler, "A class of invariant consistent tests for multivariate normality," *Communications in Statistics—Theory and Methods*, vol. 19, no. 10, pp. 3595–3618, 1990.
- [24] A. Trujillo-Ortiz, R. Hernandez-Walls, K. Barba-Rojo, and L. Cupul-Magana, *HZmvntest: Henze-Zirkler's Multivariate Normality Test*, 2007.
- [25] R. B. Agostino and M. A. Stephen, *Goodness-of-Fit Techniques*, Marcel Dekker, New York, NY, USA, 1986.
- [26] I. I. Gikhman and A. V. Skorokhod, *Introduction to the Theory of Random Processes*, Dover publication, New York, NY, USA, 1996.

Research Article

Effect of Polarization on the Correlation and Capacity of Indoor MIMO Channels

Hsun-Chang Lo,¹ Ding-Bing Lin,² Teng-Chieh Yang,¹ and Hsueh-Jyh Li³

¹Information and Communications Research Laboratories, Industrial Technology Research Institute, Hsinchu 31040, Taiwan

²Department of Electronic Engineering, National Taipei University of Technology, Taipei 10608, Taiwan

³Graduate Institute of Communication Engineering, National Taiwan University, Taipei 10617, Taiwan

Correspondence should be addressed to Hsun-Chang Lo, shunchanglo@itri.org.tw

Received 17 June 2011; Revised 30 August 2011; Accepted 31 August 2011

Academic Editor: Yan Zhang

Copyright © 2012 Hsun-Chang Lo et al. This is an open access article distributed under the Creative Commons Attribution License, which permits unrestricted use, distribution, and reproduction in any medium, provided the original work is properly cited.

We describe a simple multiple-input/multiple-output (MIMO) channel measurement system for acquiring indoor MIMO channel responses. Four configurations of the polarization diversity antenna, referred to as VVV, YYH, YVY and VHH, were studied in terms of the capacity of indoor MIMO systems. Measurements were taken for a 3×3 MIMO system in the 2.4 GHz band. In addition, the channel capacity, singular-value decomposition, and correlation coefficient were used to explain the effects of various polarization schemes on MIMO fading channels. We also propose an analysis method for polarization channel capacity; this method includes the normalization of the received power and polarization effect for different polarization schemes. The validation of the model is based upon data collected in both light-of-sight (LOS) and non-light-of-sight (NLOS) environments. From the numerical simulation results, the proposed analysis method was close to measurements made in an indoor environment.

1. Introduction

The multiple-input/multiple-output (MIMO) system proposed by Foschini [1] is a remarkable structure that achieves large capacity through parallel channeling. However, the capacity of an MIMO system is highly dependent on the correlation properties of the channels. It is well known that because of the high isolation of orthogonal polarizations, using a cross-polarization antenna scheme symmetrically at both transmitting and receiving ends can provide a higher channel capacity than a conventional antenna polarization scheme. Moreover, part of the existing infrastructure uses cross-polarized antenna elements, which could be used to support both polarization diversity and polarization multiplexing [2]. The channel capacity for MIMO systems has been investigated theoretically [3–5]. In addition, polarization diversity that employs both vertical and horizontal polarizations can make the fading correlation between co-polarized and cross-polarized channels sufficiently low, regardless of the antenna spacing [6–8].

Recently, many researchers have examined multiple polarizations for an MIMO antenna system. Andrews et al.

[9] discussed a wireless MIMO link that provides six independent signals with three electric dipoles and three magnetic dipoles to take full rank of the channel. They assumed an antenna model with ideal polarizations and a rich scattering environment and confirmed their analysis using three orthogonal electric dipoles. Li and Yu [10] compared the MIMO correlation coefficient properties and channel capacities, and displayed different polarization combinations are an efficient way for enhancing channel capacity. Svantesson [11] studied the effect of multipath angular spread and antenna radiation patterns on the channel capacity and showed that the capacity increase is due to a combination of polarization and pattern diversity. Weichselberger and Özcelik [12] introduced a formulation for narrowband MIMO channel model characterized by eigenvectors of covariance matrices and coupling matrices to fulfill the deficiencies. The structure of formulation resembles virtual channel representation [13], in which steering vectors and virtual channel representation matrix are involved.

On the other hand, one way of reducing the level of correlation between antenna elements is to provide sufficient interelement spacing. However, for the practical application

of MIMO systems to a wireless local area network, the spacing between adjacent antenna elements cannot be too large. Given this constraint, the most probable solution is a dense MIMO array with nonnegligible correlation. In addition, the use of polarization diversity may be a solution for obtaining a more compact antenna array layout since another diversity dimension can be provided to the MIMO radio channel. Therefore, modeling the polarization diversity technique is an interesting topic of study in MIMO radio channels, and it necessitates the construction of realistic MIMO radio channel models featuring both space and polarization diversity [14–16].

Dissimilar channel environments and different incoming wave angular distributions result in a distinct spatial correlation among antenna array elements, which are the main parameters that affect MIMO channel characteristics [17]. To investigate the system performance and correlation properties, we use various antenna polarization combinations in different environments for the same antenna element spacing.

The validation of the model is supported by measurement results. Using two measurement setups having several transmitting and receiving elements, four polarization schemes have been investigated in several different LOS and NLOS rooms as indoor environments. The parameters of the MIMO model are extracted from the measurement data and fed to the model to compare simulation results with the measurement results.

In this paper, we propose an analysis method, which utilizes a correlation coefficient for both transmission and reception and the average receiving power, to calculate the MIMO channel capacity in polarization systems. In addition, we derive the optimal received-power matrix for both additive white Gaussian noise (AWGN) and multipath fading channels. Furthermore, measurement results show that the proposed analysis method outperforms traditional method in polarization systems.

The remainder of this paper is organized as follows. In Section 2, the experiments on the channel measurement setup and antenna configuration are described in detail. In Section 3, we discuss the concepts of the MIMO system, including the singular-value decomposition (SVD) method for finding channel gain, subchannel correlations, and channel capacity. The normalization method for comparing the effect of various polarization schemes is mentioned in this section. In Section 4, the channel capacity and correlation coefficient of the measured channel are calculated, and some meaningful results are revealed. Finally, we present conclusions in Section 5.

2. Measurement Setup

MIMO measurements with an $M \times N$ setup, where N and M are the numbers of elements at the transmitter (Tx) and receiver (Rx), respectively, are conducted with $M = N = 3$. A simplified sketch of the MIMO measurement setup is shown in Figure 1.

To measure the response of the single-input/single-output (SISO) channel, a two-port vector network analyzer

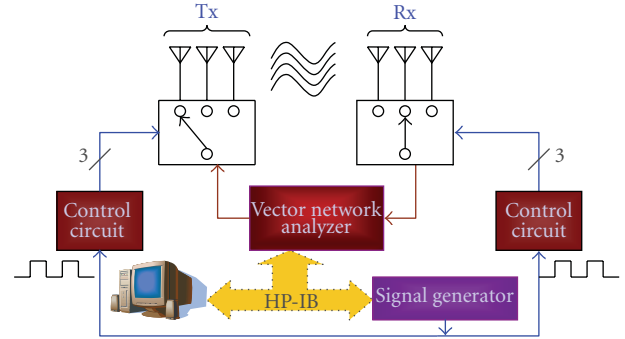


FIGURE 1: MIMO measurement system.

TABLE 1: Parameters of measurement.

Central frequency	2.4 GHz
Frequency span	500 MHz
Number of frequency points	801
Antenna type	2.4 GHz omniantenna
No. of transmit antennas	3
No. of receive antennas	3

is used. Both Tx and Rx are attached to a 1-to-3 switch with switching times of 15 s and 5 s for Tx and Rx, respectively. Furthermore, a signal generator is required to control the status of the switches. A personal computer is used to acquire the measured data and to remotely control the signal generator so that the correct clock signal is sent through the general-purpose interface bus. During the measurement, one of the transmitting antennas is switched on, and three receiving antennas are activated one after the other. Next, the second transmitting antenna is switched on, and the control circuit at the receiver activates the receiving antennas successively. The process is repeated for all the transmitting antennas. We assume that the indoor channel is quasistatic so that we can measure each radio link by controlling the switching circuits. The measuring time for each link is 5 s, so it takes about 45 s to complete a 3×3 MIMO channel matrix measurement. The parameters of our measurement are listed in Table 1.

2.1. Measurement Environment. The measurement sites are located in Electrical Engineering Building II at the National Taiwan University campus. Two dissimilar environments are selected for their different characteristics. Figure 2 shows the equipment and setting for indoor channel measurements. The size of the room is about $8 \text{ m} \times 8 \text{ m}$. The transmitting antenna array is fixed at the center of the classroom, and the receiver is placed at eight locations. These locations lie on the circumference of a circle with a radius of 3 m that is centered at the center of the room; this means that all eight locations are equidistant from the transmitter. Each receiving antenna array is moved around a 1-m^2 area to obtain channel responses for sixteen positions. As a result, we obtain a total of 128 MIMO channel matrices at the end of the experiment. Figure 3 shows the placement of equipment in two rooms on

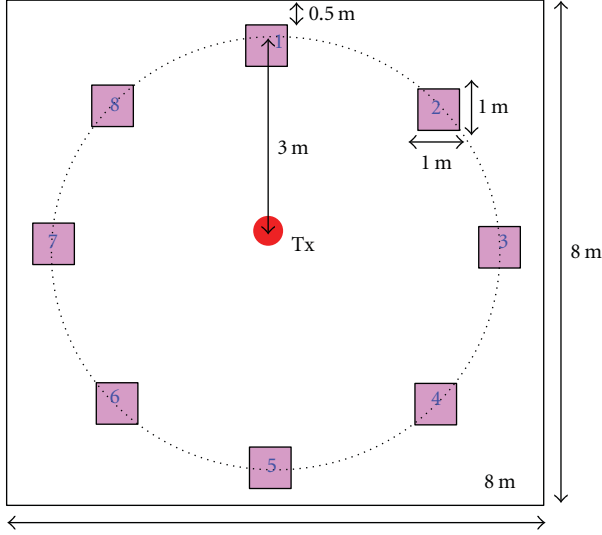


FIGURE 2: The experimental layout for indoor LOS environment.

the same floor for the NLOS environment. There is a concrete wall with a thickness of 10 cm between the two rooms. In Figure 3, the locations of the receiving and transmitting antenna arrays are denoted as “X” and “•”, respectively. The height of the antenna arrays at Tx and Rx is 1.2 m. The measurements are made in the absence of bodily movement to investigate time-stationary picocell environments.

For both environments, a large number of receiving locations are used to gather more statistical information for the environment. In addition, to remove the effect of attenuation or loss resulting from equipment, we calibrate the data by dividing the measured frequency response by that measured for 1-m Tx-Rx separation.

2.2. Antenna Configuration. In this study, we investigate different polarization configurations: vertical (V), horizontal (H), and slanting (Y) polarizations (angle of slant = $\pm 45^\circ$). The relative orientations of the transmitting antenna array and receiving antenna array are shown in Figure 4. Whenever the receiving antenna array is moved, the same relative orientation between the transmitting antenna array and the receiving antenna is maintained for the same polarization type. Figure 5 shows photos of the four different polarization combinations, in which each antenna has an omnidirectional pattern and a 5-dBi antenna gain. At both transmitting and receiving ends, the adjacent antennas are spaced half wavelengths apart. Transmission is carried out at 2.4 GHz center frequency with a frequency span of 500 MHz over 801 individual frequencies (points).

3. Narrowband MIMO Channel Model Analysis

In this section, we analyze the measurement results obtained for the MIMO radio channels used in narrowband systems. Although our measurement system is wideband, we only use data in the frequency range 2.35–2.45 GHz, corresponding to 161 frequency points in the central region, because the

antenna possesses a narrowband operational bandwidth. Thus, our discussion deals with narrowband analysis. Moreover, to analyze the capacity and eigenvalue of the measured data, we first need to normalize the data. For each location, let H_f^k denote the channel matrix measured at the k th position ($k = 1-16$) and f th frequency point.

3.1. Normalization for Different Polarizations. We discuss the relationship between polarization and channel capacity. The method for normalizing the VVV configuration is defined as follows:

$$\frac{1}{F \times K \times M \times N} \sum_f \sum_k \|H_f^k\|_F^2 = E, \quad (1)$$

$$\|H\|_F^2 = \sum_{i=1}^M \sum_{j=1}^N |h_{ij}|^2, \quad (2)$$

$$\mathbf{H} = \begin{bmatrix} h_{11} & h_{12} & \cdots & h_{1N} \\ h_{21} & h_{22} & \cdots & h_{2N} \\ \vdots & \vdots & \ddots & \vdots \\ h_{M1} & h_{M2} & \cdots & h_{MN} \end{bmatrix}, \quad (3)$$

$$\hat{H}_f^k = \frac{H_f^k}{\sqrt{E}}, \quad (4)$$

where \mathbf{H} is an $M \times N$ channel matrix at one position and one frequency point. $\|H\|_F^2$ is the square of the Frobenius norm of \mathbf{H} . Moreover, k denotes the k th position (where the total number of positions in one location is denoted as K) in each location and f denotes the f th frequency point (where the total number of frequency points is denoted as F).

The normalization method is different for the VVY case. We use the VVV case for the same location as the baseline. We first calculate the mean power of all antenna elements in the VVV case over all the frequency points and positions in the same location. We then normalize all the VVY channel matrices by the square root of the mean power for the VVV case:

$$\frac{1}{F \times K \times M \times N} \sum_f \sum_k \|H_f^k|_{\text{VVV}}\|_F^2 = E, \quad (5)$$

$$\hat{H}_f^k|_{\text{VVY}} = \frac{H_f^k|_{\text{VVY}}}{\sqrt{E}},$$

where $H_f^k|_{\text{VVV}}$ and $H_f^k|_{\text{VVY}}$ denote the channel matrices at the k th position and f th frequency point for the VVV case and VVY case, respectively. The normalization methods for the other cases are the same as the method used for VVY normalization.

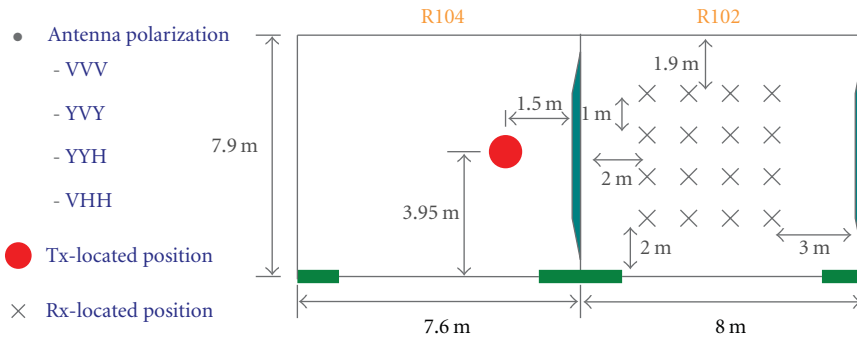


FIGURE 3: The experimental layout for indoor NLOS environment.

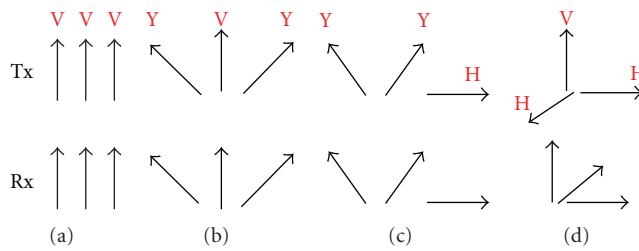


FIGURE 4: Four antenna configurations which are denoted as (a) VVV, (b) YVY, (c) YYH, and (d) VHH.

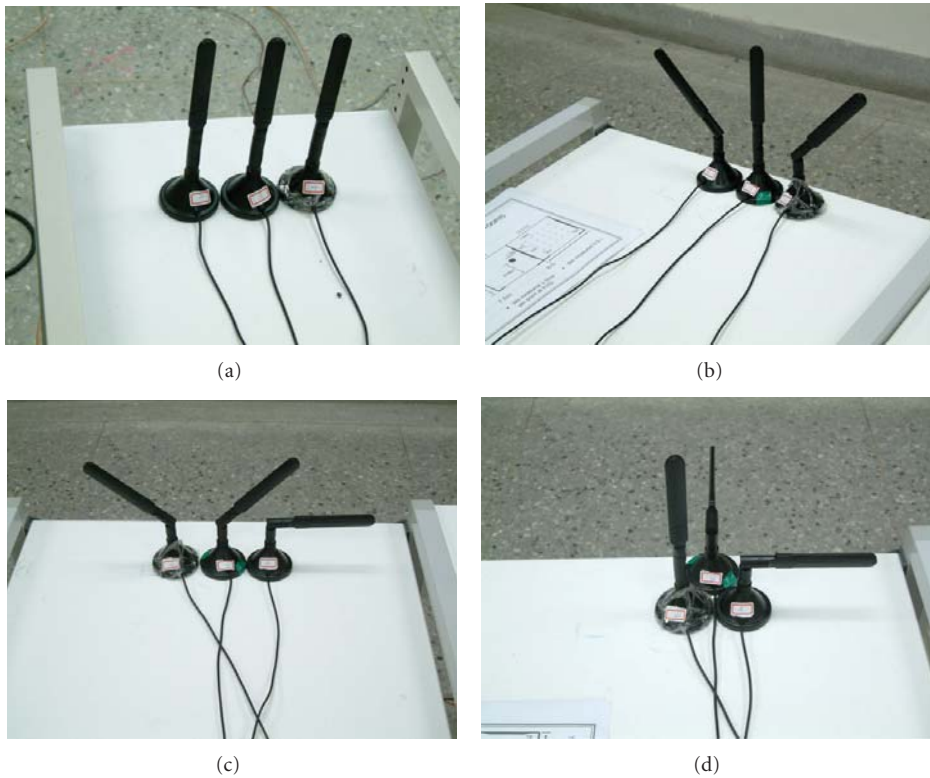


FIGURE 5: Photos of the four different polarization combinations denoted as (a) VVV, (b) YVY, (c) YYH, and (d) VHH in practical measurement environment.

3.2. *Eigenvalue and Capacity for Equal Power.* In analyzing the capacity of an MIMO system, N transmitting elements and M receiving elements are assumed, and the received signal is expressed as

$$\mathbf{y} = \mathbf{H}\mathbf{s} + \mathbf{n}, \quad (6)$$

where \mathbf{H} is an $M \times N$ channel matrix, \mathbf{s} is the transmitted signal, and \mathbf{n} is the AWGN.

For a fixed channel realization, the channel capacity has the following constraints: (1) the transmitter has no channel state information and (2) the transmitted power is equally allocated to each transmitting element. Therefore, the capacity can be expressed as [1]

$$C = \log_2 \det \left(\mathbf{I}_M + \frac{\rho}{N} \mathbf{H}\mathbf{H}^H \right) \text{ bits/s/Hz}, \quad (7)$$

where $\det(\cdot)$ denotes the determinant of a matrix, and $(\cdot)^H$ denotes a Hermitian transpose. \mathbf{I}_M is an $M \times M$ identity matrix and ρ is the average received signal-to-noise ratio.

To investigate the characteristics of \mathbf{H} , we can perform an SVD of \mathbf{H} to diagonalize \mathbf{H} and determine the eigenvalues. The SVD expansion of any matrix $\mathbf{H}(M \times N)$ is written as [18]

$$\mathbf{H} = \mathbf{U}\mathbf{\Lambda}\mathbf{V}^H, \quad (8)$$

where $\mathbf{U}(M \times M)$ and $\mathbf{V}(N \times N)$ are unitary matrices, which means that $\mathbf{U}\mathbf{U}^H = \mathbf{V}\mathbf{V}^H = \mathbf{I}$. $\mathbf{\Lambda}(M \times N)$ is nonnegative and diagonal with entries specified by

$$\mathbf{\Lambda} = \text{diag}(\sqrt{\lambda_1}, \sqrt{\lambda_2}, \dots, \sqrt{\lambda_q}, 0, \dots, 0), \quad (9)$$

where $\text{diag}(\mathbf{\Lambda})$ is a vector consisting of the diagonal elements of $\mathbf{\Lambda}$; $\lambda_1, \lambda_2, \dots, \lambda_q$ are the nonzero eigenvalues of \mathbf{W} ; $q = \min(M, N)$.

The columns of \mathbf{U} and \mathbf{V} are the eigenvectors of $\mathbf{H}\mathbf{H}^H$ and $\mathbf{H}^H\mathbf{H}$ [19], respectively. The SVD (8) shows that the channel matrix \mathbf{H} can be diagonalized to a number of independent orthogonal subchannels, where the power gain of the i th channel is λ_i [20],

$$\mathbf{W} = \begin{cases} \mathbf{H}\mathbf{H}^H, & M \leq N, \\ \mathbf{H}^H\mathbf{H}, & N < M. \end{cases} \quad (10)$$

Thus, (7) can be rewritten as [20]

$$C_{\text{EP}} = \sum_{i=1}^q \log_2 \left(1 + \frac{\rho}{N} \lambda_i \right) \text{ bps/Hz}, \quad (11)$$

where $\lambda_1, \lambda_2, \dots, \lambda_q$ are nonzero eigenvalues of \mathbf{W} in (10).

Therefore, the channel capacity is affected not only by the maximal value of λ_i but also by the minimal value of λ_i . We can define the condition number as

$$\text{condition number} = \frac{\lambda_{\max}}{\lambda_{\min}}. \quad (12)$$

If a channel has a low condition number, then its correlation is low, its diversity is high, and thus its capacity is high. The channel is then said to be ‘‘well conditioned.’’ Otherwise, the channel is referred to as being ‘‘ill conditioned’’ [21].

3.3. *Subchannel Correlation.* We modify the method of analysis of channel capacity for different polarization schemes. A different polarization configuration has a different received power owing to cross-polarization. Therefore, we consider the effect of the cross-polarization ratio (XPR) in different polarization schemes. Moreover, the use of the XPR for polarization antenna systems has been previously studied.

The XPR is defined as the ratio of the copolarized average received power to the cross-polarized average received power. The XPR has been used in the capacity analysis of different polarization combinations [22].

To obtain XPRs for different polarization cases, we normalize the VVV scheme so that the average normalized power matrix is equal to one. The average received power matrix \mathbf{P} is defined as

$$P_{i,j} = \frac{1}{K} \sum_k \frac{1}{F} \sum_f |h_{i,j}|_{k,f}^2, \quad (13)$$

$$\mathbf{P}_O = \begin{bmatrix} P_{1,1} & P_{1,2} & \cdots & P_{1,N} \\ P_{2,1} & P_{2,2} & \cdots & P_{2,N} \\ \vdots & \vdots & \ddots & \vdots \\ P_{M,1} & P_{M,2} & \cdots & P_{M,N} \end{bmatrix} \in \mathbb{R}^{M \times N}. \quad (14)$$

From (13), we obtain the matrix $\mathbf{P} \in \mathbb{R}^{M \times N}$ for different polarization schemes. Next, we obtain \mathbf{P}_O as the normalized power matrix and use the VVV case in the same location as the baseline. Other polarization schemes refer to the VVV scheme. Finally, the proposed MIMO channel matrix is written as

$$\mathbf{H} = \mathbf{R}_{H,\text{Rx}}^{1/2} \mathbf{G} \mathbf{P}_O^{1/2} \left[\mathbf{R}_{H,\text{Tx}}^{1/2} \right]^T, \quad (15)$$

$$\mathfrak{R}_H^{\text{Tx}} = \begin{bmatrix} \rho_{11}^{\text{Tx}} & \rho_{12}^{\text{Tx}} & \cdots & \rho_{1N}^{\text{Tx}} \\ \rho_{21}^{\text{Tx}} & \rho_{22}^{\text{Tx}} & \cdots & \rho_{2N}^{\text{Tx}} \\ \vdots & \vdots & \ddots & \vdots \\ \rho_{N1}^{\text{Tx}} & \rho_{N2}^{\text{Tx}} & \cdots & \rho_{NN}^{\text{Tx}} \end{bmatrix}_{N \times N}, \quad (16)$$

$$\mathfrak{R}_H^{\text{Rx}} = \begin{bmatrix} \rho_{11}^{\text{Rx}} & \rho_{12}^{\text{Rx}} & \cdots & \rho_{1M}^{\text{Rx}} \\ \rho_{21}^{\text{Rx}} & \rho_{22}^{\text{Rx}} & \cdots & \rho_{2M}^{\text{Rx}} \\ \vdots & \vdots & \ddots & \vdots \\ \rho_{M1}^{\text{Rx}} & \rho_{M2}^{\text{Rx}} & \cdots & \rho_{MM}^{\text{Rx}} \end{bmatrix}_{M \times M},$$

where \mathbf{G} is an $M \times M$ matrix containing independent and identically distributed $\text{CN}(0,1)$ elements, and \mathbf{R}_H^{Tx} and \mathbf{R}_H^{Rx} are transmitting and receiving correlation matrices respectively. Then, ρ_{ij}^{Tx} (or ρ_{ij}^{Rx}) is the correlation coefficient of the i th and j th transmitting (or receiving) antennas.

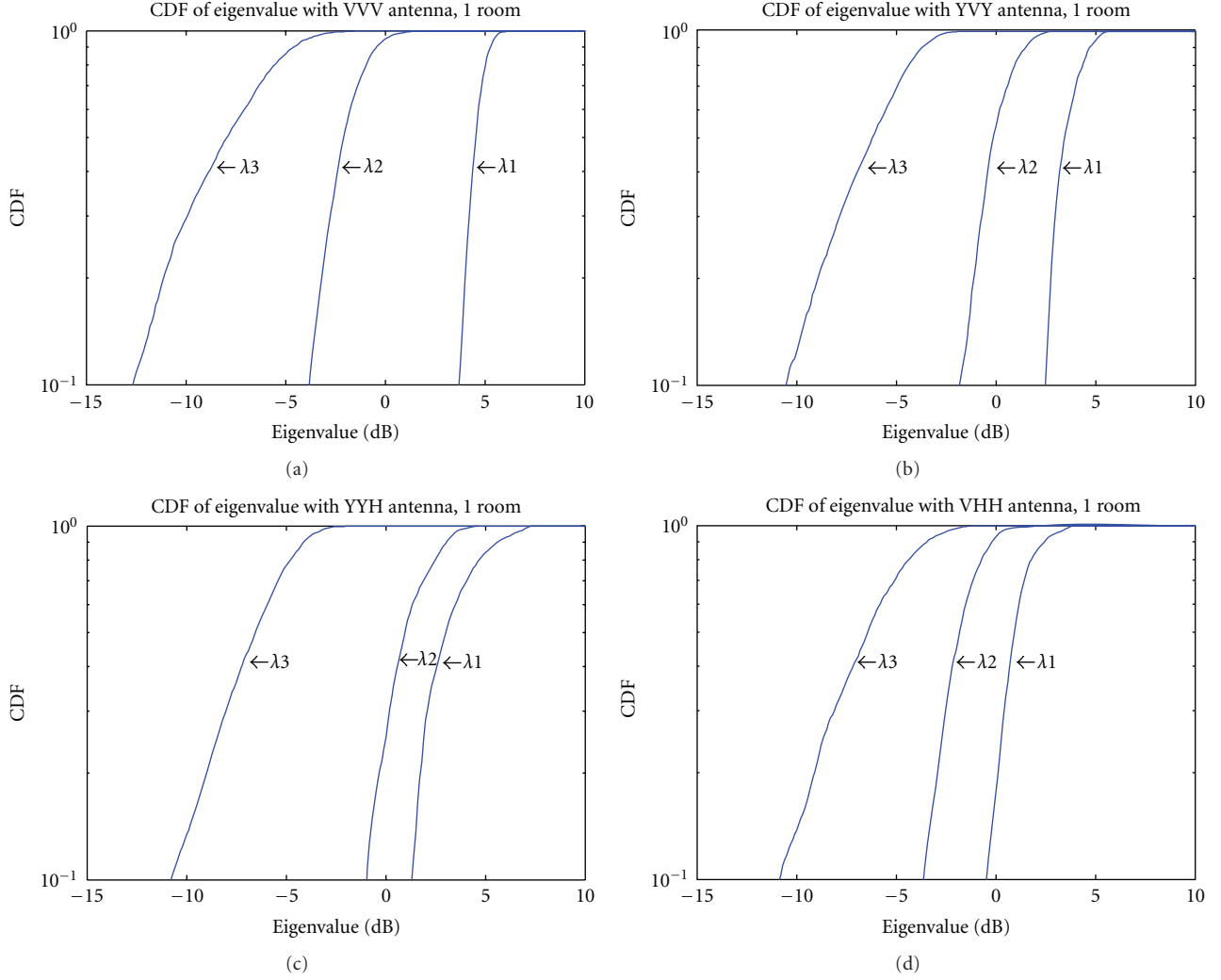


FIGURE 6: The plots of CDF versus eigenvalues when the polarization system employing (a) VVV, (b) YVY, (c) YYH, and (d) VHH cases in LOS indoor environment.

For a measured MIMO channel matrix $\mathbf{H} \in \mathbf{C}^{M \times N}$ as denoted in (3), we can thus define the transmitter and receiver correlation coefficients as

$$\begin{aligned} \rho_{n_1 n_2}^{\text{Tx}}(k, f) &= \langle h_{mn_1}, h_{mn_2} \rangle = \frac{\sum_m h_{m, n_1} h_{m, n_2}^*}{\sqrt{\sum_m |h_{m, n_1}|^2 \sum_m |h_{m, n_2}|^2}}, \\ \rho_{m_1 m_2}^{\text{Rx}}(k, f) &= \langle h_{m_1 n}, h_{m_2 n} \rangle = \frac{\sum_n h_{m_1, n} h_{m_2, n}^*}{\sqrt{\sum_n |h_{m_1, n}|^2 \sum_n |h_{m_2, n}|^2}}. \end{aligned} \quad (17)$$

Subsequently, the correlation coefficients are calculated as follows:

$$\rho_{n_1 n_2}^{\text{Tx}}(f) = \frac{1}{K} \sum_k \rho_{n_1 n_2}^{\text{Tx}}(k, f) \Rightarrow \rho_{n_1 n_2}^{\text{Tx}} = \frac{1}{F} \sum_f |\rho_{n_1 n_2}^{\text{Tx}}|,$$

$$\rho_{m_1 m_2}^{\text{Rx}}(f) = \frac{1}{K} \sum_k \rho_{m_1 m_2}^{\text{Rx}}(k, f) \Rightarrow \rho_{m_1 m_2}^{\text{Rx}} = \frac{1}{F} \sum_f |\rho_{m_1 m_2}^{\text{Rx}}|. \quad (18)$$

4. Measurement Results

Our experiment focuses on indoor measurements. We intend to gain a deeper understanding of the effects of different polarizations from our experimental results.

The first and the second MIMO scenario performances are illustrated in terms of the cumulative distribution functions (CDFs) of their eigenvalues, as shown in Figures 6 and 7, in which three subchannel gains are plotted as straight lines. We find that regardless of whether the LOS or NLOS environment is used, the largest eigenvalue (λ_1) in the VHH schemes is smaller than λ_1 of other polarization schemes owing to the significantly lower channel gain. Moreover, λ_1 is higher for the VVV scheme than for the YVY, YYH, and VHH schemes; thus, the channel capacity of the VHH

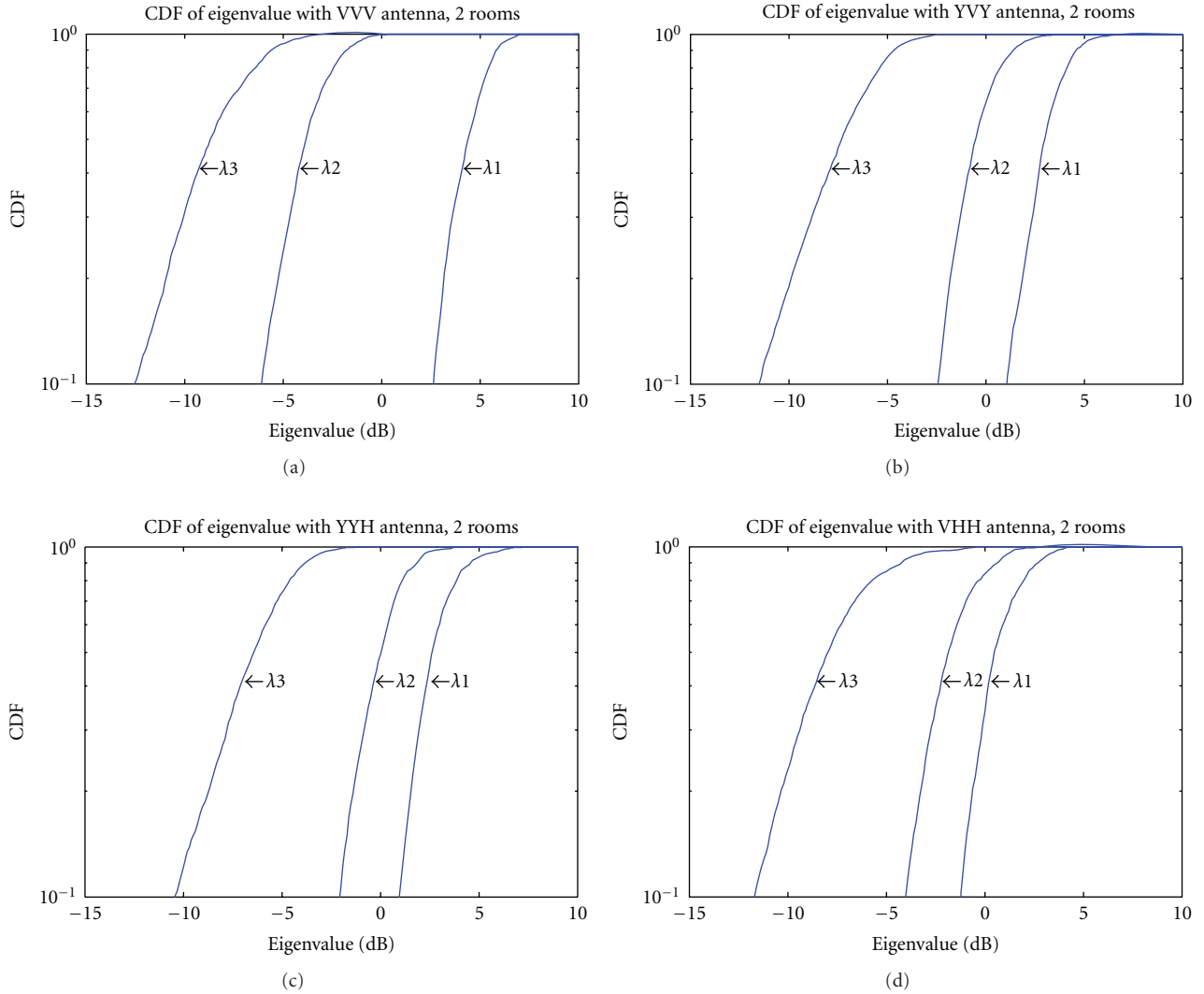


FIGURE 7: The plots of CDF versus eigenvalues when the polarization system employing (a) VVV (b) YVY (c) YYH (d) VHH cases in NLOS indoor environment.

combination in indoor environments is the smallest among the capacities of all the schemes. However, all the eigenvalues are closer to each other in the VHH case than in the other polarization cases. Hence, the VHH channel is the most well conditioned.

Let us consider the channel correlation matrices listed in Tables 2 and 3. We observe that the VVV copolarized cases have greater correlation coefficients than the other polarization cases. In addition, if the polarization between the transmitting antenna and receiving antenna is orthogonal, then the correlation coefficient is the lowest among all the polarized pairs under the same measurement environment. From this viewpoint, we study the YYH polarization scheme. The correlation coefficient $\rho_{12}(\rho_{21})$ is smaller than $\rho_{13}(\rho_{31})$ and $\rho_{23}(\rho_{32})$ owing to orthogonal polarization transmission. The same relationship holds for the YVY and VHH polarization schemes. Consequently, the correlation coefficients of

the nondiagonal matrix elements are lower; the channel of the MIMO systems is more uncorrelated; the channel has a higher capacity.

We also examine the correlation for direct path power which defines the first path in time domain among the sub-channels in the four polarization schemes. As shown in Tables 4 and 5, if the polarization between transmitting antenna and receiving antenna is orthogonal, then the correlation coefficient of the direct path power corresponds to the lowest subchannel gain among all the polarized pairs. All matrix components of VVV are 1 because of the direct path powers are close to each other. In explaining the effects of polarization combinations, we use the notation P-Q, where P and Q denote the transmitting antenna and receiving antenna, respectively. Considering the normalized power matrix (\mathbf{P}_N) in Tables 6 and 7, we note that the V-V copolarized case and the Y-Y (“V”-“H”) cross-polarized case are very

TABLE 2: Correlation matrix for different polarization schemes in LOS environment.

$\begin{pmatrix} 1 & 0.94 & 0.92 \\ 0.94 & 1 & 0.91 \\ 0.92 & 0.91 & 1 \end{pmatrix}$	$\begin{pmatrix} 1 & 0.93 & 0.92 \\ 0.93 & 1 & 0.92 \\ 0.92 & 0.92 & 1 \end{pmatrix}$
VVV, R_H^{Tx}	VVV, R_H^{Rx}
$\begin{pmatrix} 1 & 0.68 & 0.36 \\ 0.68 & 1 & 0.69 \\ 0.36 & 0.69 & 1 \end{pmatrix}$	$\begin{pmatrix} 1 & 0.68 & 0.38 \\ 0.68 & 1 & 0.69 \\ 0.38 & 0.69 & 1 \end{pmatrix}$
YVY, R_H^{Tx}	YVY, R_H^{Rx}
$\begin{pmatrix} 1 & 0.40 & 0.57 \\ 0.40 & 1 & 0.62 \\ 0.57 & 0.62 & 1 \end{pmatrix}$	$\begin{pmatrix} 1 & 0.39 & 0.58 \\ 0.39 & 1 & 0.62 \\ 0.58 & 0.62 & 1 \end{pmatrix}$
YYH, R_H^{Tx}	YYH, R_H^{Rx}
$\begin{pmatrix} 1 & 0.48 & 0.41 \\ 0.48 & 1 & 0.47 \\ 0.41 & 0.47 & 1 \end{pmatrix}$	$\begin{pmatrix} 1 & 0.49 & 0.44 \\ 0.49 & 1 & 0.47 \\ 0.44 & 0.47 & 1 \end{pmatrix}$
VHH, R_H^{Tx}	VHH, R_H^{Rx}

TABLE 3: Correlation matrix for different polarization schemes in NLOS environment.

$\begin{pmatrix} 1 & 0.92 & 0.87 \\ 0.92 & 1 & 0.90 \\ 0.87 & 0.90 & 1 \end{pmatrix}$	$\begin{pmatrix} 1 & 0.92 & 0.89 \\ 0.92 & 1 & 0.90 \\ 0.89 & 0.90 & 1 \end{pmatrix}$
VVV, R_H^{Tx}	VVV, R_H^{Rx}
$\begin{pmatrix} 1 & 0.77 & 0.54 \\ 0.77 & 1 & 0.81 \\ 0.54 & 0.81 & 1 \end{pmatrix}$	$\begin{pmatrix} 1 & 0.87 & 0.49 \\ 0.87 & 1 & 0.49 \\ 0.49 & 0.49 & 1 \end{pmatrix}$
YVY, R_H^{Tx}	YVY, R_H^{Rx}
$\begin{pmatrix} 1 & 0.37 & 0.63 \\ 0.37 & 1 & 0.68 \\ 0.68 & 0.68 & 1 \end{pmatrix}$	$\begin{pmatrix} 1 & 0.34 & 0.77 \\ 0.34 & 1 & 0.64 \\ 0.77 & 0.64 & 1 \end{pmatrix}$
YYH, R_H^{Tx}	YYH, R_H^{Rx}
$\begin{pmatrix} 1 & 0.35 & 0.21 \\ 0.35 & 1 & 0.31 \\ 0.21 & 0.31 & 1 \end{pmatrix}$	$\begin{pmatrix} 1 & 0.30 & 0.35 \\ 0.30 & 1 & 0.28 \\ 0.35 & 0.28 & 1 \end{pmatrix}$
VHH, R_H^{Tx}	VHH, R_H^{Rx}

different. The YVY cross-polarized combination shows three subchannels with considerably high gain and remaining subchannels with a lower gain; in contrast, the VVV copolarized combination shows high gains for all the subchannels, with the gains being close to each other, although the VHH scheme provides good isolation as the antenna elements are orthogonal for the transmission and reception pairs. Nevertheless, as we observe normalized received power matrices, it is almost the loss of all the subchannel gains. This phenomenon shows the benefit of adopting orthogonal polarizations. Table 8 lists the gains of different polarization schemes; these gains help to clarify the above phenomenon. As a result, in using orthogonal polarization, we lose part of the channel gain but achieve greater isolation. The same results are found for the YYH scheme.

TABLE 4: Correlation matrix of direct path power analysis for different polarization schemes in LOS environment.

$\begin{pmatrix} 1 & 1 & 1 \\ 1 & 1 & 1 \\ 1 & 1 & 1 \end{pmatrix}$	$\begin{pmatrix} 1 & 1 & 1 \\ 1 & 1 & 1 \\ 1 & 1 & 1 \end{pmatrix}$
VVV, R_H^{Tx}	VVV, R_H^{Rx}
$\begin{pmatrix} 1 & 0.95 & 0.85 \\ 0.95 & 1 & 0.95 \\ 0.85 & 0.95 & 1 \end{pmatrix}$	$\begin{pmatrix} 1 & 0.96 & 0.90 \\ 0.96 & 1 & 0.97 \\ 0.90 & 0.97 & 1 \end{pmatrix}$
YVY, R_H^{Tx}	YVY, R_H^{Rx}
$\begin{pmatrix} 1 & 0.87 & 0.96 \\ 0.87 & 1 & 0.98 \\ 0.96 & 0.98 & 1 \end{pmatrix}$	$\begin{pmatrix} 1 & 0.91 & 0.96 \\ 0.91 & 1 & 0.98 \\ 0.96 & 0.98 & 1 \end{pmatrix}$
YYH, R_H^{Tx}	YYH, R_H^{Rx}
$\begin{pmatrix} 1 & 0.27 & 0.84 \\ 0.27 & 1 & 0.38 \\ 0.84 & 0.38 & 1 \end{pmatrix}$	$\begin{pmatrix} 1 & 0.37 & 0.89 \\ 0.37 & 1 & 0.48 \\ 0.89 & 0.48 & 1 \end{pmatrix}$
VHH, R_H^{Tx}	VHH, R_H^{Rx}

TABLE 5: Correlation matrix of direct path power analysis for different polarization schemes in NLOS environment.

$\begin{pmatrix} 1 & 1 & 1 \\ 1 & 1 & 1 \\ 1 & 1 & 1 \end{pmatrix}$	$\begin{pmatrix} 1 & 1 & 1 \\ 1 & 1 & 1 \\ 1 & 1 & 1 \end{pmatrix}$
VVV, R_H^{Tx}	VVV, R_H^{Rx}
$\begin{pmatrix} 1 & 0.93 & 0.82 \\ 0.93 & 1 & 0.95 \\ 0.82 & 0.95 & 1 \end{pmatrix}$	$\begin{pmatrix} 1 & 0.91 & 0.85 \\ 0.91 & 1 & 0.93 \\ 0.85 & 0.93 & 1 \end{pmatrix}$
YVY, R_H^{Tx}	YVY, R_H^{Rx}
$\begin{pmatrix} 1 & 0.85 & 0.96 \\ 0.85 & 1 & 0.93 \\ 0.96 & 0.93 & 1 \end{pmatrix}$	$\begin{pmatrix} 1 & 0.87 & 0.92 \\ 0.87 & 1 & 0.93 \\ 0.92 & 0.93 & 1 \end{pmatrix}$
YYH, R_H^{Tx}	YYH, R_H^{Rx}
$\begin{pmatrix} 1 & 0.21 & 0.82 \\ 0.21 & 1 & 0.28 \\ 0.82 & 0.28 & 1 \end{pmatrix}$	$\begin{pmatrix} 1 & 0.29 & 0.86 \\ 0.29 & 1 & 0.32 \\ 0.86 & 0.32 & 1 \end{pmatrix}$
VHH, R_H^{Tx}	VHH, R_H^{Rx}

We now present results from the analysis of the measurement data in CDFs. The channel capacities of the four polarization schemes obtained from measurement and simulation analyses are, respectively, shown as straight and dotted lines in Figure 8 and Figure 9. The four polarization schemes—VVV, YVY, YYH, and VHH—are indicated by the symbols, \diamond , ∇ , \circ , and \square , respectively. The signal-to-noise ratio is set at 10 dB to plot the CDF of the capacity statistical properties. From the preliminary analysis result shown in Figure 8, we find that the YVY structure has the best capacity among all the investigated antenna array configurations. Moreover, when the normalized power matrix is considered with the analysis of channel capacity, the VHH scheme has the worst channel capacity among the polarization combinations.

TABLE 6: Normalized power for different polarization schemes in indoor LOS environment.

$\begin{pmatrix} 1.28 & 0.98 & 1.02 \\ 1.07 & 1.23 & 1.19 \\ 0.69 & 0.67 & 0.76 \end{pmatrix}$	$\begin{pmatrix} 1.03 & 0.70 & 0.30 \\ 0.66 & 1.3 & 60.61 \\ 0.22 & 0.74 & 1.01 \end{pmatrix}$
VVV	YVY
$\begin{pmatrix} 0.75 & 0.26 & 0.47 \\ 0.32 & 0.97 & 0.31 \\ 0.26 & 0.30 & 0.48 \end{pmatrix}$	$\begin{pmatrix} 0.75 & 0.09 & 0.14 \\ 0.10 & 0.06 & 0.11 \\ 0.13 & 0.10 & 0.23 \end{pmatrix}$
YYH	VHH

TABLE 7: Normalized power for different polarization schemes in indoor NLOS environment.

$\begin{pmatrix} 0.80 & 1.00 & 1.09 \\ 0.90 & 1.21 & 1.27 \\ 0.73 & 0.96 & 1.03 \end{pmatrix}$	$\begin{pmatrix} 1.04 & 0.55 & 0.17 \\ 0.62 & 1.03 & 0.74 \\ 0.14 & 0.50 & 1.11 \end{pmatrix}$
VVV	YVY
$\begin{pmatrix} 0.96 & 0.13 & 0.61 \\ 0.19 & 0.88 & 0.79 \\ 0.42 & 0.55 & 1.33 \end{pmatrix}$	$\begin{pmatrix} 1.00 & 0.10 & 0.12 \\ 0.13 & 0.12 & 0.16 \\ 0.12 & 0.05 & 0.61 \end{pmatrix}$
YYH	VHH

By observing the CDF of capacity analysis under different conditions, it is found that the simulation analysis method, which makes use of (15), is close to a realistic measurement environment. This method is useful for application to polarization schemes. As seen in Figure 8, using the YVY scheme in an indoor environment provides higher channel capacity owing to antenna isolation and greater total received power. As a result, we need to consider both isolation and correlation properties for describing an MIMO system that utilizes orthogonal polarized antennas. Using only one property is insufficient in determining the system performance. Therefore, the correlation property is not a sufficient measure when considering parallel transmission with orthogonal polarized schemes.

For the NLOS condition, as shown in Figure 9, we find that the YYH scheme has a higher capacity than the YVY scheme. As for the analysis result in Figure 7, λ_1 has the same power level for both the YYH and YVY schemes, but the other eigenvalues in the YYH scheme are closer to each other. Therefore, we have verified our proposed simulation analysis method and found it suitable for approximating polarization transmission and reception systems. Consequently, in attaining higher channel capacity in MIMO systems, there is a tradeoff between antenna isolation and total received power in each transceiver structure.

5. Conclusion

We introduced the concept of the MIMO system and factors that determined the channel capacity, including eigenvalues and correlation coefficients. We studied the effect of space and polarization diversity on the MIMO system in detail. Furthermore, we designed a series of experiments

TABLE 8: Average normalized power for various polarization schemes.

Measurement types	Polarization schemes			
	VVV	YVY	YYH	VHH
LOS	1	0.73	0.46	0.19
NLOS	1	0.66	0.65	0.27

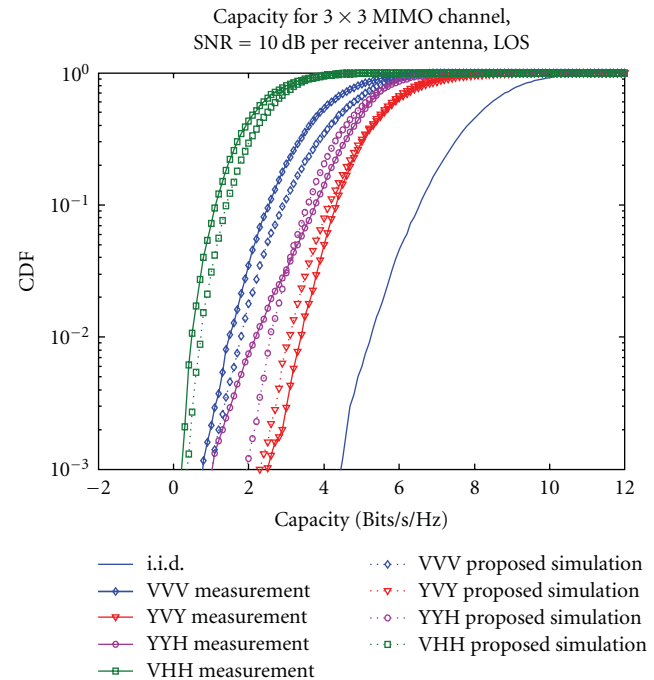


FIGURE 8: The plots of CDF versus capacities obtained by measurement analysis (solid line), proposed simulation analysis (dotted line) for dissimilar polarization systems in indoor LOS environment.

to determine the correlation between antennapolarization and the channel characteristics. From measurement data, the channel capacity and correlation coefficient were used for explaining the effects of various polarization schemes in the MIMO channels. Moreover, the concepts of normalizing the received power and the polarization effect were described in modifying the numerical analysis of the polarized channel capacity. In addition, we found that the performance of an MIMO system exploiting a copolarized antenna combination can be described simply using spatial correlation properties, but when adopting a cross-polarized antenna combination, both the isolation and correlation properties were needed to fully describe the system performance. Consequently, we found and verified the proposed algorithm of (15) which was close to realistic environment in polarization systems.

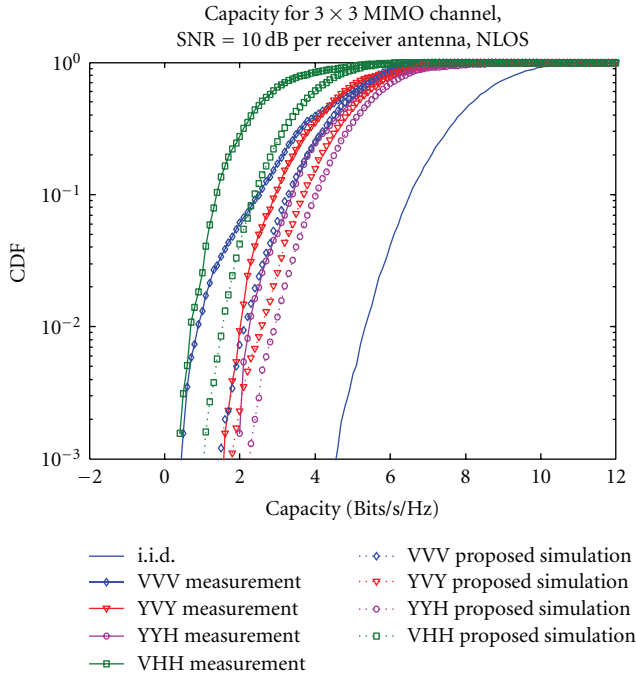


FIGURE 9: The plots of CDF versus capacities obtained by measurement analysis (solid line), proposed simulation analysis (dotted line) for dissimilar polarization systems in indoor NLOS environment.

Acknowledgment

This work was supported by the National Science Council, Taiwan, under the Grant of NSC95-2219-E-002-003 and NSC97-2218-E027-007.

References

- [1] G. J. Foschini, "Layered space-time architecture for wireless communication in a fading environment when using multi-element antennas," *Bell Labs Technical Journal*, vol. 1, no. 2, pp. 41–59, 1996.
- [2] K. Yu, M. Bengtsson, B. Ottersten, D. McNamara, P. Karlsson, and M. Beach, "Modeling of wide-band MIMO radio channels based on NLoS indoor measurements," *IEEE Transactions on Vehicular Technology*, vol. 53, no. 3, pp. 655–665, 2004.
- [3] L. Dong, H. Choo, R. W. Heath, and H. Ling, "Simulation of MIMO channel capacity with antenna polarization diversity," *IEEE Transactions on Wireless Communications*, vol. 4, no. 4, pp. 1869–1872, 2005.
- [4] J. P. Kermoal, L. Schumacher, K. I. Pedersen, P. E. Mogensen, and F. Frederiksen, "A stochastic MIMO radio channel model with experimental validation," *IEEE Journal on Selected Areas in Communications*, vol. 20, no. 6, pp. 1211–1226, 2002.
- [5] D.-S. Shiu, G. J. Foschini, M. J. Gans, and J. M. Kahn, "Fading correlation and its effect on the capacity of multielement antenna system," *IEEE Transactions on Communications*, vol. 48, pp. 502–513, 2000.
- [6] J. P. Kermoal et al., "Experimental investigation of the joint spatial and polarisation diversity for MIMO radio channel," in *Proceedings of the 4th International Symposium on Wireless Personal Multimedia Communication (WPMC '01)*, pp. 147–152, September 2001.
- [7] P. Kyritsi, D. C. Cox, R. A. Valenzuela, and P. W. Wolniansky, "Effect of antenna polarization on the capacity of a multiple element system in an indoor environment," *IEEE Journal on Selected Areas in Communications*, vol. 20, no. 6, pp. 1227–1239, 2002.
- [8] R. U. Nabar, H. Bölcskei, V. Erceg, D. Gesbert, and A. J. Paulraj, "Performance of multiantenna signaling techniques in the presence of polarization diversity," *IEEE Transactions on Signal Processing*, vol. 50, no. 10, pp. 2553–2562, 2002.
- [9] M. R. Andrews, P. P. Mitra, and R. Decarvalho, "Tripling the capacity of wireless communications using electromagnetic polarization," *Nature*, vol. 409, no. 6818, pp. 316–318, 2001.
- [10] H. J. Li and C. H. Yu, "Correlation properties and capacity of antenna polarization combinations for MIMO radio channel," in *Proceedings of the IEEE International Antennas and Propagation Symposium*, pp. 503–506, San Antonio, Tex, USA, June 2003.
- [11] T. Svantesson, "On capacity and correlation of multi-antenna systems employing multiple polarizations," in *Proceedings of the IEEE Antennas and Propagation Society International Symposium*, pp. 202–205, San Antonio, Tex, USA, June 2002.
- [12] W. Weichselberger and H. Özcelik, "A novel stochastic MIMO channel model and its physical interpretation," in *Proceedings of the 6th International Symposium on Wireless Personal Multimedia Communications (WPMC '03)*, Yokosuka, Japan, October 2003.
- [13] A. M. Sayeed, "Deconstructing multiantenna fading channels," *IEEE Transactions on Signal Processing*, vol. 50, no. 10, pp. 2563–2579, 2002.
- [14] S. R. Saunders, *Antennas and Propagation for Wireless Communication systems*, John Wiley & Sons, New York, NY, USA, 1999.
- [15] V. Jungnukel, V. Pohl, and C. von Helmolt, "Capacity of MIMO Systems with closely spaced antennas," in *Proceedings of the IEEE Semiannual Vehicular Technology Conference (VTC '02)*, chapter 3.2., Birmingham, UK, 2002.
- [16] V. R. Anreddy and M. A. Ingram, "Capacity of measured ricean and rayleigh indoor MIMO channels at 2.4 GHz with polarization and spatial diversity," in *Proceedings of the IEEE Wireless Communications and Networking Conference (WCNC '06)*, vol. 2, pp. 946–951, April 2006.
- [17] J. P. Kermoal, L. Schumacher, P. E. Mogensen, and K. I. Pedersen, "Experimental investigation of correlation properties of MIMO radio channels for indoor picocell scenarios," in *Proceedings of the 52nd Vehicular Technology Conference (VTC '00)*, vol. 1, pp. 14–21, September 2000.
- [18] V. Erceg, H. Sampath, and S. Catreux-Erceg, "Dual-polarization versus single-polarization MIMO channel measurement results and modeling," *IEEE Transactions on Wireless Communications*, vol. 5, no. 1, pp. 28–33, 2006.
- [19] I. E. Telatar, "Capacity of multi-antenna gaussian channels," Tech. Rep. BL0112170-950615-07TM, Office Official Publications of the European Communities, AT&T Bell Labs., 1995.
- [20] D. Gesbert, M. Shafi, D. S. Shiu, P. J. Smith, and A. Naguib, "From theory to practice: an overview of MIMO space-time coded wireless systems," *IEEE Journal on Selected Areas in Communications*, vol. 21, no. 3, pp. 281–302, 2003.
- [21] T. S. Rappaport, *Wireless Communications: Principles and Practices*, Prentice Hall, Upper Saddle River, NJ, USA, 2nd edition, 2002.

- [22] P. Soma, D. S. Baum, V. Erceg, R. Krishnamoorthy, and A. J. Paulraj, "Analysis and modeling of Multiple-Input Multiple-Output (MIMO) radio channel based on outdoor measurements conducted at 2.5 GHz for fixed BWA applications," in *Proceeding of IEEE International Conference on Communications*, pp. 272–276, May 2002.

Research Article

A New Generation Method for Spatial-Temporal Correlated MIMO Nakagami Fading Channel

Qiu-Ming Zhu,¹ Xiang-Bin Yu,¹ Jun-Bo Wang,^{1,2,3} Da-Zhuan Xu,¹ and Xiao-Min Chen¹

¹ College of Electronic Information Engineering, Nanjing University of Aeronautics and Astronautics, Nanjing 210016, China

² School of Software, Tsinghua University, Beijing 100084, China

³ National Mobile Communications Research Laboratory, Southeast University, Nanjing 210008, China

Correspondence should be addressed to Qiu-Ming Zhu, zhuqiuming@nuaa.edu.cn

Received 10 July 2011; Accepted 5 September 2011

Academic Editor: Yan Zhang

Copyright © 2012 Qiu-Ming Zhu et al. This is an open access article distributed under the Creative Commons Attribution License, which permits unrestricted use, distribution, and reproduction in any medium, provided the original work is properly cited.

A new generation method for spatial and temporal correlated multiple-input multiple-output (MIMO) Nakagami fading channel is proposed, which has low complexity and is applicable for arbitrary fading parameters and prespecified correlation coefficients of different subchannel. The new scheme can be divided into two steps: (1) generate independent Nakagami fading sequences for each subchannel based on a novel rejection method; (2) introduce the temporal and spatial correlation based on the relationships between Rayleigh, Gamma, and Nakagami random processes. The analysis and simulation results show that the proposed simulator has a good agreement with the theoretical model on fading envelope distribution, spatial-temporal correlation characteristic.

1. Introduction

In the past decades, more and more attentions have been given to MIMO system for its high channel capacity [1]. Many studies and measured data also showed channel fadings on different antennas are correlated. Moreover, the Nakagami fading encompasses Rayleigh and Rice fadings and shows good performance in matching experimental data with different fading parameter m [2]. Hence, correlated MIMO channel modeling and capacity evaluation become the interest of many researchers recently [3, 4]. However, few published works focus on simple and accurate generating of spatial-temporal correlated MIMO Nakagami fading channel which is important for design or laboratory test of MIMO systems.

A number of methods for generating independent Nakagami fading channels are available in the literature. Yip and Ng's method [5] based on the product of square-root beta random variates (RVs) and Rayleigh RVs is accurate but only valid for $m < 1$. The decomposition method [6] is also only valid for integer or half-integer value of m . Beaulieu and Cheng's method [7] based on the inverse cumulative distribution function of Nakagami distribution is suitable for arbitrary m but requires a different set of coefficients

by numerical computation or curve fitting. The rejection method in [8, 9] is accurate and universal but needs a set of constant coefficients determined empirically or lacks efficiency. In light of this fact, a novel simple and high-efficient generation method for arbitrary m is proposed in our simulator which yields an excellent accuracy.

Yip and Ng's method and the decomposition method are also suitable for generating temporal correlated Nakagami fadings with specific values of m . Recently, Ma and Zhang [10] proposed a universal method by constructing a new map relation between Gaussian and Nakagami sequences, but it is quite difficult to calculate the autocorrelation of the corresponding input Gaussian sequence. In [11], a simple method called rank-matching was proposed to introduce prespecified temporal correlation by rearranging the independent Nakagami sequence, while the author addressed the relationship between Rayleigh and Nakagami envelope in an approximation manner. In [6, 12, 13], techniques of channel correlation matrix decomposition for generating spatial correlated channels were reported.

In this paper, we propose a new framework for generating the correlated MIMO Nakagami fading channels which possess (1) arbitrary and different m for each subchannel; (2) arbitrary and different average fading power; (3) arbitrarily

prespecified temporal correlation coefficients; (4) arbitrary spatial correlation coefficient matrix. The new method consists of two steps: generate independent Nakagami sequence and introduce spatial-temporal correlation. Additionally, the simulation error is also analyzed and testified by numerical examples.

The rest of the paper is organized as follows. In Section 2, a general description of MIMO channel is given. In Section 3, the new framework for simulating the correlated Nakagami fading MIMO channel is described and analyzed. In Section 4, the generation approach is verified through numerical simulation. Finally, the conclusions are drawn in Section 5.

Throughout the paper, we use $[\cdot]^T$ to denote transposition. $E[\cdot]$ and $\text{var}[\cdot]$ means the expectation and variance, respectively. $\rho_R^k(\tau)$ is the temporal correlation coefficient (TCC) of the k th subchannel, and $\rho_R(k, l)$ is the spatial correlation coefficient (SCC) between subchannel k and l . $Y(a, b)$ denotes the Gamma distribution with distribution parameters a and b .

2. MIMO Channel Model

2.1. General Description. A flat fading MIMO system equipped with N transmit and M receive antennas is showed in Figure 1. The transmit and receive signals are expressed by vectorized forms, $\mathbf{X} = [x_1, x_2, \dots, x_N]^T$ and $\mathbf{S} = [s_1, s_2, \dots, s_M]^T$. The input-output relationship is given by

$$\mathbf{S} = \mathbf{H}\mathbf{X} + \mathbf{N}, \quad (1)$$

where \mathbf{N} corresponds to the additive noise matrix, \mathbf{H} is the time-variate channel fading matrix which can be expressed as

$$\mathbf{H}(t) = \begin{bmatrix} h_{1,1}(t) & h_{1,2}(t) & \cdots & h_{1,N}(t) \\ h_{2,1}(t) & h_{2,2}(t) & \cdots & h_{2,N}(t) \\ \vdots & \vdots & \ddots & \vdots \\ h_{M,1}(t) & h_{M,2}(t) & \cdots & h_{M,N}(t) \end{bmatrix}, \quad (2)$$

where $h_{i,j}(t)$ is the complex fading coefficient from j th transmit antenna to i th receive antenna. For simplicity, $\mathbf{H}(t)$ is transformed to a column vector containing MN elements,

$$\text{vec}(\mathbf{H}) = [h_{1,1}, h_{2,1}, \dots, h_{M,1}, h_{1,2}, h_{2,2}, \dots, h_{M,2}, \dots, h_{1,N}, h_{2,N}, \dots, h_{M,N}]^T, \quad (3)$$

or

$$\text{vec}(\mathbf{H}) = [h_1(t), h_2(t), \dots, h_{MN}(t)]^T. \quad (4)$$

The envelope of $h_k(t)$ follows Nakagami distribution, and the phase is uniformly distributed in $[0, 2\pi)$. The TCC of each subchannel is denoted by $\rho_k(\tau)$, and the SCC matrix of $\text{vec}(\mathbf{H})$ can be described by a $MN \times MN$ matrix ρ_R .

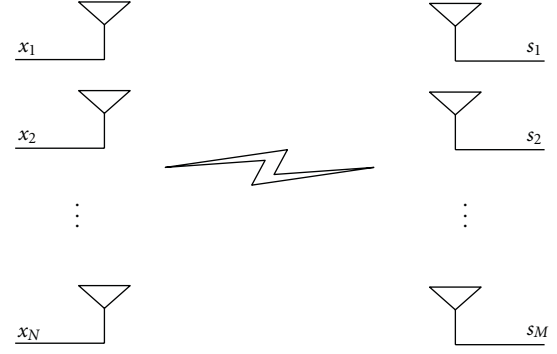


FIGURE 1: MIMO system with N transmit and M receive antennas.

2.2. Nakagami, Rayleigh, and Gamma Distribution. The probability density function (PDF) of Nakagami distribution was given in [2] as

$$f_R(r) = \frac{2}{\Gamma(m)} \left(\frac{m}{\Omega}\right)^m r^{2m-1} e^{-(m/\Omega)r^2}, \quad r \geq 0, \quad (5)$$

where $\Omega = E[r^2]$ is the mean power, $\Gamma(\cdot)$ denotes the gamma function, and the fading parameter m controls the fading degree of the propagation field.

Following [2], the squared Nakagami RV obeys a Gamma distribution and can be constructed from the sum of independent and identically distributed (i.i.d) squared Rayleigh RVs,

$$R = \sqrt{Y_1^2 + Y_2^2 + \cdots + Y_m^2}, \quad (6)$$

$$R = \sqrt{\gamma},$$

where Y_i and γ denote Rayleigh and Gamma RV, respectively, whose PDFs are defined as

$$f_Y(y) = \frac{y}{\sigma^2} \exp\left(-\frac{y^2}{2\sigma^2}\right), \quad (7)$$

$$f_\gamma(\gamma) = \frac{1}{\Gamma(a)b^a} \gamma^{a-1} e^{-\gamma/b},$$

where $\sigma^2 = \Omega/2m$, $a = m$, $b = \Omega/m$.

3. Generation of Correlated Nakagami MIMO Channel

In general, the correlated Nakagami MIMO channel simulation is to generate MN Nakagami fading channels which are temporal and spatial correlated. It is assumed that the fading parameters and correlation properties are arbitrary and different.

3.1. Generating Independent Nakagami Fading. The rejection/acceptance technique is a universal generation method for nonuniform RVs, which is summarized as follows [14]

- (1) Find a hat function $p(x)$ which satisfies the inequality

$$Cp(x) \geq q(x), \quad (8)$$

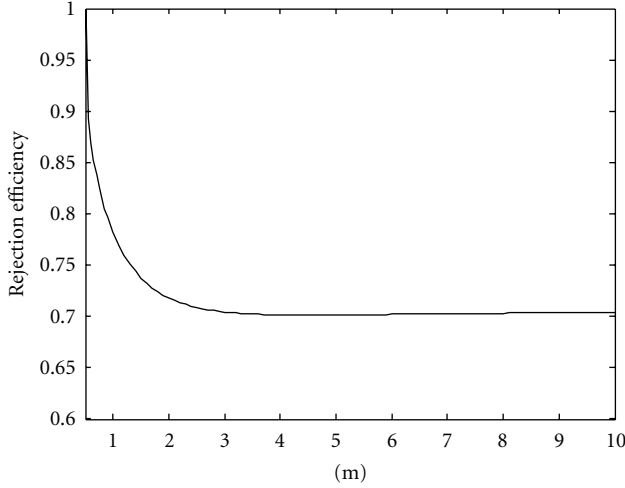


FIGURE 2: Rejection efficiency of the new method.

where $q(x)$ is the required distribution and C is the rejection constant.

- (2) Generate a RV X with PDF $p(x)$ and a RV G uniformly distributed in $[0, Cp(X)]$.
- (3) If $G \leq q(X)$, X is accepted. Otherwise, it is rejected.

The main difficulty of this technique lies in finding a hat function which is close to the required distribution and satisfies the inequality. In this paper, we adopt a new truncated Gaussian distribution function as the hat function for arbitrary m . Using (8) and strict mathematical derivation, the hat function and rejection constant are founded as

$$p(x) = \frac{(1/\sqrt{2\pi}\sigma)e^{-(x-x_0)^2/2\sigma^2}}{1/2 + (1/2)\text{erf}(x_0/\sqrt{2}\sigma)}, \quad x \geq 0, \quad (9)$$

$$c = b\sqrt{2\pi}\sigma \left(\frac{1}{2} + \frac{1}{2}\text{erf}\left(\frac{x_0}{\sqrt{2}\sigma}\right) \right),$$

where $x_0 = \sqrt{(2m-1)\Omega/2m}$, $\sigma^2 = \Omega/2m$, and

$$b = \frac{2^{3/2-m}(m/\Omega)^m(\Omega(2m-1)/m)^{m-1/2}e^{1/2-m}}{\Gamma(m)}. \quad (10)$$

An important measure for the quality of the rejection algorithm is the acceptance probability or rejection efficiency which involves the closeness between the Nakagami PDF and the hat function. Figure 2 plots the rejection efficiency curve of our proposed method. It shows that the efficiency decreases for high values of m but better than 70%. However, the rejection efficiency of [8] is only 65.75% and 66.67% in cases of $0.5 \leq m \leq 1$ and $m \geq 1$, while the method in [9] becomes inefficient as m increases and the efficiency is below 64% mostly.

3.2. Introducing Temporal Correlation. For stationary random processes, the TCC of the samples is well approximate with the TCC of their statistical ranks [15]. Reference [11, Equation (6)] gives the assumption without proving that

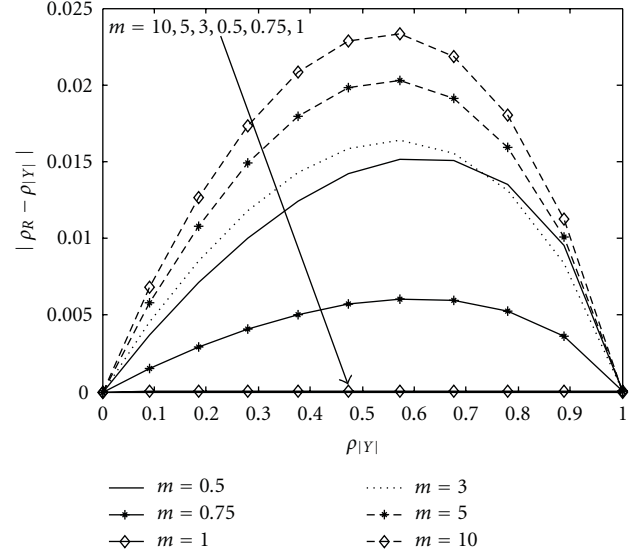
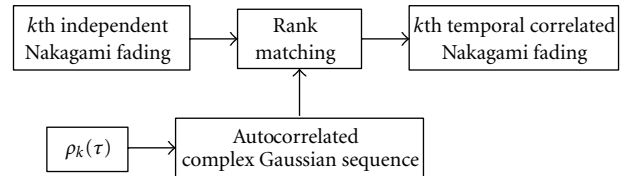
FIGURE 3: The absolute error between $\rho_R(\tau)$ and $\rho_{|Y|}(\tau)$.

FIGURE 4: Introducing temporal correlation.

the TCC of Nakagami envelope approximately equal to the corresponding Rayleigh envelope $\rho_R(\tau) \approx \rho_{|Y|}(\tau)$ which means the TCCs of their statistical ranks are almost same.

The Nakagami envelope autocorrelation function is given by [2]:

$$f_R(\tau) = \frac{\Omega\Gamma^2(m+0.5)}{m\Gamma^2(m)}F_1(-0.5, -0.5; m; \rho_{Y^2}(\tau)), \quad (11)$$

where $\rho_{Y^2}(\tau)$ is the autocorrelation coefficient of squared Rayleigh envelope and $F_1(a, b; c; d)$ is the hypergeometric function. The statistical properties of Nakagami sequence can be found as

$$E[R] = \frac{\Gamma(m+0.5)}{\Gamma(m)} \left(\frac{\Omega}{m} \right)^{1/2}, \quad (12)$$

$$\text{var}(R) = \Omega - \frac{\Omega\Gamma^2(m+0.5)}{m\Gamma^2(m)}.$$

According to the definition of autocorrelation coefficient, we obtain

$$\rho_R(\tau) = \frac{1 - F_1(-0.5, -0.5; m; \rho_{Y^2}(\tau))}{1 - (m\Gamma^2(m)/\Gamma^2(m+0.5))}. \quad (13)$$

Following [16], we have

$$\rho_{|Y|}(\tau) = \frac{1 - F_1(-0.5, -0.5; 1; \rho_{Y^2}(\tau))}{1 - 4/\pi}, \quad (14)$$

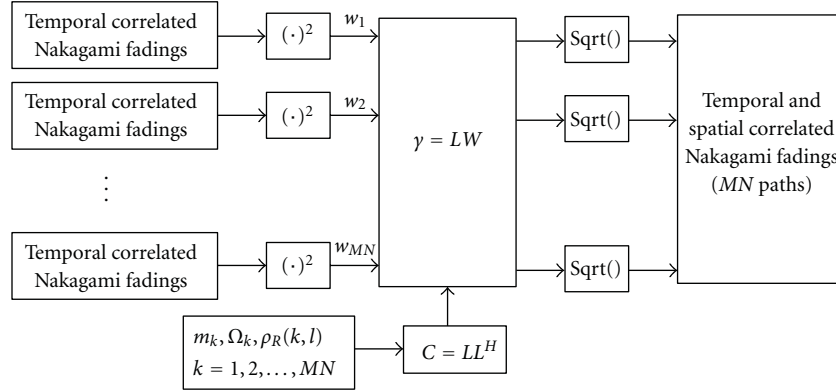


FIGURE 5: Introducing spatial correlation.

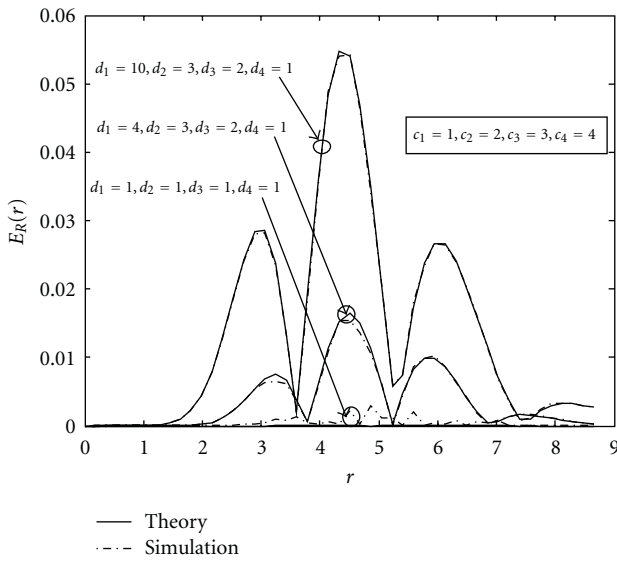


FIGURE 6: Comparison of the absolute error of Nakagami PDF.

where $\rho_{|Y|}(\tau)$ is the autocorrelation coefficient of Rayleigh envelope.

It is difficult to get the accurate relationship expression between $\rho_R(\tau)$ and $\rho_{|Y|}(\tau)$. A numerical method is used to investigate the absolute error for different m . The numerical results are plotted in Figure 3, which shows the maximum difference between two TCC curves is less than 0.025 which is fairly small for most practical purposes.

Thus, we can rearrange the Nakagami sequence to match the statistical rank of the Rayleigh sequence in order to introduce the desired temporal correlation (see Figure 4). Moreover, there are many efficient methods to generate the reference Rayleigh sequence (or complex Gaussian sequence) with desired autocorrelation, such as the AR model [17] and the MEPA method [18]. It should be emphasized that the temporal correlated complex Gaussian sequence here can be transformed to the truncated Gaussian sequence for rejecting in (9).

3.3. Introducing Spatial Correlation. We introduce the spatial correlation for MN Nakagami fading subchannels following

the flowchart in Figure 5. The key step of this procedure is generating MN correlated Gamma RVs whose square root yields the desired correlated Nakagami MIMO channel. There are two commonly used methods, the decomposition method [12] and the Simon method [19]. Although the Simon method shows better accuracy, it is more complex and has some constraints on the prespecified statistical parameters. The decomposition method is more versatile and simpler, which can be expressed as

$$\boldsymbol{\gamma} = \mathbf{L}\mathbf{w}, \quad (15)$$

where $\mathbf{w} = [w_1 \cdots w_{MN}]^T$ is the normalized Gamma RV vector, $w_i \sim \Upsilon(a_i, b_i)$ and $a_i b_i^2 = 1$, $\boldsymbol{\gamma} = [\gamma_1 \cdots \gamma_{MN}]^T$ is the desired cross-correlated Gamma RV vector, and \mathbf{L} denotes a low triangular matrix, which is the Cholesky decomposition on the covariance matrix of $\boldsymbol{\gamma}$,

$$\mathbf{C}_\gamma = \mathbf{L}\mathbf{L}^H. \quad (16)$$

It can be derived that \mathbf{C}_γ , a_i , b_i are determined by the specified simulation parameters,

$$c_\gamma(k, l) \approx \rho_R(k, l) \sqrt{\frac{(1 + 1/m_k)^2 \Omega_k^4}{m_k} \frac{(1 + 1/m_l)^2 \Omega_l^4}{m_l}}, \quad (17)$$

$$a_i = \frac{1}{b_i^2}, \quad i = 1 \sim MN,$$

$$b_i = \frac{l_{i,i}}{\sqrt{m_i \sum_{j=1}^i l_{i,j}^2 - \sum_{j=1}^{i-1} l_{i,j}/b_j}}.$$

The decomposition method assumes that the linear summation of independent Gamma RVs follows Gamma distribution. In the following, we will analyze the simulation error caused by this assumption. Firstly, the i th cross-correlated Gamma RV γ_i of (15) can be written as

$$\begin{aligned} \gamma_i &= \sum_{k=1}^i l_{i,k} w_k = l_{i,1} w_1 + l_{i,2} w_2 + \cdots + l_{i,i} w_i \\ &= w'_1 + w'_2 + \cdots + w'_i, \end{aligned} \quad (18)$$

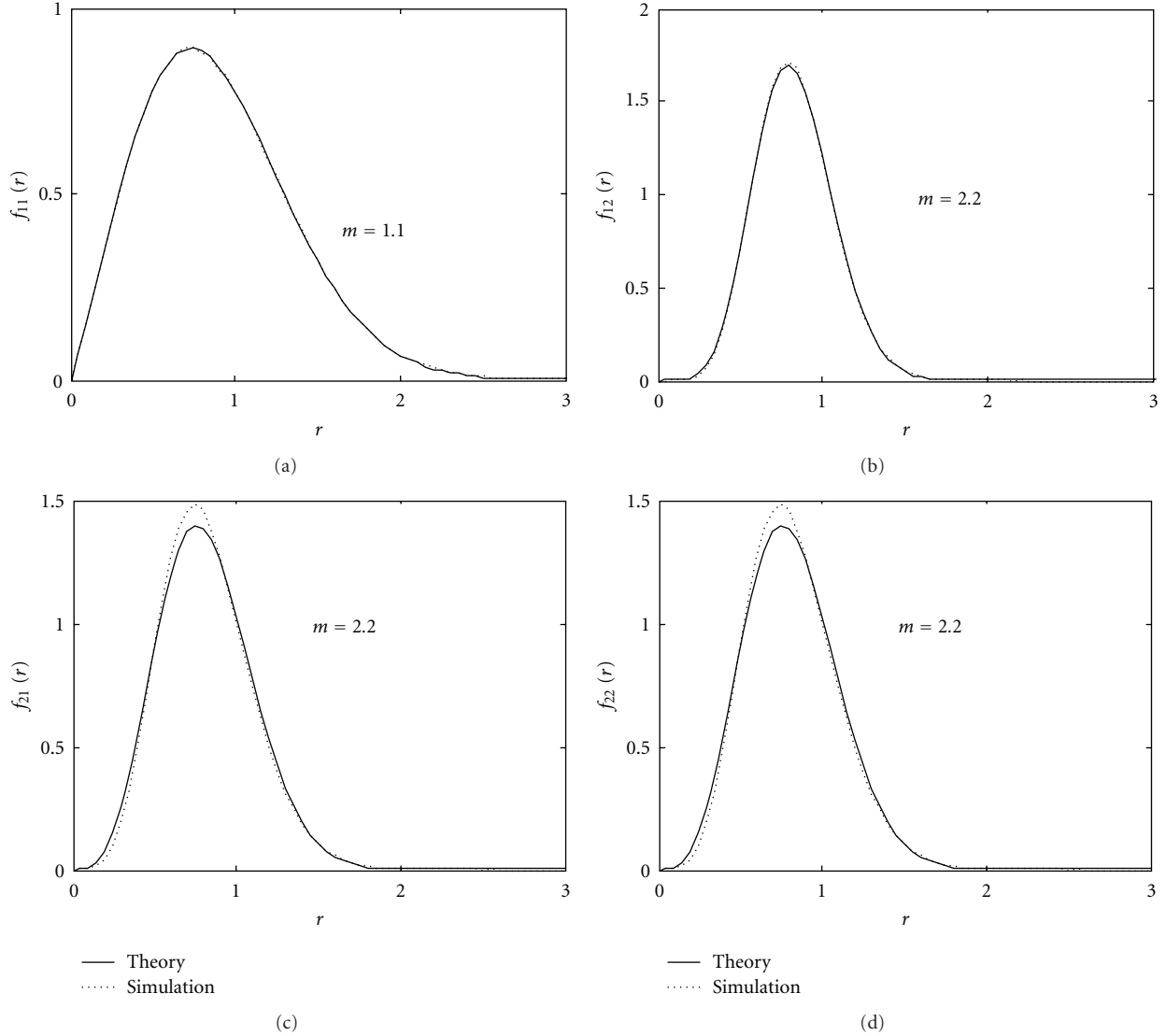


FIGURE 7: The PDFs of simulated subchannel fading envelope.

where $w'_i = l_i w_i$ denotes a new independent Gamma RV which follows $w'_i \sim \Upsilon(c_i, d_i)$, and the new distribution parameters yield

$$c_i = a_i, \quad d_i = l_i b_i. \quad (19)$$

The exact PDF of γ_i can be found as [20, Equation (2.9)]:

$$f_\gamma(z) = \frac{A \sum_{k=0}^{\infty} \delta_k z^{\rho+k-1} e^{-z/d_1}}{\Gamma(\rho+k) d_1^{\rho+k}}, \quad (20)$$

where $d_1 = \min\{d_i\}$, $A = \prod_{i=1}^n (d_1/d_i)^{c_i}$, $\rho = \sum_{i=1}^n c_i > 0$, and

$$\delta_{k+1} = \frac{1}{k+1} \sum_{i=1}^{k+1} i B_k \delta_{k+1-i}, \quad \delta_0 = 1, \quad (21)$$

where $B_k = \sum_{i=1}^n c_i (1 - d_1/d_i)^k / k$.

The straightforward transformation $R = \sqrt{\gamma}$ leads the simulation PDF of Nakagami RV as

$$f_R(r) = 2r f_\gamma(r^2). \quad (22)$$

Finally, the theoretical expression for absolute error of simulated Nakagami PDF is obtained as

$$E_R(r) = \left| 2r f_R(r^2) - \frac{2}{\Gamma(m)} \left(\frac{m}{\Omega}\right)^m r^{2m-1} e^{-(m/\Omega)r^2} \right|. \quad (23)$$

Figure 6 compares the simulated results of Nakagami PDF error with the values calculated from the exact expression (23). In the simulation, 10^6 samples of the Nakagami RV are generated by four independent Gamma RVs with different parameters sets of c_i and d_i . It can be seen that a very good agreement between the simulated results and the exact expression is obtained. Anyway, the absolute error of Nakagami PDF is very small which means the decomposition method can achieve satisfactory performance.

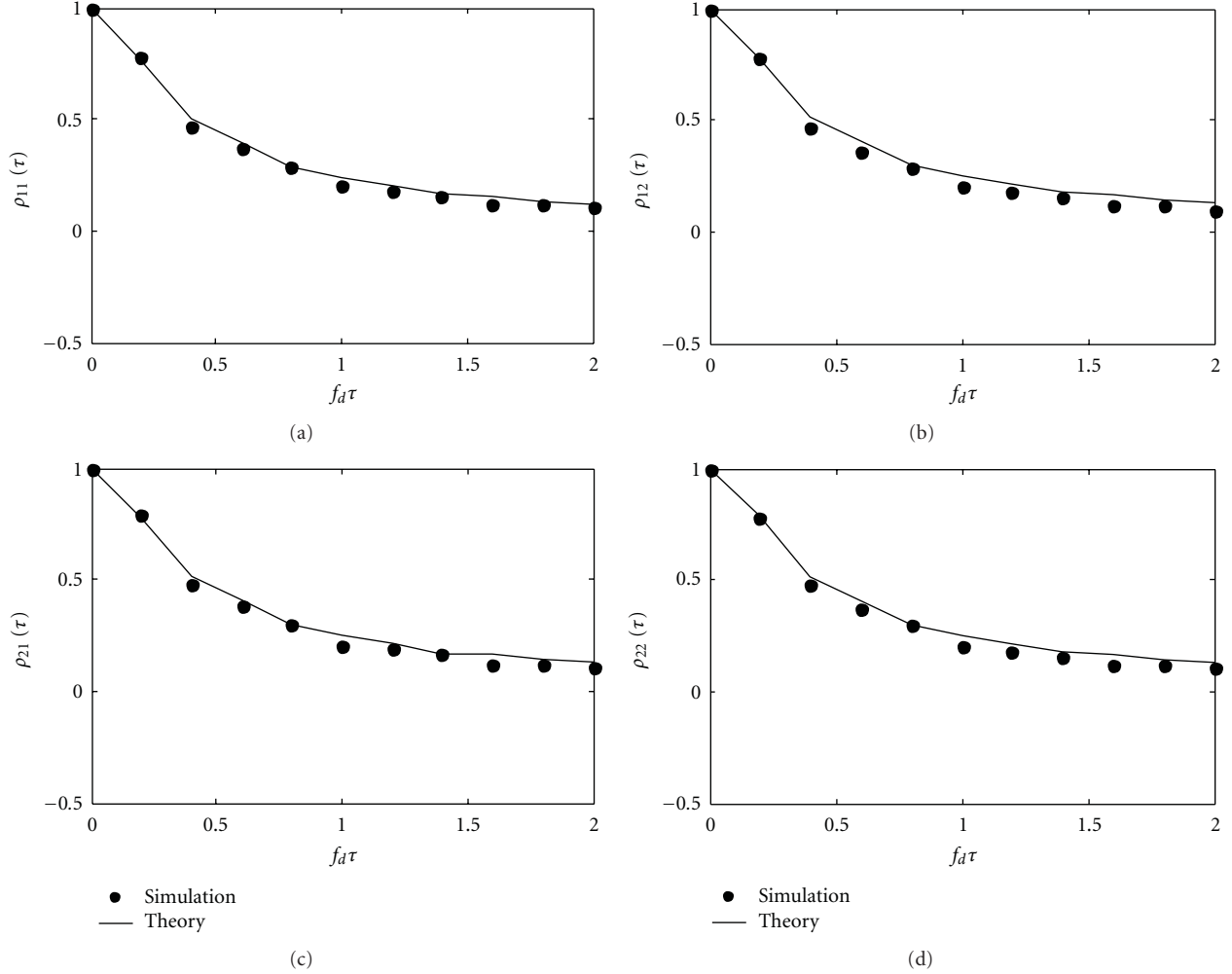


FIGURE 8: The TCCs of simulated subchannel fading envelope.

4. Simulation Results

To illustrate the behavior of the proposed channel simulator, we consider a MIMO system with $N = 2$ at the mobile station (MS), $M = 2$ at the base station (BS). The fading characteristics of four subchannels are different:

$$\mathbf{m} = \begin{bmatrix} 1.1 & 3.3 \\ 2.2 & 4.4 \end{bmatrix}, \quad \mathbf{\Omega} = \begin{bmatrix} 1 & 0.75 \\ 0.75 & 1 \end{bmatrix}. \quad (24)$$

The MS is assumed to be surrounded by several scatterers which results in a low correlation between two antennas

$$\rho_{\text{MS}} = \begin{bmatrix} 1 & 0.3 \\ 0.3 & 1 \end{bmatrix}, \quad (25)$$

while the antennas of BS set high and have no local scatterers,

$$\rho_{\text{BS}} = \begin{bmatrix} 1 & 0.91 \\ 0.91 & 1 \end{bmatrix}. \quad (26)$$

Hence, the SCC matrix is given by [21]:

$$\rho_{\text{R}} = \rho_{\text{MS}} \otimes \rho_{\text{BS}} = \begin{bmatrix} 1 & 0.91 & 0.3 & 0.273 \\ 0.91 & 1 & 0.273 & 0.3 \\ 0.3 & 0.273 & 1 & 0.91 \\ 0.273 & 0.3 & 0.91 & 1 \end{bmatrix}, \quad (27)$$

where \otimes denotes Kronecker product.

A plausible model for the angle of arrival (AOA) of the receiving signals is Von Mises distribution, which is defined as [22]:

$$p(\alpha) = \frac{\exp\{k \cos(\alpha - \alpha_0)\}}{2\pi I_0(k)}, \quad \alpha \in (-\pi, \pi]. \quad (28)$$

Under this scattering environment, the theoretical expression of TCC is given by [22] as

$$\rho_{\gamma^2}(\tau) = \left| \frac{I_0\left(\sqrt{k^2 - (2\pi f_d \tau)^2 + j4\pi k f_d \cos(\alpha_0)\tau}\right)}{I_0(k)} \right|^2, \quad (29)$$

where $I_0(\cdot)$ is the zero-order modification Bessel function, α_0 denotes the mean direction of AOA, $k \geq 0$ controls the angular spread, and f_d is the maximum Doppler frequency. Antenna arrays at both ends are assumed to be small spacing (less than half wavelength), so the temporal correlation properties of receiving signals on each receiving antenna are almost same.

In the simulation, 10^6 samples of each subchannel are generated based on the proposed scheme. Figure 7 shows that the simulated PDFs of fading envelope match the theoretical curves very well under four fading scenarios. The corresponding statistical parameters are estimated by maximum likelihood method as

$$\hat{\mathbf{m}} = \begin{bmatrix} 1.0982 & 3.3073 \\ 2.1983 & 4.4144 \end{bmatrix}, \quad \hat{\mathbf{\Omega}} = \begin{bmatrix} 1.0010 & 0.7506 \\ 0.7506 & 1.0006 \end{bmatrix}, \quad (30)$$

which is also very close to the desired ones.

We next look at the spatial and temporal correlation coefficients of the above outputs. In the simulation, we assume that four subchannels experience almost the same no-isotropic ($k = 5$) scattering scenarios for small antenna spacing. The TCC of each output channel is showed in Figure 8, where $f_d \tau$ means the normalized time delay. It is showed that the simulation curves agree well with the desired ones. The SCC matrix is calculated by output samples ending up with

$$\hat{\rho}_R = \begin{bmatrix} 1 & 0.8778 & 0.3074 & 0.2765 \\ 0.8778 & 1 & 0.2771 & 0.3110 \\ 0.3074 & 0.2771 & 1 & 0.9076 \\ 0.2765 & 0.3110 & 0.9076 & 1 \end{bmatrix}. \quad (31)$$

Comparing to (27), it is found that the relative errors are 3.54%, 2.47%, and 1.27%, respectively.

5. Conclusions

In this paper, a new framework for simulating the spatial and temporal correlated MIMO Nakagami fading channels was proposed. It can be applied on arbitrary fading parameters and prespecified spatial-temporal correlation coefficients with a satisfactory accuracy. Moreover, the new simulation method is low complexity and applicable for large-scale and real-time channel simulation scenarios. The most complex part of this simulator is to generate MN complex Gaussian sequences which can be accomplished by well-established methods.

Acknowledgments

This work is supported by National Nature Science Foundation of China (no. 61102068), the Aviation Science Foundation of China (no. 2009ZC52036), Nanjing University of Aeronautics and Astronautics Research Funding (no. NP2011036 and NS2011013), and China Postdoctoral Science Foundation funded project (no. 20110490389).

References

- [1] E. Telatar, "Capacity of multi-antenna Gaussian channels," *European Transactions on Telecommunications*, vol. 10, no. 6, pp. 585–595, 1999.
- [2] M. Nakagami, *The m-Distribution: A General Formula of Intensity Distribution of Rapid Fading Statistical Methods of Radio Wave Propagation*, W.C. Hoffman, Japan, 1960.
- [3] M. Matthaiou, D. I. Laurenson, and J. S. Thompson, "A MIMO channel model based on the Nakagami-faded spatial eigenmodes," *IEEE Transactions on Antennas and Propagation*, vol. 56, no. 5, pp. 1494–1497, 2008.
- [4] C. Zhong, K. K. Wong, and S. Jin, "Capacity bounds for MIMO Nakagami-m fading channels," *IEEE Transactions on Signal Processing*, vol. 57, no. 9, pp. 3613–3623, 2009.
- [5] K. W. Yip and T. S. Ng, "A simulation model for nakagami-m fading channels, $m < 1$," *IEEE Transactions on Communications*, vol. 48, no. 2, pp. 214–221, 2000.
- [6] Q. T. Zhang, "Decomposition technique for efficient generation of correlated Nakagami fading channels," *IEEE Journal on Selected Areas in Communications*, vol. 18, no. 11, pp. 2385–2392, 2000.
- [7] N. C. Beaulieu and C. Cheng, "Efficient nakagami- \mathcal{M} fading channel simulation," *IEEE Transactions on Vehicular Technology*, vol. 54, no. 2, pp. 413–424, 2005.
- [8] L. Cao and N. C. Beaulieu, "Simple efficient methods for generating independent and bivariate Nakagami-m fading envelope samples," *IEEE Transactions on Vehicular Technology*, vol. 56, no. 4 I, pp. 1573–1579, 2007.
- [9] M. Matthaiou and D. I. Laurenson, "Rejection method for generating Nakagami-m independent deviates," *Electronics Letters*, vol. 43, no. 25, pp. 1474–1475, 2007.
- [10] Y. Ma and D. Zhang, "A method for simulating complex nakagami fading time series with nonuniform phase and prescribed autocorrelation characteristics," *IEEE Transactions on Vehicular Technology*, vol. 59, no. 1, Article ID 5223623, pp. 29–35, 2010.
- [11] J. C. S. Silveira Santos Filho and M. D. Yacoub, "On the simulation and correlation properties of phase-envelope nakagami fading processes," *IEEE Transactions on Communications*, vol. 57, no. 4, pp. 906–909, 2009.
- [12] K. Zhang, Z. Song, and Y. L. Guan, "Simulation of nakagami fading channels with arbitrary cross-correlation and fading parameters," *IEEE Transactions on Wireless Communications*, vol. 3, no. 5, pp. 1463–1468, 2004.
- [13] L. C. Tran, T. A. Wysocki, and J. Seberry, "A generalized algorithm for the generation of correlated Rayleigh fading envelopes in radio channels," in *Proceedings of the 19th IEEE International Parallel and Distributed Processing Symposium (IPDPS'05)*, vol. 13, p. 238, Denver, Colo, USA, 2005.
- [14] A. Papoulis and S. U. Pillai, *Probability Random Variables and Stochastic Processes*, McGraw-Hill, Boston, Mass, USA, 4th edition, 2002.
- [15] E. L. Lehmann and H. L. M. D'Abbrera, *Nonparametrics: Statistical Methods Based on Ranks*, McGraw-Hill, New York, NY, USA, 1975.
- [16] W. C. Jakes, *Microwave Mobile Communications*, Wiley, New York, NY, USA, 1974.
- [17] K. E. Baddour and N. C. Beaulieu, "Autoregressive modeling for fading channel simulation," *IEEE Transactions on Wireless Communications*, vol. 4, no. 4, pp. 1650–1662, 2005.

- [18] Q. M. Zhu, D. Z. Xu, and X. M. Chen, "Modified channel model for non-isotropic scattering environments," in *Proceedings of the International Conference on Wireless Communications & Signal Processing, (WCSP '09)*, pp. 1–5, Nanjing, China, November 2009.
- [19] C. H. Simon, "Generation of Poisson and Gamma random vectors with given marginal and covariance matrix," *Journal of Statistical Computation and Simulation*, vol. 47, no. 1, pp. 1–10, 1993.
- [20] P. G. Moschopoulos, "The distribution of the sum of independent gamma random variables," *Annals of the Institute of Statistical Mathematics*, vol. 37, no. 1, pp. 541–544, 1985.
- [21] J. P. Kermoal, L. Schumacher, K. I. Pedersen, P. E. Mogensen, and F. Frederiksen, "A stochastic MIMO radio channel model with experimental validation," *IEEE Journal on Selected Areas in Communications*, vol. 20, no. 6, pp. 1211–1226, 2002.
- [22] A. Abdi, J. A. Barger, and M. Kaveh, "A parametric model for the distribution of the angle of arrival and the associated correlation function and power spectrum at the mobile station," *IEEE Transactions on Vehicular Technology*, vol. 51, no. 3, pp. 425–434, 2002.

Research Article

Multiband Planar Monopole Antenna for LTE MIMO Systems

Yuan Yao, Xing Wang, and Junsheng Yu

School of Electronic Engineering, Beijing University of Posts and Telecommunications,
Beijing 100876, China

Correspondence should be addressed to Yuan Yao, yaoy@bupt.edu.cn

Received 9 August 2011; Accepted 9 September 2011

Academic Editor: Li Yang

Copyright © 2012 Yuan Yao et al. This is an open access article distributed under the Creative Commons Attribution License, which permits unrestricted use, distribution, and reproduction in any medium, provided the original work is properly cited.

A novel multiband-printed planar monopole antenna for LTE multi-input and multi-output (MIMO) application is proposed. A meandering microstrip line-loaded monopole antenna with multiband characteristic is presented. The proposed antenna provides five frequency bands for LTE application, covering 0.7, 1.7, 2.1, 2.3, and 2.5 GHz. In order to provide low mutual coupling and envelope correlation, two of the antennas are combined with orthogonal polarizations. The mutual coupling of the antenna is lower than -13 dB across the operation bands. Both the simulated and measured results are shown to illustrate the performances of the proposed antenna.

1. Introduction

Nowadays, there are more and more interests in research on multi-input and multi-output (MIMO) systems in the wireless communication. Since it has the ability to increase the capacity of channel using the spatial properties of multipath, it is necessary to have a number of uncorrelated antennas at each end of the communication link. So it seems to be very essential to design adequate antenna due to use in MIMO systems. As revealed in many literatures [1–4], both of non-printed MIMO antennas such as planar-inverted F antennas (PIFAs) and printed MIMO antennas are proposed. However, among the antennas which are used for MIMO application, printed antennas are more appropriate due to their low cost, easy fabrication, and their capability of easily being integrated to small terminal devices. Rapid developments in the wireless communication require novel antenna designs which can be used for multifunctional systems, which means that the antenna should have more than one frequency band. A tri-band E-shaped printed monopole antenna loaded with two U-shaped resonance paths suitable for MIMO systems for WLAN application, covering 2.4, 5.4, and 5.8 GHz, is reported in [5].

In this paper a novel multiband-printed planar monopole antenna for LTE MIMO application is presented. It can provide five frequency bands for LTE applications, covering

746–787 MHz, 1710–1755 MHz, 2110–2155 MHz, 2305–2400 MHz, and 2500–2690 MHz. This multiband characteristic is obtained by loading a meandering line to an ultra-wideband planar monopole antenna. Two elements of such antennas are used for MIMO applications. The proposed structure obtains low mutual coupling and envelope correlation due to the orthogonal polarization.

2. Antenna Structure and Mechanism

As we know, printed planar monopole antennas have been widely used in wireless communication devices. They are very popular for volume-limited and wideband applications. The structure of the proposed multiband MIMO antenna is shown in Figure 1. This antenna is printed on an FR-4 substrate with relative permittivity 4.4 and thickness of 1.6 mm. The two identical antenna elements have the same structure and dimensions. The antenna has two layers, the top layer and the bottom layer. On the bottom layer there are the grounds with length L_g and width W_g . On the top layer is the microstrip line-loaded monopole. The antenna is fed by a microstrip line with width 3 mm to match 50Ω . The monopole is rectangular with width W_2 and length L_1 and L_2 . The loaded microstrip line has width W_{strip} and length of one path L_{strip} . The two antenna elements are spaced

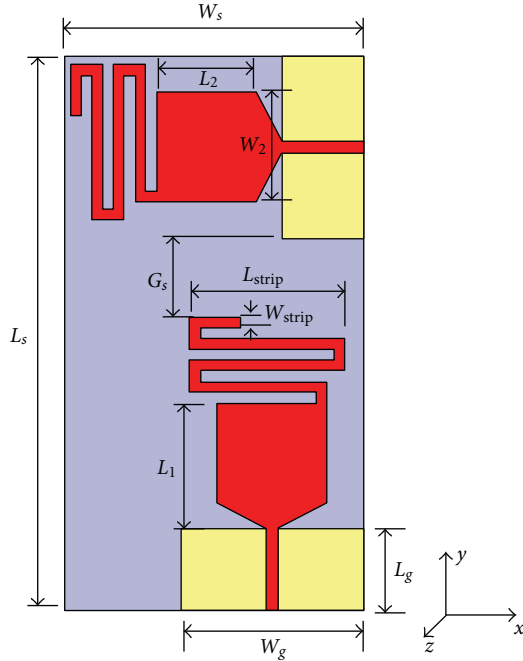


FIGURE 1: The geometry of the proposed antenna.

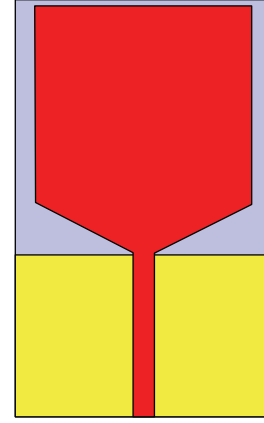
TABLE 1: Antenna dimensions.

Dimension	L_s	W_s	L_g	W_g	L_1
Size (mm)	153	83	22.7	50	34.8
Dimension	L_2	W_2	L_{strip}	W_{strip}	G_s
Size (mm)	27.7	50	40	3	20

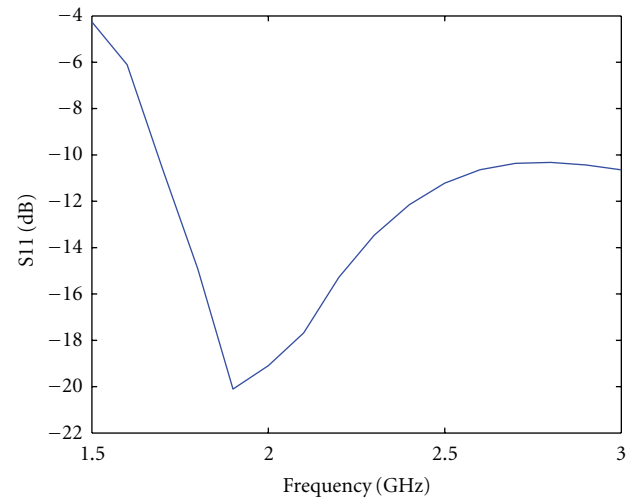
with a gap G_s . The detailed antenna dimensions are listed in Table 1.

In order to achieve a compact multiband antenna, a novel structure is proposed in this paper. The multiband characteristic is obtained by loading a meandering microstrip line to an ultra-wideband monopole element. Figure 2 shows the monopole antenna without microstrip line loaded and the return loss of this antenna. It can be seen that this kind of monopole antenna has ultra-wideband characteristics covering from 1700 MHz to 2900 MHz frequency band. However, only the monopole antenna cannot cover the LTE 700 MHz band. Then a meandering microstrip line is loaded. As shown in Figure 3 the current distribution at 750 MHz reveals the resonance at LTE 700 MHz band.

In addition to the traditional antenna parameters, such as gain, radiation pattern, and reflection coefficients, new parameters and aspects have to be included in the design for MIMO systems. Mutual coupling between antenna elements is a key factor to achieve high antenna performance in the MIMO antenna configuration. For a low mutual coupling, antennas must be far away from each other. But the space for the internal antenna is not enough to obtain low correlation and mutual coupling. In this paper we present a structure for the MIMO antenna elements, in which the identical two antenna elements are orthogonally placed. Then the two antenna elements have orthogonal polarization which



(a) Structure



(b) S11 results

FIGURE 2: The structure and return loss of the ultra-wideband monopole antenna.

can reduce the mutual coupling between the two antennas. Figure 4 shows the simulated 3D radiation patterns of the two antenna elements. It can be seen that the two antenna elements have orthogonal polarizations.

3. Simulation and Measurement Results

To validate the above analysis, the proposed structure is simulated in HFSS and measured in an anechoic chamber. A prototype of the proposed antenna as shown in Figure 5 was fabricated and tested, and the detailed dimensions can be found in Table 1. Figure 6 shows the simulated and measured return loss, which agree well. The measured -10 dB return loss bandwidths are 745–790 MHz and 1700–3000 MHz, which cover the whole LTE bands. The mutual coupling between the two ports is less than -13 dB across the common bandwidth, as shown in Figure 7.

Figures 8 and 9 show the radiation patterns of the antenna 1 and the antenna 2 at 760 MHz, 1750 MHz, 2150 MHz,

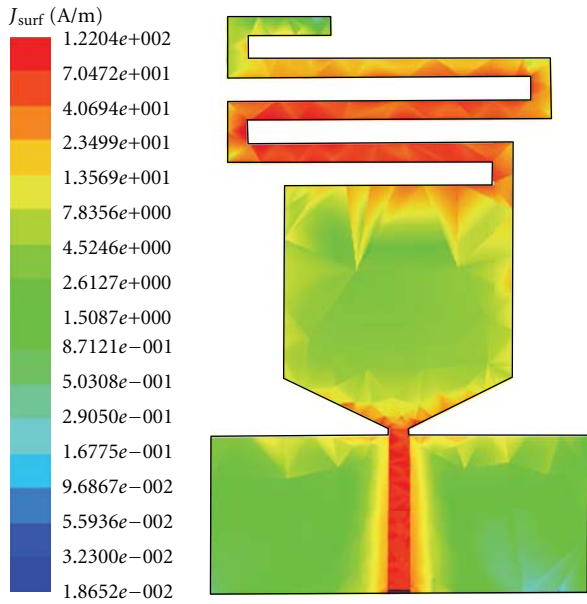


FIGURE 3: Current distribution at 750 MHz.

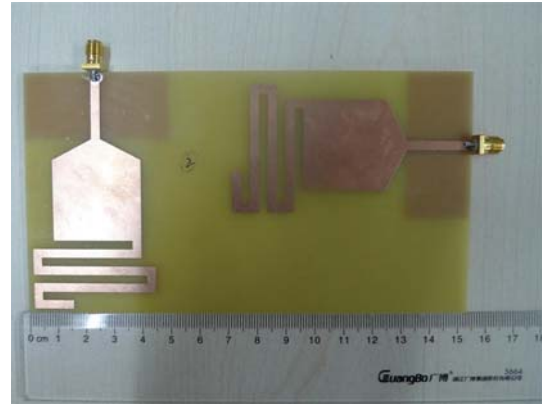
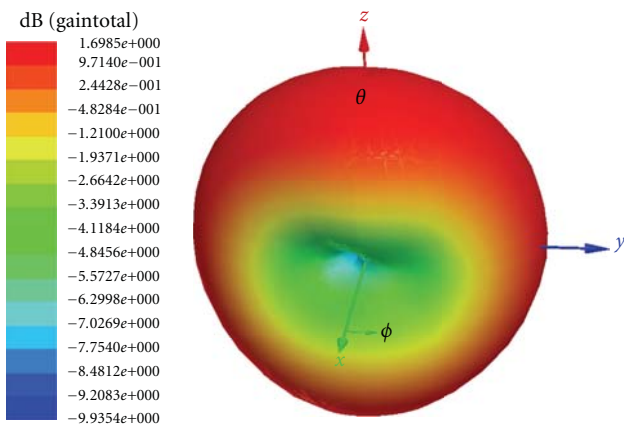
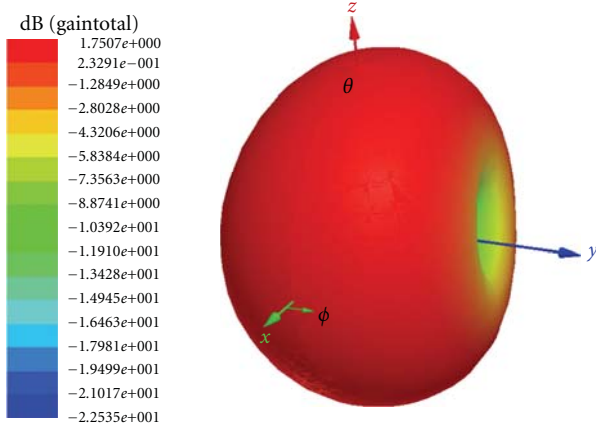


FIGURE 5: Photograph of the fabricated antenna.



(a)



(b)

FIGURE 4: 3D radiation patterns of the two antenna elements.

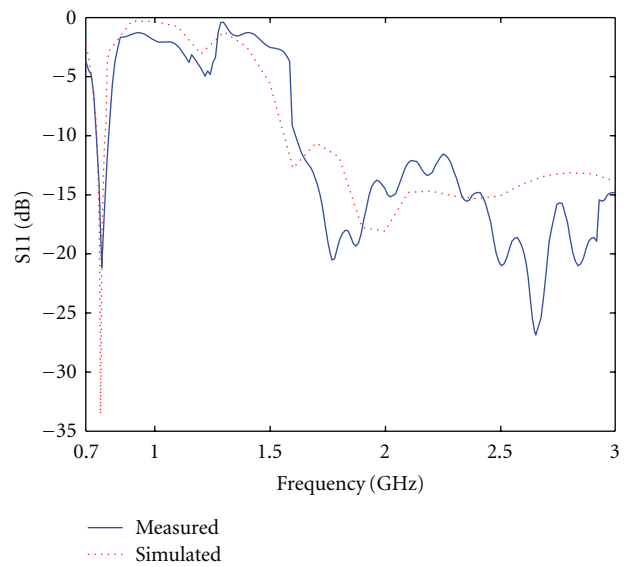


FIGURE 6: Simulated and measured S11 of the proposed antenna.

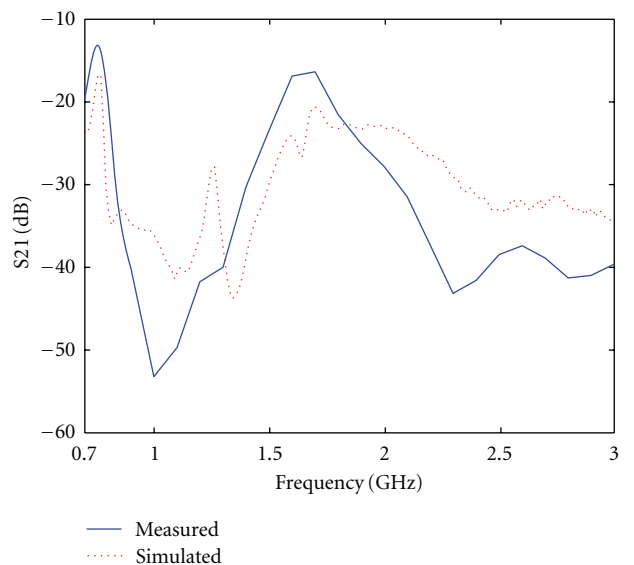


FIGURE 7: Simulated and measured S21 of the proposed antenna.

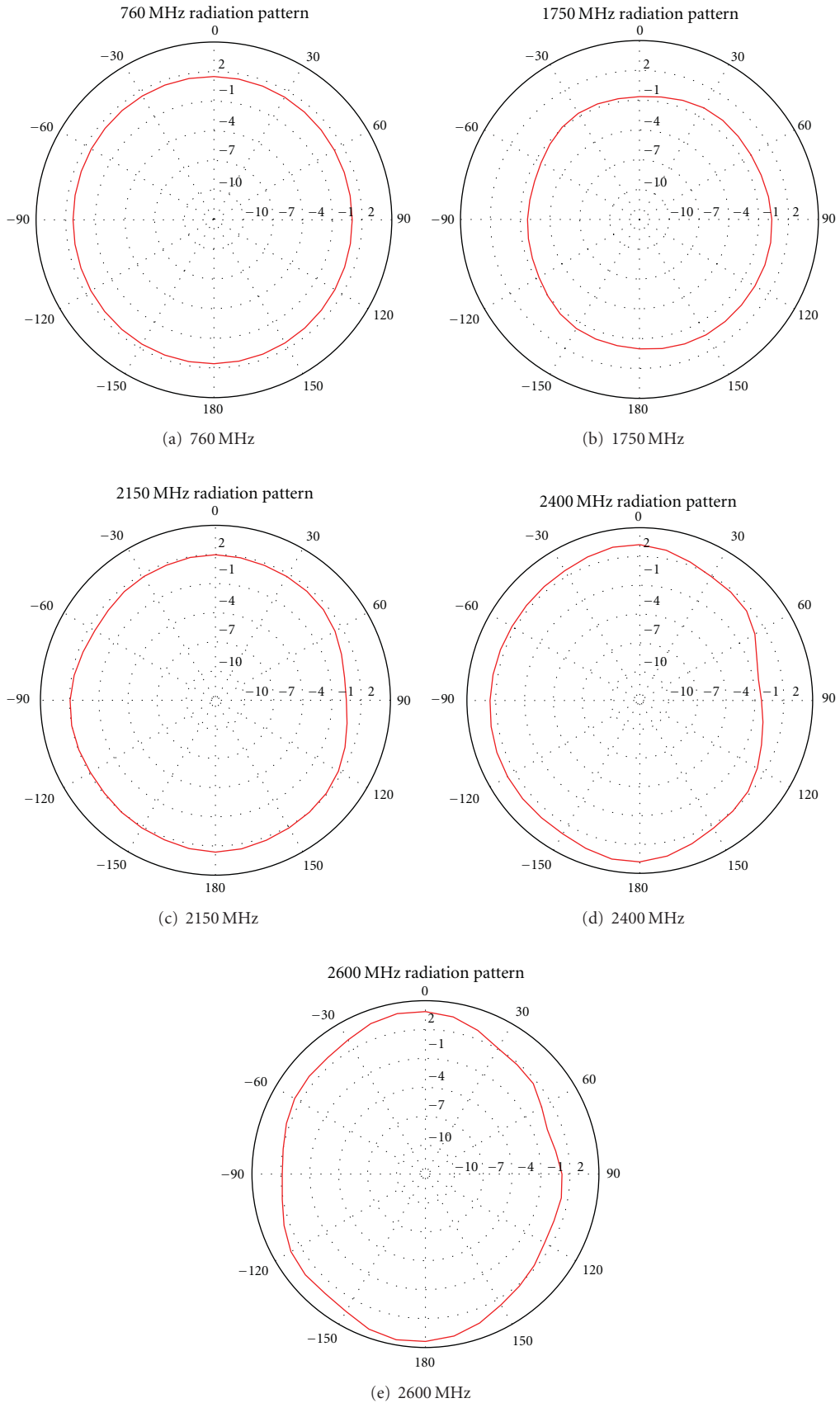


FIGURE 8: Radiation patterns of antenna 1 in x-z plane.

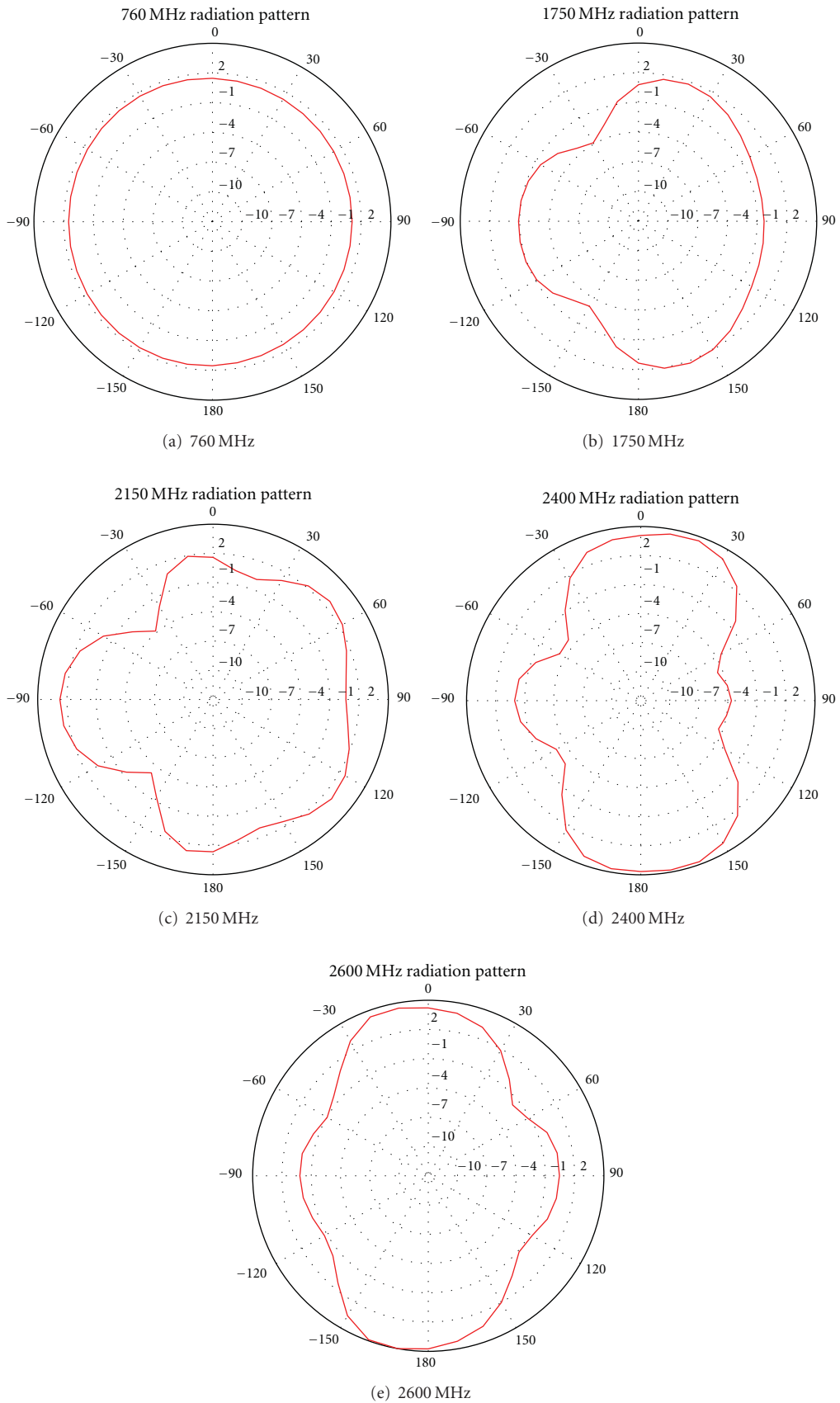


FIGURE 9: Radiation patterns of antenna 2 in y - z plane.

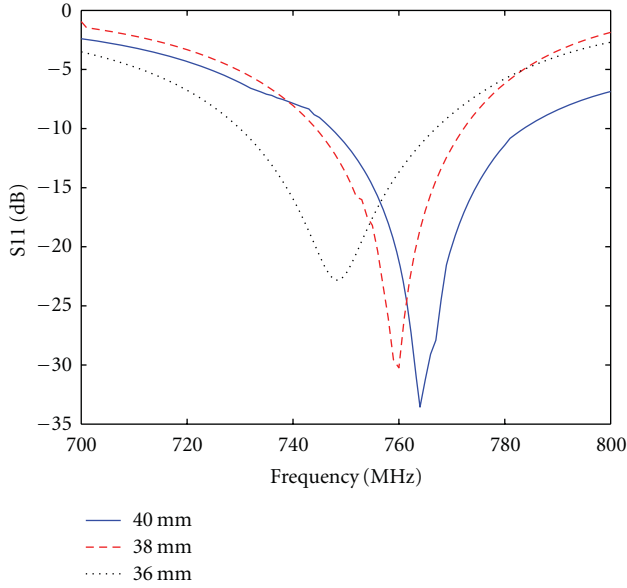


FIGURE 10: S11 of the antenna with different L_{strip} .

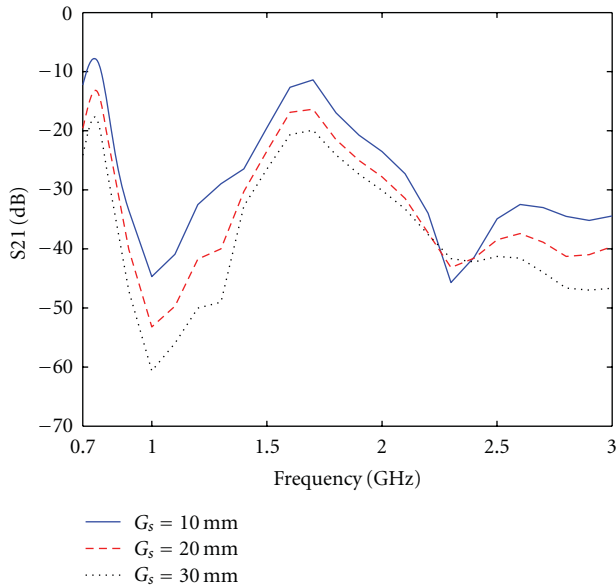


FIGURE 11: S21 of the antenna with different G_s .

2400 MHz, and 2600 MHz. The antenna 1 has an omnidirectional vertically polarized pattern in x - z plane and the antenna 2 generates horizontally polarized radiation in y - z plane. The omnidirectional patterns can enhance and increase the channel capacity [6]. Thus the proposed antenna is more attractive for MIMO application.

4. Parameter Study

For the purpose of optimized performance, parametric studies of the dimensions of the antenna structure are carried out. First, we analyze the length of the meandering microstrip

line. As presented in Figure 10, the resonant frequency at LTE 700 of the antenna is changeable. The resonant frequency goes up when the length is longer and goes down when the length is smaller.

The isolation between two polarizations will be affected by the dimension of spacing G_s . In principle, the larger the spacing is, the lower of the mutual coupling will be. As shown in Figure 11, the spacing is changed from 10 mm to 30 mm and the mutual coupling is from below -9 dB to below -19 dB.

5. Conclusion

In this paper a design of multiband planar monopole antenna for LTE MIMO system has been proposed and implemented. Simulated and measured results showed that the antenna can cover five LTE frequency bands and has high isolation. The proposed antenna will provide better propagation channel and enhance the capacity of MIMO system.

Acknowledgment

This work is supported by the Fundamental Research Funds for the Central Universities.

References

- [1] A. R. Mallahzadeh, S. F. Seyyedrezaei, N. Ghahvehchian, S. Mohammad Ali Nezhad, and S. Mallahzadeh, "Tri-band printed monopole antenna for WLAN and WiMAX MIMO systems," in *Proceedings of the 5th European Conference on Antennas and Propagation (EUCAP '11)*, pp. 548–551, April 2011.
- [2] H. T. Chattha, Y. Huang, X. Zhu, and Y. Lu, "Dual-feed PIFA diversity antenna for wireless applications," *Electronics Letters*, vol. 46, no. 3, pp. 189–190, 2010.
- [3] Q. Luo, J. R. Pereira, and H. M. Salgado, "Reconfigurable dual-band C-shaped monopole antenna array with high isolation," *Electronics Letters*, vol. 46, no. 13, pp. 888–889, 2010.
- [4] Y. Li, Z. Zhang, W. Chen, Z. Feng, and M. F. Iskander, "A dual-polarization slot antenna using a compact CPW feeding structure," *IEEE Antennas and Wireless Propagation Letters*, vol. 9, pp. 191–194, 2010.
- [5] S. M. Ali Nezhad and H. R. Hassani, "A novel triband E-shaped printed monopole antenna for MIMO application," *IEEE Antennas and Wireless Propagation Letters*, vol. 9, pp. 576–579, 2010.
- [6] R. G. Vaughan and J. B. Andersen, "Antenna diversity in mobile communication," *IEEE Transactions on Vehicular Technology*, vol. 36, no. 4, pp. 149–172, 1987.

Research Article

Design of Ultra-Wideband MIMO Antenna for Breast Tumor Detection

Liting Wang¹ and Bin Huang²

¹ School of Biomedical Engineering, Capital Medical University, No. 10 Xitoutiao, You An Men, Beijing 100069, China

² Guilin Airforce Academy, No. 90 Kaifeng Road, Guilin 541003, China

Correspondence should be addressed to Liting Wang, wanglt@ccmu.edu.cn

Received 21 July 2011; Accepted 24 August 2011

Academic Editor: Yuan Yao

Copyright © 2012 L. Wang and B. Huang. This is an open access article distributed under the Creative Commons Attribution License, which permits unrestricted use, distribution, and reproduction in any medium, provided the original work is properly cited.

A MIMO antenna composed by microstrip line-fed circular slot antenna is proposed. This antenna is used in ultra-wideband microwave imaging systems aimed for early breast cancer detection. The antenna is designed to operate across the ultra-wideband frequency band in the air. The mutual coupling between the antenna elements has been investigated to be low enough for MIMO medical imaging applications. Both the simulation and measurement results are shown to illustrate the performances of the proposed antenna.

1. Introduction

Breast cancer is one of the most common types of cancer and a major cause of death among women. However, a high percentage of the cases can be cured if they are detected in time. An important tool for detection is the mammogram, which exploits the differences between the scattering cross-section of normal and malignant tissues to X-rays. But this technique presents important limitations [1]. Recently, an alternative approach is to use microwave imaging, which has the potential advantages of low cost, improved safety, and greater availability [2, 3]. The working principle of microwave imaging techniques is based on the dielectric contrast between the malignant tumor tissues and the healthy ones [4]. In these techniques the tumor is identified from the processing of the scattered signals collected at the antennas. Several approaches can be found in the literatures. However techniques based on ultra-wideband signals have recently woken up a great deal of interest [5–7]. MIMO technique is also applied to this application [8]. In [9], an electrically switched array transmits and receives an ultra-wideband signal. Measurements are time aligned to estimate the return in a particular volumetric pixel. In [10], ultra-wideband MIMO concepts applied to tumor detection are explicitly addressed.

In this paper a novel ultra-wideband MIMO antenna is designed with this goal in mind. It can provide ultra-wideband characteristic, covering 2.3 GHz–12.2 GHz. This ultra-wideband characteristic is obtained by loading a rectangular patch to circular slot antenna. Two elements of such antennas are used for MIMO applications. The proposed structure obtains low mutual coupling and envelope correlation due to the orthogonal polarization.

2. Antenna Structure and Mechanism

As we know, wide slot antennas have received more attention due to their ultra-wideband characteristic. They are very popular for volume-limited and wideband applications. The structure of the proposed UWB MIMO antenna is shown in Figure 1. This antenna is printed on a FR-4 substrate with relative permittivity 4.4 and thickness of 1 mm. The two identical antenna elements have the same structure and dimensions. The antenna has two layers, the top layer and the bottom layer. On the bottom layer there are the grounds with length L_s and width W_s . There are the circular slots in the bottom ground with radius R_c . And in the circular slots there are the rectangular patches with length of L_p and width W_p . On the top layer is the microstrip line with circular patch.

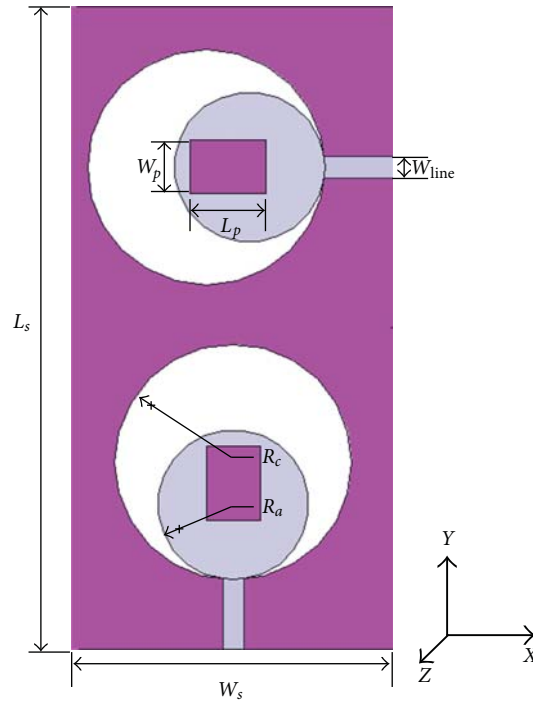


FIGURE 1: The geometry of the proposed antenna.

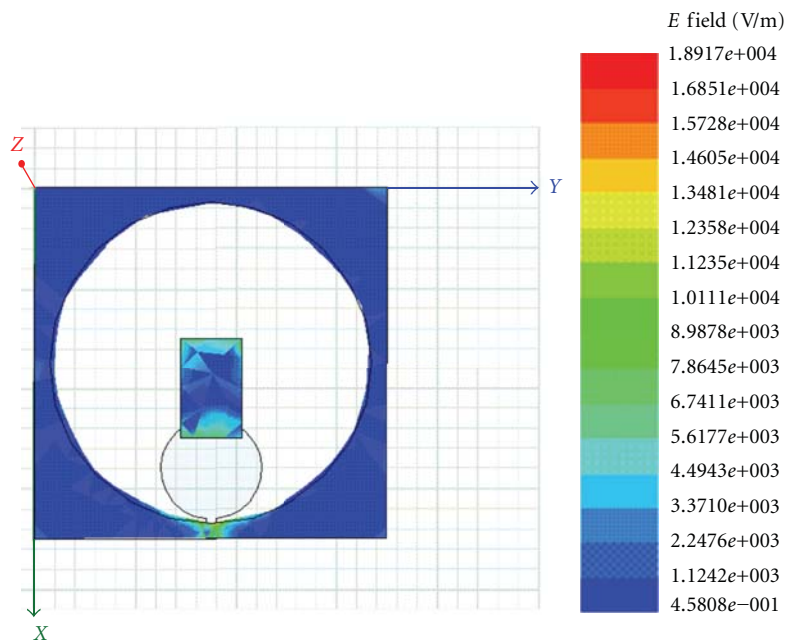


FIGURE 2: Current distribution at 4 GHz.

The fed line with width W_{line} to match 50Ω and the radius of the circular patch is R_a . The two identical antenna elements are connected with no spacing between them. The detailed antenna dimensions are listed in Table 1.

According to Babinet's theory, the slot antenna can be solved through analyzing its complementary antenna. So the circular slot in this paper can be seen as equivalent to a disk

monopole antenna which is already studied [11, 12]. The circular slot antenna has wideband characteristic covering from 6 to 10 GHz. And the rectangular patch in the slot greatly impacts the impedance bandwidth characteristics of the antenna. Figure 2 shows the current distributions on the circular slot antenna with rectangular patch at 4 GHz. It can be seen that the rectangular patch resonates at 4 GHz and

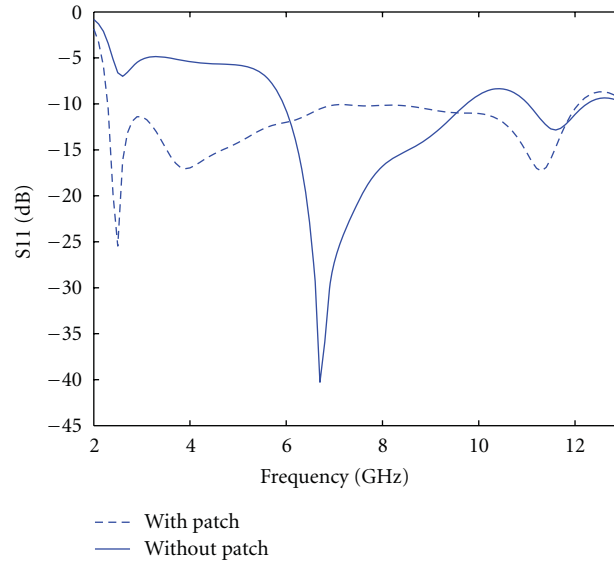


FIGURE 3: Return loss of the slot antenna with and without the rectangular patch.

TABLE 1: Antenna dimensions.

Dimension	L_s	W_s	L_p	W_p	R_c	R_a	W_{line}
Size (mm)	70	35	10	6	16	5	2

widens the frequency band. Figure 3 shows the return loss of the antenna with and without rectangular patch. Thus the proposed antenna has ultra-wideband characteristic.

Compared with the traditional antenna parameters, such as gain, radiation pattern, and reflection coefficients, new parameters and aspects have to be included in the design for MIMO systems. Mutual coupling between antenna elements is a key factor to achieve high antenna performance in the MIMO antenna configuration. For a low mutual coupling, antennas must be far away from each other. But the space for the internal antenna is not enough to obtain low correlation and mutual coupling. In this paper we present a structure for the MIMO antenna elements, in which the identical two antenna elements are orthogonally placed. Then the two antenna elements have orthogonal polarization which can reduce the mutual coupling between the two antennas. Figure 4 shows the simulated 3D radiation patterns of the two antenna elements. It can be seen that the two antenna elements have orthogonal polarizations.

3. Simulation and Measurement Results

Both the simulation and measurement are carried out to verify the above analysis. The proposed structure is simulated in HFSS and measured in an anechoic chamber. The fabricated proposed UWB MIMO antenna is shown in Figure 5. The detailed dimensions can be found in Table 1. Figure 6 shows the simulated and measured return loss, which agree well. The measured -10 dB return loss bandwidths are from 2.3 GHz to 12.2 GHz, which covers an ultra-wideband. The

mutual coupling between the two ports is less than -15 dB across the common bandwidth, as shown in Figure 7.

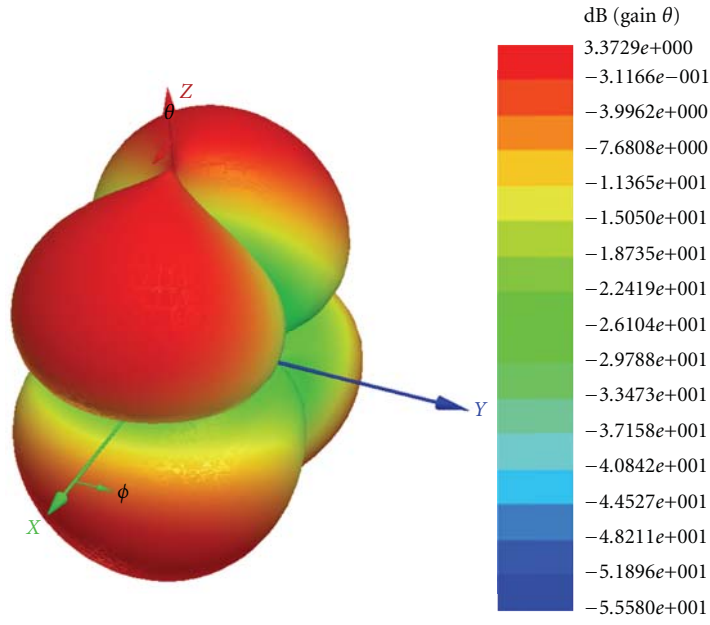
Figures 8 and 9 show the radiation patterns of the antenna 1 and the antenna 2 at 3 GHz, 6 GHz, and 8 GHz at E-plane and H-plane, respectively. The antenna 1 has bidirectional vertically polarized patterns, and the antenna 2 generates horizontally polarized radiations. Thus the proposed antenna is more attractive for ultra-wideband MIMO application for breast tumor detection.

4. Parameter Study

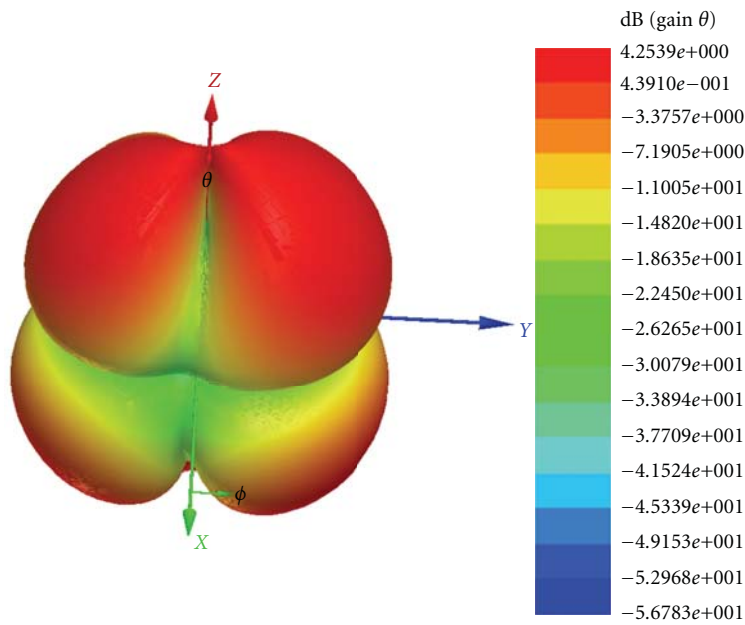
For the purpose of optimized performance, parametric studies of the dimensions of the antenna structure are carried out. First, we analyze the length of the rectangular patch in the slot. As shown in Figure 10, when the length equals 8 mm, the lower frequency band is bad. And when the length is 10 mm, the impedance matching is good over the whole band. When the length is 12 mm, even though its lower frequency band is better than 10 mm, the middle frequency band is worse. Thus the 10 mm is the best length.

Second, we analyze the radius of the microstrip circular patch. The radius varied from 4 mm, 5 mm, to 6 mm while other parameters are fixed. As shown in Figure 11, when the radius is 4 mm, the return loss at 5 GHz–6 GHz and 9 GHz–11 GHz is bad. When the radius is 5 mm, the impedance matching is good. When the radius equals 6 mm, the return loss gets worse. Thus, the radius is 5 mm in the proposed antenna.

The isolation between two polarizations will be affected by the dimension of spacing. In principle, the larger of

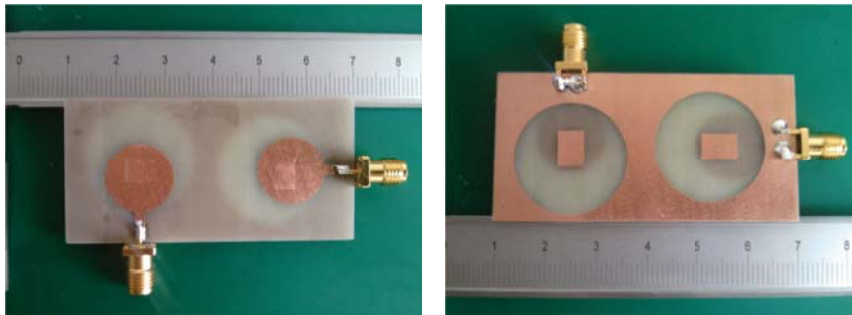


(a)



(b)

FIGURE 4: 3D radiation patterns of the two antenna elements.



(a) top layer

(b) bottom layer

FIGURE 5: Fabricated proposed antenna.

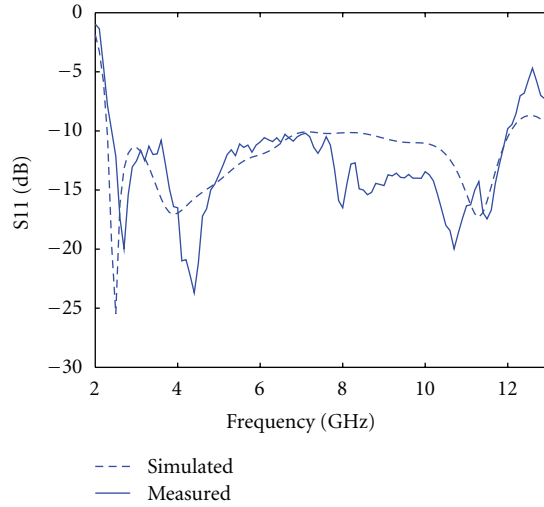


FIGURE 6: Simulated and measured S_{11} .

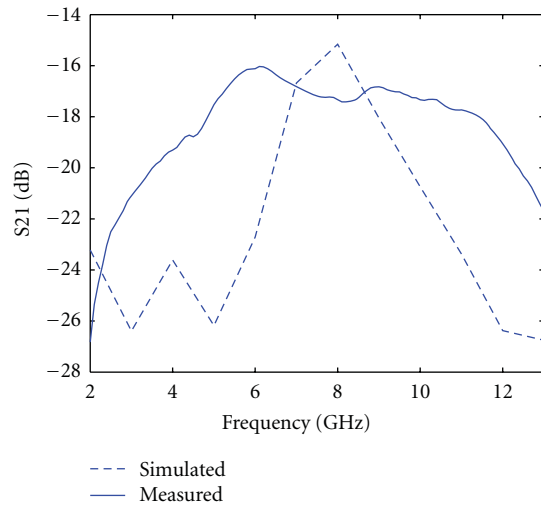
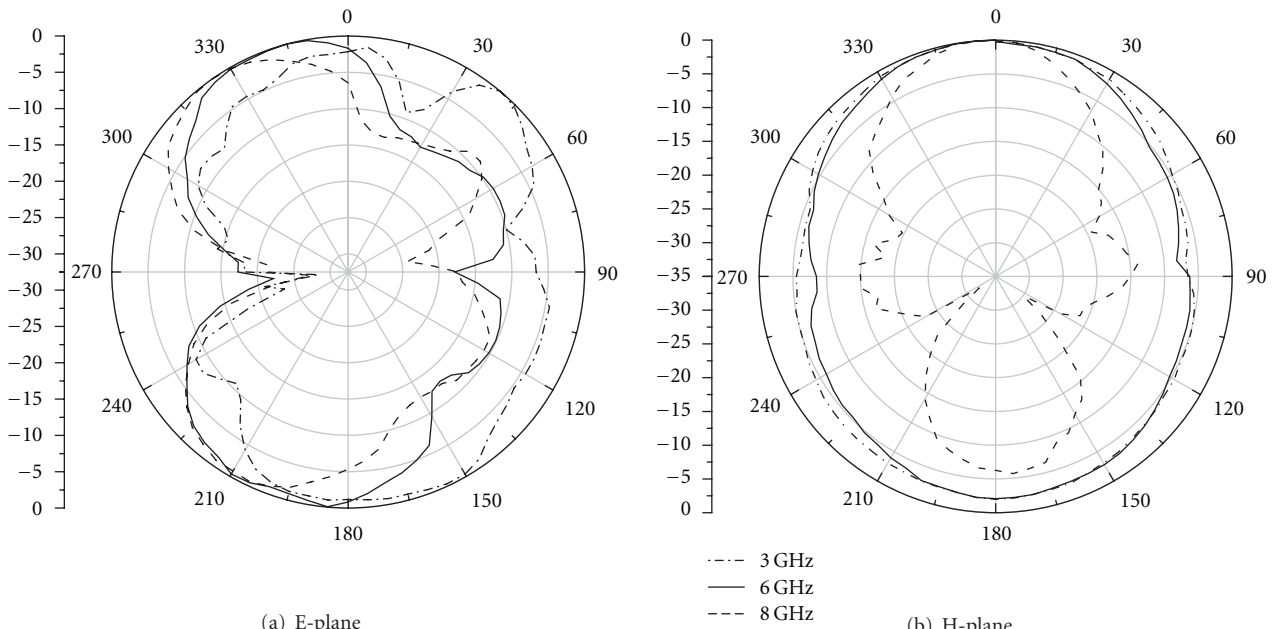


FIGURE 7: Simulated and measured S_{21} .



(a) E-plane (b) H-plane
 FIGURE 8: Radiation patterns of antenna 1 at 3 GHz, 6 GHz and 8 GHz.

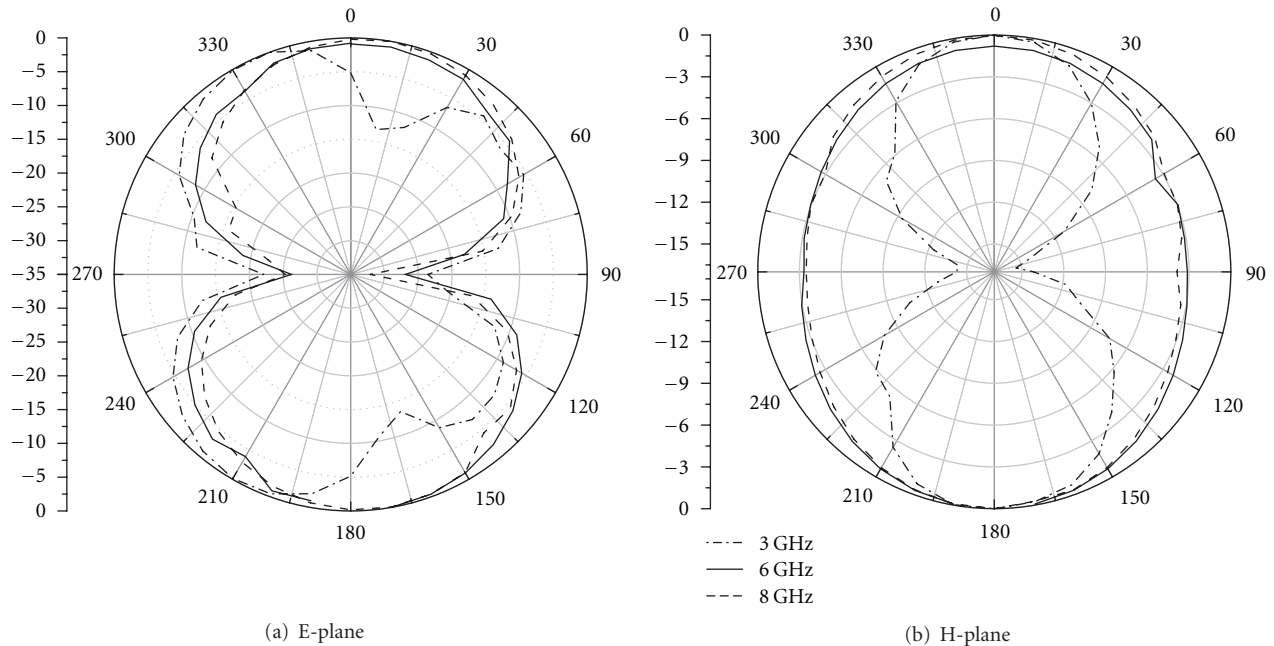
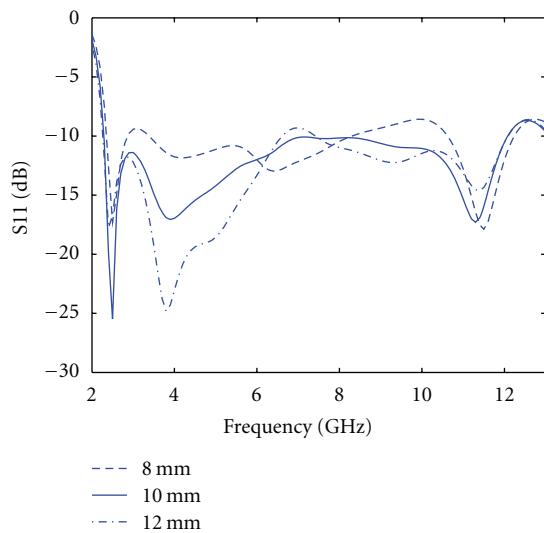
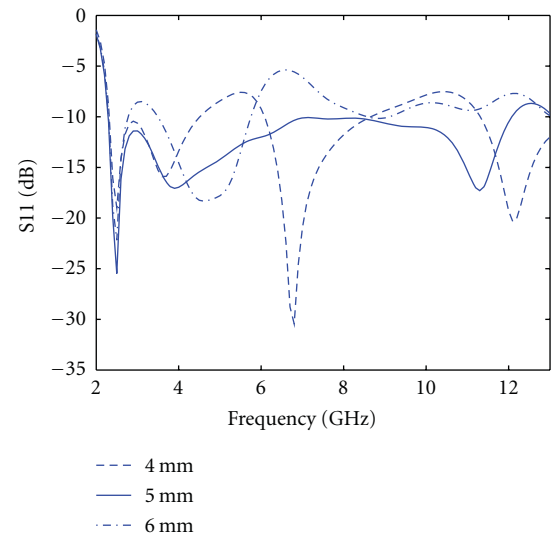


FIGURE 9: Radiation patterns of antenna 2 in y-z plane.

FIGURE 10: S11 of the antenna with different L_p .FIGURE 11: S11 of the antenna with different R_a .

the spacing, the lower of the mutual coupling will be obtained. In this paper the spacing of the two antenna elements is zero which means that the grounds of the two antenna elements are connected without any gap and the mutual coupling is lower than -15 dB over the entire band so there is no need to increase the gap between the two antenna elements.

5. Conclusion

In this paper a design of ultra-wideband MIMO antenna for breast tumor detection has been proposed and implemented. Simulated and measured results showed that the antenna can

cover from 2.3 GHz to 12.2 GHz and has high isolation. The proposed antenna will provide better performance to detect breast tumor.

References

- [1] M. Klemm, I. J. Craddock, J. A. Leendertz, A. Preece, and R. Benjamin, "Radar-based breast cancer detection using a hemispherical antenna array - Experimental results," *IEEE Transactions on Antennas and Propagation*, vol. 57, no. 6, pp. 1692–1704, 2009.
- [2] A. Lazaro, R. Villarino, and D. Girbau, "Design of tapered slot Vivaldi antenna for UWB breast cancer detection," *Microwave*

- and Optical Technology Letters*, vol. 53, no. 3, pp. 639–643, 2011.
- [3] Y. Xie, B. Guo, J. Li, and P. Stoica, “Novel multistatic adaptive microwave imaging methods for early breast cancer detection,” *Eurasip Journal on Applied Signal Processing*, vol. 2006, Article ID 91961, 13 pages, 2006.
- [4] M. Lazebnik, D. Popovic, L. McCartney et al., “A large-scale study of the ultrawideband microwave dielectric properties of normal, benign and malignant breast tissues obtained from cancer surgeries,” *Physics in Medicine and Biology*, vol. 52, no. 20, pp. 6093–6115, 2007.
- [5] Y. Chen, E. Gunawan, K. S. Low, S. C. Wang, Y. Kim, and C. B. Soh, “Pulse design for time reversal method as applied to ultrawideband microwave breast cancer detection: a two-dimensional analysis,” *IEEE Transactions on Antennas and Propagation*, vol. 55, no. 1, pp. 194–204, 2007.
- [6] S. K. Davis, B. D. Van Veen, S. C. Hagness, and F. Kelcz, “Breast tumor characterization based on ultrawideband microwave backscatter,” *IEEE Transactions on Biomedical Engineering*, vol. 55, no. 1, pp. 237–246, 2008.
- [7] I. Hilger, C. Geyer, G. Rimkus et al., “Could we use UWB sensing for breast cancer detection?” in *Proceedings of the 4th European Conference on Antennas and Propagation (EuCAP '10)*, pp. 1–4, April 2010.
- [8] O. T. Z. Daniel, Z. Yuanjin, and L. Zhiping, “Design and experimental investigation of UWB microwave imaging via MIMO beamforming,” in *Proceedings of the IEEE International Conference on Ultra-Wideband (ICUWB '10)*, pp. 851–854, September 2010.
- [9] S. K. Davis, H. Tandradata, S. C. Hagness, and B. D. Van Veen, “Ultrawideband microwave breast cancer detection: a detection-theoretic approach using the generalized likelihood ratio test,” *IEEE Transactions on Biomedical Engineering*, vol. 52, no. 7, pp. 1237–1250, 2005.
- [10] D. W. Bliss and K. W. Forsythe, “MIMO radar medical imaging: self-interference mitigation for breast tumor detection,” in *Proceedings of the 40th Asilomar Conference on Signals, Systems, and Computers (ACSSC '06)*, pp. 1558–1562, November 2006.
- [11] J. Powell and A. Chandrakasan, “Spiral slot patch antenna and circular disc monopole antenna for 3.1–10.6 GHz,” *IEEE Transactions on Antennas and Propagation*, vol. 46, no. 2, pp. 44–49, 1998.
- [12] Z. H. Song, J. R. Qi, J. H. Qiu, and T. X. Zhou, “Study of properties of the circular monopole ultra-wideband antenna,” *Journal of Harbin Engineering University*, vol. 28, no. 1, pp. 26–30, 2007.

Research Article

Design of Compact Dual-Polarized Antennas for MIMO Handsets

Wenhua Chen, Xin Wang, and Zhenghe Feng

State Key Laboratory on Microwave and Digital Communications, Tsinghua University, Beijing 100084, China

Correspondence should be addressed to Wenhua Chen, chenwh@tsinghua.edu.cn

Received 11 June 2011; Accepted 19 July 2011

Academic Editor: Yuan Yao

Copyright © 2012 Wenhua Chen et al. This is an open access article distributed under the Creative Commons Attribution License, which permits unrestricted use, distribution, and reproduction in any medium, provided the original work is properly cited.

A design method of compact dual-polarized antennas has been proposed for multiple input and multiple output (MIMO) handset application. For the sake of high isolation in dual polarizations, a printed monopole and a hybrid slot antenna are combined using a coplanar waveguide (CPW) and microstrip hybrid feeding structure. The proposed topology will result in orthogonal current distribution modes for the different polarizations, which effectively reduces the mutual coupling of the two modes. The operation mechanism of the feeding structure is analyzed in principle and verified by simulation. Simulated and measured results show this compact dual-polarized antenna achieves isolation between the two ports of better than 25 dB, and the relative bandwidth is wider than 23.5%.

1. Introduction

Researches on multiple input and multiple output (MIMO) technology are very popular in wireless communication area, since more than 1 Gbps data transmission rate can be achieved using MIMO technology. As revealed in many literatures [1, 2], the performance of MIMO system sensitively depends on the status of the channel, including radio propagation, multipath effect, and antenna radiation pattern. Recently much attention has been attracted to antenna selection in MIMO system because of its better performance and low cost [3]. Compared with the other components in wireless transceiver, the antennas are much cheaper. Thereby, we can use adequate antennas to perform better channel status and approach the maximum capacity of MIMO system. Several antenna selection schemes [4–8] have been studied extensively so far, such as space selection, radiation pattern selection and polarization selection. In these selection schemes, the polarization selection has more potential for future application due to its compact size and easy fabrication. As shown in previous literature [4, 5], the capacity of MIMO system can be enhanced by using switchable polarization schemes in the redundant elements of MIMO system.

In this paper, based on our proposed dual-polarized antenna in [9], a detailed design method of compact dual-polarized MIMO antennas is presented and discussed. This antenna combines a printed monopole [10, 11] fed by

coplanar waveguide and a hybrid slot antenna [12–15] fed by coupling microstrip line to generate vertical and horizontal polarized radiation, respectively. Low mutual coupling is guaranteed by the orthogonality of different current modes. The structure is planar and can be easily fabricated by general printed circuit board (PCB) techniques, thus it is convenient to be integrated into portable transceivers. Parametric studies have been carried out to investigate the dimensional sensitivities of the proposed antenna structure. Measured *S*-parameters and radiation patterns are presented to validate the proposed design.

2. Antenna Configuration and Mechanism

As we know, printed monopole antennas have been widely used in handsets. Meanwhile, quarter wavelength slot antennas with microstrip feeding line are easy to be integrated into PCB, so they are also popular for volume limited and wideband application. If these two types of antennas can be combined together, a compact dual polarized antenna with inherited low design complexity and fabrication cost can be realized for mobile terminals. As shown in Figure 1, the current distribution of printed monopole antennas and quarter wavelength slot antennas are presented and compared schematically. For a symmetrical feeding structure, the current distribution in monopole antenna is symmetrical

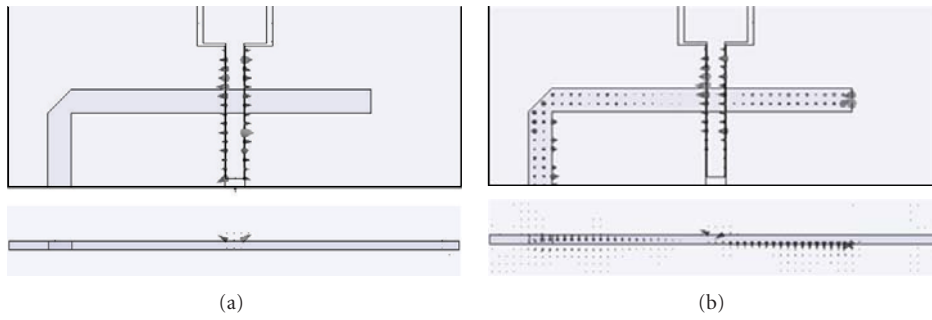


FIGURE 5: Electric field distribution with different feeding ports: (a) CPW and (b) microstrip.

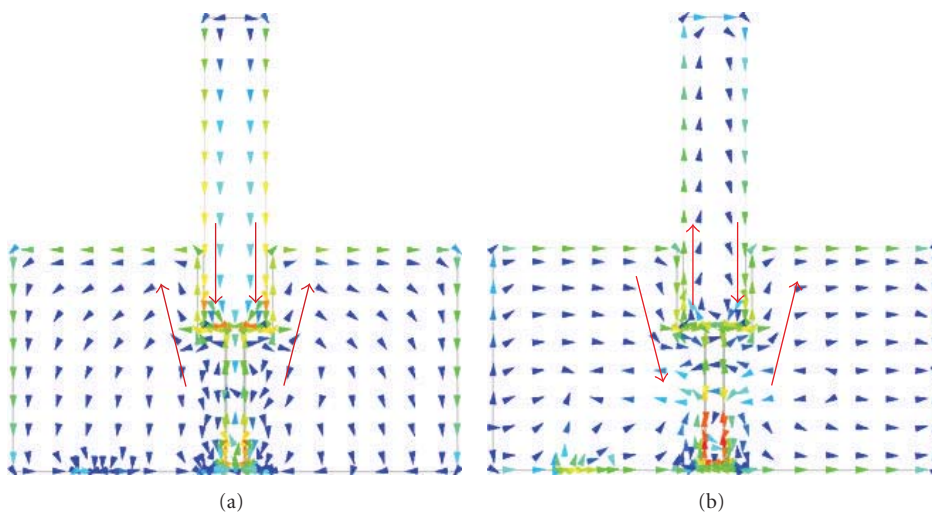


FIGURE 6: Current distribution in different modes, (a) CPW feeding and (b) microstrip feeding.

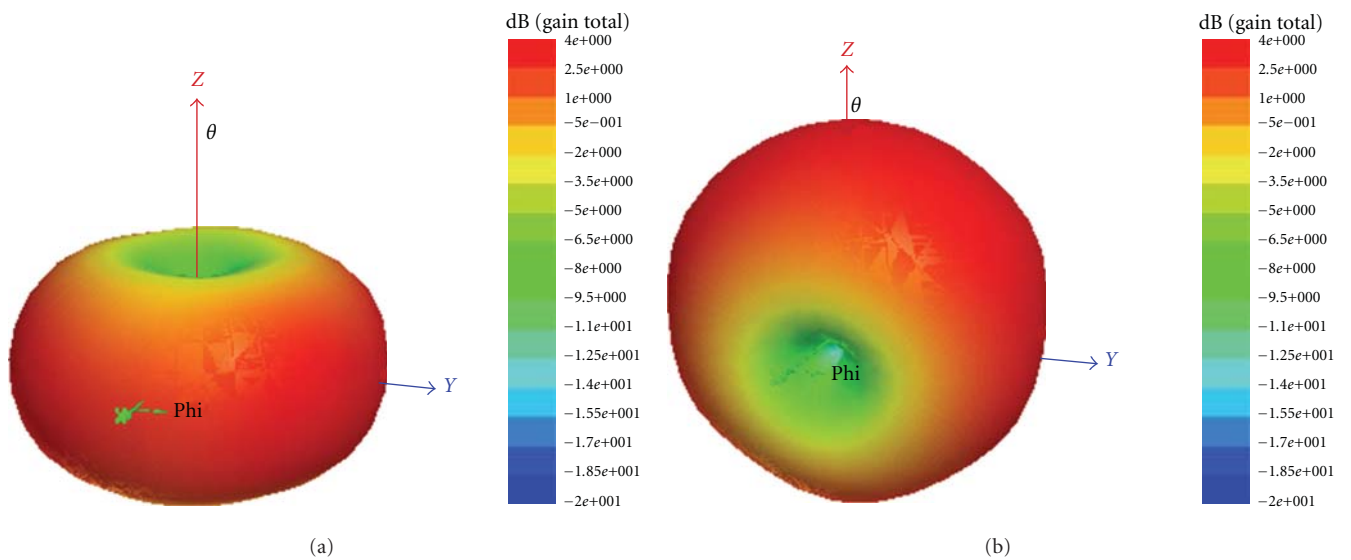


FIGURE 7: Simulated 3D radiation patterns fed by different ports, (a) CPW and (b) microstrip.

TABLE 1: Antenna dimensions.

Dimension	Size (mm)	Dimension	Size (mm)	Dimension	Size (mm)
Wg	50	Lg	25	d	19.3
Wm	7	Lm	25	gm	0.7
W	2	Lc	15.5	g	0.1
Wf	2.6	Lf	15	Pf	9.5

port, in which two-sided ground planes are connected together via its outer conductor. In Figure 3, the electric field distribution within CPW feeding mode and microstrip feeding mode are plot in theory. As illustrated in Figure 3, in the CPW feeding, the electric fields are symmetrical and in the opposite direction whereas the electric fields using microstrip feeding are in the same direction. Thereby, the current distribution induced by the combination of CPW and microstrip feeding is consistent with the requirements of dual polarized antennas. Actually the derived slot antenna consists of two neighboring slot antennas. Since the spacing between the two slots is very small, the magnetic current excited by the microstrip line will be equivalent in terms of magnitude and phase. Finally, the two slots can be viewed as a single hybrid slot for far field radiation.

The transition from slot line to microstrip is presented in Figure 4(a), and the electric field distributions in slot line as well as the microstrip line which is coupled from the slot line are shown. Furthermore, as shown in Figure 4(b), considering two paralleled and close slot lines, in which the electric fields are equal and in phase, as a result, the electric fields induced by the same feeding slot line will have the same characteristics. Consequently the combined feeding effect of two slot lines will be equivalent to the single slot line. Oppositely, in Figure 4(c), if the electric fields are equal and out of phase, the coupled electric field in microstrip line will be canceled with each other, no electronic field will transmit on the microstrip line. Based on this analytical investigation, the microstrip feeding port is shielded from the CPW port, which means that high isolation between the CPW and microstrip feeding ports can be achieved.

3. Experimental Results

To validate the above analysis, the proposed structure is simulated in HFSS firstly. Figure 5 shows the electric field distributions in top view and cross-section, which agree well with the above analysis. In the case of CPW feeding, the electric field in the two slots is an even mode. As we expect, the coupling between the two ports is very small and can be neglected. On the other hand, when the microstrip feeding port is active, the current distribution in two slots is an odd mode. Figure 6 shows the simulated current distributions at 2.35 GHz with one port excited and the other is terminated with 50 Ohm matching load. When the monopole is excited, the current flows on the left and right halves are mostly symmetrical and in phase. In this situation, the monopole antenna can radiate efficiently, and a vertical polarized and almost omnidirectional radiation pattern is realized. While with the hybrid slot antenna excited, the

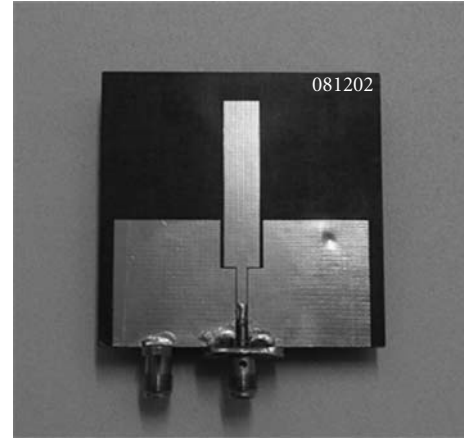


FIGURE 8: The prototype picture.

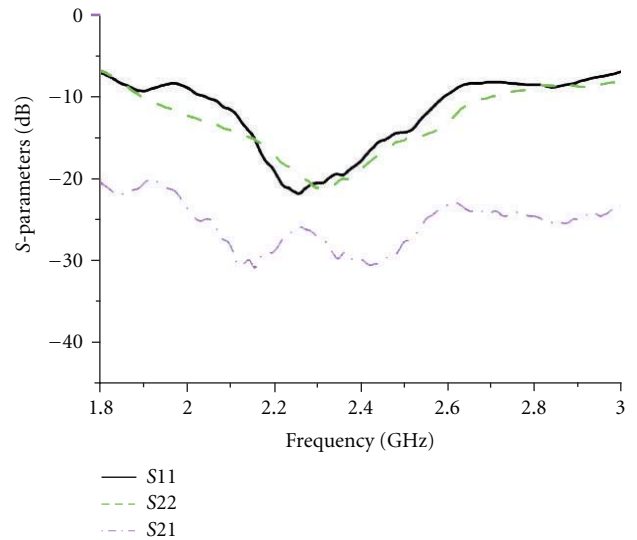


FIGURE 9: Measured S-parameters.

current flows on the two edges of the monopole are mostly 180 degrees out of phase, thus the monopole antenna is idle at this time. Consequently, the horizontal polarized radiation is attributed to the current distribution on the ground plane. Herein, electric fields in feeding ports and current distributions on the metal planes both demonstrate the operation mechanism of the proposed feeding topology, which leads to a high isolation between dual polarizations.

Generally wider monopole results in a wider bandwidth; however, the isolation between dual polarizations will be

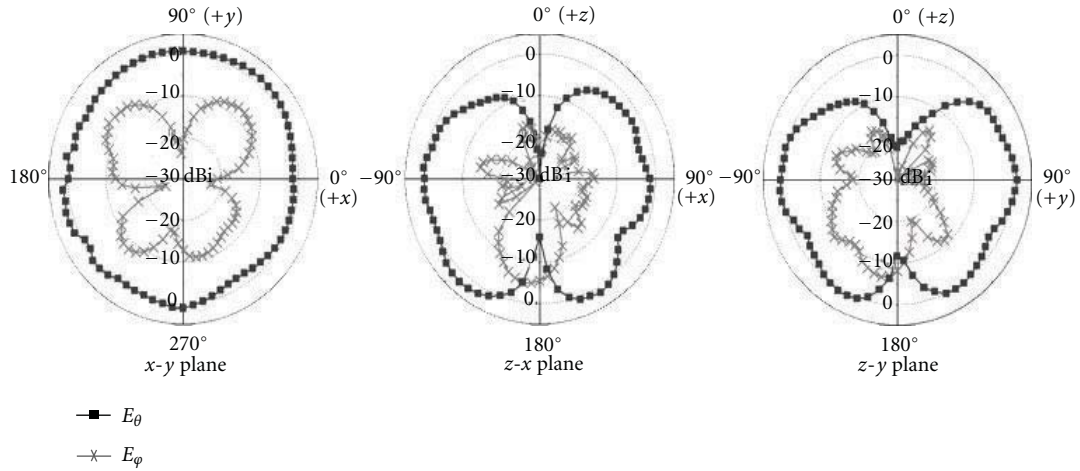


FIGURE 10: Measured radiation patterns of the monopole.

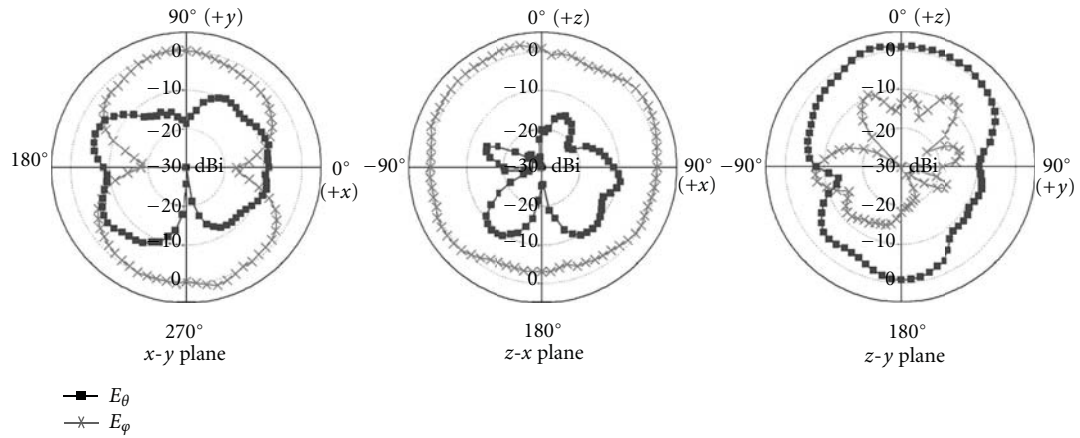


FIGURE 11: Measured radiation patterns of the hybrid slot antenna.

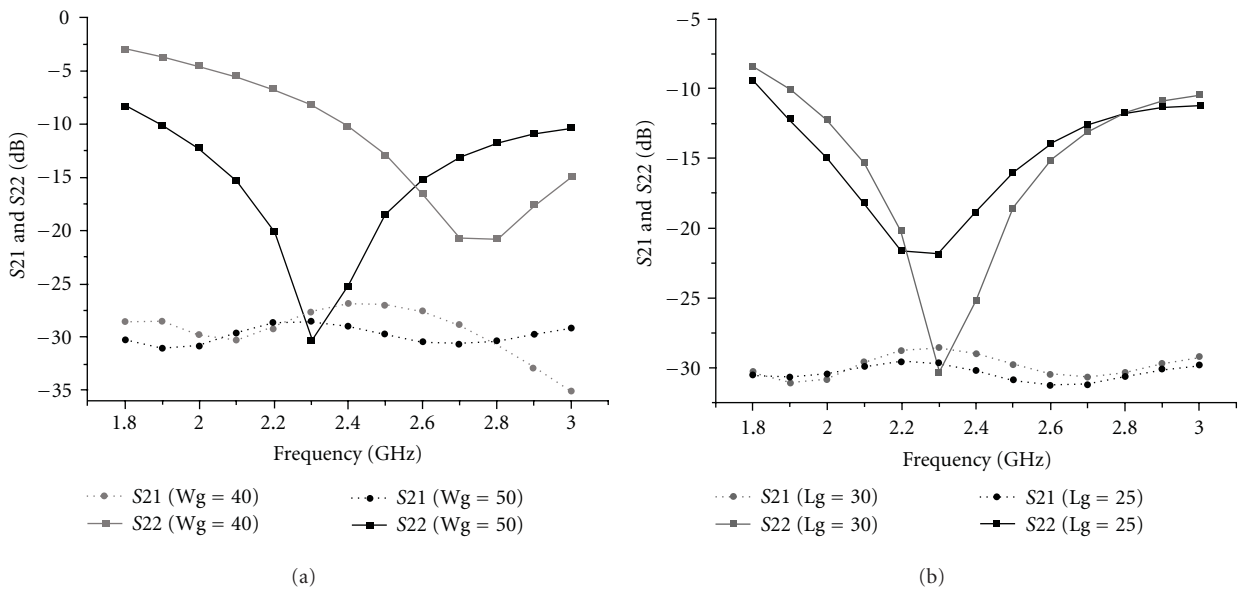


FIGURE 12: The effect of the ground dimension, (a) ground width W_g and (b) ground length L_g .

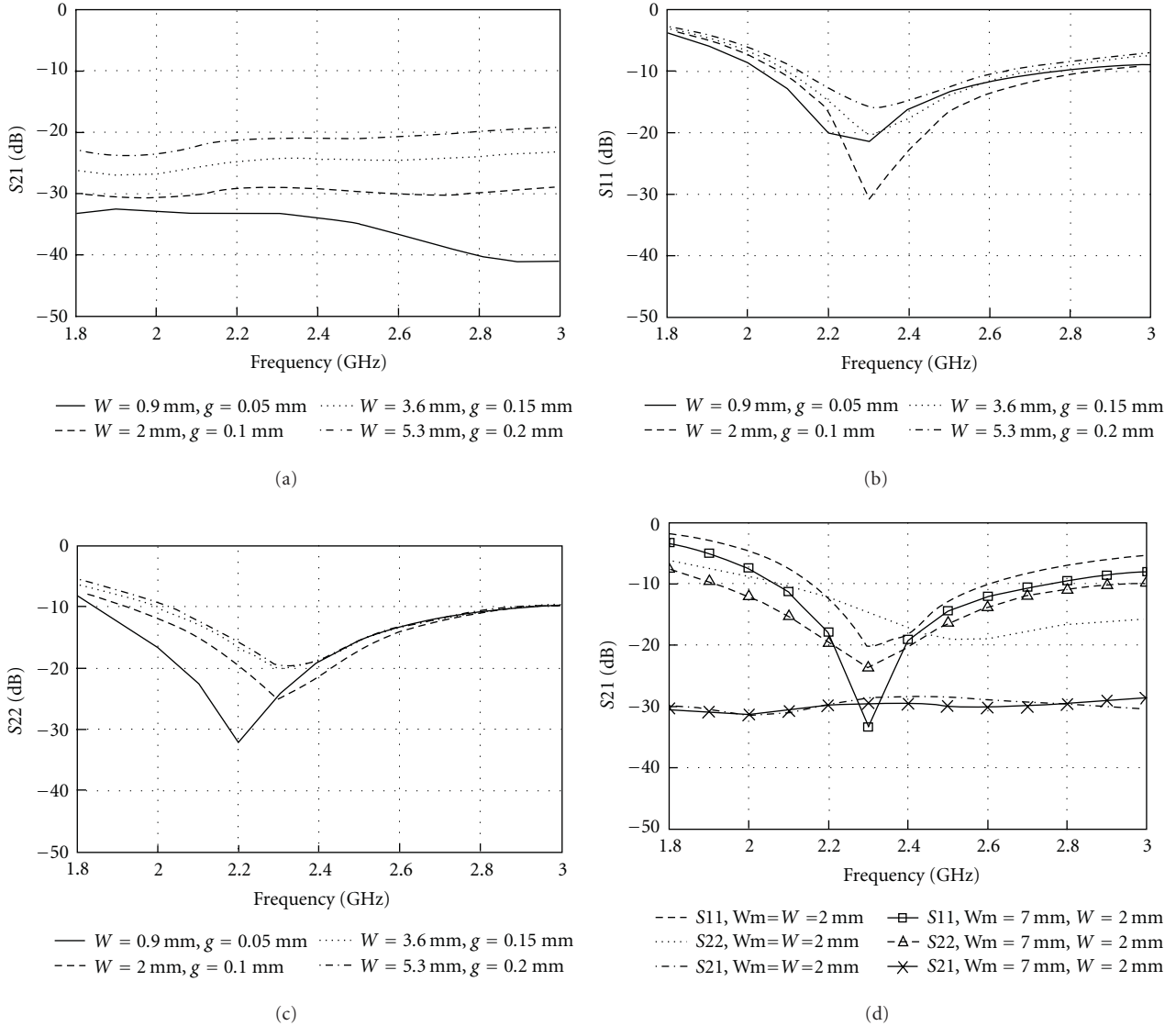


FIGURE 13: Parametric study of the dimensions.

deteriorated. As a solution, a ladder configuration monopole is adopted in this design. Since the widths of two segments can be tuned separately, the bandwidth matching and isolation optimization can approach the ideal point without tradeoff. Moreover, this ladder structure will increase the length of the slot for a given ground size, which is also helpful for size reduction. In Figure 7, the simulation 3D radiation patterns fed by different ports are presented, and the gain of the antenna is around 4dBi in both cases.

A prototype of the proposed antenna as shown in Figure 8 was fabricated and tested, the detailed dimensions can be found in Table 1. Figure 9 shows the measured S-parameters. The measured 10 dB return loss bandwidths are 2.04–2.59 GHz (23.5%) for the monopole and 1.89–2.70 GHz (35%) for the hybrid slot antenna. The mutual coupling between the two ports is less than -25 dB across the common bandwidth. Figures 10 and 11 show the measured radiation patterns of the monopole and the hybrid slot

antenna at 2.35 GHz. The monopole has an omnidirectional vertically polarized pattern in x - y plane and donut-shaped patterns in the elevation planes. The hybrid slot generates bidirectional and horizontally polarized radiation in x - y plane.

Because open-ended quarter wavelength slot antennas are utilized in this design, radiation in some level will appear in the open-ended direction. It can be anticipated that the radiated field is similar to a horizontal located dipole. Limited by the dimension of the ground plane, the reflection effect of the ground plane will not be significant, thus the radiation pattern z - y plane is close to an omnidirectional pattern. Comparing the radiation patterns in different planes and polarizations, it can be seen that these patterns are complementary in space and polarization dimensions. Benefit from these good characteristics, this proposed antenna can be employed for space and angular diversities in MIMO system.

TABLE 2: The dimensions of 50 Ohm CPW.

Width W (mm)	Gap g (mm)	Gap/wavelength
0.9	0.05	0.011
2.0	0.1	0.024
3.6	0.15	0.043
5.3	0.2	0.064

4. Parametric Studies

For the purpose of optimized performance, parametric studies of the dimensions of the ground plane are carried out. As presented in Figure 12(a), the resonant frequency of port 2 relies on the width of the ground plane, which is consistent with above analysis. According to the comparison in Figure 12(b), the length of the ground plane has effect on S22 parameter, the match performance can be improved by increasing the length of the ground plane.

The isolation between two polarizations will be affected by the dimension of CPW. In principle, the characteristic impedance of CPW depends on the ratio of the gap and the central strip width, which provides much freedom for designing. As listed in Table 2, different kinds of 50 Ohm CPW have been presented, as well as the ratio of the gap spacing and the related wavelength. Base on these feeding structures, the isolation S21 between two ports can be calculated, and the simulated results are given in Figure 13(a). From this figure, increasing the width of CPW, that means the spacing between two gaps is wider, the coupling between two ports is stronger than before; however the isolation is still acceptable. In Figures 13(b) and 13(c), the return losses in two ports are computed with different dimensions, obviously the dimensions of CPW will not affect the matching status significantly.

In order to evaluate the performance of the ladder feeding structure, the simulated S-parameters with and without ladder are illustrated. It can be seen that the resonant frequency of the monopole does not change, and isolation between the two polarizations is not varied, but the frequency bandwidth of antenna is enhanced. At the same time, owing to the increase of slot length, the resonant frequency of the hybrid slot will move towards lower frequency.

5. Conclusion

In this paper a design method of compact dual polarized antennas has been proposed and implemented for MIMO system. To isolate the dual polarizations, a novel feeding structure is invented. Simulated and measured results showed the two polarizations are highly isolated by combining the printed monopole and hybrid slot antenna. The proposed antenna will provide better propagation channel and enhance the capacity of MIMO system.

Acknowledgments

This paper was supported by the National Basic Research Program of China (2010CB32740) and National High Technology Research and Development Program of China

(863 Program) under Contract 2009AA011503, and also the National Science and Technology Major Project of the Ministry of Science and Technology of China (Grant no. 2009ZX03007-003 and 2012ZX03001009-003).

References

- [1] A. J. Paulraj, D. A. Gore, R. U. Nabar, and H. Bolcskei, "An overview of MIMO communications—a key to gigabit wireless," *Proceedings of the IEEE*, vol. 92, no. 2, pp. 198–217, 2004.
- [2] A. N. González and B. Lindmark, "The effect of antenna orientation and polarization on MIMO capacity," in *Proceedings of the IEEE Antennas and Propagation Society International Symposium*, pp. 434–437, July 2005.
- [3] I. Berenguer, X. Wang, and V. Krishnamurthy, "Adaptive MIMO antenna selection via discrete stochastic optimization," *IEEE Transactions on Signal Processing*, vol. 53, no. 11, pp. 4315–4329, 2005.
- [4] C. B. Dietrich, K. Dietze, J. R. Nealy, and W. L. Stutzman, "Spatial, polarization, and pattern diversity for wireless handheld terminals," *IEEE Transactions on Antennas and Propagation*, vol. 49, no. 9, pp. 1271–1281, 2001.
- [5] B. A. Cetiner, J.-Y. Qian, G. P. Li, and F. De Flaviis, "A reconfigurable spiral antenna for adaptive MIMO systems," *Eurasip Journal on Wireless Communications and Networking*, vol. 2005, no. 3, pp. 382–389, 2005.
- [6] A. Grau, J. Romeu, S. Blanch, L. Jofre, H. Jafarkhani, and F. De Flaviis, "Performance enhancement of the alamouti diversity scheme using polarization-reconfigurable antennas in different fading environments," in *Proceedings of the IEEE Antennas and Propagation Society International Symposium*, pp. 133–136, July 2006.
- [7] H.T. Hui, "Practical dual-helical antenna array for diversity/MIMO receiving antennas on mobile handsets," in *Proceedings of the IEE Proceedings of Microwaves, Antennas and Propagation*, vol. 152, no. 5, pp. 367–372, October 2005.
- [8] B. A. Cetiner, H. Jafarkhani, J.-Y. Qian, H. J. Yoo, A. Grau, and F. De Flaviis, "Multifunctional reconfigurable MEMS integrated antennas for adaptive MIMO systems," *IEEE Communications Magazine*, vol. 42, no. 12, pp. 62–70, 2004.
- [9] X. Wang, W. Chen, and Z. Feng, "Compact dual-polarized antenna combining printed monopole and halfslot antenna for MIMO applications," in *Proceedings of the IEEE International Symposium on Antennas and Propagation*, pp. 1–4, June 2009.
- [10] M. J. Ammann and M. John, "Optimum design of the printed strip monopole," *IEEE Antennas and Propagation Magazine*, vol. 47, no. 6, pp. 59–61, 2005.
- [11] D. Su, J. J. Qian, H. Yang, and D. Fu, "A novel broadband polarization diversity antenna using a cross-pair of folded dipoles," *IEEE Antennas and Wireless Propagation Letters*, vol. 4, no. 1, pp. 433–435, 2005.
- [12] S. I. Latif, L. Shafai, and S. K. Sharma, "Bandwidth enhancement and size reduction of microstrip slot antennas," *IEEE Transactions on Antennas and Propagation*, vol. 53, no. 3, pp. 994–1003, 2005.
- [13] S. K. Sharma, L. Shafai, and N. Jacob, "Investigation of wide-band microstrip slot antenna," *IEEE Transactions on Antennas and Propagation*, vol. 52, no. 3, pp. 865–872, 2004.
- [14] Y. Li, Z. Zhang, W. Chen, Z. Feng, and M. F. Iskander, "A dual-polarization slot antenna using a compact CPW feeding

structure," *IEEE Antennas and Wireless Propagation Letters*, vol. 9, pp. 191–194, 2010.

- [15] K.-L. Wong, H.-C. Tung, and T.-W. Chiou, "Broadband dual-polarized aperture-coupled patch antennas with modified H-shaped coupling slots," *IEEE Transactions on Antennas and Propagation*, vol. 50, no. 2, pp. 188–191, 2002.

Research Article

Impact of Mutual Coupling and Polarization of Antennas on BER Performances of Spatial Multiplexing MIMO Systems

Jianfeng Zheng, Yue Li, and Zhenghe Feng

State Key Laboratory of Microwave and Digital Communication, Tsinghua University, Beijing 100084, China

Correspondence should be addressed to Jianfeng Zheng, zjf98@mails.tsinghua.edu.cn

Received 11 May 2011; Accepted 26 May 2011

Academic Editor: Yuan Yao

Copyright © 2012 Jianfeng Zheng et al. This is an open access article distributed under the Creative Commons Attribution License, which permits unrestricted use, distribution, and reproduction in any medium, provided the original work is properly cited.

This paper is aimed at studying the impacts of mutual coupling, matching networks, and polarization of antennas on performances of Multiple-Input Multiple-Output (MIMO) systems employing Spatial Multiplexing (SM). In particular, the uncoded average Bit Error Rate (BER) of MIMO systems is investigated. An accurate signal analysis framework based on circuit network parameters is presented to describe the transmit/receive characteristics of the matched/unmatched antenna array. The studied arrays consist of matched/unmatched compact copolarization and polarization diversity antenna array. Monte-Carlo numerical simulations are used to study the BER performances of the SM MIMO systems using maximum-likelihood and/or zero-forcing detection schemes. The simulation results demonstrate that the use of matching networks can improve the BER performance of SM MIMO systems significantly, and the BER performance deterioration due to antenna orientation randomness can be compensated by use of polarization diversity antenna arrays.

1. Introduction

The emerging Multiple-Input Multiple-Output (MIMO) wireless communication techniques are attentively studied in the last decades because these can prominently improve the transmission rates and qualities of wireless communication systems [1–4]. The MIMO wireless communication techniques are the key technologies for future wideband wireless communications. An important challenge of implementation of MIMO wireless communication techniques on mobile terminals and access points is to place multiple antennas in a physical size constrained volume. The serious mutual coupling between compact antennas will cause impedance mismatch and the element active pattern distortions, thus make the performance of MIMO communication systems to degrade [5–8].

Prior works show the uses of multiport matching networks and polarization antennas to construct compact antenna arrays in limited volumes while maintain the channel capacity of MIMO systems. In [8–11] multiport decoupling and matching networks are utilized to reduce the mutual coupling between antenna elements of compact

receive arrays. The results show that when lossless matching networks are used, the MIMO systems with compact receive arrays of which the spacings between antennas elements are only 0.1λ can approach the similar channel capacity to MIMO systems with largely spaced antenna arrays, where λ is the wavelength. Polarization diversity antenna are also considered to improve the capacity further while maintaining the array size as studied in [12–15].

To realize the transmission rate and quality advantages of MIMO wireless communication systems, specified space-time coding schemes must be used, such as Spatial Multiplexing (SM) scheme [16, 17], and Space-Time Block Coding (STBC) scheme [18]. The obvious measurable criterion for space-time coding systems is the Bit Error Rate (BER) over approached transmission rates. Thus, the BER performance of space-time coding systems would be considered to evaluate the impacts of mutual coupling, matching networks and polarization diversity on MIMO wireless communications.

Prior works usually use analytical channel model to study the performance of space-time coding systems, such as complex Gaussian distributed channel models or correlation separated channel models [17–19]. Though the performance

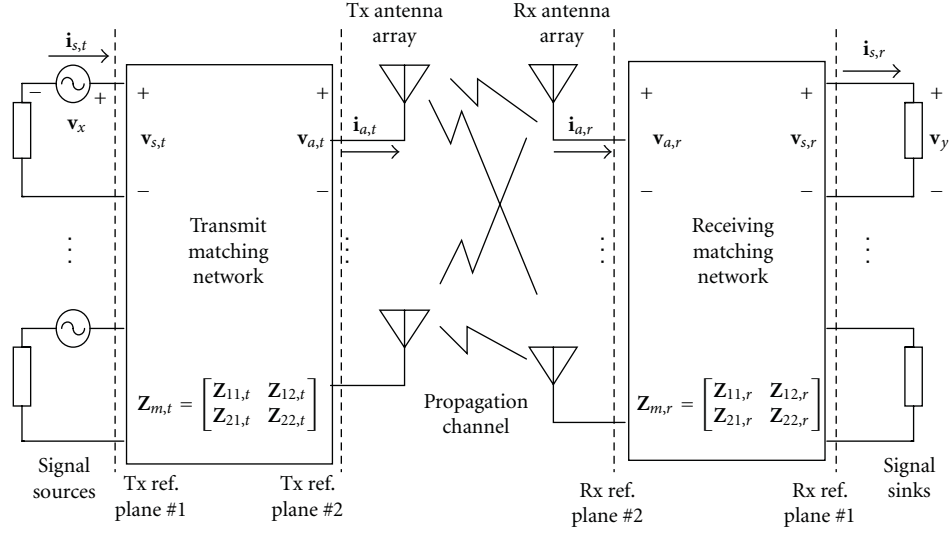


FIGURE 1: Analysis framework of the MIMO systems considering mutual coupling and matching networks.

analyses of space-time coding schemes based on analytical channel models are important and effective for MIMO systems with nearly ideal antennas, those analyses are not appropriate for studying the impacts of mutual coupling and polarization diversity of compact antennas on BER performances of MIMO systems. This is because the analytical models usually ignore the influence of specified antennas and radio frequency branches and do not reflect the physical characteristics of the channels; thus the analytical models can not be used to evaluate the design of antenna arrays and/or RF branches for MIMO systems using specific space-time coding schemes [20].

The paper studies the impacts of mutual coupling, matching networks, and polarization diversity on BER performances of SM MIMO systems using the accurate circuit network signal model. The rest of the paper is divided into 4 sections: in Section 2, the complete system model based on circuit network parameters is presented; in Section 3, the BER performances of SM MIMO systems are studied, and the effects of the mutual coupling and matching networks are investigated; the impacts of polarization diversity antenna are studied in Section 4; in Section 5, the conclusions are drawn.

2. Analysis Framework

The RF chains of MIMO systems are shown in Figure 1, consisting of transmitters, matched transmit antenna array, propagation channel, matched receive antenna array, and receivers. The matching networks are assumed to be passive and lossless but are not needed to be reciprocal.

The n_t independent signal sources with real output impedance R_0 , which is the characteristic impedance of the RF system and the transmission line, are used to create the transmitted signals, respectively. The currents on the RF system ports can be represented as

$$\mathbf{i}_{s,t} = (R_0\mathbf{I} + \mathbf{Z}_{s,t})^{-1}\mathbf{v}_x, \quad (1)$$

where $\mathbf{Z}_{s,t}$ is the input impedance matrix of the (matched) transmit antenna array as in Figure 1, and \mathbf{v}_x is the voltage vector of signal sources. In most communication systems, the power constraint is dependent on the transmit power P_0 of the signal sources. The transmit power constraint can be expressed as [21]

$$E[\mathbf{v}_x^H \mathbf{v}_x] \leq 4R_0P_0 = K_t, \quad (2)$$

where $E[\cdot]$ is the expectation operation and K_t is the mean square limitation of the signal voltages. Prior works commonly assumed constant radiated power to avoid the impact of mutual coupling of transmit antenna on SNR and thereby channel capacity [9]. However, the coupling between transmit antennas will demand signal sources to output more power, that is, a higher transmit power, to guarantee a constant radiated power, while the cost of improving the signal sources' transmit power is expensive. Thus, that constant radiated power limitation is obviously critical.

Because the mismatch between signal sources and coupled transmit antennas causes a reflection which may seriously reduce the gain realized by the antennas and interact with the signal sources to cause unstable operation of these components, a transmit matching network with Z-parameter matrix $\mathbf{Z}_{m,t}$ is used to compensate the impact of coupling between transmit antenna arrays on the MIMO performance. Given the multiport nature of the RF system, the impedance matrix of the transmit matching networks is represented using a block impedance matrix description as

$$\mathbf{Z}_{m,t} = \begin{bmatrix} \mathbf{Z}_{ss,t} & \mathbf{Z}_{sa,t} \\ \mathbf{Z}_{as,t} & \mathbf{Z}_{aa,t} \end{bmatrix}, \quad (3)$$

where the subscriber "a" and "s" refer to antenna and RF system ports as in Figure 1, respectively. Thus the input impedance matrix of matched transmit antenna array is $\mathbf{Z}_{s,t} = \mathbf{Z}_{ss,t} - \mathbf{Z}_{sa,t}(\mathbf{Z}_{aa,t} + \mathbf{Z}_{aa,t})^{-1}\mathbf{Z}_{as,t}$.

The current vector on the antenna ports can be related to signal source voltages as

$$\mathbf{i}_{a,t} = \underbrace{\left[(\mathbf{Z}_{a,t} + \mathbf{Z}_{aa,t})^{-1} \mathbf{Z}_{as,t} \right]}_{\mathbf{T}_t} (R_0 \mathbf{I} + \mathbf{Z}_{s,t})^{-1} \mathbf{v}_x, \quad (4)$$

where $\mathbf{Z}_{a,t}$ is the impedance matrix of transmit antenna array, and \mathbf{T}_t is the transfer function relating source voltages to antenna currents. When the transmit antenna array is directly connected to the sources, $\mathbf{T}_t = (R_0 \mathbf{I} + \mathbf{Z}_{a,t})^{-1}$.

The radiate electric fields $\mathbf{E}_{tx}(\mathbf{k}_t)$ in the far-field region of the transmitter can be related to the current $\mathbf{i}_{a,t}$ on the n_t antenna ports using the radiate electric pattern $\mathbf{E}_{a,t}(\mathbf{k}_t)$ as [22]

$$\mathbf{E}_{tx}(\mathbf{k}_t) = \sum_{n=1}^{n_t} \mathbf{e}_{n,a,t}(\mathbf{k}_t) \mathbf{i}_{n,a,t} = \mathbf{E}_{a,t}(\mathbf{k}_t) \mathbf{i}_{a,t}, \quad (5)$$

where $\mathbf{k}_t = [\theta_t \ \phi_t]^T$ represents a direction in solid angle with elevation θ_t and azimuth angles ϕ_t , respectively. The function $\mathbf{e}_{n,a,t}(\mathbf{k}_t)$, which is the n th column of $\mathbf{E}_{a,t}(\mathbf{k}_t)$, represents radiate electric wave fields represented in \mathbf{k}_t for unit driving current ($\mathbf{i}_n = 1$) with all other antenna element ports open-circuited. The radiate fields in the far-field region is normalized by the spherical wave factor $e^{-jk_0 r_t}/r_t$, with k_0 the free-space wave number, and r_t is the distance from the center of the sphere to the \mathbf{r}_t point, so the radiate electric patterns depend only on the observation angle [23].

The characteristics of propagation channel can be represented by the transfer function $\mathbf{\Gamma}_{rt}(-\mathbf{k}_r, \mathbf{k}_t)$ relating the inward wave fields impinging receive antenna arrays to the output forward wave fields from transmit antenna arrays as [12, 22]

$$\mathbf{E}_{rx}(-\mathbf{k}_r) = \oint_{\mathbf{k}_r} \mathbf{G}_{rt}(-\mathbf{k}_r, \mathbf{k}_t) \mathbf{E}_{tx}(\mathbf{k}_t) d\mathbf{k}_t, \quad (6)$$

where $\mathbf{E}_{rx}(-\mathbf{k}_r)$ denotes the inward signal wave fields in receive solid angle $-\mathbf{k}_r$, and the minus sign “-” before \mathbf{k}_r denotes that the wave is toward the receiver.

We represent the radiate pattern of the m th coupled receive element referenced to the receive coordinate origin as $\mathbf{e}_{m,a,r}(\mathbf{k}_r)$. By reciprocity, the open-circuited voltages on receive antenna ports are then given as [10, 22]

$$\mathbf{v}_{a,r}^{(o)} = -j \frac{4\pi}{k_0 \eta} \oint_{\mathbf{k}_r} \mathbf{E}_{a,r}^T(\mathbf{k}_r) \mathbf{E}_{rx}(-\mathbf{k}_r) d\mathbf{k}_r, \quad (7)$$

where $\mathbf{E}_{a,r}(\mathbf{k}_r)$ represent the $2 \times n_r$ dimension matrix with m th column $\mathbf{e}_{m,a,r}(\mathbf{k}_r)$, and η is the characteristic wave impedance.

Terminate the coupled receive antenna array with receive matching network $\mathbf{Z}_{m,r}$, which composes of block matrix $\mathbf{Z}_{ss,r}, \mathbf{Z}_{sa,r}, \mathbf{Z}_{as,r}, \mathbf{Z}_{aa,r}$ in a similar way with transmit matching network. The open-circuited voltages on the receive ports are

$$\mathbf{v}_{s,r}^{(o)} = \mathbf{Z}_{sa,r} (\mathbf{Z}_{aa,r} + \mathbf{Z}_{a,r})^{-1} \mathbf{v}_{a,r}^{(o)}, \quad (8)$$

where $\mathbf{Z}_{a,r}$ is the impedance matrix of receive antenna array.

Similar with the transmitter, we assume the receive sinks are identically independent and the input impedances are R_0 , then the voltages $\mathbf{v}_{x,r}$ and $\mathbf{v}_{n,r}$ on receive loads induced from inward waves and receiver noises, respectively, can be expressed as [11]

$$\mathbf{v}_{x,r} = \underbrace{(R_0 \mathbf{I} + \mathbf{Z}_{s,r})^{-1} [\mathbf{Z}_{sa,r} (\mathbf{Z}_{aa,r} + \mathbf{Z}_{a,r})]}_{\mathbf{T}_r} \mathbf{v}_{a,r}^{(o)}, \quad (9a)$$

$$\mathbf{v}_{n,r} = -G_r \mathbf{i}_n, \quad (9b)$$

where $\mathbf{Z}_{s,r} = \mathbf{Z}_{ss,r} - \mathbf{Z}_{sa,r} (\mathbf{Z}_{aa,r} + \mathbf{Z}_{a,r})^{-1} \mathbf{Z}_{as,r}$ is the impedance matrix of the matched receive antenna array as in Figure 1, \mathbf{T}_r is the transfer function relating open-circuited voltages on antenna ports to voltages on receive loads, G_r represents the matched gain of the receive sinks, and \mathbf{i}_n is the effective noise-source current vector of the receive sinks [11].

Following the above, the system model of MIMO system can be described as

$$\underbrace{\mathbf{y}}_{\mathbf{y}} = \underbrace{\mathbf{T}_r \mathbf{H}_0 \mathbf{T}_t}_{\mathbf{H}} \underbrace{\mathbf{v}_x}_{\mathbf{x}} + \underbrace{(-G_r \mathbf{i}_n)}_{\mathbf{n}}, \quad (10)$$

where $\mathbf{H}_0 = \oint_{\mathbf{k}_r} \oint_{\mathbf{k}_t} \mathbf{E}_{a,r}^T(-\mathbf{k}_r) \mathbf{G}_{rt}(-\mathbf{k}_r, \mathbf{k}_t) \mathbf{E}_{a,t}(\mathbf{k}_t) d\mathbf{k}_t d\mathbf{k}_r$ is the transfer function between the currents on the transmit antenna ports and the open-circuited signal voltages on the receive antenna ports, \mathbf{n} denotes the noise. \mathbf{y} and \mathbf{x} represent the received and transmitted signals, respectively. While \mathbf{H} is changed with different transmit and/or receive matching networks, \mathbf{H}_0 is not changed for given transmit and receive antenna arrays terminated with different matching networks.

3. Impacts of Mutual Coupling on BER Performances of Layered Space-Time Coding MIMO Systems

3.1. Mutual Coupling and Multiport Matching Networks. Tight mutual coupling in conjunction with closely spaced antennas results in significant gain reduction caused by power mismatch. The gain reduction decreases the antenna arrays' ability to transmit energy to or extract energy from the fields. The MIMO systems require dissipation of large amounts of transmitted power to guarantee the SNR. A potential solution to the problem would be to apply transmit and receive matching networks leading from signal sources/sinks to the coupled antenna arrays thereby to avoid the effects of mismatch. Prior works have revealed the impacts of receive matching networks on channel capacity. In this paper, impacts of both transmit and receive matching networks on BER performances of SM MIMO systems are studied.

The investigations of the BER performances of MIMO system, which is dependent on the transmit and receive matching networks, would be incomplete without considering the optimal matching networks. These decouple and match the impedances of the transmit and receive antenna arrays to the characteristic impedance of RF system, that

is, to make $\mathbf{Z}_{s,t/r} = R_0\mathbf{I}$. Insertion of a lossless receive matching network between the receive antennas and sinks can increase the power collected when $\mathbf{Z}_{a,r} \neq R_0\mathbf{I}$. And similarly, insertion of a lossless transmit matching network between the transmitters and the transmit antennas can also decrease the required transmit power of signal sources when fixed (but arbitrary) driving antenna currents $\mathbf{i}_{a,t}$ (and thereby the transmit fields) are demanded when $\mathbf{Z}_{a,t} \neq R_0\mathbf{I}$. For the antenna arrays' ability to transmit and receive power to/from fields is improved, the BER performances of MIMO systems with matched transmit and receive antenna arrays are also better than that with unmatched antenna arrays.

The section firstly presents a significantly simplified proof that when the impedances of transmit and receive antenna arrays are decoupled and matched to characteristic impedance of the RF system, the equivalent impedances on the transmit and receive antenna ports towards the matching networks are intrinsically equal to the conjugates of impedances of transmit and receive antenna array respectively. Then, the section provides the assertion that when optimal transmit and/or receive matching networks are used, the collected power on the loads is maximized for arbitrary fixed inward wave fields $\mathbf{E}_{rx}(-\mathbf{k}_r)$ to the receiver, and the required signal sources' transmit power is minimized for transmit currents $\mathbf{i}_{a,t}$ on the transmit antenna ports.

Lemma 1. Consider the optimal matching networks that satisfy $\mathbf{Z}_{s,t/r} = \mathbf{Z}_{1,t/r} = R_0\mathbf{I}$, the optimal matching networks intrinsically maintain that

$$\mathbf{Z}_{2,t/r} = \mathbf{Z}_{a,t/r}^H, \quad (11)$$

where $\mathbf{Z}_{1,t/r}$ and $\mathbf{Z}_{2,t/r}$ are the respective impedances on the transmit/receive matching networks and antenna ports towards the matching networks as shown in Figure 1.

Proof. The input impedance of the matched transmit/receive antenna array on RF system ports can be expressed as

$$\mathbf{Z}_{1,t/r} = \mathbf{Z}_{ss,t/r} - \mathbf{Z}_{sa,t/r}(\mathbf{Z}_{a,t/r} + \mathbf{Z}_{aa,t/r})^{-1}\mathbf{Z}_{as,t/r} = R_0\mathbf{I}. \quad (12)$$

Assuming $\mathbf{Z}_{as,t/r}$ and $\mathbf{Z}_{sa,t/r}$ are invertible (it omits the cases that $\mathbf{Z}_{as,t/r}$ and $\mathbf{Z}_{sa,t/r}$ are singular. Results pertaining to the singular case can be obtained in the limit of vanishing added loss. Henceforth, we shall make no explicit reference to singular cases), we draw

$$\mathbf{Z}_{a,t/r}^H = \mathbf{Z}_{sa,t/r}^H(\mathbf{Z}_{aa,t/r}^H - R_0\mathbf{I})^{-1}\mathbf{Z}_{sa,t/r}^H - \mathbf{Z}_{sa,t/r}^H. \quad (13)$$

And for the matching network is lossless, that is,

$$\begin{bmatrix} \mathbf{Z}_{aa,t/r} & \mathbf{Z}_{as,t/r} \\ \mathbf{Z}_{sa,t/r} & \mathbf{Z}_{ss,t/r} \end{bmatrix} + \begin{bmatrix} \mathbf{Z}_{aa,t/r} & \mathbf{Z}_{as,t/r} \\ \mathbf{Z}_{sa,t/r} & \mathbf{Z}_{ss,t/r} \end{bmatrix}^H = 0. \quad (14)$$

We get $\mathbf{Z}_{aa,t/r} = -\mathbf{Z}_{aa,t/r}^H$, $\mathbf{Z}_{as,t/r} = -\mathbf{Z}_{ss,t/r}^H$, and $\mathbf{Z}_{sa,t/r} = -\mathbf{Z}_{sa,t/r}^H$, thus

$$\mathbf{Z}_{a,t/r}^H = \mathbf{Z}_{aa,t/r} - \mathbf{Z}_{as,t/r}(\mathbf{Z}_{ss,t/r} + R_0\mathbf{I})^{-1}\mathbf{Z}_{sa,t/r}. \quad (15)$$

The impedance towards matching networks on the antenna ports is

$$\mathbf{Z}_{2,t/r} = \mathbf{Z}_{aa,t/r} - \mathbf{Z}_{as,t/r}(\mathbf{Z}_{ss,t/r} + R_0\mathbf{I})^{-1}\mathbf{Z}_{sa,t/r}. \quad (16)$$

Thus we can draw the conclusion that when the matching network that transfer the antenna impedance to $R_0\mathbf{I}$ is connected to the RF systems, the impedance towards matching networks on the antenna ports is equal to the conjugate of the impedance of coupled antenna array as

$$\mathbf{Z}_{2,t/r} = \mathbf{Z}_{a,t/r}^H. \quad (17)$$

□

Firstly, we consider the effect of optimal receive matching networks on the sum collected power on the loads. For any given inward wave fields $\mathbf{E}_{rx}(-\mathbf{k}_r)$, the characteristics of the antenna array can be represented with equivalent source voltages $\mathbf{V}_{a,r}^{(o)}$ and impedance matrix $\mathbf{Z}_{a,r}$. The received power on the sinks is

$$P_r = \frac{(\mathbf{T}_r \mathbf{v}_{a,r}^{(o)})^H \mathbf{T}_r \mathbf{v}_{a,r}^{(o)}}{2R_0}. \quad (18)$$

According to the maximum power transfer theorem that the output power is maximized when the impedance matrix of the terminations is equal to the conjugate of the impedance matrix of the sources [21], and noting the optimal receive matching networks are lossless, we derive

$$P_r(\mathbf{Z}_{m,r,\text{opt}}) \geq P_r(\mathbf{Z}_{m,r}). \quad (19)$$

Secondly, we consider the effect of optimal matched matching networks on required transmit power of the signal generators. For any given currents $\mathbf{i}_{a,t}$ on the transmit antenna ports, the required transmit power of the signal generators satisfies

$$P_x(\mathbf{Z}_{m,t}, \mathbf{i}_{a,t}) = \frac{\mathbf{v}_x^H(\mathbf{Z}_{m,t}, \mathbf{i}_{a,t}) \mathbf{v}_x(\mathbf{Z}_{m,t}, \mathbf{i}_{a,t})}{4R_0}, \quad (20)$$

where $\mathbf{v}_x(\mathbf{Z}_{m,t}, \mathbf{i}_{a,t}) = \mathbf{T}_t^{-1}(\mathbf{Z}_{m,t})\mathbf{i}_{a,t}$ denotes the voltage vector of signal generators as to excite the antenna currents $\mathbf{i}_{a,t}$ with transmit matching network $\mathbf{Z}_{m,t}$.

According to [21], the exchangeable power of the signal sources can be expressed as

$$P_e(\mathbf{Z}_{m,t}, \mathbf{i}_{a,t}) \geq P_x(\mathbf{Z}_{m,t}, \mathbf{i}_{a,t}) \quad (21)$$

Because the transmit matching networks are passive, the outputted power of the transmit amplifiers must be not less than the radiated power [21]. According that, exchangeable power is the maximum power that can be delivered from the signal sources, we get correctness.

$$P_e(\mathbf{Z}_{m,t}, \mathbf{i}_{a,t}) \geq \frac{\text{Re}\{\mathbf{i}_{a,t}^H \mathbf{Z}_{a,t} \mathbf{i}_{a,t}\}}{2}. \quad (22)$$

For the maximum power will be outputted when the impedance matrix of the terminations is equal to the

conjugate of source impedance matrix, and the optimal transmit matching network is lossless, we get

$$P_e(\mathbf{Z}_{m,t,\text{opt}}, \mathbf{i}_{a,t}) = P_x(\mathbf{Z}_{m,t,\text{opt}}, \mathbf{i}_{a,t}) = \frac{\text{Re}\{\mathbf{i}_{a,t}^H \mathbf{Z}_{a,t} \mathbf{i}_{a,t}\}}{2}, \quad (23)$$

where $P_x(\mathbf{Z}_{m,t,\text{opt}}, \mathbf{v}_{a,t})$ is the transmit power of the signal sources on the transmit antenna ports when the optimal matching network $\mathbf{Z}_{m,t,\text{opt}}$ is applied to excited currents $\mathbf{i}_{a,t}$.

Relating (23) and (24), we derive that

$$P_e(\mathbf{Z}_{m,t}, \mathbf{i}_{a,t}) \geq P_e(\mathbf{Z}_{m,t,\text{opt}}, \mathbf{i}_{a,t}). \quad (24)$$

This shows that the matching networks not only maximize the received power but also minimize the required transmit power. Thus, it is also deserved that the matching networks will improve the BER performance of SM MIMO systems with compact antenna arrays, which is studied in the following.

3.2. Configurations of Numerical Simulations. To demonstrate applications of the analysis framework developed in the paper and illustrate the impacts of mutual coupling and matching networks on channel capacity of MIMO systems between coupled antenna arrays, the simulation constructs the MIMO systems using network framework to explore the possible gain from matching networks as compared to the systems without matching networks.

At first, the section provides the representative parallel dipole antenna arrays, construction of optimal matching networks, and path-based channel model and then demonstrates how to calculate the channel transfer function connected with these models. After the transmit power limitation is set according to the SNR of a reference SISO system, the BERs of the SM MIMO systems with different spaced antennas are calculated with numerical simulation. The configuration of the modulation schemes and detection methods is also presented.

Dipole antennas as very basic antenna element are used to construct the antenna arrays as in Figure 2. All antenna properties (i.e., active gain, pattern, and self- and mutual-coupling impedance) of parallel dipoles are calculated by a standard electromagnetic simulator software tool [24]. To minimize the effects of mismatch for the reference single antenna element, the length of the dipole with a 0.01λ diameter is adjusted to about 0.47λ to make the reactance of the dipole nearly equal to 0 with a real resistance about $R_0 = 72$ ohm, where λ is the wave length. The VSWR of the isolated antenna is less than 1.05 in the carrier frequency. The transmit and receive antenna arrays have the same array configuration for all results presented here, and the largest spacing between the antenna elements is L while the distance between adjacent antenna elements is d as shown in Figure 2. The matching networks that satisfy $\mathbf{Z}_{s,t/r} = R_0 \mathbf{I}$ are used to construct the transmit and receive optimal matching networks as addressed in [25]. Specifically, $\mathbf{h} = \mathbf{jI}$ is chosen.

When the transmit and receive arrays and scattering objects are all in the farfield of one another, a single path-based model can be used to approximate the channel. In flat

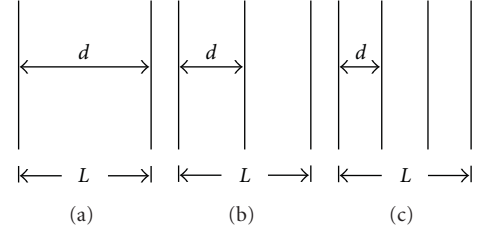


FIGURE 2: Configurations of the parallel dipoles.

fading channel, the channel transfer function relating receive wave fields to transmit wave fields is described as [12]

$$\mathbf{G}_{rt}(-\mathbf{k}_r, \mathbf{k}_t) = \sum_i \beta_i \delta(\mathbf{k}_r - \mathbf{k}_{l,r}, \mathbf{k}_t - \mathbf{k}_{l,t}), \quad (25)$$

where δ represents the delta function, and

$$\beta_l = \begin{bmatrix} \beta_{\theta\theta,l} & \beta_{\theta\phi,l} \\ \beta_{\phi\theta,l} & \beta_{\phi\phi,l} \end{bmatrix}. \quad (26)$$

The Cross Polarization Discrimination (XPD) is defined as

$$\text{XPD} = \frac{E\left\{\sum_l [\beta_{\theta\phi,l}^2 + \beta_{\phi\theta,l}^2]\right\}}{E\left\{\sum_l [\beta_{\theta\theta,l}^2 + \beta_{\phi\phi,l}^2]\right\}}. \quad (27)$$

Thus, incorporating with active radiate patterns of transmit and receive antenna arrays, the channel response \mathbf{H}_0 is

$$\mathbf{H}_0 = \sum_l \mathbf{E}_{a,r}^T(\mathbf{k}_{l,r}) \beta_l \mathbf{E}_{a,t}(\mathbf{k}_{l,t}). \quad (28)$$

In the computations, 1000 random realizations of the path-based, clustered channel model [26, 27] are generated based on a parameter set for 2.5 GHz to model a typical indoor channel for mobile communications, refer to (28).

Because the SNR is affected by the antenna arrays and the matching networks, the normalized SNR assumption is not appropriate. In this paper, the power constraint that limits the output power of signal generators is applied as shown. The single-input single-output system between standard dipoles is used as the reference system. The transmit power limitation is obtained as

$$K_0 = E[\mathbf{v}_x^H \mathbf{v}_x] = \gamma_1 \frac{\sigma_n^2}{E[H_1 H_1^H]}, \quad (29)$$

where γ_1 is the assumed SNR of the reference SISO system, H_1 is the channel transfer function of SISO system according to the random channel realizations, and $E(\cdot)$ is the expectation operation.

In the simulations, the power limitations are constrained by the number of the transmit antennas (individual data streams), that is, $K_t = n_t K_0$. The details of the configurations are listed in Table 1.

In each realization of the channel model, a frame consisting of 50 signal symbols in each individual antenna

TABLE 1: Configurations of the simulation.

n_t/n_r	Source code	Modulation	Bit rate	Power
2	Gray code	4QAM	2	$2P_0$
3	Gray code	4QAM	3	$3P_0$
4	Gray code	4QAM	4	$4P_0$

is transmitted, that is, an information sequence of 100 bits for 4QAM modulation constellation is adopted. Type of mapping employed for mapping symbols to ideal constellation points is Gray code scheme. For the BER performances of MIMO systems are also relative to the receive schemes, maximum likelihood (ML) [28], that is, spherical-decoding scheme [29], and/or zero forcing (ZF) [30], detection methods are employed to detect and decide the received information respectively in receivers.

3.3. Simulation Results. The BER performances of the SM MIMO systems are affected by the spacings between the used linear antenna arrays. When the spacings are large enough to make the mutual coupling between adjacent antennas be ignorable, the MIMO systems work quite good. But when the spacings are less than 0.5λ , the mutual coupling reduces the transmit and receive power efficiencies and distorts the radiation patterns, thereby deteriorate the performance of space-time coding MIMO systems.

In Figure 3, the BER performances of space-time coding MIMO systems relative to SNR with $n_t = n_r = 2, 3, 4$ and $d = 0.1, 0.2, 0.3\lambda$ are considered. As shown, matching networks improve the performance of SM MIMO systems significantly. When matching networks are not used, the differences of BER performances are significant when different spacings d are considered. However, when matching networks are used, the BER performances of the SM MIMO systems with different antenna arrays are nearly same for the multiport matching networks can compensate the power mismatch caused by mutual coupling. The SM MIMO systems employing matching networks outperform the systems without matching networks, for example, the MIMO systems with $d = 0.1\lambda$, and matching networks even perform better than the MIMO systems with $d = 0.3\lambda$ but without matching networks.

As in Figures 3(a) and 3(b), when $n_r = n_t = 2$ and $d = 0.1\lambda$, the SNR gain of matching networks are about 7 and 7.2 dB for 10^{-3} bit error probability with $K = 0$ and $K = 10$, respectively, where K is the K -factors of Ricean channel [20]. And when $n_r = n_t = 2$ and $d = 0.2\lambda_0$, the SNR gain of matching networks are about 1.5 dB and 1 dB for 10^{-3} bit error probability with $K = 0$ and $K = 10$. When d is increased, the SNR gain of matching networks is decreased for the impact of mutual coupling between antennas are less serious. When the numbers of the transmit and receive antennas increase, the SNR gains of the matching networks become more significantly. As in Figures 3(c) and 3(d), the SNR gains of matching networks are about 7 dB and 5 dB with $d = 0.2\lambda_0$ spaced antennas when $K = 0$ and $K = 10$. In Figures 3(e) and 3(f), the SM MIMO systems with $n_t = 4$ and $n_r = 4$ are considered. The SNR gains of matching networks

for MIMO systems with $d = 0.2\lambda$ is 8 and 9 dB for $K = 0$ and $K = 10$. When matching networks are employed, the MIMO systems with $d = 0.1, 0.2$, and 0.3λ nearly have the same BER performances, which are much better than the performance of MIMO systems without matching networks.

The BER performance of MIMO systems with same array size is considered in Figure 4, where the length L of array is equal to $(n_r/n_t - 1 \times d)$ and referenced SNR is 16 dB. As shown, the BER probability of the SM MIMO systems without matching networks increases along the shrinking of spacings when spacings are less than $\sim 0.5\lambda$. However, the BER performances of MIMO systems with matching networks almost maintains when the spacings shrank. When the spacings d between adjacent antennas are larger than 0.5λ , both the systems with and without matching networks have the similar performance. That is, matching networks are more likely to be used when closely spaced antennas are utilized.

4. Impacts of Polarization Diversity on BER Performance of Layered Space-Time Coding MIMO Systems

Although the matching networks can prove the BER performance of narrow band MIMO systems with compact arrays, the implementations of the matching networks are very difficult when the spacings between antenna elements shrink and will limit the application of matching networks on wideband MIMO systems [31]. To resolve the difficulty of constructing matching networks, the polarization diversity antennas are usually used in MIMO systems. The section studies the BER performance of MIMO systems with polarization diversity antenna and compares the performance with that of MIMO systems with linear arrays.

Polarization diversity Antennas are commonly used in communications for decades to obtain diversity gain [32], compensate the power loss causing from polarization mismatch [33], and so on. For the polarization diversity is adopted in addition to spatial diversity, the mutual coupling between polarization diversity antenna is reduced compared to linear arrays when the two kinds of antenna arrays occupy similar volumes. As in [12–14], the use of polarization diversity antenna is a potential solution to construct multiple antennas in volume constraint mobile terminals for mobile communications.

Though mutual coupling is reduced, the array gains of antenna arrays with polarization diversity are usually lessened compare to copolarization antennas. Thus, when the cross-polarization components of the propagation channel are not abundant, there is power loss caused from the reducing of array gain. To compare the performances of MIMO systems with copolarization and polarization diversity antennas when mutual coupling and matching networks are taken into account, in-depth and comprehensive simulations are carried out.

The paper adopts different dual-polarization antennas and linear arrays as shown in 0, which have the same sizes when the element numbers of the antenna arrays are same (The area that the antennas cover is indicated in gray.) as

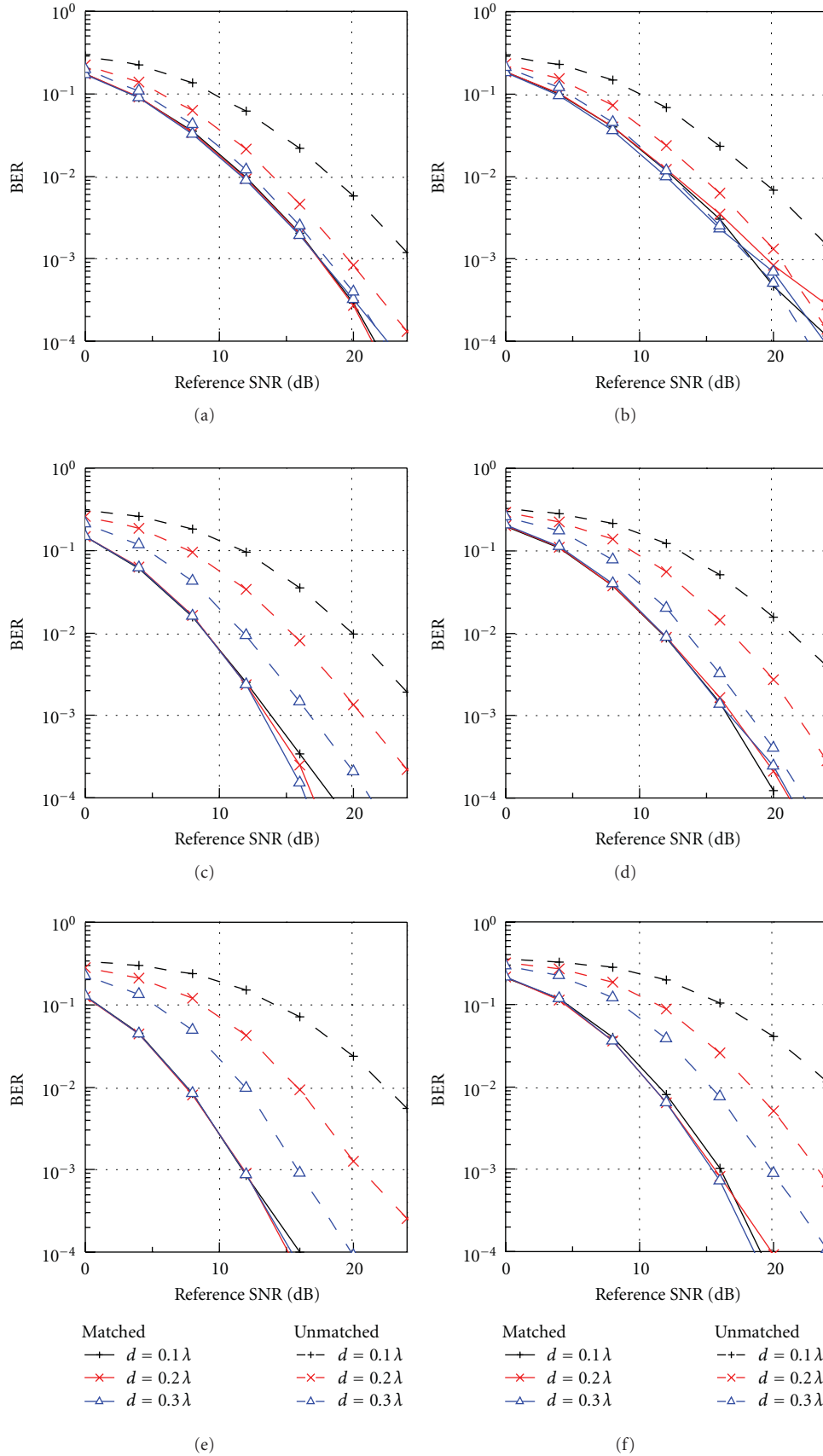


FIGURE 3: BER performances of the SM MIMO systems with linear arrays in Rayleigh and Rician scenarios: (a) $n_t/n_r = 2, K = 0$; (b) $n_t/n_r = 2, K = 10$; (c) $n_t/n_r = 3, K = 0$; (d) $n_t/n_r = 3, K = 10$; (e) $n_t/n_r = 4, K = 0$; (f) $n_t/n_r = 4, K = 10$.

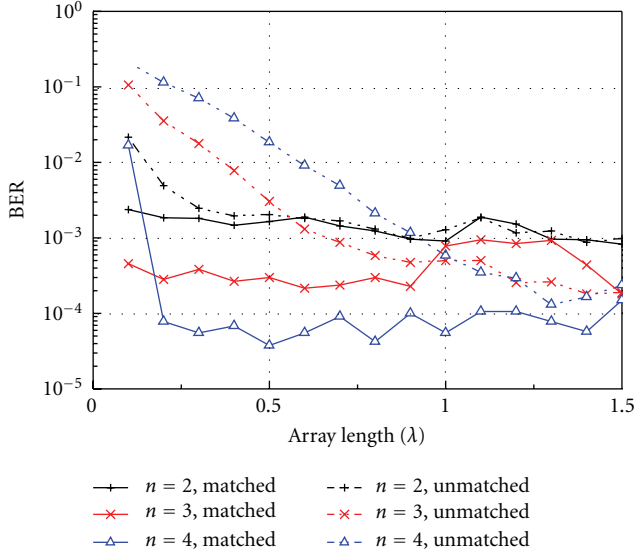


FIGURE 4: Impacts of spacings between antenna elements on BER performances of the SM MIMO systems with linear arrays in Rayleigh scenarios.

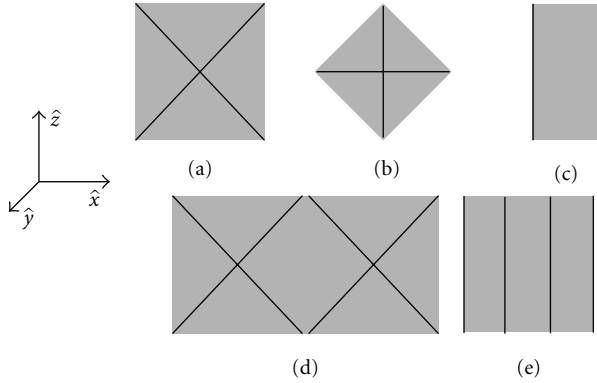


FIGURE 5: Schemes of Antenna Arrays.

shown in Figure 5. The sizes of the arrays are $l_0^2/2$ and l_0^2 when $n_{t/r} = 2$ and 4 respectively. XPD is used to measure the richness of cross polarization components in propagation channels.

4.1. Impacts of Polarization Diversity on BER Performances of MIMO Systems with ML and ZF Receivers. Firstly, the ML receive scheme is considered. The comparisons of the SM MIMO systems using polarization diversity and copolarization antennas are shown in Figure 6. The simulation results of XPD = 0 are shown in Figures 6(a) and 6(b). When matching networks are used, as in Figure 6(a), MIMO systems with linear arrays perform better than the systems with polarization diversity antenna. Considering the 10^{-3} bit error probability, the SNR gains of linear arrays are 3 and 2 dB compared to polarization diversity antenna when $n_{t/r} = 2$ and 4. When matching networks are not used, the MIMO systems with linear array perform better than the systems with polarization diversity antennas when $n_{t/r} = 2$ but

worse than that when $n_{t/r} = 4$. This is because the mutual coupling of linear arrays increases more significantly than that of polarization diversity antennas when the numbers of antennas increase. The simulation results of XPD = -6 dB are shown in Figures 6(c) and 6(d). For the cross polarization components of the propagation channel are short, the performance differences of matched MIMO system with linear array and polarization diversity antennas are larger than that when XPD = 0. The results are similar when matching networks are used.

Secondly, the ZF receive scheme is considered as shown in Figure 7. The simulation results of XPD = 0 is shown in Figures 7(a) and 7(b). When cross polarization components in the propagation channel are rich, the MIMO systems with polarization diversity antennas perform better than the systems with copolarization antennas no matter the matching networks are used or not. The simulation results of XPD = -6 dB is shown in Figures 7(c) and 7(d). When $n_{t/r} = 4$, MIMO systems with polarization diversity antenna perform much better than MIMO systems with copolarization antennas. When $n_{t/r} = 2$, the systems with polarization diversity and copolarization diversity perform similarly.

In general, when the number of antennas is small and the sizes of the arrays are not extremely limited, the use of polarization diversity in MIMO systems which employ ML receivers does not bring considerable benefits especially when matching networks are adopted. But when ZF receivers are adopted, the MIMO systems with polarization diversity antenna are more attractive.

4.2. Impacts of Antenna Orientation Randomness on BER Performances of MIMO Systems with Different Antennas. When applied in handheld devices, the main disadvantage of MIMO systems with arrays consisting of parallel dipoles is the sensitivity to polarization mismatch due to random orientation of devices. If the transmit and receive array are orthogonal, only the cross polarization components are received; thus, the SNR is very low. For polarization diversity antenna can receive inward fields with different polarization, the uses of polarization diversity antenna in MIMO systems are potential to compensate the effects of polarization mismatch [34, 35].

In the simulation, the orientations of the transmit antenna arrays are fixed, while the receive antennas are rotated against the center point randomly. Here, both the transmit and the receive antennas are matched. The radiation patterns of the rotated antennas are drawn by the Euler vector rotation formula as in [36].

As shown in Figure 8, the SM MIMO systems with polarization diversity antenna perform better than the SM MIMO system with parallel antennas. The BER performance of the SM MIMO systems with the randomly rotated receive antennas is similar with that with orientation-fixed antennas when polarization diversity antennas are adopted. However, when parallel dipoles are adopted, the BER performance of the SM MIMO systems with randomly rotated receive antennas deteriorates significantly than that with orientation-fixed antennas. That holds no matter when cross polarization components are rich (XPD = 0 dB) or lacking (XPD = -6 dB).

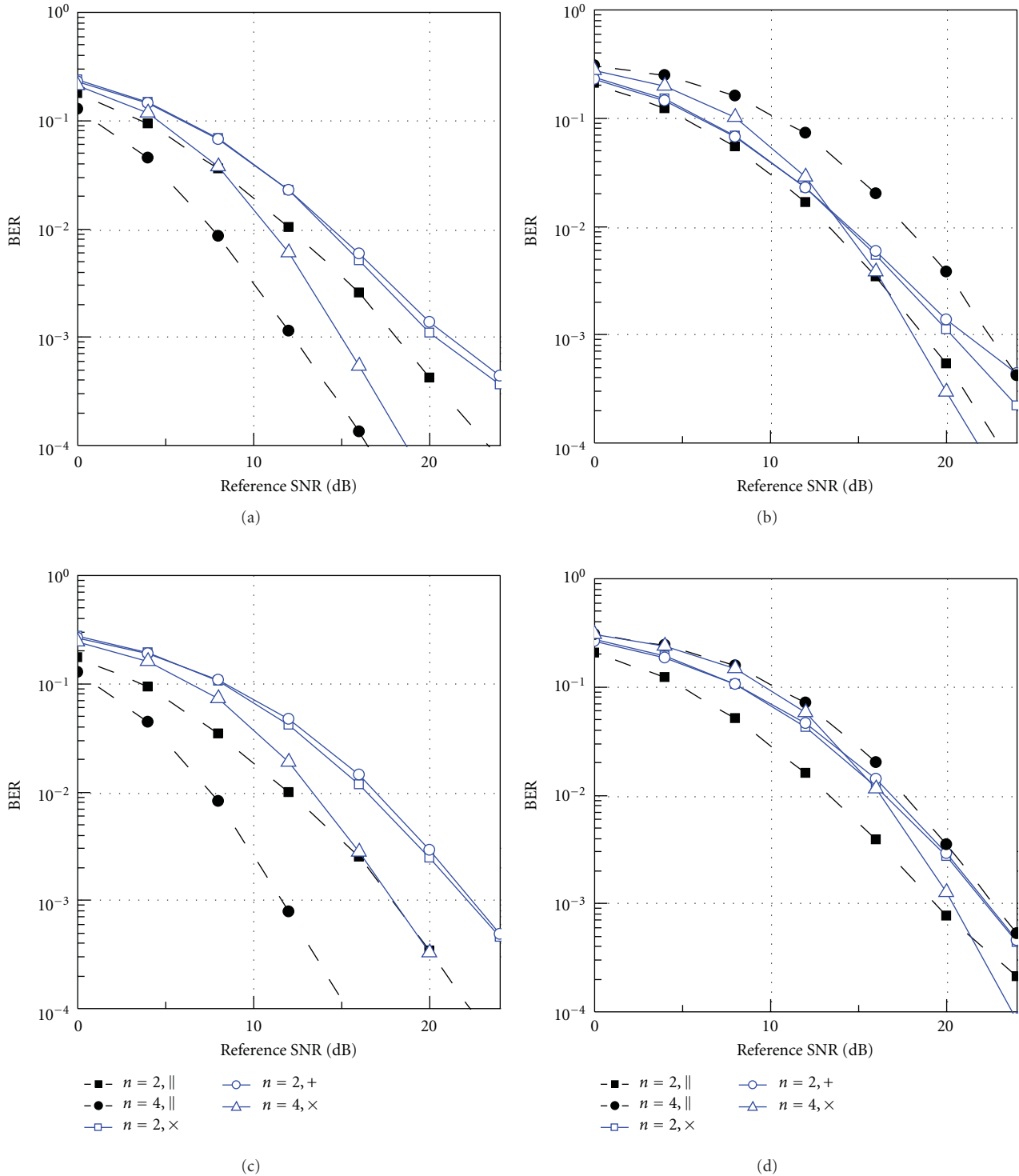


FIGURE 6: BER performances of maximum-likelihood receivers for the SM MIMO systems with polarization diversity when: (a) matched, XPD = 0 dB; (b) unmatched, XPD = 0 dB; (c) matched, XPD = -6 dB; (d) unmatched, XPD = -6 dB.

5. Conclusion

The paper adopts an accurate signal analysis framework based on circuit network parameters to investigate the transmit/receive characteristics of the matched/unmatched

antenna array and the impact of matching networks on the BER performance of the SM MIMO systems. The numerical simulation results show that the matching networks can improve the BER performance of the SM MIMO systems when the antennas are closely spaced. And the narrow

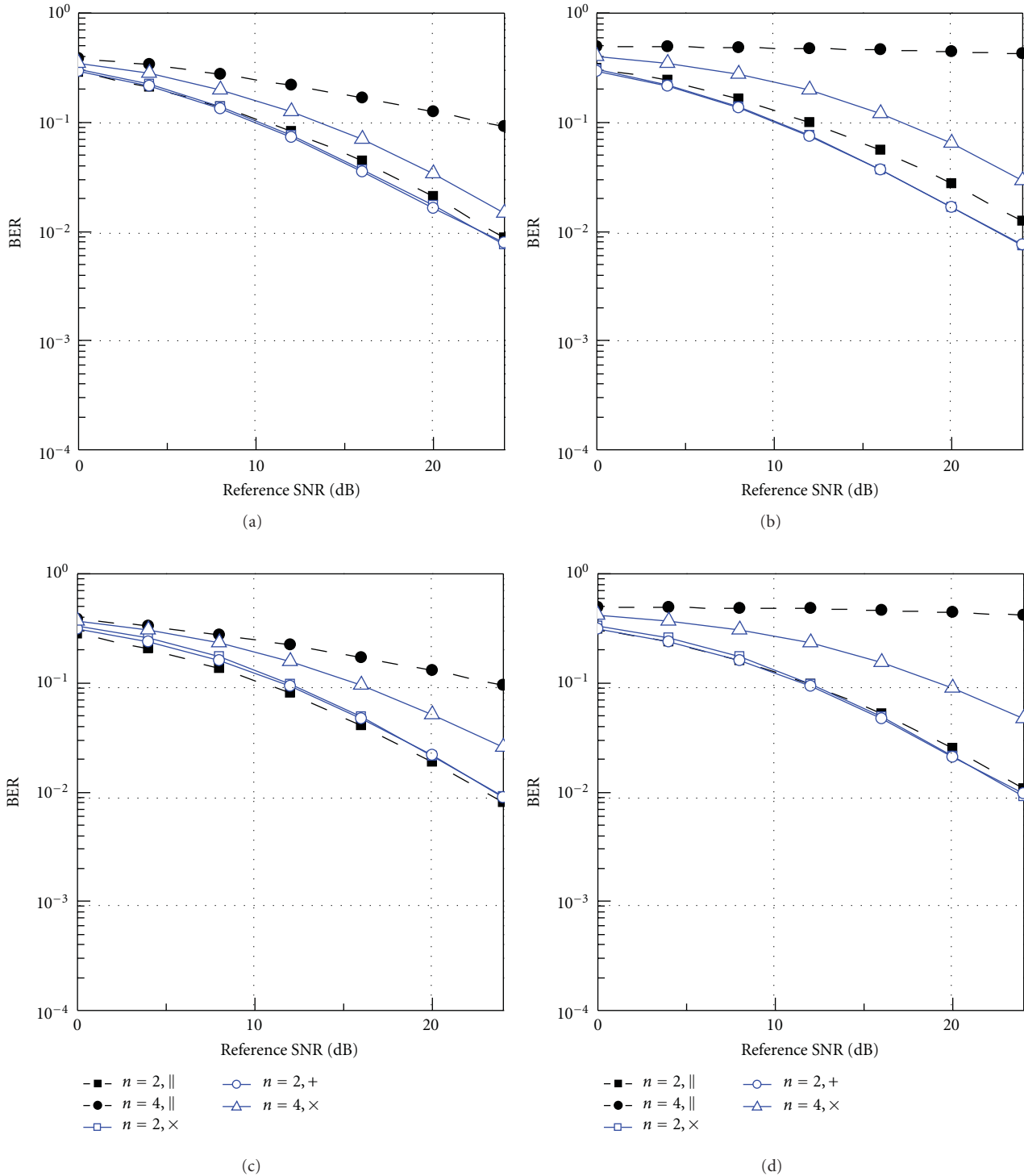


FIGURE 7: BER performances of zero-forcing receivers for space-time coding MIMO systems with polarization diversity when: (a) matched, XPD = 0 dB; (b) unmatched, XPD = 0 dB; (c) matched, XPD = -6 dB; (d) unmatched, XPD = -6 dB.

band MIMO systems with lossless matching networks will maintain the BER performance even when the spacings between antenna elements are around 0.1λ .

The impacts of polarization diversity antennas on BER performance of the SM MIMO systems are also considered. It shows, when comparing to MIMO systems with

matched antennas, the performance improvements due to polarization diversity antennas are not significant. But when antenna orientation randomness is present, the MIMO systems with polarization diversity antennas do perform better than MIMO systems with copolarization antennas whenever the antennas are matched or not matched.

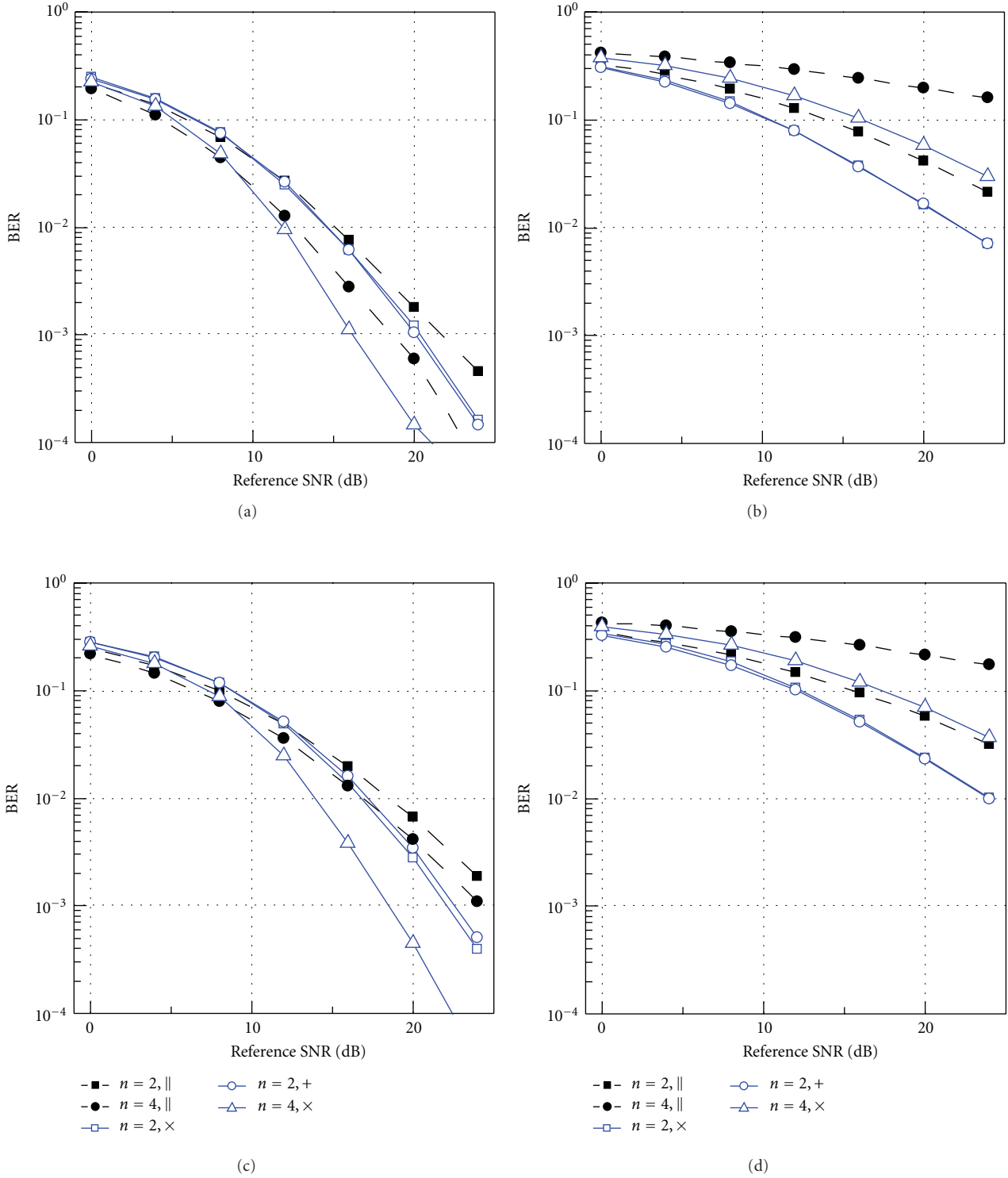


FIGURE 8: Impact of orientation randomness on BER performances of the SM MIMO systems with matching networks when: (a) XPD = 0 dB, ML receiver; (b) XPD = 0 dB, ZF receiver; (c) XPD = -6 dB, ML receiver; (d) XPD = -6 dB, ZF receiver.

Acknowledgments

This work is supported by the National Basic Research Program of China under Contract 2007CB310605. It is also

supported in part by the National Science and Technology Major Project of the Ministry of Science and Technology of China 2010ZX03007-001-01 and the Chuanxin Foundation of Tsinghua University.

References

- [1] G. J. Foschini and M. J. Gans, "On limits of wireless communications in a fading environment when using multiple antennas," *Wireless Personal Communications*, vol. 6, no. 3, pp. 311–335, 1998.
- [2] I. E. Telatar, "Capacity of multi-antenna Gaussian channels," *European Transactions on Telecommunications*, vol. 10, no. 6, pp. 585–595, 1999.
- [3] J. H. Winters, "Optimum combining in digital mobile radio with cochannel interference," *Journal on Selected Areas in Communications*, vol. 2, no. 4, pp. 528–539, 1984.
- [4] A. Paulraj and T. Kailath, "Increasing capacity in wireless broadcast systems using distributed transmission/directional reception," *US Patent*, vol. 5, pp. 345–599, 1994.
- [5] I. J. Gupta and A. A. Ksienski, "Effect of mutual coupling on the performance of adaptive arrays," *IEEE Transactions on Antennas and Propagation*, vol. 31, no. 5, pp. 785–791, 1983.
- [6] C. W. Waldschmidt, S. Schulteis S, and W. Wiesbeck, "Complete RF system model for analysis of compact MIMO arrays," *IEEE Transactions on Vehicular Technology*, vol. 53, no. 3, pp. 579–586, 2004.
- [7] R. Janaswamy, "Effect of element mutual coupling on the capacity of fixed length linear arrays," *IEEE Antennas and Wireless Propagation Letters*, vol. 1, pp. 157–160, 2002.
- [8] P. N. Fletcher, M. Dean, and A. R. Nix, "Mutual coupling in multi-element array antennas and its influence on MIMO channel capacity," *Electronics Letters*, vol. 39, no. 4, pp. 342–344, 2003.
- [9] J. W. Wallace and M. A. Jensen, "Mutual coupling in MIMO wireless systems: a rigorous network theory analysis," *IEEE Transactions on Wireless Communications*, vol. 3, no. 4, pp. 1317–1325, 2004.
- [10] M. L. Morris, M. A. Jensen, and J. W. Wallace, "Superdirectivity in MIMO systems," *IEEE Transactions on Antennas and Propagation*, vol. 53, no. 9, pp. 2850–2857, 2005.
- [11] M. J. Gans, "Channel capacity between antenna arrays-part II: amplifier noise dominates," *IEEE Transactions on Communications*, vol. 54, no. 11, pp. 1983–1992, 2006.
- [12] A. S. Y. Poon, R. W. Brodersen, and D. N. C. Tse, "Degrees of freedom in multiple-antenna channels: a signal space approach," *IEEE Transactions on Information Theory*, vol. 51, no. 2, pp. 523–536, 2005.
- [13] M. R. Andrews, P. P. Mitra, and R. deCarvalho, "Tripling the capacity of wireless communications using electromagnetic polarization," *Nature*, vol. 409, no. 1, pp. 316–318, 2001.
- [14] A. S. Konanur, K. Gosalia, S. H. Krishnamurthy, B. Hughes, and G. Lazzi, "Increasing wireless channel capacity through MIMO systems employing co-located antennas," *IEEE Transactions on Microwave Theory and Techniques*, vol. 53, no. 6, pp. 1837–1844, 2005.
- [15] X. Gao, H. Zhong, Z. Zhang, Z. Feng, and M. F. Iskander, "Low-profile planar tri-polarization antenna for WLAN communications," *IEEE Antennas and Wireless Propagation Letters*, vol. 9, Article ID 5419043, pp. 83–86, 2010.
- [16] G. Foschini, "Layered space-time architecture for wireless communication in a fading environment when using multi-element antennas," *Bell Labs Technical Journal*, vol. 1, no. 2, pp. 41–59, 1996.
- [17] V. Tarokh, N. Seshadri, and A. R. Calderbank, "Space-time codes for high data rate wireless communication: performance criterion and code construction," *IEEE Transactions on Information Theory*, vol. 44, no. 2, pp. 744–765, 1998.
- [18] V. Tarokh, H. Jafarkhani, and A. R. Calderbank, "Space-time block codes with full diversity," *IEEE Transactions on Information Theory*, vol. 45, no. 5, pp. 1456–1467, 1999.
- [19] R. U. Nabar, H. Bölcskei, V. Erceg, D. Gesbert, and A. J. Paulraj, "Performance of multi-antenna signaling techniques in the presence of polarization diversity," *IEEE Transactions on Signal Processing*, vol. 50, no. 10, pp. 2553–2562, 2002.
- [20] K. Yu and B. Ottersten, "Models for MIMO propagation channels," *Wireless Communications and Mobile Computing*, vol. 2, no. 7, pp. 653–666, 2002.
- [21] H. A. Haus and R. B. Adler, *Circuit Theory of Linear Noisy Networks*, McGraw-Hill, New York, NY, USA, 1961.
- [22] J. A. Kong, *Electromagnetic Wave Theory*, Wiley, New York, NY, USA, 1990.
- [23] G. Y. Wen, J. Perry, and Y. H. Qi, "The foster reactance theorem for antennas and radiation Q," *IEEE Transactions on Antennas and Propagation*, vol. 48, no. 3, pp. 401–408, 2000.
- [24] EM Software & Systems-S. A., (PTY) Ltd., FEKO 5.3, Aug. 2006.
- [25] J. Weber, K. Blau, R. Stephan R, and M. A. Hein, "Miniaturized antenna arrays using decoupling networks with realistic elements," *IEEE Transactions on Microwave Theory and Techniques*, vol. 54, no. 6, pp. 2733–2740, 2006.
- [26] Q. Spencer, B. Jeffs, M. Jensen M, and A. L. Swindlehurst, "Modeling the statistical time and angle of arrival characteristics of an indoor multipath channel," *IEEE Journal on Selected Areas in Communications*, vol. 18, no. 3, pp. 347–360, 2000.
- [27] J. W. Wallace, M. A. Jensen, A. L. Swindlehurst, and B. D. Jeffs, "Experimental characterization of the MIMO wireless channel: data acquisition and analysis," *IEEE Transactions on Wireless Communications*, vol. 2, no. 2, pp. 335–343, 2003.
- [28] G. Raleigh and J. Cioffi, "Spatio-temporal coding for wireless communication," *IEEE Transactions on Communications*, vol. 46, no. 3, pp. 357–366, 1998.
- [29] B. Hassibi and H. Vikalo, "On the sphere-decoding algorithm I. Expected complexity," *IEEE Transactions on Signal Processing*, vol. 53, no. 8, pp. 2806–2818, 2005.
- [30] H. Bölcskei, D. Gesbert, C. B. Papadias, and A.-J. van der Veen, *Space-Time Wireless Systems: From Array Processing to MIMO Communications*, chapter 12, Cambridge University Press, New York, NY, USA, 2006.
- [31] B. K. Lau, "Impact of matching network on bandwidth of compact antenna arrays," *IEEE Transactions on Antennas and Propagation*, vol. 54, no. 11, pp. 1983–1992, 2006.
- [32] R. G. Vaughan, "Polarization diversity in mobile communications," *IEEE Transactions on Vehicular Technology*, vol. 39, no. 3, pp. 177–186, 1990.
- [33] D. C. Cox, "Antenna diversity performance in mitigating the effects of portable radiotelephone orientation and multipath propagation," *IEEE Transactions on Communications*, vol. 31, no. 5, pp. 620–628, 1983.
- [34] J. Valenzuela-Valdés, M. García-Fernández, A. Martínez-González, and D. Sánchez-Hernández, "The role of polarization diversity for MIMO systems under Rayleigh-fading environments," *IEEE Antennas and Wireless Propagation Letters*, vol. 5, no. 1, pp. 534–536, 2006.
- [35] D. Landon and C. Furse, "Recovering handset diversity and MIMO capacity with polarization-agile antennas," *IEEE Transactions on Antennas and Propagation*, vol. 55, no. 1, pp. 3333–3340, 2007.
- [36] L. C. Biedenharn and J. D. Louck, *Angular Momentum in Quantum Physics*, Addison-Wesley, Reading, Mass, USA, 1981.